

## Atomic layer deposition for Li-ion batteries

***Citation for published version (APA):***

Hornsveld, N. (2022). *Atomic layer deposition for Li-ion batteries: Novel chemistries, surface reactions and film properties*. [Phd Thesis 1 (Research TU/e / Graduation TU/e), Applied Physics and Science Education]. Eindhoven University of Technology.

***Document status and date:***

Published: 26/01/2022

***Document Version:***

Publisher's PDF, also known as Version of Record (includes final page, issue and volume numbers)

***Please check the document version of this publication:***

- A submitted manuscript is the version of the article upon submission and before peer-review. There can be important differences between the submitted version and the official published version of record. People interested in the research are advised to contact the author for the final version of the publication, or visit the DOI to the publisher's website.
- The final author version and the galley proof are versions of the publication after peer review.
- The final published version features the final layout of the paper including the volume, issue and page numbers.

[Link to publication](#)

***General rights***

Copyright and moral rights for the publications made accessible in the public portal are retained by the authors and/or other copyright owners and it is a condition of accessing publications that users recognise and abide by the legal requirements associated with these rights.

- Users may download and print one copy of any publication from the public portal for the purpose of private study or research.
- You may not further distribute the material or use it for any profit-making activity or commercial gain
- You may freely distribute the URL identifying the publication in the public portal.

If the publication is distributed under the terms of Article 25fa of the Dutch Copyright Act, indicated by the "Taverne" license above, please follow below link for the End User Agreement:

[www.tue.nl/taverne](http://www.tue.nl/taverne)

***Take down policy***

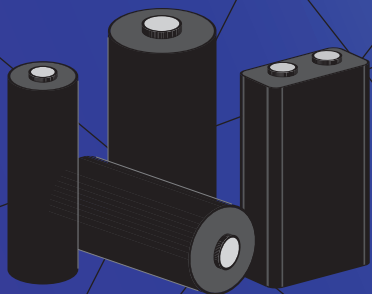
If you believe that this document breaches copyright please contact us at:

[openaccess@tue.nl](mailto:openaccess@tue.nl)

providing details and we will investigate your claim.

# Atomic layer deposition for Li-ion batteries

Novel chemistries, surface reactions and film properties



Norah Hornsveld



# Atomic layer deposition for Li-ion batteries

Novel chemistries, surface reactions and film properties

PROEFSCHRIFT

ter verkrijging van de graad van doctor aan de Technische Universiteit Eindhoven,  
op gezag van de rector magnificus prof.dr.ir. F.P.T. Baaijens, voor een commissie  
aangewezen door het College voor Promoties, in het openbaar te verdedigen op  
woensdag 26 januari 2022 om 16:00 uur

door

Norah Hornsveld

geboren te Soest

Dit proefschrift is goedgekeurd door de promotoren en de samenstelling van de promotiecommissie is als volgt:

voorzitter: prof.dr.ir. G.M.W. Kroesen  
1e promotor: prof.dr. M. Creatore  
2e promotor: prof.dr.ir. W.M.M. Kessels  
leden: dr.ir. J. Beckers  
dr.ir. M. Huijben (Universiteit Twente)  
prof.dr. B. Koopmans  
prof.dr.ir. J.R. van Ommen (Technische Universiteit Delft)  
adviseur: dr. J. Dendooven (Universiteit Gent)

*Het onderzoek dat in dit proefschrift wordt beschreven, is uitgevoerd in overeenstemming met de TU/e Gedragscode Wetenschapsbeoefening.*

### **Funding information**

This research was financially supported by the Dutch program “A green Deal in Energy Materials” ADEM Innovation Lab.



Cover and layout design by Norah Hornsveld  
Printed and bound by Ipskamp printing, Enschede

A catalogue record is available from the Eindhoven University of Technology Library  
ISBN: 978-90-386-54423

# Contents

	List of abbreviations	6
<b>1</b>	<b>Introduction</b>	<b>9</b>
1.1	Lithium-ion batteries	10
1.2	Current trends in Li-battery chemistries and strategies	13
1.3	Opportunities of ALD for Li-ion batteries	21
1.4	Research questions and thesis outline	22
<b>2</b>	<b>ALD of artificial electrode-electrolyte interphase films</b>	<b>31</b>
2.1	The electrode-electrolyte interface	32
2.2	Artificial electrode-electrolyte interphases	34
2.3	Artificial interphase films synthesized by ALD	36
2.4	Conclusions	43
<b>3</b>	<b>ALD principles and diagnostics</b>	<b>51</b>
3.1	ALD basics and capabilities	52
3.2	Characterization of the ALD process	56
3.3	Characterization of the film properties	63
<b>4</b>	<b>Plasma-assisted and thermal ALD of electrochemically active <math>\text{Li}_2\text{CO}_3</math></b>	<b>71</b>
4.1	Introduction	72
4.2	Experimental	73
4.3	Results and discussion	75
4.4	Conclusions	87
	Appendix	91
<b>5</b>	<b>QMS of <math>\text{Li}_2\text{CO}_3</math> film growth by thermal and plasma-assisted ALD</b>	<b>95</b>
5.1	Introduction	96
5.2	Experimental	97
5.3	Results and discussion	98
5.4	Conclusions	106
	Appendix	110
<b>6</b>	<b>ALD of LiF using <math>\text{LiN}(\text{SiMe}_3)_2</math> and <math>\text{SF}_6</math> plasma</b>	<b>115</b>
6.1	Introduction	116
6.2	Experimental	117
6.3	Results and discussion	120
6.4	Conclusions	133
	Appendix	139

<b>7</b>	<b>ALD of aluminum phosphate using AlMe<sub>3</sub>, PO(OMe)<sub>3</sub> and O<sub>2</sub> plasma</b>	<b>149</b>
7.1	Introduction	150
7.2	Experimental	152
7.3	Results and discussion	155
7.4	Conclusions	171
	Appendix	175
<b>8</b>	<b>Conclusions and outlook</b>	<b>183</b>
8.1	Conclusions	184
8.2	Perspectives of future work	187
	<b>Summary</b>	<b>193</b>
	<b>Contributions of the author</b>	<b>197</b>
	<b>List of publications</b>	<b>199</b>
	<b>Acknowledgements</b>	<b>201</b>
	<b>Curriculum Vitae</b>	<b>205</b>



## List of abbreviations

Abbreviation	Full name
ALD	Atomic layer deposition
CEI	Cathode-electrolyte interphase
CVD	Chemical vapor deposition
EEl	Electrode-electrolyte interphase
EBS	Elastic backscattering
EDX	Energy dispersive X-ray spectroscopy
EIS	Electrochemical impedance spectroscopy
EMA	Effective medium approximation
ERD	Elastic recoil detection
GPC	Growth per cycle
GPSC	Growth per supercycle
IBA	Ion beam analysis
ICP	Inductively coupled plasma
LCO	Lithium cobalt oxide
LFP	Lithium iron phosphate
LiPON	Lithium phosphorus oxynitride
LMNO	Lithium manganese nickel oxide
LMO	Lithium manganese oxide
LTO	Lithium titanate oxide
MLD	Molecular layer deposition
NCA	Lithium nickel cobalt aluminum oxide
NMC	Lithium nickel manganese cobalt oxide
PVD	Physical vapor deposition
QMS	Quadrupole mass spectrometer
RBS	Rutherford backscattering spectroscopy
sALD	Spatial atomic layer deposition
SE	Spectroscopic ellipsometry
SEI	Solid-electrolyte interphase
SEM	Scanning electron microscopy
TEM	Transmission electron microscopy
XPS	X-ray photoelectron spectroscopy
XRD	X-ray diffraction





# 1

## Introduction

---

---

The present chapter introduces the field of Li-ion batteries and highlights the relevance of atomic layer deposition (ALD) in this field. In the first section the working principle of a Li-ion battery is described, including the typical materials used. In the following section the current trends in Li-battery chemistries and strategies are presented. In the next section, the opportunities of ALD for Li-ion batteries are briefly reviewed. Finally, the main objective and research questions of this thesis are outlined.

## 1.1 Lithium-ion batteries

With the increasing trend of devices to become mobile and wireless, batteries become more and more important. Batteries as chemical devices are ideal for storing electrical energy in the form of chemical energy. Moreover, batteries will play a crucial role in the future energy system and the strive to create a carbon-neutral society. This is due to the rapid rise of e-mobility, but also to their capacity to balance supply and demand within the electricity system. Numerous different rechargeable battery chemistries exist nowadays, typical examples being lead acid, nickel-cadmium, and nickel metal hydride batteries. Li-ion batteries are now taking dominance for a wide range of applications, due to their high energy and power density over earlier generation batteries. The energy density relates to the amount of energy that can be stored per battery unit, whereas power density relates to the maximum amount of energy that can be (dis)charged per battery unit per unit of time. Batteries with a higher energy density will be able to store larger amounts of energy, while batteries with a higher power density will be able to release higher amounts of energy a lot quicker. In Figure 1.1 a comparison between different battery systems is illustrated in terms of energy density relative to weight and size. As the names imply, the gravimetric energy density, defines the battery energy density in weight ( $\text{Wh} \cdot \text{kg}^{-1}$ ), while the volumetric energy density, reflects the battery energy density in volume ( $\text{Wh} \cdot \text{l}^{-1}$ ). For example, a battery with a higher gravimetric energy density will be lighter than a similar battery with a lower gravimetric energy density. The energy density range for Li-ion batteries is rather broad, as it covers a wide range of Li-ion chemistries, each having their own advantages, targeting different applications. Li-ion batteries are adopted as energy storage solution for applications varying in size from microsystems, portable electronics, electric vehicles up to grid-scale energy storage.<sup>1</sup>

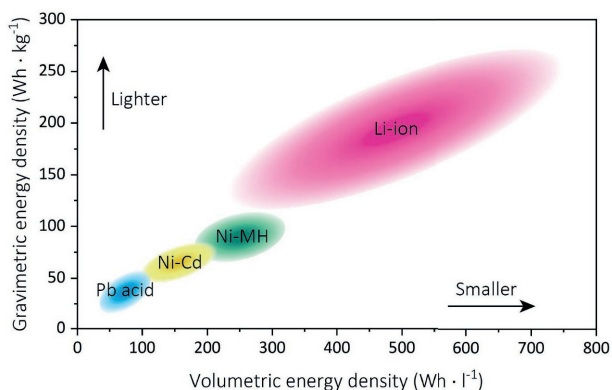


**Figure 1.1** Comparison of energy densities for several rechargeable battery types. Li-ion batteries are ahead of most other battery types in these respects. Lithium-sulfur, sodium-ion and lithium-air batteries are beyond the scope of this research and therefore not shown.

For portable applications, the market share of the Li-ion cell is over 75 %.<sup>2</sup> Electric vehicles cover a huge class of applications ranging from bikes and cars to trucks, ships and planes. Despite their technological promise, Li-ion batteries still have several shortcomings, particularly regarding safety. Li-ion batteries are extremely sensitive to high temperatures and are inherently flammable. For example, Li-ion batteries can be damaged and tend to overheat at high voltages. Safety mechanisms are required to limit voltage and internal pressure, which can increase weight and limit performance in some cases. Li-ion batteries are also subject to capacity loss after a few years and are relatively expensive compared to, for example, Ni-Cd batteries. Moreover, despite the high energy density of Li-ion compared to other kinds of batteries, they are still around a hundred times less energy dense than gasoline (which contains  $12,700 \text{ Wh} \cdot \text{kg}^{-1}$ ). Further advancement of Li-ion battery technology is necessary to meet the future needs regarding energy and power density, weight, charging time, lifetime, safety, and costs. The energy density of Li-ion batteries increased from  $80 \text{ Wh} \cdot \text{kg}^{-1}$  in the 1990s to state-of-the-art  $250 \text{ Wh} \cdot \text{kg}^{-1}$ , with an average growth rate of 7 - 8 % per year.<sup>3</sup> The main reason for this increase is the development of new battery chemistries. This is further discussed in section 1.2.

### 1.1.1 Working principle

The three primary components of a Li-ion battery cell are the negative and positive electrodes and the electrolyte. Li-ion batteries rely on the shuttle of Li-ions back and forth between the two electrodes during charge-discharge cycles. The basics of Li-ion batteries are explained using Figure 1.2 by adopting the most common battery chemistry, i.e. the combination of a graphite anode and a  $\text{LiCoO}_2$  cathode. Strictly speaking, the roles of anode and cathode switch when going from discharging to charging state. Here we use the terms defined during discharging as referred to in the battery literature.<sup>4</sup> During charging, the electrolyte carries positively charged lithium ions from the cathode to the anode. Conventionally, Li-ion batteries use liquid electrolytes, containing a high concentration of a Li salt (e.g.,  $\text{LiPF}_6$  or  $\text{LiClO}_4$ ) to ensure ionic conductivity between the two electrodes. The electrolyte does not conduct electrons. Moreover, the separator prevents physical contact between the anode and cathode and blocks the flow of electrons inside the battery. The release of lithium ions from the cathode induces free electrons which lead to the generation of an electrical current flowing through the positive current collector and the external circuit towards the negative current collector and into the anode. While the battery is discharging, the opposite reaction happens. The anode releases lithium ions, which diffuse towards the cathode. The latter generates a flow of electrons through the negative current collector and the external circuit towards the positive current collector and into the cathode, providing an electric current to the device being powered (cell phone, computer, etc.).

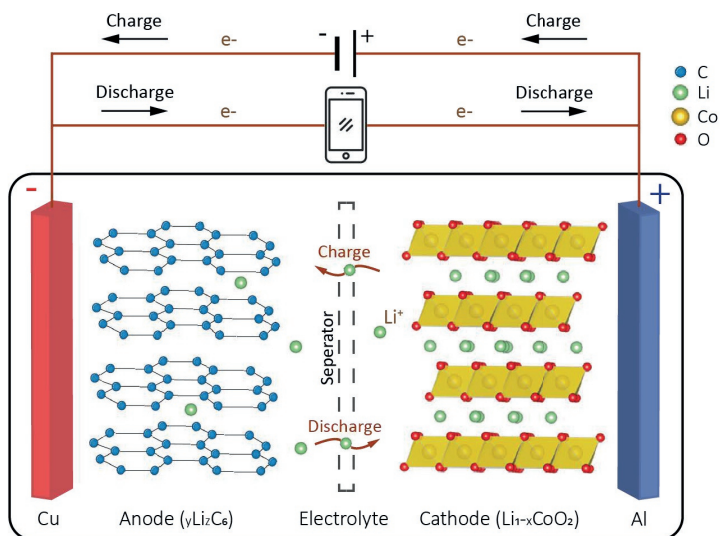
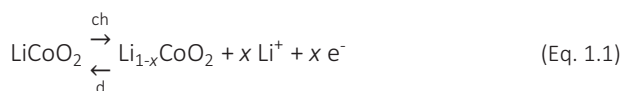
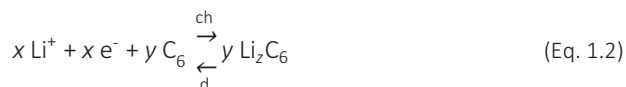


**Figure 1.2** A schematic representation of a typical lithium-ion battery. During discharge, the graphite anode de-intercalates lithium ions and releases electrons. The lithium ions are transported through the electrolyte, while electrons travel through the external circuit generating electricity. Ions and electrons move in the opposite direction during the charging phase. The chemistry at the electrodes is explained using equation 1.1-1.3.

The working mechanism of a Li-ion battery can be understood more clearly when considering the reactions occurring at each electrode. During charging, the cobalt is partially oxidized from  $\text{Co}^{3+}$  into  $\text{Co}^{4+}$  and Li-ions ( $\text{Li}^+$ ) are released:

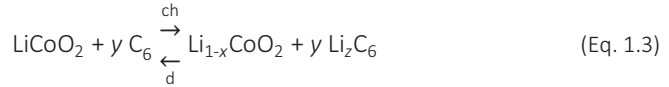


The reverse occurs during discharging: electrons are accepted by the cathode,  $\text{Co}^{4+}$  is reduced to  $\text{Co}^{3+}$  and intercalation of Li-ions takes place to balance the charge. To prevent irreversible structure changes of the  $\text{LiCoO}_2$  electrode, not all  $\text{Li}^+$  ions can be removed and therefore,  $x$  should be less than 0.5. Upon charging,  $\text{Li}^+$  ions are transported into a graphite ( $\text{C}_6$ ) electrode and are subsequently reduced:



Here,  $z = x/y$  and has a maximum value of 1. During discharging the reverse occurs, where the graphite releases electrons and de-intercalates Li-ions which dissolve into

the electrolyte. The full reaction taking place (left to right: discharging, right to left: charging) is then:



The reactions at both anode and cathode must be highly reversible for hundreds of charge/discharge cycles.

When the  $\text{LiCoO}_2$  is fully delithiated, the battery is fully charged. The output potential of the cell finds its origin in the electrochemical potential difference of the electrodes. In general, the standard redox potential of the electrode redox reaction should be low for the anode (e.g., 0.065 - 0.25 V vs  $\text{Li}/\text{Li}^+$  for graphite) and high for the cathode (e.g., 3.9 V vs  $\text{Li}/\text{Li}^+$  for  $\text{LiCoO}_2$ ), leading to a high cell voltage. In the lithium battery community, the electrode potentials are referred to the  $\text{Li}/\text{Li}^+$  system since in a lithium battery the anode typically is Li metal or lithium intercalated in graphite with a redox potential very close to the metal  $\text{Li}/\text{Li}^+$  electrode.

Theoretically, the energy density of the battery is determined by the amount of Li that can be stored reversibly in the electrodes, and by the difference in standard reduction potential between them. This can be seen from following equation:

$$E = Q_{tot} \cdot \Delta V \quad (\text{Eq. 1.4})$$

Here,  $E$  is the total energy stored in the battery,  $Q_{tot}$  is the total charge that flowed during the charging, and  $\Delta V$  is the voltage during the charging.<sup>5</sup> Since both the voltage and Li-ion charge capacity ( $Q_{tot}$ ) are determined by the electrodes, these fully determine the battery's energy density. A battery is commonly characterized by its potential and capacity. The capacity is generally expressed in mAh (1 mAh corresponds to 3.6 C of charge). Another way to characterize the battery is by expressing the energy density as  $\text{Wh} \cdot \text{kg}^{-1}$  (as shown in Figure 1.1), this then incorporates both charge and potential into one quantity.

## 1.2 Current trends in Li-battery chemistries and strategies

A significant improvement in the performance of Li-ion batteries is needed to meet the future needs of our society. This also requires new designs that cover specific purposes. The energy density is a main concern regarding portable and micro-electronics to extend operating time. In contrast, batteries for stationary energy storage particularly need high power output for a short period of time. For electric vehicles, both high power and high energy density are required. The latter would enable a long driving range. Often several additional criteria need to be fulfilled, such as long life, low cost, long autonomy, and high degree of safety, thereby also



minimizing their environmental impact. To date, not any battery configuration meets all the criteria, although many promising developments could enable improved performance. However, the choice of battery for any application will still involve some compromise, as ultimately it might be impossible to develop the 'ideal' battery. Yet, intensive research is being pursued to develop novel, high performance and long-lasting electrodes and electrolytes while keeping in consideration environmental issues as well as wide availability of raw materials.

### 1.2.1 Electrodes

In most cases, carbon materials, such as graphite, are used as anodes, whereas air-stable Li-based metal oxides (usually cobalt, nickel or manganese) are employed as cathodes. Graphite as well as the counter-electrode  $\text{LiCoO}_2$  are typical examples of intercalation-type electrodes. Here, specific lattice sites are available within the crystal structure of the host material, and lithium can diffuse to those sites over diffusion planes in the case of layered materials such as graphite and  $\text{LiCoO}_2$ , or by three-dimensional channels in the case of an open structure such as spinel  $\text{LiMn}_2\text{O}_4$ . Intercalation electrodes typically have less potential lithium storage than conversion electrodes and alloying electrodes, but a better reversibility and coulombic efficiency (the ratio of discharge capacity to charge capacity within the same cycle). Instead, conversion electrodes, such as  $\text{Fe}_3\text{O}_4$  or  $\text{Mn}_3\text{O}_4$ ,<sup>6</sup> and alloying electrodes, such as Sn and Si,<sup>7</sup> offer energy densities up to an order of magnitude higher than intercalation electrodes, but suffer from low coulombic efficiencies and severe volume expansions, respectively. The latter can cause stress formation, electrode fracture and delamination from the current collector. These drawbacks render them less suited for continued cycling. There is a great deal of interest in the development of high-capacity anode materials as well as cathode materials. Hereafter, the state-of-the-art anode and cathode chemistries are being discussed.

#### *Anodes*

Graphite is still applied in the great majority of commercially available Li-ion batteries.<sup>8</sup> The theoretical specific capacity of graphite is  $372 \text{ mAh} \cdot \text{g}^{-1}$  when  $\text{LiC}_6$  is formed. Graphite is currently approaching its theoretical capacity limit. The intercalation of lithium proceeds occurs between 0.1 V and 0.2 V vs  $\text{Li}^+/\text{Li}$  and increases the interlayer distance by ca. 10%.<sup>9</sup> Despite the reliable performance of this anode, there is a number of shortcomings. The major issue is the lithium plating because of the low working potential of graphite (ca. 0.1 V vs  $\text{Li}^+/\text{Li}$ ) and overpotentials at high currents. High currents are needed due to the high charging speed required nowadays. Lithium plating not only causes battery performance decay but is also a safety issue. Consequently, it is of interest to use anodes with a lithiation potential higher than the one of graphite.<sup>10</sup>

Therefore, metal oxides are being investigated as alternatives. Among them,  $\text{Li}_4\text{TisO}_{12}$  (LTO) is especially attractive, even considering the disadvantages of relatively low specific capacity ( $175 \text{ mAh} \cdot \text{g}^{-1}$ ) and relatively high redox potential (1.2 - 2.0 V vs  $\text{Li}^+/\text{Li}$ ). The LTO unit cell volume changes only by 0.2 % upon cycling.<sup>11</sup> Therefore, it is a structurally stable material with excellently reversible  $\text{Li}^+$  de-/insertion. In addition to a negligible volume change, the common benefits of LTO include no electrolyte decomposition, no electrode-electrolyte interphase (EEI) formation, and thereby better safety and cyclability. Nevertheless, it is characterized by a relatively low intrinsic electronic conductivity ( $< 10^{-13} \text{ S} \cdot \text{cm}^{-1}$ ) and low  $\text{Li}^+$  diffusion coefficient, and therefore less suitable for high power applications.<sup>12</sup>

Li metal is considered as the ultimate anode material due to its high theoretical capacity ( $3860 \text{ mAh} \cdot \text{g}^{-1}$  compared to  $372 \text{ mAh} \cdot \text{g}^{-1}$  for graphite) and low redox potential ( $-3.04 \text{ V}$  vs standard hydrogen electrode). Yet, there are concerns related to its adoption, such as dendrite formation, electrolyte consumption as a result of irreversible reaction with metallic lithium, mechanical instabilities and resultant low coulombic efficiency.<sup>13</sup> These shortcomings lead to short lifetime and safety problems. The issues can be partly addressed using artificial EEI layers, as discussed later in section 1.2.4.

Finally, silicon is potentially the best replacement for the graphite anode material because it has a high theoretical gravimetric capacity of  $4200 \text{ mAh} \cdot \text{g}^{-1}$ .<sup>14</sup> The large difference in capacity between silicon and graphite arises because a silicon atom can bond with up to about four lithium ions ( $\text{Li}_{4.4}\text{Si}$ ) while it takes six carbon atoms to bond with only one lithium ion ( $\text{LiC}_6$ ). Si anodes display an appropriate average voltage of ca.  $0.4 \text{ V}$  vs  $\text{Li}^+/\text{Li}$ . Moreover, it is abundant and non-toxic. Unfortunately, Si suffers from poor cyclability due to the large volume change (280% during full-capacity cycling at room temperature), leading to subsequent mechanical and chemical degradation. The problems arising from volume changes can be partly addressed by the synthesis of Si nanoparticles, nanowires, nanotubes, nanofibers, nanorods, thin films and nanosheets, as discussed in section 1.2.3. Another strategy to tackle the volume change issue and electrolyte decomposition is the use of EEI layers. Finally, it is worth mentioning the route of adopting graphite and Si (or  $\text{SiO}_x$ ) in blends and composites, which improve volumetric performance while retaining good cyclability. The presence of oxygen allows a trade-off between volume expansion and initial coulombic efficiency.<sup>15</sup>

### ***Cathodes***

The first lithium-ion cathode material,  $\text{LiCoO}_2$  (LCO), which was commercialized in 1991 by Sony,<sup>16</sup> is still the most popular cathode for lithium-ion batteries due to its high capacity and good cyclability.<sup>17</sup> The theoretical specific capacity of LCO is  $274 \text{ mAh} \cdot \text{g}^{-1}$ ; however, practical utilization is limited to about 50 %. Only half of the lithium ions ( $x = 0.5$ ) are inserted and extracted electrochemically in the structure of  $\text{Li}_{1-x}\text{CoO}_2$

to produce the electrical energy owing to its structural instability at higher voltage of 4.2 V vs  $\text{Li}^+/\text{Li}$ .<sup>18</sup> Intensive studies have been done to overcome these issues, for example by coating the cathode with nanosized metal oxides (such as  $\text{Al}_2\text{O}_3$ ,  $\text{ZrO}_2$ , or  $\text{ZnO}$ ) as artificial EEI. Drawbacks of LCO cathodes are the relatively high costs, toxicity, and availability of cobalt.

Lithium manganese oxide,  $\text{LiMn}_2\text{O}_4$  (LMO), was introduced a few years later,<sup>19</sup> followed by  $\text{LiNi}_{0.5}\text{Mn}_{1.5}\text{O}_4$  (LNMO),  $\text{LiNi}_{1-x-y}\text{Al}_x\text{Co}_y\text{O}_2$  (NCA),<sup>20</sup> and  $\text{LiNi}_{1-x-y}\text{Mn}_x\text{Co}_y\text{O}_2$  (NMC).<sup>21</sup> LMO forms a three-dimensional spinel structure that improves the ion flow, which results in lower internal resistance and improved current handling. A further advantage of spinel structures is their high thermal stability and enhanced safety. However, the disadvantage is that LMO suffers from severe capacity fading during discharging/charging. LMO has a more moderate theoretical specific energy than cobalt, namely  $148 \text{ mAh} \cdot \text{g}^{-1}$ . The practical specific capacity approaches to  $120 \text{ mAh} \cdot \text{g}^{-1}$ . Several attempts have been made for synthesizing modified  $\text{LiMn}_2\text{O}_4$  doped with various elements to inhibit capacity fading and improve the electrochemical performance. The Ni-substituted spinel LMNO is one of the most studied high-voltage (above  $\sim 4.2 \text{ V}$  vs  $\text{Li}^+/\text{Li}$ ) cathode materials. Nickel confers higher charge density by increasing the voltage of the battery to values of  $4.7 \text{ V}$  vs  $\text{Li}^+/\text{Li}$ . However, the high operating potential of these cathodes leads to electrolyte decomposition and formation of detrimental by-products.<sup>22</sup> Furthermore, LMNO shows the phenomenon of Mn dissolution in the electrolyte during cycling, which leads to faster ageing of the entire electrochemical system.<sup>23</sup> The introduction of NCA led to an outstanding increase in specific energy and longer lifetime. NMC significantly improved lifetime and safety, but at the cost of lower energy density.<sup>24</sup> Nickel is known for its high specific energy but poor stability; manganese has the benefit of forming a spinel structure to achieve low internal resistance but offers a low specific energy. Combining the metals enhances each other strengths. NMC electrodes with a stoichiometry of  $\text{LiNi}_{0.33}\text{Mn}_{0.33}\text{Co}_{0.33}\text{O}_2$  have a theoretical specific capacity of  $280 \text{ mAh} \cdot \text{g}^{-1}$ . NMC is the battery of choice for, for instance, power tools and e-bikes.

Lithium transition metal phosphates with an olivine structure were first introduced late nineties.<sup>25</sup> Since then, various transition metals and combinations have been investigated, such as iron, manganese, vanadium, cobalt, and nickel. The reversible charging mechanism involves the transition between different crystalline phases, e.g.,  $\text{LiFePO}_4$  (LFP) and  $\text{FePO}_4$ . The maximum theoretical specific capacity of LFP is  $170 \text{ mAh} \cdot \text{g}^{-1}$ . The main drawback of LFP is its low electrical conductivity. Therefore, all the LFP cathodes under consideration are actually  $\text{LiFePO}_4/\text{C}$ .<sup>26</sup> Because of low cost, low toxicity, well-defined performance and long-term stability,  $\text{LiFePO}_4$  is finding a number of applications in vehicles, utility scale stationary applications and backup power. The Chinese electric bus market, for example, is currently dominated by LFP-based lithium-ion cells.<sup>27</sup>

### 1.2.2 Electrolytes

In classical Li-ion batteries the electrolytes are in liquid phase and consists of a lithium salt, such as  $\text{LiPF}_6$ ,  $\text{LiBF}_4$ , or  $\text{LiClO}_4$ , dissolved in an organic solvent, such as ethylene carbonate, dimethyl carbonate or diethyl carbonate. Typical ionic conductivities of liquid electrolyte at room temperature ( $20\text{ }^\circ\text{C}$ ) are in the range of  $10^{-2}$  -  $10\text{ S} \cdot \text{cm}^{-1}$ . Liquid electrolyte batteries typically possess bulky electrodes which are a mixture of electrode material, conductive additives (e.g. carbon black) and a binder. A schematic of the structure is shown in Figure 1.3. The liquid electrolyte penetrates the porous network, facilitating the  $\text{Li}^+$  transport. A separator is adopted between the anode and cathode and soaked in the liquid electrolyte. The main function of a separator is to keep the two electrodes apart to prevent electrical short circuits while also allowing the transport of lithium ions. The biggest drawback of the use of these types of electrolytes is the presence of the flammable organic solvent, which poses a significant safety risk due to the possibility of leaks. In addition, batteries with liquid electrolytes can suffer of limited power output because of the long distance that Li-ions need to diffuse through. Another issue when using liquid electrolytes is their instability in contact with the electrodes. High cathode potentials or low anode potentials typically give rise to an electrode-electrolyte interphase (EEI) when using a liquid electrolyte. The EEI might stabilize the contact between the electrode and the liquid electrolyte as it prevents further contact between the two compounds. A typical example is seen in graphite, which can only be used due to the formation of a stable EEI. However, an EEI typically adds a significant impedance component to the system, reducing the power output of the device. At present no good electrolytes are

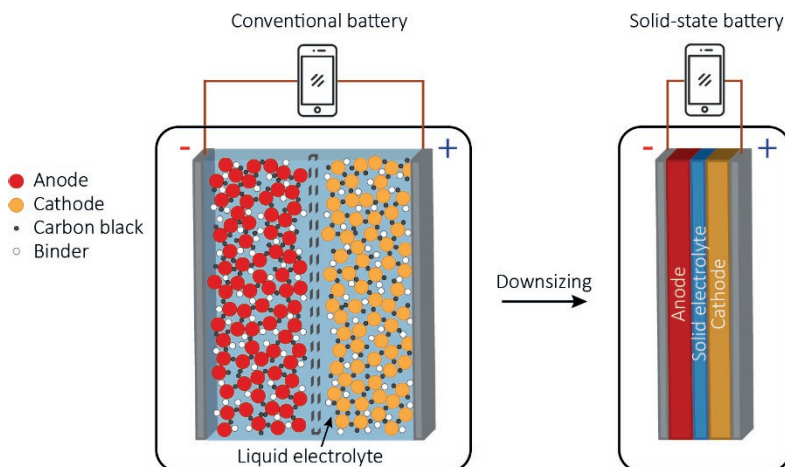


**Figure 1.3** Schematic of the cross-sections of a conventional and a solid-state Li-ion battery structure.

found that are stable or form a stabilizing EEI in contact with high voltage electrode materials.

Therefore, recent advances in battery research involve the application of solid electrolytes. The main benefits of solid electrolytes are that there is no risk of leaks and electrolyte decomposition issues are greatly reduced. Solid electrolytes typically have a better electrochemical stability window, a higher thermal stability and good electronic resistivity. Moreover, the separator and safety packaging can be omitted, increasing the energy density, and allowing for a simplified battery structure. Solid-state batteries rely on the construction of solid films of anode, solid electrolyte and cathode material, sequentially on a substrate (or vice versa). Figure 1.3 shows the schematic cross-section of such a lithium battery structure. However, the main limitation of solid electrolytes is their ionic conductivity which is lower than that of their liquid counterparts.<sup>28,29</sup> Solid-state electrolytes are classified as organic and inorganic solid electrolytes. Organic electrolytes are feasible for flexible battery designs owing to their soft intrinsic features. However, these materials face other issues, such as low  $\text{Li}^+$  conductivity ( $< 10^{-5} \text{ S} \cdot \text{cm}^{-1}$  at room temperature), large ionic transfer resistance, and oxidation at high voltages.<sup>30</sup> Inorganic solid electrolytes consists of an inorganic material in the crystalline or glassy state, which conducts ion by diffusion through the lattice.<sup>31</sup> Inorganic solid-state electrolytes can be oxide-, sulfide- or phosphate-based. Yet, the highest Li-ion conductivity in a solid material was reported to be  $\sim 10^{-2} \text{ S} \cdot \text{cm}^{-1}$  in the sulfide-based, superionic conductor  $\text{Li}_{10}\text{GeP}_2\text{S}_{12}$ .<sup>32</sup> Although this structure has excellent lithium conductivity, it proves highly reactive. The limited stability of this material prevents its practical use. Other typical examples of high performing electrolytes are the garnet structured  $\text{Li}_{6.75}\text{La}_3\text{Zr}_{1.75}\text{Nb}_{0.25}\text{O}_{12}$  ( $\sim 10^{-4} \text{ S} \cdot \text{cm}^{-1}$ ),<sup>33</sup> and the perovskite  $\text{Li}_{3x}\text{La}_{2/3-x}\text{TiO}_3$  ( $\sim 10^{-4} \text{ S} \cdot \text{cm}^{-1}$ ).<sup>34</sup> Despite their high ionic conductivities, these materials are not suitable for use in batteries. One frequent problem with high ionic conductive electrolytes is the limited stability window, e.g.,  $\text{Li}_{3x}\text{La}_{2/3-x}\text{TiO}_3$  gets reduced below 1.5 V vs  $\text{Li}^+/\text{Li}$ . Another issue is the required annealing temperature to limit the influence of grain boundaries. Annealing lead to intermixing between the different battery components, which might lead to the onset of electronic conductivity. So far, the most successful solid electrolyte seems to be nitrogen doped lithium phosphate glass ( $\text{Li}_x\text{PO}_y\text{N}_z$ ). Although LiPON does not have an extremely high lithium conductivity ( $\sim 10^{-6} \text{ S} \cdot \text{cm}^{-1}$ ), it shows a remarkably wide electrochemical stability window ranging from 0 up to 5.5 V vs  $\text{Li}^+/\text{Li}$ . Furthermore, it has a low electronic conductivity ( $\sim 10^{-14} \text{ S} \cdot \text{cm}^{-1}$ ) and thus allows batteries with very low self-discharge rates. A way to compensate for the lower ionic conductivity of solid electrolytes is by further downscaling the thickness of the solid electrolyte layers. A 100 nm thick electrolyte layer with conductivity of  $10^{-6} \text{ S} \cdot \text{cm}^{-1}$  will have the same ionic resistance as a 10  $\mu\text{m}$  electrolyte with conductivity of  $10^{-4} \text{ S} \cdot \text{cm}^{-1}$ . Therefore, their thickness is typically limited to a few tens of nm to guarantee sufficient Li-ion transport. Currently, solid-

state batteries have found use in pacemakers, radio-frequency identification (RFID) and wearable devices. Increase in utilization of solid-state batteries in healthcare, wearable and drone applications boosts the growth of solid-state batteries.

### 1.2.3 Nano-structuring

Currently, there is a trend in conventional Li-ion batteries towards nano-structuring of the electrode materials.<sup>1,35,36</sup> Commercial battery electrodes are mostly based on micrometer-sized particles of electrode material, which are mixed with binder compounds and conductive additives to form the electrode (see Figure 1.4a). When going to smaller particle sizes the surface-to-volume ratio will increase and hence also the power output will increase. However, downscaling the particles to nanometer scale would cause an increase in undesired side-reactions and solid electrolyte interphase formation due to the large surface area exposed to the liquid. For the emerging solid-state batteries (see Figure 1.4b-d) such a trend towards nano-structuring can also be observed. Although the system in Figure 1.4b has a large amount of electrode material (thick films), the long charging times prevent the usage of the full practical capacity. When downscaling the layer thickness, the diffusion distance of the lithium ion reduces (Figure 1.4c). Therefore, charging and discharging requires less time, leading to a higher power output. In addition, this allows usage of the full electrode capacity since extreme charging times are no longer required. However, the capacity per footprint area is constrained by the limited thickness of the thin-film device. The film thickness is constrained by low ion and electron diffusion, similar to the constraints in particle size in conventional batteries.<sup>36,37</sup> Nano-structuring of thin-film batteries has the potential to increase storage capacity

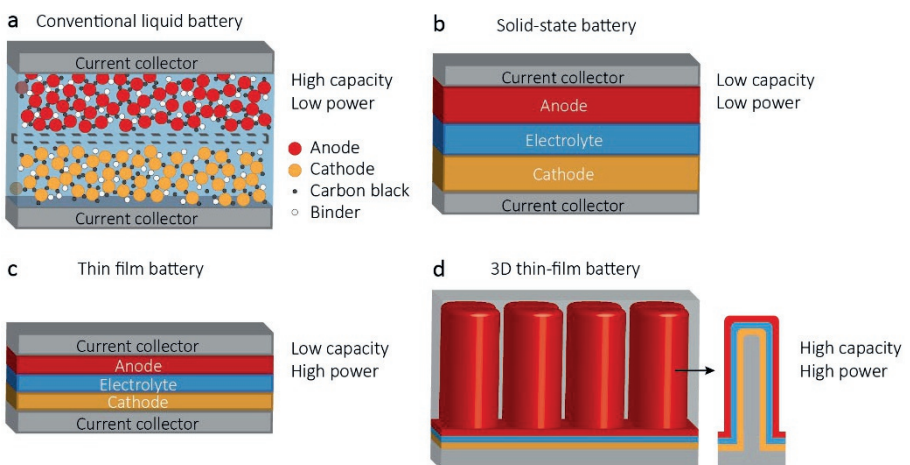


**Figure 1.4:** Different battery architectures and their properties in terms of capacity and power.

without compromising on power density. Using nano-structuring the total amount of electrode material, and thus storage capacity, is increased without the need to increase the film thickness (see Figure 1.4d).<sup>38</sup> In Li-ion battery literature, nano-structured batteries are typically referred to as 3D batteries. Calculations show that theoretically, capacities can be increased multifold compared to planar thin-film batteries and can even surpass that of coin cells.<sup>39</sup> For example, a capacity 10 times larger than that of planar thin-film batteries (i.e.,  $1 \text{ mAh} \cdot \text{cm}^{-2}$ ) could be achieved by using an aspect ratio (AR) of 200 with an electrode thickness of 100 nm or an AR of 50 with an electrode thickness of 370 nm. By using a large contact area with the electrolyte and/or the current collector, the solid electrolytes with low conductivity are compatible and a high power output is obtained.

#### **1.2.4 Electrode-electrolyte interphase**

At the electrode surfaces, an electrode-electrolyte interphase (EEI) is formed from decomposition products of the electrolytes. The formation of an EEI layer occurs when the redox potential of the electrodes used in a battery lies outside the electrochemical window of the electrolyte. This is further explained in Chapter 2. As mentioned before, the EEI might stabilize the contact between the electrode and the liquid electrolyte as it prevents further contact between the two components. However, it typically adds a resistance to the system, reducing the power output of the device. Moreover, EEI formation and growth consume active lithium and electrolyte materials, leading to an increasing battery resistance and thus degradation of the battery performance. The EEI is mainly formed during the first few charging cycles. In comparison to the EEI on the cathode, the EEI on the anode is more unstable due to the evident reduction reactions and the larger volume expansion of anode materials (e.g. Li and Si). A good quality EEI allows  $\text{Li}^+$  transport while blocking further electrolyte decomposition.<sup>40</sup> An ideal EEI film should restrain dendrite growth, surface roughening, and reduce the unexpected side reactions at the electrode-electrolyte interface. While not completely understood, this nanometer scale EEI film is of paramount importance to the performance of the battery.

To achieve good interface compatibility between the electrolyte and electrode, artificial EEIs were proposed to stabilize the interfaces. Fabrication of artificial EEIs has drawn increasing attention due to its effectiveness in performance improvement, the promise of scalable manufacturing, and more important, the tunability of properties in all aspects. The physical and chemical properties of artificial EEI's can be finely designed and tuned to address the previously mentioned drawbacks of natural EEI.<sup>41,42</sup> Artificial EEIs were shown to improve the performance of essentially all (novel) electrodes previously mentioned in section 1.2.1. An artificial EEI can be fabricated by physically coating functional materials on the electrode surface. In this regard, both the conventional solution casting method as well as more advanced

methods, including chemical vapor deposition (CVD), physical vapor deposition (PVD) and atomic layer deposition (ALD), are currently being explored at research level.<sup>41</sup>

### 1.3 Opportunities of ALD for Li-ion batteries

ALD is a thin film deposition process first emerged in 1970s, credited to Suntola et al.<sup>43</sup> Distinguished from other deposition techniques, such as chemical vapor deposition (CVD), physical vapor deposition (PVD) and solution-based methods, ALD operates with a unique mechanism based on sequential and self-limiting half reactions. Therefore, excellent uniformity and conformality on demanding substrate topologies and precise growth control with Angstrom-level resolution can be achieved. The ALD principles are further discussed in Chapter 2. The first application of ALD for lithium-ion batteries was already reported in 2000, when thin  $V_2O_5$  films were investigated as Li-ion battery cathodes.<sup>44</sup> Several years later, ALD was used for interface modification (TiN on  $Li_4Ti_5O_{12}$ ).<sup>45</sup> The first summary of ALD in batteries appeared in 2012 by Meng et al.<sup>46</sup> Stimulated by the ALD's characteristics, ALD is attracting an increasing interest to explore opportunities in the field of Li-ion batteries.<sup>47</sup> This is evident from the yearly number of publications on ALD for Li-ion battery applications as shown in Figure 1.5. The yearly publication yield is saturating in the last three years; however, the yearly citation count keeps increasing. The total number of publications today is around 1000 and the number of citations is around 50,000. Moreover, the online ALD database shows an ever increase in number of available ALD chemistries.<sup>48</sup> This shows the possibility to explore more and more different battery chemistries using ALD.

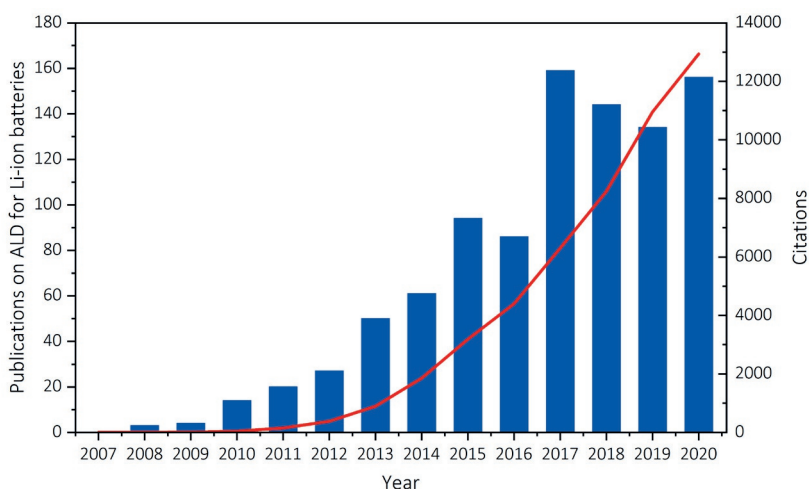


**Figure 1.5** The yearly number of publications (blue bars) and citations (red line) on ALD for Li-ion batteries from 2007-2020, analyzed from Web of Science.



The application of nanolayers prepared by atomic layer deposition (ALD) has attracted notable interest from the battery community because of the excellent conformality and precise growth control that can be achieved. These merits enable processing virtually on any substrate, from powders to porous substrates, or any other complex electrode surface structures for next generation batteries. When going to smaller electrode particle sizes to increase the surface-to-volume ratio and hence increase the power output of conventional batteries, decomposition of the electrolyte during cycling could also increase. This adverse effect can be reduced or possibly prevented by modifying the surface of the particles by applying a passivating or protective artificial EEI film. Such films need to be ultrathin to have sufficient  $\text{Li}^+$  or electron conductivities while excellent conformality is needed to be sufficiently protective. For example, improved stability was demonstrated by depositing  $\text{Al}_2\text{O}_3$  on  $\text{LiCoO}_2$  particles.<sup>49</sup> In addition, ALD offers tunable film composition and relatively low deposition temperatures to design coatings specifically applicable to certain electrodes. Furthermore, ALD is considered an enabling technology for several concepts of nanostructured Li-ion batteries.<sup>38</sup> ALD is used for accurately exploiting various high-performance Li-ion battery components including anodes, cathodes and electrolytes, controlled in thickness at sub-nm level. Even current collectors or coatings for enhancing battery manufacturability (sacrificial coatings) can be deposited by ALD. In this thesis we will focus on the research area of ALD to deposit films which can serve as artificial EEI films, as outlined through the research objectives in next section.

## 1.4 Research questions and thesis outline

ALD is proven to be very suitable for the deposition of thin films serving as artificial EEI in Li-ion batteries. A large part of literature studies focuses on the application of ALD artificial EEIs and the effect on the battery performance instead of investigating possibilities of the ALD process itself. The current work aims to develop and understand existing and novel plasma-assisted and thermal ALD chemistries to deposited thin films which can serve as artificial EEI. Specifically, lithium carbonate ( $\text{Li}_2\text{CO}_3$ ), lithium fluoride ( $\text{LiF}$ ), and aluminum phosphate ( $\text{AlP}_x\text{O}_y$ ) are selected. Application of this materials as artificial EEI has been demonstrated in literature, as will be addressed in detail in Chapter 2.  $\text{Li}_2\text{CO}_3$  is useful as artificial EEI due to its good chemical and electrochemical stability and purely ionically conductive behavior.  $\text{LiF}$  is also known to have a good chemical and electrochemical stability and, just like  $\text{Li}_2\text{CO}_3$ , it also exists in spontaneously generated EEI films.  $\text{AlP}_x\text{O}_y$  is shown to effectively impede side-reactions and improve thermal stability of certain electrodes. Despite the widespread investigation of these materials, there are only few studies in literature focusing on the characterization of the ALD process, as well as on the in-depth analysis of the film properties. By exploring the tunability of the ALD process more freedom in

design of film properties will be obtained. Such studies are particularly useful to be able to rationally design ALD films, and ultimately to improve the battery interphase and thus the performance of the batteries. Moreover, plasma-assisted ALD processes are currently less explored and potentially interesting in the field of Li-ion batteries. Plasma-assisted ALD processes can have unique properties and benefits which allow further expanding the possibilities of ALD. This includes more freedom in, for instance, film composition, crystallographic properties, and mechanical properties. These advantages could also be beneficial for the application in (thin-film) Li-ion batteries. For example, (ionic) conductivity often depends on the film composition and crystallographic properties and the mechanical properties are important for anodes that undergo large volume changes.

### **1.4.1 Research questions**

A research question central to this project has been formulated as a guideline for the work described in the remaining chapters: *Can the adoption of plasma in ALD processes for materials which can potentially be useful in Li-ion batteries lead to more freedom in the design of film properties and in general in improved processing and film properties?*

The main research question has been divided into five key sub-questions to give more structure to the research. These sub-questions are outlined and briefly explained below:

- *What are the film growth characteristics (saturation curves, growth-per-cycle, temperature window) of the selected processes?*  
When developing new ALD processes, it is necessary to investigate the growth process. Investigation of the growth process provides insight, for example, into the growth per cycle, temperature dependence and processing time.
- *How can we tune the film properties using the ALD process parameters?*  
ALD process parameters can influence the film properties and therefore the film quality. Insight into the film properties will also provide a better understanding of the films. In this work, we mainly investigated the dependence of the processing temperature and plasma exposure time on the film properties, such as the stoichiometry.
- *What are the underlying reaction mechanisms of the selected ALD processes?*  
To gain more insight into the deposition process, the reaction products of the ALD processes are analyzed. Insight into the surface reactions can help to understand why a certain film stoichiometry is obtained for the as-deposited films. Moreover, it can give insights into the benefits of using plasma as a coreactant.

- *What are the differences between the plasma-assisted processes and their thermal counterparts?*

The model systems studied in this research are very suitable for mapping the differences between plasma-assisted and thermal ALD. A comparison in terms of growth behavior but also chemical, crystallographic, optical, electrochemical properties of the films will be useful.

- *What are the merits of plasma-assisted ALD processes for deposition of materials which could serve as artificial EEI?*

Besides pointing out the differences between plasma-assisted and thermal ALD, it is also interesting to specifically investigate the benefits and the potential of plasma-assisted ALD. As mentioned before, plasma-assisted ALD could offer more freedom in film properties. However, recombination of reactants at surfaces in plasma-assisted ALD can potentially lead to poor uniformity and conformality. The conformality is especially interesting to demonstrate the applicability for 3D battery architectures. Therefore, this thesis also proves the ability to deposit thin films conformally in high-aspect-ratio structures.

### **1.4.2 Thesis outline**

In Chapter 2, the EEI and the need for artificial EEIs in Li-ion batteries is further explained. Moreover, the relevance of ALD for artificial EEIs is extensively discussed. A thorough review on the existing ALD processes specifically for EEI films is carried out. This study gives insight into which ALD materials already have been tested and what the results were.

In Chapter 3, the ALD principles are explained in more detail. The common denominator among the next chapters of this thesis is the adoption of diagnostics during the ALD process, such as spectroscopic ellipsometry and mass spectrometry, to identify the surface reaction mechanisms and to learn how to tune the properties of the deposited films. Therefore, the frequently used characterization tools are explained as well.

Next, in Chapter 4, the investigation of the plasma-assisted and thermal of ALD  $\text{Li}_2\text{CO}_3$  is presented.  $\text{Li}_2\text{CO}_3$  ALD is considered an attractive model process for incorporating Li into multicomponent (ternary) ALD materials, since it is a highly stable compound with respect to process stability and ease of postdeposition analysis of the films. In the case-study of  $\text{Li}_2\text{CO}_3$ , the differences between the plasma-assisted process using  $\text{LiO}^t\text{Bu}$  and  $\text{O}_2$  plasma and the thermal process using  $\text{LiO}^t\text{Bu}$ ,  $\text{H}_2\text{O}$  and  $\text{CO}_2$  are identified in terms of film growth, reaction mechanism, stability upon ambient exposure and conductivity.

Next, in Chapter 5, the investigation of the reaction products of the ALD processes described in Chapter 4 is discussed. From the results, the reaction mechanism for thermal ALD of  $\text{Li}_2\text{CO}_3$  suggested in other studies could be confirmed and a reaction

mechanism for plasma-assisted ALD of  $\text{Li}_2\text{CO}_3$  was proposed. The influence of certain process parameters on the reaction products was also investigated.

In Chapter 6, the process development of LiF by ALD using  $\text{LiN}(\text{SiMe}_3)_2$  as precursor and  $\text{SF}_6$  plasma as coreactant is described. The adoption of  $\text{SF}_6$  plasma as coreactant is relatively new and was only used for ALD of  $\text{AlF}_3$ . The film properties of the as-deposited LiF films and the influence of the plasma exposure time on the film properties were investigated. Moreover, also the gas phase reaction products were investigated, and a reaction mechanism was formulated.

After, in Chapter 7, the process development of ALD  $\text{Al}_x\text{PO}_y$  using  $\text{PO}(\text{OMe})_3$  and  $\text{AlMe}_3$  as precursors and an  $\text{O}_2$  plasma as coreactant is described. The material properties as well as the possibility to tune those properties by varying the ALD parameters were investigated. In line with the other ALD studies, a reaction mechanism was proposed based on the identification of the gas phase reaction products.

At last, in Chapter 8, general conclusions on the work in this thesis are presented. The conclusions answer the research questions as outlined in previous section. Moreover, perspectives of future work are given.

## References

1. M. Armand and J.-M. Tarascon. Building better batteries. *Nature* **451**, 652–657 (2008).
2. J.-M. Tarascon and M. Armand. Issues and challenges facing rechargeable lithium batteries. *Nature* **414**, 359–367 (2001).
3. A. C. Luntz, J. Voss and K. Reuter. Interfacial challenges in solid-state Li-ion batteries. *J. Phys. Chem. Lett.* **6**, 4599–4604 (2015).
4. D. Linden. *Handbook of batteries*. (McGraw-Hill Professional, 2011).
5. J. B. Goodenough and Y. Kim. Challenges for rechargeable Li batteries. *Chem. Mater.* **22**, 587–603 (2010).
6. S.-H. Yu, X. Feng, N. Zhang, et al. Understanding conversion-type electrodes for lithium rechargeable batteries. *Acc. Chem. Res.* **51**, 273–281 (2018).
7. N. Nitta, F. Wu, J. T. Lee, et al. Li-ion battery materials: Present and future. *Mater. Today* **18**, 252–264 (2015).
8. J. Asenbauer, T. Eisenmann, M. Kuenzel, et al. The success story of graphite as a lithium-ion anode material - fundamentals, remaining challenges, and recent developments including silicon (oxide) composites. *Sustain. Energy Fuels* **4**, 5387–5416 (2020).
9. D. Billaud, E. McRae and A. Hérold. Synthesis and electrical resistivity of lithium-pyrographite intercalation compounds (stages I, II and III). *Mater. Res. Bull.* **14**, 857–864 (1979).
10. X. L. Yao, S. Xie, C. H. Chen, et al. Comparisons of graphite and spinel  $\text{Li}_{1.33}\text{Ti}_{1.67}\text{O}_4$  as anode materials for rechargeable lithium-ion batteries. *Electrochim. Acta* **50**, 4076–4081 (2005).
11. T. Ohzuku, A. Ueda and N. Yamamoto. Zero-strain insertion material of  $\text{Li}[\text{Li}_{1/3}\text{Ti}_{5/3}]\text{O}_4$  for rechargeable lithium cells. *J. Electrochem. Soc.* **142**, 1431–1435 (1995).
12. Y.-Q. Wang, L. Gu, Y.-G. Guo, et al. Rutile- $\text{TiO}_2$  nanocoating for a high-rate  $\text{Li}_4\text{Ti}_5\text{O}_{12}$  anode of a lithium-ion battery. *J. Am. Chem. Soc.* **134**, 7874–7879 (2012).
13. Y. Zhang, T.-T. Zuo, J. Popovic, et al. Towards better Li metal anodes: Challenges and strategies. *Mater. Today* **33**, 56–74 (2020).
14. A. Casimir, H. Zhang, O. Ogoke, et al. Silicon-based anodes for lithium-ion batteries: Effectiveness of materials synthesis and electrode preparation. *Nano Energy* **27**, 359–376 (2016).
15. Y. Reynier, C. Vincens, C. Leys, et al. Practical implementation of Li doped  $\text{SiO}$  in high energy density 21700 cell. *J. Power Sources* **450**, 227699 (2020).
16. K. Mizushima, P. C. Jones, P. J. Wiseman, et al.  $\text{Li}_x\text{CoO}_2$  ( $0 < x \leq 1$ ): a new cathode material for batteries of high energy density. *Mater. Res. Bull.* **15**, 783–789 (1980).

17. Y. Lyu, X. Wu, K. Wang, et al. An overview on the advances of LiCoO<sub>2</sub> cathodes for lithium-ion batteries. *Adv. Energy Mater.* **11**, 1–29 (2021).
18. J. N. Reimers and J. R. Dahn. Electrochemical and in situ X-ray diffraction studies of lithium intercalation in Li<sub>x</sub>CoO<sub>2</sub>. *J. Electrochem. Soc.* **139**, 2091–2097 (1992).
19. M. M. Thackeray, P. J. Johnson, L. A. de Picciotto, et al. Electrochemical extraction of lithium from LiMn<sub>2</sub>O<sub>4</sub>. *Mater. Res. Bull.* **19**, 179–187 (1984).
20. K. K. Lee, W. S. Yoon, K. B. Kim, et al. Characterization of LiNi<sub>0.85</sub>Co<sub>0.10</sub>M<sub>0.05</sub>O<sub>2</sub> (M = Al, Fe) as a cathode material for lithium secondary batteries. *J. Power Sources* **97–98**, 308–312 (2001).
21. N. Yabuuchi, Y. Koyama, N. Nakayama, et al. Solid-state chemistry and electrochemistry of LiCo<sub>1/3</sub>Ni<sub>1/3</sub>Mn<sub>1/3</sub>O<sub>2</sub> for advanced lithium-ion batteries. *J. Electrochem. Soc.* **152**, A1434 (2005).
22. L. Yang, B. Ravdel and B. L. Lucht. Electrolyte reactions with the surface of high voltage LiNi<sub>0.5</sub>Mn<sub>1.5</sub>O<sub>4</sub> cathodes for lithium-ion batteries. *Electrochem. Solid-State Lett.* **13**, 95–98 (2010).
23. L. Yang, M. Takahashi and B. Wang. A study on capacity fading of lithium-ion battery with manganese spinel positive electrode during cycling. *Electrochim. Acta* **51**, 3228–3234 (2006).
24. M. Armand, P. Axmann, D. Bresser, et al. Lithium-ion batteries – Current state of the art and anticipated developments. *J. Power Sources* **479**, (2020).
25. A. K. Padhi, K. S. Nanjundaswamy and J. B. Goodenough. Phospho-olivines as positive-electrode materials for rechargeable lithium batteries. *J. Electrochem. Soc.* **144**, 1188–1194 (1997).
26. A. Eftekhari. LiFePO<sub>4</sub>/C nanocomposites for lithium-ion batteries. *J. Power Sources* **343**, 395–411 (2017).
27. M. Xiao. China's electric bus market dominance driving demand for lithium-iron-phosphate batteries. *Commercial vehicles* [www.interactanalysis.com/chinas-electric-bus-market-dominance-driving-demand-for-lithium-iron-phosphate-batteries](http://www.interactanalysis.com/chinas-electric-bus-market-dominance-driving-demand-for-lithium-iron-phosphate-batteries) (2019).
28. A. Mauger, M. Armand, C. M. Julien, et al. Challenges and issues facing lithium metal for solid-state rechargeable batteries. *J. Power Sources* **353**, 333–342 (2017).
29. F. Zheng, M. Kotobuki, S. Song, et al. Review on solid electrolytes for all-solid-state lithium-ion batteries. *J. Power Sources* **389**, 198–213 (2018).
30. K. Kerman, A. Luntz, V. Viswanathan, et al. Review - Practical challenges hindering the development of solid state Li ion batteries. *J. Electrochem. Soc.* **164**, A1731–A1744 (2017).
31. J. C. Bachman, S. Muy, A. Grimaud, et al. Inorganic solid-state electrolytes for lithium batteries: mechanisms and properties governing ion conduction. *Chem. Rev.* **116**, 140–162 (2016).

32. N. Kamaya, K. Homma, Y. Yamakawa, et al. A lithium superionic conductor. *Nat. Mater.* **10**, 682–686 (2011).
33. S. Ohta, T. Kobayashi and T. Asaoka. High lithium ionic conductivity in the garnet-type oxide  $\text{Li}_{7-X}\text{La}_3(\text{Zr}_{2-X}\text{Nb}_X)\text{O}_{12}$  ( $X = 0-2$ ). *J. Power Sources* **196**, 3342–3345 (2011).
34. Y. Sun, P. Guan, Y. Liu, et al. Recent progress in lithium lanthanum titanate electrolyte towards all solid-state lithium ion secondary battery. *Crit. Rev. Solid State Mater. Sci.* **44**, 265–282 (2019).
35. Y. Wang, H. Li, P. He, et al. Nano active materials for lithium-ion batteries. *Nanoscale* **2**, 1294–1305 (2010).
36. P. G. Bruce, B. Scrosati and J. M. Tarascon. Nanomaterials for rechargeable lithium batteries. *Angew. Chemie - Int. Ed.* **47**, 2930–2946 (2008).
37. D. R. Rolison, J. W. Long, J. C. Lytle, et al. Multifunctional 3D nanoarchitectures for energy storage and conversion. *Chem. Soc. Rev.* **38**, 226–252 (2009).
38. H. C. M. Knoop, M. E. Donders, M. C. M. van de Sanden, et al. Atomic layer deposition for nanostructured Li-ion batteries. *J. Vac. Sci. Technol., A* **30**, 010801 (2012).
39. S. Moitzheim, J. E. Balder, R. Ritasalo, et al. Toward 3D thin-film batteries: optimal current-collector design and scalable fabrication of  $\text{TiO}_2$  thin-film electrodes. *ACS Appl. Energy Mater.* **2**, 1774–1783 (2019).
40. A. Wang, S. Kadam, H. Li, et al. Review on modeling of the anode solid electrolyte interphase (SEI) for lithium-ion batteries. *npj Comput. Mater.* **4**, (2018).
41. R. Xu, X. B. Cheng, C. Yan, et al. Artificial interphases for highly stable lithium metal anode. *Matter* **1**, 317–344 (2019).
42. M. Du, K. Liao, Q. Lu, et al. Recent advances in the interface engineering of solid-state Li-ion batteries with artificial buffer layers: Challenges, materials, construction, and characterization. *Energy Environ. Sci.* **12**, 1780–1804 (2019).
43. T. Suntola and J. Antson. Methods for producing compound thin films, 4058430. (1977).
44. J. C. Badot, S. Ribes, E. B. Yousfi, et al. Atomic layer epitaxy of vanadium oxide thin films and electrochemical behavior in presence of lithium ions. *Electrochem. Solid-State Lett.* **3**, 485–488 (2000).
45. M. Q. Snyder, S. A. Trebukhova, B. Ravdel, et al. Synthesis and characterization of atomic layer deposited titanium nitride thin films on lithium titanate spinel powder as a lithium-ion battery anode. *J. Power Sources* **165**, 379–385 (2007).
46. X. Meng, X. Q. Yang and X. Sun. Emerging applications of atomic layer deposition for lithium-ion battery studies. *Adv. Mater.* **24**, 3589–3615 (2012).
47. Y. Zhao, L. Zhang, J. Liu, et al. Atomic/molecular layer deposition for energy storage and conversion. *Chem. Soc. Rev.* **50**, 3889–3956 (2021).
48. AtomicLimits. ALD database. [www.atomiclimits.com/alddbatabase](http://www.atomiclimits.com/alddbatabase) (2021).

49. I. D. Scott, Y. S. Jung, A. S. Cavanagh, et al. Ultrathin coatings on nano-LiCoO<sub>2</sub> for Li-ion vehicular applications. *Nano Lett.* **11**, 414–418 (2011).





# 2

## ALD of artificial electrode-electrolyte interphase films

---

---

In this chapter, the electrode-electrolyte interphase and the need for artificial electrode-electrolyte interphase films in Li-ion batteries are further explained. In addition, a literature review on the use of ALD for the fabrication of such films is presented. From the results, it can be concluded that ALD is an excellent method for this purpose. In this regard, the possibilities and opportunities are also discussed.

## 2.1 The electrode-electrolyte interface

The influence of the interface between the electrode and electrolyte is one of the main obstacles restraining the improvement of lithium-based battery performance. Interfacial reactions between the electrode and electrolyte always occur in Li-ion batteries. Such interfacial reactions could be beneficial when they stabilize the cycling performance and improve battery safety by preventing decomposition of the electrolytes. However, interfacial reactions might also lead to unfavorable phenomena such as additional resistance and consumption of active lithium and electrolyte materials that can compromise the overall performance of Li-ion batteries.<sup>1</sup> Therefore, this interface is the key to understand battery electrochemistry.

The formation of an electrode-electrolyte interphase (EEI) layer occurs when the redox potential of the battery electrodes lies outside the electrochemical window of the electrolyte, which is schematically shown in Figure 2.1. An anode with an electrochemical potential ( $\mu_A$ ) above the stability window of the electrolyte will reduce the electrolyte unless an EEI creates a barrier to electron transfer from the anode to the electrolyte. Likewise, a cathode with a  $\mu_C$  below the stability window of the electrolyte will oxidize the electrolyte unless an EEI blocks electron transfer from the electrolyte to the cathode.<sup>2</sup> Therefore, thermodynamic stability requires that the position of the electrode electrochemical potentials  $\mu_A$  and  $\mu_C$  lie within the window of the electrolyte. This then constrains the voltage  $V_{cell}$  of a battery to:

$$eV_{cell} = \mu_A - \mu_C \leq \text{stability window} \quad (\text{Eq. 2.1})$$

where  $e$  is the electron charge. A passivating EEI layer can increase the electrochemical stability.<sup>2,3</sup>

When the interphase develops at the anode side, it is typically referred to as solid-electrolyte interphase (SEI), whereas when it is generated at the surface of the cathode, it is defined cathode-electrolyte interphase (CEI). Both CEI and SEI are collectively named the EEI.<sup>4</sup> The spontaneously formed SEI on the state of the art graphite anode can for example provide acceptable lifetime in commercial Li-ion batteries, even though more than 50 % capacity loss in a decent lithium ion battery can be attributed to the EEI growth.<sup>5</sup> Moreover, as was reported in Chapter 1, elemental Li would be the ideal anode, but the  $\mu_A$  of Li lies above the electrochemical stability window of practical, known electrolytes. Li can therefore only be used as an anode when a passivating SEI layer is formed. However, on repeated charge/discharge cycles, this spontaneously formed SEI can experience local mechanical failure, resulting in the formation of dendrites that can grow across the electrolyte and short-circuit a cell of the battery leading to safety issues (see also next paragraph). In general, this means that we either need an anode with a  $\mu_A$  matched to the electrolyte reduction potential and a cathode with a  $\mu_C$  matched to the electrolyte oxidation potential or stable, passivating EEI layers. The EEI's must also have respectable ionic

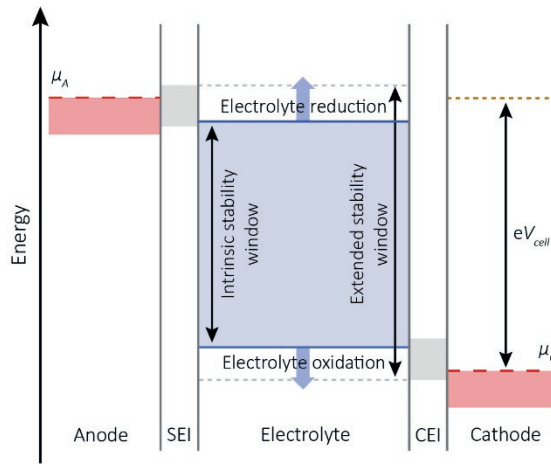


**Figure 2.1** Schematic energy diagram of the electrolyte stability. The variables  $\mu_A$  and  $\mu_C$  are the redox potential of the anode and cathode, respectively. The high  $\mu$  in the anode and low  $\mu$  in the cathode are beyond the stability window of the electrolyte. The observed electrochemical window is extended by the interphases, which account for the gap of  $\mu$  between electrolyte and electrodes across the interfaces.

conductivity and electronic insulation between the electrode and the electrolyte, which permits fast  $\text{Li}^+$ -ion transfer and isolates the unwanted side reactions caused by electrons, respectively.<sup>3</sup>

In the past decades, various review papers have been published on the topic of EEI's in conventional liquid batteries.<sup>4,6,7</sup> In conventional Li-ion batteries the dominating factors influencing the formation of the EEI are the initial surface specific adsorption behavior and the solvated coordinate structure of the electrolyte solution. The specific adsorption of the ions and solvents on the electrode determine the initial structure and chemical composition of the interphase, and the solvated coordinate structure of the bulk electrolyte functions as supply to maintain and repair the interphase during cycling.<sup>4</sup> The SEI on the anode mainly consists of decomposition products of liquid electrolytes on the anode surface. The decomposition of these products is often undesirable as it could also lead to safety issues. The problems become even more serious in anodes that undergo large volume changes during cycling. The SEI is typically more unstable compared to the CEI, due to the evident reduction reactions and the larger volume expansion of anode materials.<sup>8</sup> In some cases the SEI permanently consumes Li-ions, leading to reduced coulombic efficiency of batteries.<sup>9</sup> The CEI on the cathode mainly originates from dissolution of cathode elements into the electrolyte solution. For instance, HF generated in certain electrolytes (e.g.  $\text{LiPF}_6$ ) during cycling tends to dissolve the components of the cathode materials. This would then result in rapid deterioration of battery performance.<sup>10</sup> In comparison to the SEI, there has been rather limited effort to

investigate the interphase formation on the cathode. Therefore, the electrolyte oxidation on the cathode and the composition and properties of the CEI are less understood. Recently, more reports became available regarding the chemical composition and formation mechanism of the CEI.<sup>4,11</sup>

In solid-state batteries, interphase formation is strongly reduced compared to liquid batteries. However, still interfacial impedance can dominate the internal resistance. Several recent reviews investigate the interphase formed in solid-state-batteries.<sup>12,13</sup> As described in Chapter 1, the ionic conductivity of most solid-state electrolytes is lower than the ionic conductivity of liquid electrolytes. Even though some solid electrolytes can achieve high ionic conductivity, they face several instability issues at the interface. The interfacial compatibility between solid electrolytes and electrodes is usually poor and significant improvement is needed for application in solid-state batteries. The overall ionic conductivity is not only determined by the ionic conductivity of the electrolyte. The ionic transport of  $\text{Li}^+$  at the interfaces also plays a role and therefore ultimately defines the rate performance of these batteries. Therefore, the overall electrochemical impedance could be high, even when a solid electrolyte with excellent ionic conductivity is adopted. Moreover, in solid-state batteries it is still challenging to prevent Li dendrite penetration, even for electrolytes with high mechanical strength. Based on the available experimental and theoretical results, it appears unlikely that any solid-electrolyte material in use today is absolutely stable against high-voltage cathodes as well as Li metal; thus, either the spontaneous formation or the engineering of stable passivation layers will be required.<sup>13</sup>

## 2.2 Artificial electrode-electrolyte interphases

In sight of the drawbacks of native EEs, tremendous efforts have been made to artificially engineer the electrode-electrolyte interphase. In this regard, surface modification and thin film synthesis have proven effective approaches to reduce unwanted side reactions. Herewith, the capacity retention, rate capability, columbic efficiency, and even thermal stability of electrode materials can be improved.<sup>10,14–17</sup> The capacity retention is the ability of a battery to retain its capacity after the battery has been stored for a given amount of time. The rate capability is the number of times the battery can discharge in one hour without overheating or damaging the battery, expressed as the C-rate. The effect of the SEI on a Li anode during cycling is schematically shown in Figure 2.2.<sup>18</sup> In Figure 2.2a, a metastable solid–electrolyte interphase between the Li metal electrolyte is shown. The partial dissolution of the native SEI ( $\text{Li}_2\text{CO}_3$ ,  $\text{LiOH}$ , and  $\text{Li}_2\text{O}$ ) leads to a porous structure where the Li-ion concentration is locally enhanced, thereby promoting Li dendrite formation and growth. A reactive mixed-conducting interphase between the Li metal electrode and the electrolyte is formed. Figure 2.2b shows the Li metal modified by an artificial SEI

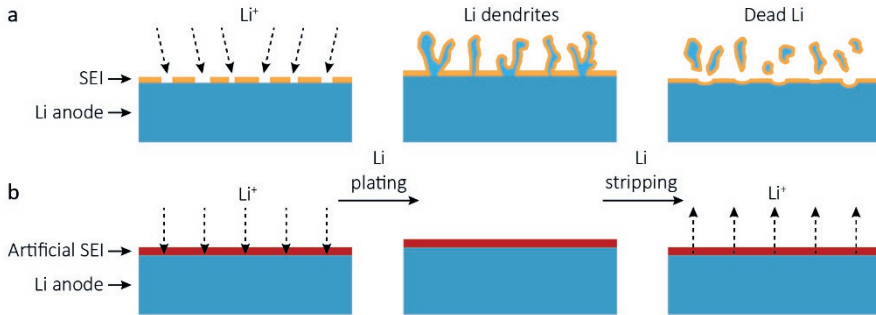


**Figure 2.2** Schematics of the formation of different SEIs on the Li anode during cycling: a) the bare Li metal, where the cracking of SEI results in the formation of Li-ion flux “hot spots” and Li dendrites which could lead to dead Li and b) the Li metal including an artificial SEI, where dendrite formation is suppressed and Li-ion conductivity allows for more uniform distribution of Li-ion flux.

during cycling. Here, Li dendrite formation is suppressed as a result of the mechanical properties and Li-ion conductivity of the SEI. Ideally, the EEI should meet the following requirements: i) ultrathin and continuous (full protection of the electrode is critical); ii) electrochemically stable; iii) excellent adhesion on the electrode to resist delaminating; iv) mechanically robust to resist cracking and prevent breaching by lithium dendrites; v) electronically insulating to ensure lithium plating; vi) lithium ionic conductivity to facilitate uniform transport of lithium ions into/out of the electrode materials.<sup>1,19</sup> However, in the case of liquid batteries where particle electrodes are being used and the artificial EEI is applied to the particles/powder separately, the EEI also needs to be electrically conductive. This is further explained in Section 2.3.

So far, carbon, metal oxides (e.g.  $\text{Al}_2\text{O}_3$ ,  $\text{TiO}_2$ ,  $\text{ZnO}$ ,  $\text{ZrO}_2$ ,  $\text{MgO}$ ,  $\text{SiO}_2$ ,  $\text{CeO}_2$ ), metal carbonates (e.g.  $\text{Li}_2\text{CO}_3$ ), metal aluminates, metal phosphates (e.g.  $\text{AlPO}_4$ ,  $\text{Li}_3\text{PO}_4$ ), metal fluorides ( $\text{AlF}_3$ ,  $\text{LiF}$ ,  $\text{LiAlF}_4$ ), metal oxyfluorides (e.g.  $\text{BiOF}$ ), metal hydroxides, and glass composites ( $\text{Li}_2\text{O}-2\text{B}_2\text{O}_3$ ) have been investigated as artificial EEI. Electrode materials usually differ in their inherent properties, thus the artificial EEI is expected to be selected exclusively for a specific electrode. Carbon has been applied for a wide range of electrode materials and showed excellent results in improving the electrochemical performances of both anodes and cathodes. The carbon EEI can act as a multifunctional layer between the electrode and the electrolyte, attributed to its excellent electrical conductivity, superior chemical/electrochemical stability and unique physical properties.<sup>14</sup> The electrically conductive nature of carbon is useful when it is applied to particle/powder electrodes. Especially on  $\text{LiMPO}_4$  (where  $\text{M}$  = metal) and graphite electrodes valuable results were achieved. The use of metal oxides as artificial EEI is very common. Metal oxides can react with acid species in electrolytes thereby preventing the electrodes from being destroyed. Moreover, these layers block direct contact between the anode and cathode and improve the

safe performance of batteries that can overheat. Metal oxides can, for example, be used to protect LMNO. As described in Chapter 1, LNMO is a promising candidate to use as cathode for high power next-generation Li-ion batteries and can be used as particle electrode. LMNO has an operating voltage up to 4.7 V, which unfortunately also leads to degradation of the interface structure.<sup>20</sup> Surface modification using metal oxide EEs can be utilized in solving these issues. The layer suppresses deposition of electrolyte material on the electrode and protects the electrode surface, for example, from HF corrosion with excellent Li-ions diffusion capacity. To date, the surface of LNMO particles has been modified by various materials, for instance, Al<sub>2</sub>O<sub>3</sub>,<sup>21</sup> FePO<sub>4</sub>,<sup>22</sup> TiO<sub>2</sub>,<sup>23</sup> Co<sub>3</sub>O<sub>4</sub>,<sup>24</sup> and La<sub>2</sub>O<sub>3</sub>.<sup>25</sup> Among these materials, Al<sub>2</sub>O<sub>3</sub> is the most popular and extensively researched one. However, metal oxides are usually insulators which decrease the overall ionic conductivity of the battery and work against the interfacial mass change of electrodes. The artificial EEs are usually thin enough to decrease the overall ionic conductivity significantly. Nevertheless, a Li-ion conductive-material could be more desirable. For example, amorphous lithium phosphate compounds are decent lithium-ion conductors (in the order of 10<sup>-6</sup> - 10<sup>-10</sup> S · cm<sup>-1</sup>). Using lithium phosphates as artificial EEI both enhances the Li-ion conductivity and inhibits the interfacial side reaction.<sup>26,27</sup> The materials investigated also include chemistries which are proposed as solid-state electrolyte material for thin film batteries. The materials specifically fabricated by atomic layer deposition (ALD) will be discussed in the next paragraph.

### 2.3 Artificial interphase films synthesized by ALD

As already discussed in Chapter 1, recent advances demonstrate that ALD is a very useful tool for addressing various challenges, and offering a variety of capabilities, in Li-ion batteries. ALD is a precise, highly efficient route to modify Li-ion electrodes with ultrathin films. For adapting to the various surface structures of electrodes, continuous and conformal deposition is necessary, especially in the case of thin-film batteries. ALD has the ability to form conformal films on powder samples, porous substrates, and other complex surface structures.<sup>28</sup> ALD can be directly practiced on either battery powders or prefabricated electrodes with the (sub-)nanometer thin films (see Figure 2.3a–c). Traditionally, solution-based methods have been widely used for coating battery electrode powders with thick protective films of several tens of nanometers to microns. It must be noted that to date ALD is the only technique enabling to directly deposit on prefabricated electrodes. In many cases, direct deposition on prefabricated electrodes is more favorable, since interparticle electronic pathways are not disrupted while the electrode integrity is greatly improved (see Figure 2.3b). Additionally, the direct deposition of artificial interphase films on the electrode benefits from the relatively low deposition temperature of ALD (25 - 300 °C). The capabilities of ALD also allow to protect electrodes with complex

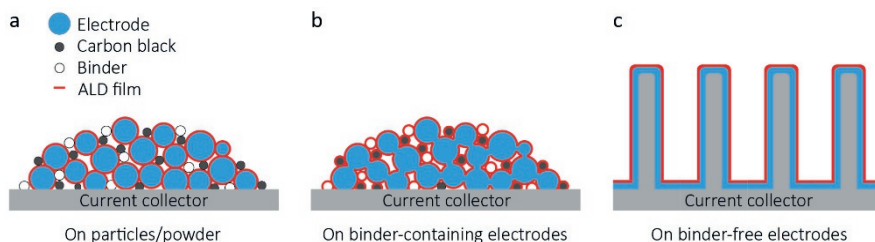


**Figure 2.3** Illustration of ALD strategies for modifying battery electrodes. ALD deposition on a) electrode particles, b) binder-containing electrodes and c) binder-free electrodes.

nanostructures like in 3D solid-state batteries (see Figure 2.3c). Since 2010, ALD has been extensively investigated as approach to improve the performance of the anode and cathode. In the next sections, we focus on the state-of-the-art progress of employing ALD to tailor the electrode-electrolyte interface to achieve optimal performance of the electrode. The ALD films are deposited on planar as well as 3D-structured electrodes, such as nanoparticles and nanotubes.

### 2.3.1 ALD films on the anode

A summary of the ALD chemistries investigated as artificial SEI is given in Table 2.1. As shown from the table, the battery performance was enhanced by films with thicknesses from a few ångströms to a few nanometers. The ALD films on the anode mainly address the problems resulting from the spontaneously formed SEI from the decomposition products of electrolytes on the anode surface at the low electrochemical potential. The specific capacity, columbic efficiency, rate capability and thermal stability are improved by reduction of the spontaneously formed SEI. For example, on graphite anodes 0.5 - 5 nm thick  $\text{Al}_2\text{O}_3$  and  $\text{TiO}_2$  films have been reported to suppress SEI formation at  $\sim 0.7$  V (vs  $\text{Li}^+/\text{Li}$ ).<sup>29–31</sup> Especially at high working temperatures the results show that ALD  $\text{Al}_2\text{O}_3$  is more stable than the spontaneously formed SEI.<sup>29</sup> For LTO anodes 1 - 2 nm thick ALD  $\text{Al}_2\text{O}_3$  or  $\text{ZrO}_2$  films were found to improve the cycling performance in an extended voltage range (0.1 - 2.5 V).<sup>32,33</sup> Moreover, electrochemical impedance spectroscopy (EIS) analysis demonstrated a decrease in resistance across the SEI layer by using  $\text{Al}_2\text{O}_3$ ,  $\text{ZrO}_2$ , and  $\text{TiO}_2$  films for both graphite and LTO. This implies that SEI formation on the anode was indeed suppressed. A different study showed using *in situ* scanning ion conductance microscopy that unprotected MnO had drastically increased surface roughness after cycling due to the formation of SEI. At the same time, a 9 Å  $\text{Al}_2\text{O}_3$  covered MnO showed unaffected surface roughness, proving that ALD  $\text{Al}_2\text{O}_3$  inhibited the growth of a spontaneously formed SEI.<sup>34</sup>

For anodes that experience large volume changes during cycling, the problems resulting from SEI formation become even more serious. The volume change could



**Table 2.1** Summary of ALD films applied as SEI.

ALD chemistry	Precursor(s)	Coreactant(s)	Anode	Thickness (nm)	Ref.
Al <sub>2</sub> O <sub>3</sub>	AlMe <sub>3</sub>	H <sub>2</sub> O	Graphite	~ 0.5 - 45	29,31
			LTO	~ 2.2	32
			Fe <sub>3</sub> O <sub>4</sub>	~ 0.2	42
			MoO <sub>3</sub>	~ 0.4	43
			SnO <sub>2</sub>	1 - 3	40
			MnO	~ 0.9	34
			Si	2 - 4	35
			Li	2.5 - 4	47
TiO <sub>2</sub>	AlMe <sub>3</sub>	O <sub>2</sub> <sup>a</sup>	Si	3	39
	TiCl <sub>4</sub>	H <sub>2</sub> O	Graphite	32 - 40	30
	TiCl <sub>4</sub>	H <sub>2</sub> O	ZnO	~ 11	41
	TiI <sub>4</sub>	H <sub>2</sub> O	Graphite	3 - 30	31
	Ti(Me <sub>2</sub> N) <sub>4</sub>	H <sub>2</sub> O	Mn <sub>3</sub> O <sub>4</sub>	~ 0.2	65
ZnO	Ti(OCHMe <sub>2</sub> ) <sub>4</sub>	O <sub>2</sub> <sup>a</sup>	Si	3 - 10	38,39
	Zn(C <sub>2</sub> H <sub>5</sub> ) <sub>2</sub>	H <sub>2</sub> O	Si	3	66
ZrO <sub>2</sub>	Zr(NMe <sub>2</sub> ) <sub>4</sub>	H <sub>2</sub> O	LTO	~ 1	33
HfO <sub>2</sub>	Hf(NMe <sub>2</sub> ) <sub>4</sub>	H <sub>2</sub> O	SnO <sub>2</sub>	0.6	67
TiN	TiCl <sub>4</sub>	NH <sub>3</sub>	LTO	~ 5.8	68
	TiCl <sub>4</sub>	N <sub>2</sub> <sup>a</sup>	Si	3 - 5	37,39
LiAlO <sub>2</sub>	LiO <sup>t</sup> Bu, AlMe <sub>3</sub>	H <sub>2</sub> O	Graphite	~ 1.5	45
			Ni <sub>3</sub> S <sub>2</sub>	12	44
Li <sub>x</sub> Al <sub>y</sub> S	LiO <sup>t</sup> Bu, Al(NMe <sub>2</sub> ) <sub>3</sub>	H <sub>2</sub> S	Li	25	46
LiF	LiO <sup>t</sup> Bu	HF pyridine	Li	8	19

LTO = Li<sub>4</sub>Ti<sub>5</sub>O<sub>12</sub>. <sup>a</sup>The use of a plasma during the coreactant step was not mentioned in these studies.

break the anode, thereby exposing the electrode, resulting in the formation of a new SEI. As mentioned earlier, EEs should have good toughness to better accommodate volume expansion and contraction during cycling. The ALD films were shown to reduce the serious pulverization of such anode materials, including Si,<sup>35–39</sup> SnO<sub>2</sub>,<sup>40</sup> ZnO,<sup>41</sup> Fe<sub>3</sub>O<sub>4</sub>,<sup>42</sup> and MnO.<sup>34</sup> These are all high capacity anodes with an intrinsically low stability. In the preceding chapter it was discussed that nano-structured electrodes can also improve cycling for anodes that experience large volume changes. For instance, Si-based nanotubes are receiving significant scientific attention as potential high energy density anodes for Li-ion batteries. However, their cycling performance still requires further improvement. Performance enhancement of Si nanotubes by Al<sub>2</sub>O<sub>3</sub>, TiO<sub>2</sub> and TiN ALD films was demonstrated by Lotfabad et al. and they found that the best performance was achieved for TiO<sub>2</sub> ALD.<sup>39</sup> Another study by Wang et al. reported Al<sub>2</sub>O<sub>3</sub> ALD could improve the performance SnO<sub>2</sub> nanoparticle electrodes.<sup>40</sup>

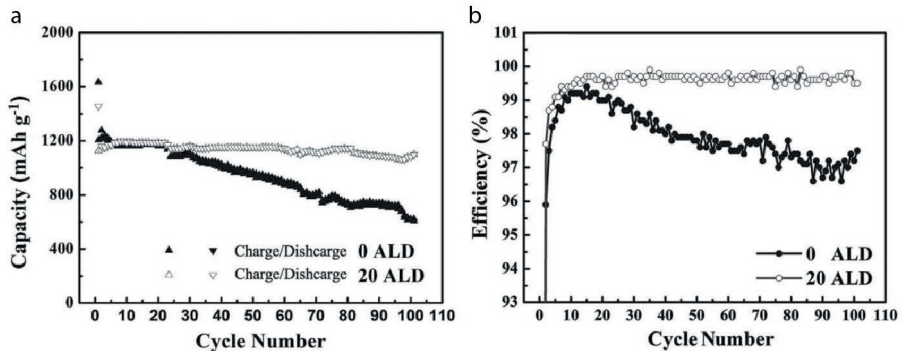


**Figure 2.4** a) The capacity and b) coulombic efficiency comparison of a bare Si electrode and a 20 ALD cycles Al<sub>2</sub>O<sub>3</sub> coated Si electrode. Adapted from ref. 35.

The optimal Al<sub>2</sub>O<sub>3</sub> film thickness varied with the size of the nanoparticles. In addition to cycling lifetime, great improvement in coulombic efficiency was obtained by ALD films for anode materials that undergo large volume changes (see the example in Figure 2.4).<sup>35–40,43</sup> This is due to reduced cracking of the anode, avoiding the generation of bare anode surfaces and thus SEI formation.

So far, we mainly discussed dielectric ALD films applied as artificial SEI. In most cases it was shown that when the films are a few nm thick they do not add a significant impedance component to the overall resistance of the battery. As mentioned before, the performance of the battery could probably be improved for many applications by using ionically conductive artificial SEI films. The maximum acceptable film thickness will then become less critical. Therefore, solid-state electrolytes have been proposed as artificial EEI to replace the more extensively researched metal oxides.<sup>44</sup> Besides, the good functioning of the poor ionic conductor Al<sub>2</sub>O<sub>3</sub> most likely has to do with the fact that it converts to the ionic conductor Li-Al-O glass during cycling. This information promoted the use of ALD solid-state electrolytes, such as LiAlO<sub>2</sub> and Li<sub>x</sub>Al<sub>y</sub>S, as artificial SEI. Li-ion conductive ALD LiAlO<sub>2</sub> ( $\sigma = 5.6 \cdot 10^{-8} \text{ S} \cdot \text{cm}^{-1}$ ) was shown to improve the electrochemical stability of graphite electrodes.<sup>45</sup> Li<sub>x</sub>Al<sub>y</sub>S ALD films ( $2.5 \cdot 10^{-7} \text{ S} \cdot \text{cm}^{-1}$ ) stabilize the Li–electrolyte interface and reduce (up to five times) the interfacial impedance of Li metal anodes in contact with organic electrolyte.<sup>46</sup>

Another approach is to select a naturally present SEI component, such as Li<sub>2</sub>CO<sub>3</sub> or LiF as artificial SEI. These materials can be especially interesting for Li anodes. Studies of ALD Al<sub>2</sub>O<sub>3</sub> on Li anodes showed that it is soluble in acids and bases,<sup>47</sup> and Li<sub>x</sub>Al<sub>y</sub>S on Li anodes showed it highly reactive with oxygen and water vapor.<sup>46</sup> Obviously, degradation of these ALD films can compromise their ability to protect the Li surface, leading to reduced cycle life. Lithium carbonate is considered a potential electrode passivating film due to its good electrochemical stability and purely ionically conductive behavior. To our knowledge, Li<sub>2</sub>CO<sub>3</sub> ALD films have not yet been tested as

artificial SEI on the anode. However,  $\text{Li}_2\text{CO}_3$  films and additives fabricated by other techniques have been shown to improve the electrode performance. For example, it was demonstrated that the cycling stability and reversible capacity of  $\text{FeO}_3$  nanocrystallines was enhanced by adding  $\text{Li}_2\text{CO}_3$  coating through a ball milling process.<sup>48</sup> In Chapter 4 and Chapter 5, the thermal and plasma-assisted ALD processes of  $\text{Li}_2\text{CO}_3$  and the influence of the process parameters on the film properties are extensively investigated. Also, ionic conductivity for both plasma-assisted and thermal ALD films are measured for the first time. The properties of these layers and the possibility to tune these properties show that these processes are very promising for the application as artificial SEI.  $\text{LiF}$  has various interesting qualities. For example, it is chemically inert on lithium metal, is electrochemically stable from 0 - 6.4 V,<sup>49</sup> is electronically insulating, and has a relatively high shear modulus of 55 GPa.<sup>50</sup> It has been reported that lithium dendrite growth can be suppressed by materials having a shear modulus at least two times higher than metallic Li (4 GPa).<sup>51</sup> Moreover, metal fluorides are expected to be stable against attack of fluoric acid. ALD of  $\text{LiF}$  using  $\text{LiO}^t\text{Bu}$  as precursor and  $\text{HF}$  as coreactant was tested as SEI on Li electrodes and was shown to provide excellent electrochemical stability and coulombic efficiency in liquid organic electrolytes.<sup>19</sup> The ALD process has been studied to a lesser extent and the tunability of the film properties using the process parameters was not investigated in this study. Moreover, the  $\text{HF}$  precursor is potentially dangerous and corrosive, and although  $\text{HF}$ -pyridine solutions provide a safer alternative to anhydrous  $\text{HF}$  and the use of compressed gas cylinders is avoided, strict safety precautions are still required. Therefore, it is interesting to study new ALD processes and investigate the tunability of the film properties. In Chapter 6, a new ALD chemistry has been demonstrated to prepare  $\text{LiF}$  films using  $\text{LiN}(\text{SiMe}_3)_2$  and  $\text{SF}_6$  plasma. Herein, the ALD process is extensively studied, and it was found that the easy-to-handle and readily-available  $\text{SF}_6$  plasma is a promising alternative to coreactants such as  $\text{TiF}_4$ , or  $\text{HF}$ -pyridine for ALD of lithium fluorides. Moreover, the uniformity and conformality studies show promising results which could be interesting for Li-ion battery applications.

### 2.3.2 ALD films on the cathode

A summary of the ALD chemistries investigated as artificial CEI is given in Table 2.2. ALD films on the cathode aim to increase the lifetime of the battery mainly by preventing the problems originating from dissolution of cathode elements into the electrolyte. Various studies show that ALD metal oxides improve the cycling stability and energy density of cathodes such as LCO,<sup>52-54</sup> LMO,<sup>55</sup> and high-voltage Mn-containing cathode materials.<sup>21,22,56-58</sup> As described before, LCO can only be used up to half of its theoretical capacity.  $\text{Co}^{4+}$  will dissolve into the electrolyte if more than half of the lithium ions are extracted, resulting in structural changes to LCO and therefore degradation of the battery performance. So far, < 1 nm thick  $\text{Al}_2\text{O}_3$ ,<sup>52-54</sup>  $\text{TiO}_2$ ,<sup>53</sup> and  $\text{ZrO}_2$ ,<sup>53</sup> films have been found to effectively protect from  $\text{Co}^{4+}$  dissolution

**Table 2.2** Summary of ALD films applied as CEI.

ALD chemistry	Precursor(s)	Coreactant(s)	Cathode	Thickness (nm)	Ref.
Al <sub>2</sub> O <sub>3</sub>	AlMe <sub>3</sub>	H <sub>2</sub> O	LCO	< 1	52–54,69
			LMO	0.5 - 2	55
			LNMO	< 1	21
			NMC	0.5 - 3	60,70,71
			V <sub>2</sub> O <sub>5</sub>	0.5 - 2.5	72
TiO <sub>2</sub>	Ti(OCHMe <sub>2</sub> ) <sub>4</sub>	H <sub>2</sub> O	LCO	0.3 - 6.5	53
			LMO	1 - 5	55
			NMC	1	71
ZnO	Zn(CH <sub>2</sub> Me) <sub>2</sub>	H <sub>2</sub> O	LCO	~ 0.5	69
ZrO <sub>2</sub>	Zr(NMe <sub>2</sub> ) <sub>4</sub>	H <sub>2</sub> O	LCO	0.3 - 6.5	53
	Zr(O <sup>t</sup> Bu)	H <sub>2</sub> O	LMO	0.5 - 3	73
MgO	Mg(EtCp) <sub>2</sub>	H <sub>2</sub> O	NMC	0.7	74
CeO <sub>2</sub>	Ce( <i>i</i> PrCp) <sub>3</sub>	H <sub>2</sub> O	NMC	1.5 - 5	75
LiAlO <sub>2</sub>	LiO <sup>t</sup> Bu, AlMe <sub>3</sub>	H <sub>2</sub> O	LNMO	~ 1.5	45
LiTaO <sub>3</sub>	LiO <sup>t</sup> Bu and Ta(OEt) <sub>5</sub>	H <sub>2</sub> O	NMC	0.5 - 6	59
Li <sub>x</sub> PO <sub>y</sub> N <sub>z</sub>	LiO <sup>t</sup> Bu, PO(OMe) <sub>3</sub>	H <sub>2</sub> O, N <sub>2</sub> plasma	RuO <sub>2</sub>	17	76
LiF	LiO <sup>t</sup> Bu, TiF <sub>4</sub>	-	NMC	~ 1	58
Li <sub>x</sub> AlF <sub>y</sub>	LiO <sup>t</sup> Bu, AlCl <sub>3</sub> , TiF <sub>4</sub>	-	NMC	~ 2	58
AlF <sub>3</sub>	AlMe <sub>3</sub> , CH <sub>2</sub> (COCF <sub>3</sub> ) <sub>2</sub>	O <sub>3</sub>	LNMO	2.4	56
	AlCl <sub>3</sub> , TiF <sub>4</sub>	-	NMC	~ 2	58
MgF <sub>2</sub>	CH <sub>2</sub> (COCF <sub>3</sub> ) <sub>2</sub> , Mg(EtCp) <sub>2</sub>	-	LNMO	~ 0.5	57
FePO <sub>4</sub>	FeCp <sub>2</sub> , PO(OMe) <sub>3</sub>	O <sub>3</sub> , H <sub>2</sub> O	LNMO	0.5 - 4	22
AlPO <sub>4</sub>	AlMe <sub>3</sub> , PO(OMe) <sub>3</sub>	H <sub>2</sub> O	LNMO	0.2 - 5	64

LCO = LiCoO<sub>2</sub>, LMO = LiMn<sub>2</sub>O<sub>4</sub>, LNMO = LiNi<sub>0.5</sub>Mn<sub>1.5</sub>O<sub>4</sub>, NMC = LiNi<sub>1-x-y</sub>Mn<sub>x</sub>Co<sub>y</sub>O<sub>2</sub>.

into electrolytes. In comparison with TiO<sub>2</sub> and ZrO<sub>2</sub> films, Al<sub>2</sub>O<sub>3</sub> exhibited the best cycling stability and capacity retention, while ALD ZrO<sub>2</sub> showed the best rate capability.<sup>53</sup> Therefore, it is possible that mixed ALD chemistries, such as Al<sub>2</sub>O<sub>3</sub>-ZrO<sub>2</sub> and Al<sub>2</sub>O<sub>3</sub>-ZrO<sub>2</sub>-Al<sub>2</sub>O<sub>3</sub>, deposited using, for example, ALD supercycles would work even better to improve the electrochemical properties of LCO. For LMO, the influence of ALD Al<sub>2</sub>O<sub>3</sub> and TiO<sub>2</sub> was investigated.<sup>55</sup> Both coatings can partially solve the solvent decomposition. Unfortunately, the kinetic bottleneck posed by 1 nm Al<sub>2</sub>O<sub>3</sub> is still greater than the uncoated LMO, leading to worsened rate capability. Most of the solvent decomposition is prevented using ALD TiO<sub>2</sub>, resulting in smoother electrodes (see Figure 2.5). The absence of the decomposition layer and lithium conducting properties of the ALD TiO<sub>2</sub> films results in an improved rate capability for the ALD TiO<sub>2</sub> coated LMO electrode.

High-voltage Mn-containing cathodes, such as NMC and NCA, are currently being considered as replacements for LiCoO<sub>2</sub> because of their high working voltage and high specific capacity. As mentioned in the previous chapter, the high working voltage of

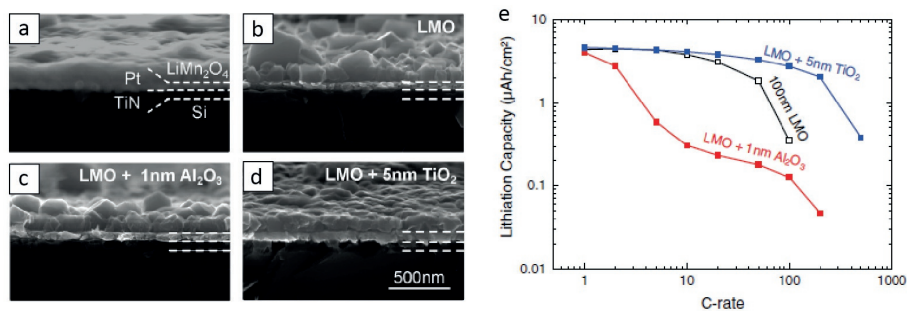


**Figure 2.5** Cross section SEM images of a) the as-received LMO, and the samples post electrochemical cycling: b) bare LMO, c) LMO with 1 nm of ALD Al<sub>2</sub>O<sub>3</sub>, and d) LMO with 5 nm of ALD TiO<sub>2</sub> and e) delithiation capacity of the LMO electrodes under study. Adapted from ref. <sup>55</sup>.

these cathodes (4.5 - 4.8 V vs Li<sup>+</sup>/Li) is of course beneficial, but can also cause serious problems. These high-voltage cathode materials suffer from Mn<sup>2+</sup> dissolution into the electrolyte.<sup>59</sup> This would lead to a decrease in capacity loss of these cathodes if Mn<sup>2+</sup> is permanently lost. Moreover, Mn<sup>2+</sup> in the electrolytes could migrate to the anode and deposit on the anode surface.<sup>45</sup> Ultrathin metal oxide ALD films, such as Al<sub>2</sub>O<sub>3</sub>, TiO<sub>2</sub>, MgO and CeO<sub>2</sub> are essentially a physical barrier between cathode and electrolytes and suppress the dissolution of Mn in the electrolyte. For example, a Al<sub>2</sub>O<sub>3</sub>-coated NMC could deliver a discharge capacity of 140 mAh · g<sup>-1</sup> after 100 cycles compared to a discharge capacity of 103 mAh · g<sup>-1</sup> for pristine NMC.<sup>60</sup>

Also on the cathode side, solid-state electrolytes have been proposed as a lithium ion- conducting EEI to replace the more commonly used metal oxides. For example, LiTaO<sub>3</sub> ALD films have been shown to improve the performance of NMC at high voltages.<sup>59</sup> LiTaO<sub>3</sub> showed an ionic conductivity of  $2 \cdot 10^{-8} \text{ S} \cdot \text{cm}^{-1}$  at room temperature.<sup>61</sup> The cycling stability and rate capability of NMC were greatly improved, as indicated by electrochemical testing. When cycled between 3.0 and 4.8 V, NMC with 10 ALD cycles of LiTaO<sub>3</sub> delivered a discharge capacity of 122 mAh · g<sup>-1</sup> after 100 charge/discharge cycles in comparison with 59 mAh · g<sup>-1</sup> for bare NMC.<sup>59</sup>

LiF, Li<sub>x</sub>AlF<sub>y</sub>, AlF<sub>3</sub> and MgF<sub>2</sub> have the advantage to be stable against hydrofluoric attack. This can be useful when a fluoride containing electrolyte is used. Moreover, metal fluorides have been predicted to have the widest electrochemical stability windows, especially at high potential. Therefore, these materials would be ideal coatings for high-voltage cathode materials.<sup>62</sup>

FePO<sub>4</sub> and AlPO<sub>4</sub> also show an improvement in comparison with metal oxides as artificial CEI. The reason may be attributed to the strong P=O bond, which is very resistant to chemical attack. Moreover, high thermal stability of AlPO<sub>4</sub> can be attributed to the strong covalency of the PO<sub>4</sub> polyanions with the Al<sup>3+</sup> ions in AlPO<sub>4</sub>.<sup>63</sup> Studies show that a LMNO cathode with ALD AlPO<sub>4</sub> film demonstrates improved

capacity retention with prolonged cycle life compared to the bare LMNO cathode.<sup>64</sup> It was found that the  $\text{AlPO}_4$  ALD film improved thermal stability and effectively impeded the side-reactions occurring at high voltage, resulting in significantly improved electrochemical performance and safety. Just like  $\text{Li}_2\text{CO}_3$  and  $\text{LiF}$  ALD, which were discussed in the previous section, also the  $\text{AlPO}_4$  ALD process itself has been relatively little studied. Furthermore, it appears from various literature studies that it is difficult to get a high phosphorus content in the film. This will be further discussed in Chapter 7, in which the development of a new ALD chemistry to deposited  $\text{Al}_x\text{PO}_y$  films using an  $\text{O}_2$  plasma as coreactant is presented. It is shown that the use of an  $\text{O}_2$  plasma can offer advantages to more commonly used thermal ALD processes of  $\text{AlP}_x\text{O}_y$ , such as the ability to increase the phosphorus content, and deliver high quality ALD films.

When ALD is used to deposit an artificial CEI, direct contact with the electrolyte solution is prevented, phase transition is suppressed, the structural stability is improved, and the disorder of cations in crystal sites is decreased. This results in a decrease in side-reactions and heat generation during cycling. Thereby, improvement of reversible capacity, coulomb efficiency, rate capability and overcharge tolerance has been achieved.<sup>10</sup> Different ALD films show different results, but the main reason is not clear. In various cases, such as LCO and LMO, the improvement in electrochemical performance is in line with the toughness of the CEI. Besides this, electrochemical and thermal stability and conductivity seem to play a role.

## 2.4 Conclusions

Artificial EEIs are very promising in terms of improving Li-ion batteries as is required for many battery applications. ALD can be used in a variety of configurations and in different battery concepts, such as particle-based, 3D-structured, and 3D solid-state micro-batteries. The effect on the battery performance has been tested for various ALD chemistries useful as artificial EEI. From these literature results it can be concluded that different artificial EEI films increase the stability and decrease side reactions between the electrode and electrolyte, leading to improvement of electrochemical performance. Improvement in reversible capacity, coulomb efficiency, cycling behavior and rate capability is obtained. To further improve the performance, a better understanding of the ALD process and film properties can be useful. It is also interesting to investigate the tunability of the film properties using the ALD process parameters. Moreover, as shown from the tables in previous sections, the existing literature studies do not yet explore the possibility to use plasma-assisted ALD for the fabrication of artificial EEIs. Plasma-assisted ALD could allow for more freedom in process parameters. In other words, there are still several opportunities to expand the available ALD chemistries useful as artificial EEI as well as to improve understanding in the fabrication process itself.

## References

1. J. Liu and X. Sun. Elegant design of electrode and electrode/electrolyte interface in lithium-ion batteries by atomic layer deposition. *Nanotechnology* **26**, 024001 (2015).
2. P. Peljo and H. H. Girault. Electrochemical potential window of battery electrolytes: The HOMO-LUMO misconception. *Energy Environ. Sci.* **11**, 2306–2309 (2018).
3. J. B. Goodenough and Y. Kim. Challenges for rechargeable Li batteries. *Chem. Mater.* **22**, 587–603 (2010).
4. C. Yan, R. Xu, Y. Xiao, et al. Toward critical electrode/electrolyte interfaces in rechargeable batteries. *Adv. Funct. Mater.* **30**, 1909887 (2020).
5. R. Fong, U. von Sacken and J. R. Dahn. Studies of lithium intercalation into carbons using nonaqueous electrochemical cells. *J. Electrochem. Soc.* **137**, 2009–2013 (1990).
6. P. Verma, P. Maire and P. Novák. A review of the features and analyses of the solid electrolyte interphase in Li-ion batteries. *Electrochim. Acta* **55**, 6332–6341 (2010).
7. K. Xu. Electrolytes and interphases in Li-ion batteries and beyond. *Chem. Rev.* **114**, 11503–11618 (2014).
8. A. Wang, S. Kadam, H. Li, et al. Review on modeling of the anode solid electrolyte interphase (SEI) for lithium-ion batteries. *npj Comput. Mater.* **4**, (2018).
9. H. Wu and Y. Cui. Designing nanostructured Si anodes for high energy. *Nano Today* **7**, 414–429 (2012).
10. C. Li, H. P. Zhang, L. J. Fu, et al. Cathode materials modified by surface coating for lithium ion batteries. *Electrochim. Acta* **51**, 3872–3883 (2006).
11. Q. Li, Y. Wang, X. Wang, et al. Investigations on the fundamental process of cathode electrolyte interphase formation and evolution of high-voltage cathodes. *ACS Appl. Mater. Interfaces* **12**, 2319–2326 (2020).
12. L. Xu, S. Tang, Y. Cheng, et al. Interfaces in solid-state lithium batteries. *Joule* **2**, 1991–2015 (2018).
13. Y. Xiao, Y. Wang, S. H. Bo, et al. Understanding interface stability in solid-state batteries. *Nat. Rev. Mater.* **5**, 105–126 (2020).
14. H. Li and H. Zhou. Enhancing the performances of Li-ion batteries by carbon-coating: Present and future. *Chem. Commun.* **48**, 1201–1217 (2012).
15. J. Li, N. J. Dudney, J. Nanda, et al. Artificial solid electrolyte interphase to address the electrochemical degradation of silicon electrodes. *ACS Appl. Mater. Interfaces* **6**, 10083–10088 (2014).
16. R. Xu, X. B. Cheng, C. Yan, et al. Artificial interphases for highly stable lithium metal anode. *Matter* **1**, 317–344 (2019).

17. Z. Chen, Y. Qin, K. Amine, et al. Role of surface coating on cathode materials for lithium-ion batteries. *J. Mater. Chem.* **20**, 7606–7612 (2010).
18. Y. Liu, D. Lin, P. Y. Yuen, et al. An artificial solid electrolyte interphase with high Li-ion conductivity, mechanical strength, and flexibility for stable lithium metal anodes. *Adv. Mater.* **29**, 1605531 (2017).
19. L. Chen, K. S. Chen, X. Chen, et al. Novel ALD chemistry enabled low-temperature synthesis of lithium fluoride coatings for durable lithium anodes. *ACS Appl. Mater. Interfaces* **10**, 26972–26981 (2018).
20. H. Wang, X. Xie, X. Wei, et al. A new strategy to stabilize capacity and insight into the interface behavior in electrochemical reaction of LiNi<sub>0.5</sub>Mn<sub>1.5</sub>O<sub>4</sub>/graphite system for high-voltage lithium-ion batteries. *ACS Appl. Mater. Interfaces* **9**, 33274–33287 (2017).
21. J. W. Kim, D. H. Kim, D. Y. Oh, et al. Surface chemistry of LiNi<sub>0.5</sub>Mn<sub>1.5</sub>O<sub>4</sub> particles coated by Al<sub>2</sub>O<sub>3</sub> using atomic layer deposition for lithium-ion batteries. *J. Power Sources* **274**, 1254–1262 (2015).
22. B. Xiao, J. Liu, Q. Sun, et al. Unravelling the role of electrochemically active FePO<sub>4</sub> coating by atomic layer deposition for increased high-voltage stability of LiNi<sub>0.5</sub>Mn<sub>1.5</sub>O<sub>4</sub> cathode material. *Adv. Sci.* **2**, 1500022 (2015).
23. S. Tao, F. Kong, C. Wu, et al. Nanoscale TiO<sub>2</sub> membrane coating spinel LiNi<sub>0.5</sub>Mn<sub>1.5</sub>O<sub>4</sub> cathode material for advanced lithium-ion batteries. *J. Alloys Compd.* **705**, 413–419 (2017).
24. M. M. Deng, Z. F. Tang, Y. Shao, et al. Enhancing the electrochemical performances of LiNi<sub>0.5</sub>Mn<sub>1.5</sub>O<sub>4</sub> by Co<sub>3</sub>O<sub>4</sub> surface coating. *J. Alloys Compd.* **762**, 163–170 (2018).
25. J. Gao, T. Yuan, S. Luo, et al. Boosting lithium ion storage of lithium nickel manganese oxide via conformally interfacial nanocoating. *J. Colloid Interface Sci.* **570**, 153–162 (2020).
26. S. X. Zhao, H. Ding, Y. C. Wang, et al. Improving rate performance of LiFePO<sub>4</sub> cathode materials by hybrid coating of nano-Li<sub>3</sub>PO<sub>4</sub> and carbon. *J. Alloys Compd.* **566**, 206–211 (2013).
27. R. Zhao, L. Li, T. Xu, et al. One-step integrated surface modification to build a stable interface on high-voltage cathode for lithium-ion batteries. *ACS Appl. Mater. Interfaces* **11**, 16233–16242 (2019).
28. X. Meng, X. Q. Yang and X. Sun. Emerging applications of atomic layer deposition for lithium-ion battery studies. *Adv. Mater.* **24**, 3589–3615 (2012).
29. Y. S. Jung, A. S. Cavanagh, L. A. Riley, et al. Ultrathin direct atomic layer deposition on composite electrodes for highly durable and safe Li-Ion batteries. *Adv. Mater.* **22**, 2172–2176 (2010).
30. M. L. Lee, C. Y. Su, Y. H. Lin, et al. Atomic layer deposition of TiO<sub>2</sub> on negative electrode for lithium ion batteries. *J. Power Sources* **244**, 410–416 (2013).



31. H. Y. Wang and F. M. Wang. Electrochemical investigation of an artificial solid electrolyte interface for improving the cycle-ability of lithium ion batteries using an atomic layer deposition on a graphite electrode. *J. Power Sources* **233**, 1–5 (2013).
32. D. Ahn and X. Xiao. Extended lithium titanate cycling potential window with near zero capacity loss. *Electrochem. commun.* **13**, 796–799 (2011).
33. J. Liu, X. Li, M. Cai, et al. Ultrathin atomic layer deposited ZrO<sub>2</sub> coating to enhance the electrochemical performance of Li<sub>4</sub>Ti<sub>5</sub>O<sub>12</sub> as an anode material. *Electrochim. Acta* **93**, 195–201 (2013).
34. A. L. Lipson, K. Puntambekar, D. J. Comstock, et al. Nanoscale investigation of solid electrolyte interphase inhibition on li-ion battery MnO electrodes via atomic layer deposition of Al<sub>2</sub>O<sub>3</sub>. *Chem. Mater.* **26**, 935–940 (2014).
35. Y. He, X. Yu, Y. Wang, et al. Alumina-coated patterned amorphous silicon as the anode for a Lithium-Ion battery with high Coulombic efficiency. *Adv. Mater.* **23**, 4938–4941 (2011).
36. X. Xiao, P. Lu and D. Ahn. Ultrathin multifunctional oxide coatings for lithium ion batteries. *Adv. Mater.* **23**, 3911–3915 (2011).
37. A. Kohandehghan, P. Kalisvaart, K. Cui, et al. Silicon nanowire lithium-ion battery anodes with ALD deposited TiN coatings demonstrate a major improvement in cycling performance. *J. Mater. Chem. A* **1**, 12850–12861 (2013).
38. E. Memarzadeh Lotfabad, P. Kalisvaart, K. Cui, et al. ALD TiO<sub>2</sub> coated silicon nanowires for lithium ion battery anodes with enhanced cycling stability and coulombic efficiency. *Phys. Chem. Chem. Phys.* **15**, 13646–13657 (2013).
39. E. M. Lotfabad, P. Kalisvaart, A. Kohandehghan, et al. Si nanotubes ALD coated with TiO<sub>2</sub>, TiN or Al<sub>2</sub>O<sub>3</sub> as high performance lithium ion battery anodes. *J. Mater. Chem. A* **2**, 2504–2516 (2014).
40. D. Wang, J. Yang, J. Liu, et al. Atomic layer deposited coatings to significantly stabilize anodes for Li ion batteries: Effects of coating thickness and the size of anode particles. *J. Mater. Chem. A* **2**, 2306–2312 (2014).
41. J. H. Lee, M. H. Hon, Y. W. Chung, et al. The effect of TiO<sub>2</sub> coating on the electrochemical performance of ZnO nanorod as the anode material for lithium-ion battery. *Appl. Phys. A* **102**, 545–550 (2011).
42. E. Kang, Y. S. Jung, A. S. Cavanagh, et al. Fe<sub>3</sub>O<sub>4</sub> nanoparticles confined in mesocellular carbon foam for high performance anode materials for lithium-ion batteries. *Adv. Funct. Mater.* **21**, 2430–2438 (2011).
43. L. A. Riley, A. S. Cavanagh, S. M. George, et al. Conformal surface coatings to enable high volume expansion Li-Ion anode materials. *ChemPhysChem* **11**, 2124–2130 (2010).
44. X. Song, S. Li, X. Li, et al. A lattice-matched interface between in situ/artificial SEIs inhibiting SEI decomposition for enhanced lithium storage. *J. Mater. Chem. A* **8**, 11165–11176 (2020).

45. J. S. Park, X. Meng, J. W. Elam, et al. Ultrathin lithium-ion conducting coatings for increased interfacial stability in high voltage lithium-ion batteries. *Chem. Mater.* **26**, 3128–3134 (2014).
46. Y. Cao, X. Meng and J. W. Elam. Atomic layer deposition of  $\text{Li}_x\text{Al}_y\text{S}$  solid-state electrolytes for stabilizing lithium-metal anodes. *ChemElectroChem* **3**, 858–863 (2016).
47. L. Chen, J. G. Connell, A. Nie, et al. Lithium metal protected by atomic layer deposition metal oxide for high performance anodes. *J. Mater. Chem. A* **5**, 12297–12309 (2017).
48. Y. Yang, Y. Liu, K. Pu, et al. Highly stable cycling of amorphous  $\text{Li}_2\text{CO}_3$ -coated  $\alpha$ - $\text{Fe}_2\text{O}_3$  nanocrystallines prepared via a new mechanochemical strategy for Li-ion batteries. *Adv. Funct. Mater.* **27**, 1605011 (2017).
49. W. D. Richards, L. J. Miara, Y. Wang, et al. Interface stability in solid-state batteries. *Chem. Mater.* **28**, 266–273 (2016).
50. L. S. Combes, S. S. Ballard and K. A. McCarthy. Mechanical and thermal properties of certain optical crystalline materials. *J. Opt. Soc. Am.* **41**, 215–222 (1951).
51. C. Monroe and J. Newman. The impact of elastic deformation on deposition kinetics at lithium/polymer interfaces. *J. Electrochem. Soc.* **152**, A396 (2005).
52. Y. S. Jung, A. S. Cavanagh, A. C. Dillon, et al. Enhanced stability of  $\text{LiCoO}_2$  cathodes in lithium-ion batteries using surface modification by atomic layer deposition. *J. Electrochem. Soc.* **157**, A75–A81 (2010).
53. X. Li, J. Liu, X. Meng, et al. Significant impact on cathode performance of lithium-ion batteries by precisely controlled metal oxide nanocoatings via atomic layer deposition. *J. Power Sources* **247**, 57–69 (2014).
54. I. D. Scott, Y. S. Jung, A. S. Cavanagh, et al. Ultrathin coatings on nano- $\text{LiCoO}_2$  for Li-ion vehicular applications. *Nano Lett.* **11**, 414–418 (2011).
55. F. Mattelaer, P. M. Vereecken, J. Dendooven, et al. The influence of ultrathin amorphous ALD alumina and titania on the rate capability of anatase  $\text{TiO}_2$  and  $\text{LiMn}_2\text{O}_4$  lithium ion battery electrodes. *Adv. Mater. Interfaces* **4**, 1–11 (2017).
56. A. Shapira, O. Tiurin, N. Solomatin, et al. Robust  $\text{AlF}_3$  atomic layer deposition protective coating on  $\text{LiMn}_{1.5}\text{Ni}_{0.5}\text{O}_4$  particles: an advanced Li-ion battery cathode material powder. *ACS Appl. Energy Mater.* **1**, 6809–6823 (2018).
57. A. Kraytsberg, H. Drezner, M. Auinat, et al. Atomic layer deposition of a particularized protective  $\text{MgF}_2$  film on a Li-ion battery  $\text{LiMn}_{1.5}\text{Ni}_{0.5}\text{O}_4$  cathode powder material. *ChemNanoMat* **1**, 577–585 (2015).
58. J. Xie, A. D. Sendek, E. D. Cubuk, et al. Atomic layer deposition of stable  $\text{LiAlF}_4$  lithium ion conductive interfacial layer for stable cathode cycling. *ACS Nano* **11**, 7019–7027 (2017).
59. X. Li, J. Liu, M. N. Banis, et al. Atomic layer deposition of solid-state electrolyte coated cathode materials with superior high-voltage cycling behavior for lithium ion battery application. *Energy Environ. Sci.* **7**, 768–778 (2014).

60. L. A. Riley, S. Van Atta, A. S. Cavanagh, et al. Electrochemical effects of ALD surface modification on combustion synthesized  $\text{LiNi}_{1/3}\text{Mn}_{1/3}\text{Co}_{1/3}\text{O}_2$  as a layered-cathode material. *J. Power Sources* **196**, 3317–3324 (2011).
61. J. Liu, M. N. Banis, X. Li, et al. Atomic layer deposition of lithium tantalate solid-state electrolytes. *J. Phys. Chem. C* **117**, 20260–20267 (2013).
62. Y. Zhao, L. Zhang, J. Liu, et al. Atomic/molecular layer deposition for energy storage and conversion. *Chem. Soc. Rev.* **50**, 3889–3956 (2021).
63. R. B. King. *Encyclopedia of Inorganic Chemistry*. (Wiley & Sons, 2005).
64. S. Deng, B. Xiao, B. Wang, et al. New insight into atomic-scale engineering of electrode surface for long-life and safe high voltage lithium ion cathodes. *Nano Energy* **38**, 19–27 (2017).
65. W. Mao, W. Yue, Z. Xu, et al. Novel hoberman sphere design for interlaced  $\text{Mn}_3\text{O}_4@\text{CNT}$  architecture with atomic layer deposition-coated  $\text{TiO}_2$  overlayer as advanced anodes in Li-ion battery. *ACS Appl. Mater. Interfaces* **12**, 39282–39292 (2020).
66. B. Zhu, N. Liu, M. McDowell, et al. Interfacial stabilizing effect of  $\text{ZnO}$  on Si anodes for lithium ion battery. *Nano Energy* **13**, 620–625 (2015).
67. N. Yesibolati, M. Shahid, W. Chen, et al.  $\text{SnO}_2$  anode surface passivation by atomic layer deposited  $\text{HfO}_2$  improves li-ion battery performance. *Small* **10**, 2849–2858 (2014).
68. M. Q. Snyder, S. A. Trebukhova, B. Ravdel, et al. Synthesis and characterization of atomic layer deposited titanium nitride thin films on lithium titanate spinel powder as a lithium-ion battery anode. *J. Power Sources* **165**, 379–385 (2007).
69. Y. S. Jung, A. S. Cavanagh, A. C. Dillon, et al. Enhanced stability of  $\text{LiCoO}_2$  cathodes in lithium-ion batteries using surface modification by atomic layer deposition. *J. Electrochem. Soc.* **157**, A75 (2010).
70. Y. Seok Jung, A. S. Cavanagh, Y. Yan, et al. Effects of atomic layer deposition of  $\text{Al}_2\text{O}_3$  on the  $\text{Li}[\text{Li}_{0.20}\text{Mn}_{0.54}\text{Ni}_{0.13}\text{Co}_{0.13}]\text{O}_2$  cathode for lithium-ion batteries. *J. Electrochem. Soc.* **158**, A1298 (2011).
71. X. Zhang, I. Belharouak, L. Li, et al. Structural and electrochemical study of  $\text{Al}_2\text{O}_3$  and  $\text{TiO}_2$  coated  $\text{Li}_{1.2}\text{Ni}_{0.13}\text{Mn}_{0.54}\text{Co}_{0.13}\text{O}_2$  cathode material using ALD. *Adv. Energy Mater.* **3**, 1299–1307 (2013).
72. D. Liu, Y. Liu, S. L. Candelaria, et al. Atomic layer deposition of  $\text{Al}_2\text{O}_3$  on  $\text{V}_2\text{O}_5$  xerogel film for enhanced lithium-ion intercalation stability. *J. Vac. Sci. Technol. A Vacuum, Surfaces, Film.* **30**, 01A123 (2012).
73. J. Zhao, G. Qu, J. C. Flake, et al. Low temperature preparation of crystalline  $\text{ZrO}_2$  coatings for improved elevated-temperature performances of Li-ion battery cathodes. *Chem. Commun.* **48**, 8108–8110 (2012).
74. M. R. Laskar, D. H. K. Jackson, S. Xu, et al. Atomic layer deposited  $\text{MgO}$ : a lower overpotential coating for  $\text{Li}[\text{Ni}_{0.5}\text{Mn}_{0.3}\text{Co}_{0.2}]\text{O}_2$  cathode. *ACS Appl. Mater. Interfaces* **9**, 11231–11239 (2017).

75. Y. Gao, R. L. Patel, K. Y. Shen, et al. Boosting the electrochemical performance of  $\text{Li}_{1.2}\text{Mn}_{0.54}\text{Ni}_{0.13}\text{Co}_{0.13}\text{O}_2$  by atomic layer-deposited  $\text{CeO}_2$  coating. *ACS Omega* **3**, 906–916 (2018).
76. C. F. Lin, M. Noked, A. C. Kozen, et al. Solid electrolyte lithium phosphous oxynitride as a protective nanocladding layer for 3D high-capacity conversion electrodes. *ACS Nano* **10**, 2693–2701 (2016).



## ALD principles and diagnostics

---

---

The application of artificial electrode-electrolyte interphases (EELs) by ALD and the effect on the battery performance have been extensively discussed in the previous chapter. To further improve the performance of the EELs, a better understanding of the fabrication of such layers, i.e. the ALD process itself and the film properties, is useful. Moreover, the development of new ALD chemistries enables the deposition of films with tunable and better properties. This chapter provides a detailed explanation of the ALD process and the process variables. Various important parameters can be distinguished for ALD, e.g., precursor/coreactant, temperature and substrate chemistry. It is essential that decisions on the choice of these parameters are taken in an educated way. The chapter also presents an overview of commonly used characterization tools in this thesis which are useful to get a better understanding of the process and the as-deposited films. This forms the basis for the subsequent chapters, which focus on the characterization of novel and existing ALD processes useful as artificial EEL.

### 3.1 ALD basics and capabilities

ALD is a process enabling material growth precisely controlled at the atomic level, featuring the cyclic repetition of chemical reactions (see Figure 3.1). The ALD process is explained on the basis of the well-known model system of  $\text{Al}_2\text{O}_3$  using  $\text{Al}(\text{CH}_3)_3$  as precursor and  $\text{H}_2\text{O}$  as coreactant. The  $\text{Al}_2\text{O}_3$  ALD cycle consists of two self-limiting half-reactions (half cycles). An initial surface terminated with OH groups is assumed. The first step consists of the precursor exposure; the  $\text{Al}(\text{CH}_3)_3$  precursor reacts with the OH surface groups, forming Al-O bonds and releasing volatile  $\text{CH}_4$ . The adsorbed precursor results in a surface terminated with  $-\text{CH}_3$  groups which are not reactive upon further exposure of the surface to the precursor, limiting the amount of precursor that can adsorb. In the second half-cycle  $\text{H}_2\text{O}$  is introduced. The  $\text{H}_2\text{O}$  molecules react with the  $-\text{CH}_3$  groups, releasing  $\text{CH}_4$  and leaving behind a surface saturated by OH groups. The purge step after each reaction step is crucial to preserve the self-limiting nature of ALD reactions as it physically separates the precursors and coreactants and thus prevents any reactions to occur. After the two ALD half-cycles, the surface is again reactive to the precursor. Repeating these steps in a cyclic fashion, one can grow a targeted material with a desired thickness in an accurately controlled mode. During one cycle of the  $\text{Al}_2\text{O}_3$  ALD process  $\sim 0.1$  nm of material is deposited. ALD film growth is highly uniform and yields excellent conformality because at every available surface reaction site no more than one precursor/reactant molecule can chemisorb regardless of the incoming precursor/coreactant flux (see section 3.2.2). This is referred to as self-limiting growth behavior. The ALD characteristics bring a number of additional benefits, such as excellent tunability in materials composition and crystallinity, and opportunities for new materials. So far, ALD has been shown to fabricate a large variety of inorganic materials, such as metal oxides, metal sulfides, metal nitrides, metal fluorides, complex compounds, et cetera.

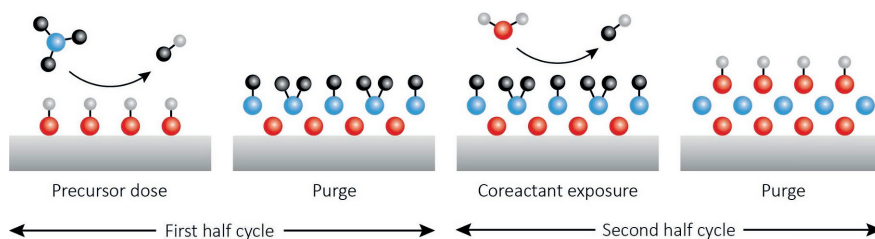


**Figure 3.1** A general ALD growth process for metal oxides. The first half-cycle consists of self-limiting adsorption of precursor molecules on the available surface groups and a purge step to remove the volatile reaction by-products and the excess of precursor dosed. During the second half-cycle, the surface is exposed to reactant molecules that react in a self-limiting way with the surface groups of the adsorbed precursor. The second half-cycle is completed by another purge step to remove the volatile reaction by-products and the excess of reactant dosed.

### 3.1.1 ALD reactor

ALD-growth is observed in a specific temperature window, in which all the requirements for self-limiting growth are present (i.e. no precursor or coreactant condensation, no precursor decomposition and sufficient reactivity). Control of the temperature and the exposure to the precursor gasses and vapors is achieved in a so-called ALD reactor. This is typically a chamber at vacuum pressure in which the precursor and reactant are dosed to the substrate surface. In this work the thermal and remote plasma ALD reactor FlexAL (Oxford Instruments) was adopted, which is schematically illustrated in Figure 3.2. The reactor consists of a rotary and turbo molecular pump system such that it can reach a base pressure of  $< 10^{-6}$  Torr by overnight pumping. The process table temperature can be set from 25 - 400 °C and the reactor wall from 25 - 120 °C. ALD processes such as  $\text{Al}_2\text{O}_3$  using  $\text{Al}(\text{CH}_3)_3$  and  $\text{H}_2\text{O}$  rely solely on thermal energy to drive chemical reactions. Hence, they are also called thermal ALD processes. ALD processes in which the reactivity of the reactants is enhanced by adding other forms of energy are defined as “energy enhanced” ALD processes. Examples of such “energy-enhanced” reactants are: ozone, plasma and photons. The ALD reactor used in this research project can be used for thermal ALD and is also ozone- and plasma-operated. The plasma source is connected to five types of reactant gasses, as illustrated in Figure 3.2. In this work mainly plasma-assisted ALD is investigated. Plasma-assisted ALD is therefore further explained in section 3.1.2. The reactor is also equipped with *in situ* diagnostics, namely an ellipsometer and a mass spectrometer. Using *in situ* diagnostics, fundamental insight into the film growth

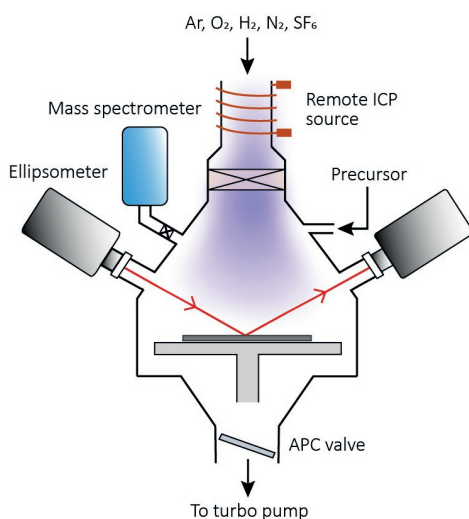


**Figure 3.2** A schematic showing the ALD reactor. The pump unit as well as the inductively coupled plasma (ICP) are connected to the deposition chamber through gate valves. The reactor is equipped with a mass spectrometer and ellipsometer.



and reaction mechanisms governing the ALD processes can be inferred. Moreover, *in situ* techniques provide the opportunity to monitor, optimize and control the ALD process. The common diagnostics used to characterize the ALD processes in this work are discussed in section 3.2.

### 3.1.2 Plasma-assisted ALD

The reaction of the precursor at the surface with the coreactant typically needs a certain activation energy. Therefore, the deposition temperatures of most processes typically range between 100 °C and 350 °C. In some cases, where temperature sensitive substrates are being used (such as polymers for flexible electronics), this temperature range is inadequate. In general, the reactivity is drastically increased going from thermal ALD to plasma-assisted ALD.<sup>1</sup> Plasma-assisted ALD was used for the first time in 1991 by De Keijser and Van Oordorp of the Philips Research Laboratories in the Netherlands for the deposition of gallium arsenide (GaAs) using hydrogen plasma.<sup>2</sup> Since then, more and more ALD processes are being developed in which plasma is used.<sup>3</sup>

A plasma is generated by applying electrical power to the source gas during the reactant step such that the gas breaks down. A plasma, containing electrons and ions in addition to (reactive) neutrals, is often described as the fourth state of matter. More specifically, free electrons in the plasma typically ionize and dissociate the coreactant molecules resulting in the generation of highly reactive species, such as radicals (e.g., O, H, depending on the reactant gas). These reactive species will subsequently react with the adsorbed precursor to form the thin film. In this work a remote plasma configuration is used, as depicted in Figure 3.2. Compared to direct plasma ALD, the plasma source is placed further from the substrate and the substrate itself is not part of the plasma creation zone.

Typically, simple gases are taken as coreactants, such as O<sub>2</sub>, H<sub>2</sub> or N<sub>2</sub>. In the case of the previously described model system of Al<sub>2</sub>O<sub>3</sub>, H<sub>2</sub>O is being used as a coreactant for thermal ALD, whereas O<sub>2</sub> plasma is typically used for plasma-assisted ALD. An O<sub>2</sub> plasma is also used for the Li<sub>2</sub>CO<sub>3</sub> and AlP<sub>x</sub>O<sub>y</sub> ALD processes in this work. The implementation of plasma results in a more complicated chemistry since one coreactant molecule will form several plasma species that can undergo different reactions at the surface. In an oxygen plasma, already 11 different species can be found: molecular oxygen (O<sub>2</sub>), metastable molecular oxygen, atomic oxygen (O), metastable atomic oxygen, and ozone (O<sub>3</sub>) as neutral species, electrons (e<sup>-</sup>), O<sup>-</sup>, O<sub>2</sub><sup>-</sup>, and O<sub>3</sub><sup>-</sup> as negatively charged species and O<sup>+</sup> and O<sub>2</sub><sup>+</sup> as positively charged species.<sup>4</sup> Obviously, a complexity of possible reactions can take place. Moreover, the reaction of these oxygen species with the adsorbed inorganic precursor will release additional molecules that are introduced in the plasma. These new species can also be redeposited which further increases the complexity. Hence, a thorough optimization of the plasma parameters must always be considered. Plasma-assisted ALD processes

need to be understood to be able to improve and design new processes more rationally. To this end, also the reaction mechanisms of the precursor and reactants with the surface should be investigated (this is further discussed in section 3.2.3).

As previously discussed, the introduction of a plasma step in an ALD process can be advantageous due to increased reactivity. In addition, there are several additional merits which can be present for plasma-assisted ALD:

- Additional control over film properties such as density, crystallinity or stoichiometry.<sup>5</sup> The functionality of the films for specific applications can be tuned by modulating the film characteristics during film growth.
- The possibility of using low deposition temperatures.<sup>1</sup> Especially in low pressure processing plasmas the overall temperature of the system will remain low because only electrons get heated while energy transfer to other particles is limited due to infrequent collisions.
- A wide variety of substrate materials can be used. Due to the high reactivity at low temperatures, a wider variety of substrate materials can be used with respect to thermal ALD.
- Higher growth rates are often obtained.<sup>1</sup> Since the plasma reacts very effectively with the surface, enhanced surface coverage and therefore enhanced growth rates can be reached.
- Dense films can be deposited.<sup>1</sup> The efficient reactions can lead to the generation of more active surface sites which could result in dense packing of the film compared to thermal ALD.
- High purity films can be deposited.<sup>1</sup> The plasma reaction with the precursor is often very efficient which can result in high purity layers. However, redeposition from the ligand combustion products or surface fragments needs to be considered.
- A wide variety of precursors can be used.<sup>6</sup> The high reactivity of the plasma enables the use of less reactive precursors that would not work in a conventional thermal ALD process.
- Prior to the film deposition, the reactor walls can be conditioned and the substrate can be cleaned or pretreated by a plasma. The latter can be used to create active sites onto the substrate to facilitate ALD reactions in the following step when the precursor is introduced.

### 3.1.3 ALD recipes

Details about an ALD process are generally illustrated in the ALD recipe. The ALD recipe is the list of all dosing steps and times required to run and reproduce the ALD process. The model system described in Figure 3.1 is commonly labelled as a process with an AB cycle to indicate the use of one precursor and one coreactant. A schematic illustration of several types of ALD cycles is shown in Figure 3.3. Below the different types of ALD cycles, the processes are listed which are developed in this work. Li<sub>2</sub>O, LiOH and LiF can be deposited using an AB cycle. Doped and ternary materials can be

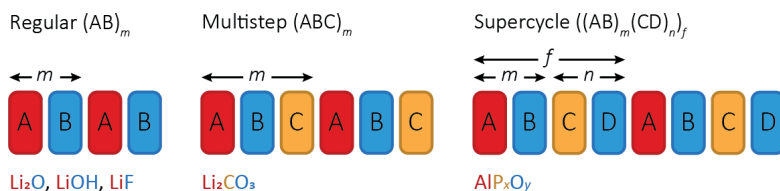


**Figure 3.3** Different types of cycles that can be used in ALD processes. In the regular AB cycle, A is the precursor dosing step and B the coreactant dosing step. The multistep ABC cycle involves the dosing of three different species. The  $(AB)_m(CD)_n$  supercycle is defined by  $m$  repetitions of the AB cycle followed by  $n$  times the repetition of a CD cycle. Subsequently this sequence is repeated  $f$  times.

synthesized by ALD using a multistep ABC cycle or supercycle process. Thermal ALD of  $\text{Li}_2\text{CO}_3$  needs a multistep approach. However, when plasma ALD is used, a regular AB cycle can be used for the deposition of  $\text{Li}_2\text{CO}_3$  (see Chapter 5). In the supercycle approach, an ALD process is designed by combining different AB processes together. The supercycle  $(AB)_m(CD)_n$  is made by repeating  $m$  times the AB cycle and  $n$  times the CD cycle. The supercycle is repeated  $f$  times in order to achieve the desired thickness. The  $\text{AlP}_x\text{O}_y$  process was developed using a supercycle scheme. Herein, the supercycle consists of  $n$   $\text{PO}_x$  cycle(s) and 1  $\text{Al}_2\text{O}_3$  cycle. This is further explained in Chapter 7.

The specific dosing and purge times and the overall duration of one cycle depend on the specific precursor and coreactants used as well as on the reactor volume and design. Further details are generally reported, such as the temperature of the substrate or the reactor base pressure, to be able to reproduce the recipe. When plasma-assisted ALD is being used, it is useful to know the type of plasma source, its geometry and the distance from the substrate, as well as the pressure of the gas used while the plasma is ignited, since all those parameters can affect the plasma characteristics.

## 3.2 Characterization of the ALD process

This section gives more insight into the characterization of the ALD process during process development. Development of ALD processes is useful either to enable fabrication of new materials by ALD, or to improve existing ALD materials. In this respect, the most frequently used experimental techniques of the research in this dissertation are highlighted.

### 3.2.1 Growth per cycle

An ALD process is typically characterized by its growth per cycle (GPC) value. The film growth rate is controlled by the surface coverage achieved during each half-cycle. If the exposure time of the surface to the precursor or coreactant is sufficient, the surface coverage reaches saturation, i.e. all accessible functional groups have reacted.

The GPC is determined by the ratio between the film thickness after a certain number of cycles and the number of cycles. A widely used approach to measure the thickness of the layer is the use of spectroscopic ellipsometry (SE). SE allows to determine the thickness of the layer with accuracy at Å level, along with its optical constants. The GPC can also be measured by other techniques, such as ion beam analysis (IBA). From IBA, which is explained in section 3.3, the GPC can be evaluated in terms of the number of atoms deposited per unit area per cycle. In this dissertation, both SE and IBA are being used for better accuracy. In Figure 3.4a, a typical graph is shown of the thickness evolution as a function of the number of cycles. The GPC can be obtained by dividing the thickness by the number of ALD cycles. However, it is often observed that a linear fit through all measured data points does not intersect the origin. This can be explained by the nucleation behavior of the ALD process. Nucleation occurs until the film is completely closed. The reaction of the precursor and coreactant with the initial substrate and the reaction of the precursor and coreactant with a closed film of the material to be grown usually lead to different growth per cycle values. The initial GPC can be lower or higher when compared to the GPC for linear film growth. These instances are referred to as surface inhibited growth or surface enhanced growth, respectively. Surface enhanced growth is, for example, observed for the LiF ALD process on Si substrates covered with 10 Al<sub>2</sub>O<sub>3</sub> ALD cycles, as shown in Chapter 6.

When referring to the ideal ALD process, the film growth is described as occurring ‘atomic layer by atomic layer’. The actual GPC, measured experimentally, is a fraction of a monolayer of the deposited material. The GPC depends on the surface coverage after each dosing step. Consequently, parameters such as the surface concentration of the functional groups and the reactivity between the precursor and the substrate

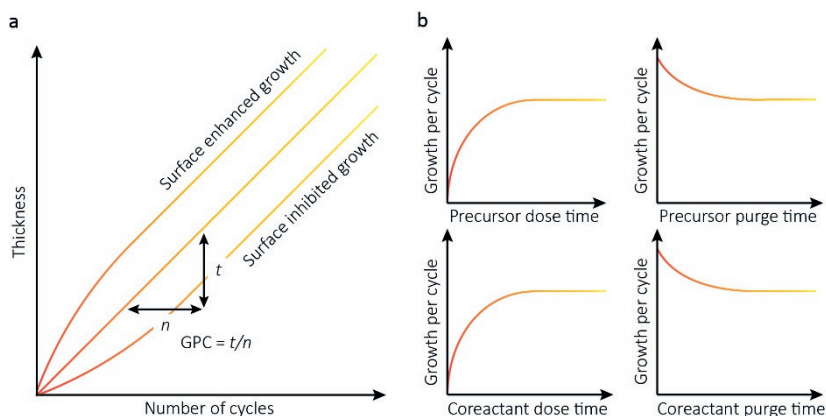


**Figure 3.4** a) Film thickness as a function of the number of ALD cycles for normal as well as surface enhanced and surface inhibited growth and b) the saturation behavior in a typical ALD process showing the growth per cycle as a function of the precursor dose time, precursor purge time, coreactant dose time and coreactant purge time.

### Spectroscopic ellipsometry

Using SE, the change of polarization of a light beam upon reflection or transmission is measured. The experimental setup usually is composed of a source, polarizer, analyzer, and a detector (see Figure 3.5). The known incident radiation interacts with the sample and is measured by a detector. The polarization change is quantified by the amplitude ratio,  $\Psi$ , and the phase difference,  $\Delta$ . The values of  $\Psi$  and  $\Delta$  are determined by measuring the complex reflectance ratio  $\rho$ . The polarization state of the light incident upon the sample may be decomposed into a perpendicular (s) and a parallel (p) component, compared to the plane of incidence. The amplitudes of the s and p components, after reflection and normalized to their initial value, are denoted by  $r_s$  and  $r_p$ , respectively. The measured complex reflectance ratio is the ratio of  $r_p$  over  $r_s$ :

$$\rho = \frac{r_p}{r_s} = \tan(\Psi) \cdot e^{i\Delta} \quad (\text{Eq. 3.1})$$

The values of  $\Psi$  and  $\Delta$  cannot be converted directly into the optical constants of the sample. A model must be established, which considers the optical constants and thickness parameters of all individual layers of the sample including the correct layer sequence. Subsequent optimization of the model parameters is needed to obtain agreement between the experimental and theoretical data. This is done using an iterative procedure (least-squares minimization) in which the unknown optical constants and/or thickness parameters are varied, and the  $\Psi$  and  $\Delta$  values are calculated. The calculated values which match the experimental data best provide the optical constants and thickness parameters of the sample.

SE measurements can be performed *in situ*, by following the growth process every  $x$  number of cycles, or *ex situ*, to determine the properties of a thin film at the end of an ALD process. The *ex situ* SE measurements are more accurate for the determination of the film optical properties, because multi-angle data acquisition is available. The *in situ* approach provides understanding of how the ALD process evolves in different stages, i.e. from the initial nucleation to bulk growth.

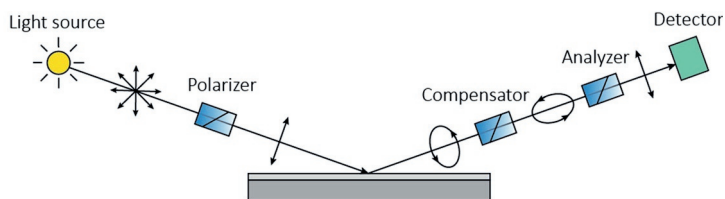


**Figure 3.5** A schematic of the experimental setup of spectroscopic ellipsometry.

can limit the amount of precursor reacting with the surface. Furthermore, the steric hindrance caused by the chemisorbed precursor at the surface can make functional groups in close proximity to the one where chemisorption has occurred, less accessible to other precursor molecules. For  $\text{Li}_2\text{CO}_3$ , in each cycle approximately  $1/5^{\text{th}}$  of a monolayer was deposited using thermal ALD and about  $1/4^{\text{th}}$  to  $1/3^{\text{rd}}$  of a monolayer is deposited for plasma-assisted ALD each cycle. Typical values of GPC range from about  $0.3 \text{ \AA}$  to  $1.4 \text{ \AA}$ . GPC values vary, depending on the selected material as well as the combination of precursor and co-reactant.

The self-limiting nature of the chemical reactions leads to growth independent of the precursor flux. Once the reactions have saturated (i.e. enough precursor and coreactant has been introduced), additional exposure to the precursor or coreactant does not lead to further growth, as illustrated in Figure 3.4b. The purge step reaches saturation when reactions between precursors and coreactants in gas phase are suppressed. The optimal dosing and purging time can be extracted from the graphs. This also holds for plasma-assisted ALD. Only if independence of the GPC for longer precursor and plasma pulse times and a linear dependence of the film thickness on the applied number of ALD cycles can be shown, the growth of plasma-assisted processes is ALD like. No etching phenomena of the plasma with the substrate and/or deposited film should be observed.

Another characteristic experimental behavior of ALD processes is the dependence of the GPC on the process temperature. Figure 3.6 shows a schematic representation of the GPC as a function of the deposition temperature. Classically, the ALD temperature window is defined as the temperature range within which an ALD process shows no GPC dependence from the temperature. In real cases, the GPC can

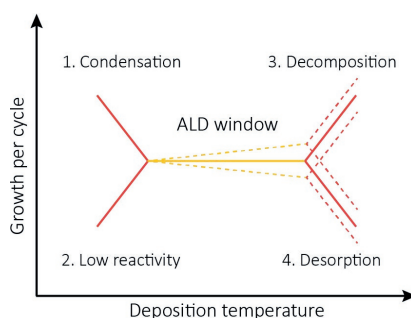


**Figure 3.6** Schematic representation of both the theoretical ALD temperature window (continuous line) and the experimentally observed temperature window (striped line). Slight variations in GPC occur due to the variation in concentration of surface groups, film density or composition with temperature. Outside the ALD temperature window more dramatic changes in GPC may be seen. At lower temperatures 1) precursor or coreactant condensation or 2) low reactivity can be observed. At higher temperatures 3) precursor or coreactant decomposition or 4) desorption of the film itself or the reactive surface groups may take place.

still exhibit a dependence from the temperature within the ALD window due to the variation in concentration of surface groups, film density or composition. A typical example is the decrease of the surface concentration of –OH groups leading to the decrease in GPC for ALD  $\text{Al}_2\text{O}_3$ , especially for the plasma-assisted process.<sup>7</sup> Similar results have been obtained for plasma-assisted ALD of  $\text{Al}_x\text{PO}_y$  as presented in Chapter 7. Variations within the ALD-window could be larger for plasma-assisted ALD due to different reaction mechanisms and a much higher energy transfer to the surface. Moreover, optimization of a plasma-assisted ALD process can in some cases be more complex compared to ALD because not only dose and purge times and deposition temperatures must be tuned, but also the plasma itself. Usually the plasma exposure time, plasma power and pressure influence the properties of the films. Outside the ALD window there are different chemical and physical processes which can disrupt the ALD behavior. Some precursors and coreactants can condense on the surface at lower deposition temperatures, resulting in an increase in GPC. Alternatively, the reactivity of the molecules with the surface sites can be too low because of limited thermal energy at low temperatures, which prevents saturation of the reaction and leads to a decrease in growth. At higher temperatures, the precursors or coreactants can decompose, leading to a CVD component and an increase in growth. Furthermore, the film itself or the reactive surface groups involved may desorb or etch above a certain temperature, leading to a decrease in growth.<sup>8</sup>

### **3.2.2 Uniformity and conformality**

As a result of the ALD self-limiting nature, films deposited by ALD can show very high uniformity over large areas, as one can simply keep supplying precursor until the reactions have saturated over the entire surface with no fear of over-exposure in areas closer to the precursor inlet. Additionally, the films also show very good conformality, meaning deposition of a uniform film in deep trenches or around 3-dimensional structures is possible.<sup>8</sup> Co-existence of precursor and coreactant in the reactor would lead to parasitic chemical vapor deposition (CVD) growth. The difference between CVD and ALD is illustrated in Figure 3.7. CVD is also a thin film deposition technique, but the reactions occur in the gas phase as well as at the surface and are not self-limiting. CVD is a flux-controlled process, meaning that the growth rate on a surface is directly related to the flux of source species. It is generally not desirable to have a CVD contribution in an ALD process, since it can result in the loss of control over the deposition in terms of uniformity and conformality. For plasma-assisted ALD the highly reactive plasma species tend to recombine at the surface, which could lead to the loss of reactive species. In some cases, the path of the reactive species in plasma-assisted ALD might be too long to reach the whole surface of the trenches for a conformal deposition on high aspect ratio substrates. However, in various studies in this thesis it was shown that good conformality can also be obtained by plasma-assisted ALD. These results are presented in Chapters 4, 6 and 7.

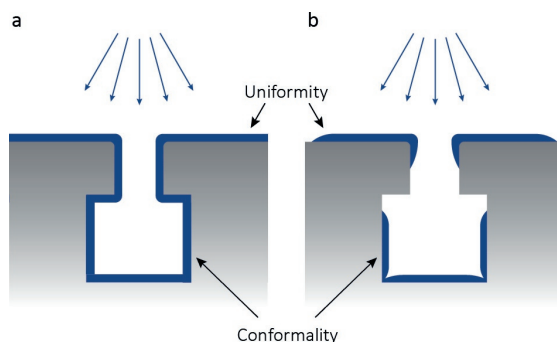


**Figure 3.7** The uniformity and conformality for a) surface-controlled and b) flux-controlled deposition techniques (i.e. CVD) on a challenging 3-dimensional substrate (gray). In ALD, the film coats every surface uniformly, while a flux-controlled deposition technique causes effects such as shadowing and insufficient film penetration into trenches.

### 3.2.3 ALD chemistry

To understand the relation between (plasma-assisted) processes and the material properties, a more detailed insight into the reaction mechanism is needed. This knowledge can then be used to tune the process and the properties of the deposited films. The specific details on the reaction mechanisms are strongly dependent on the particular ALD process. The reaction mechanisms largely depend on the chosen precursors and coreactants, but also on, for example, the exposure times, the temperature and the pressure. To gain insight into the ALD chemistry of the selected processes, knowledge on the surface reaction products in each step of the process is essential.

In this regard, quadrupole mass spectrometry (QMS) is a very useful tool, especially when developing new ALD processes. For all the developed ALD processes in this work, mass spectrometry was used to identify the species present in the reactor. The ALD process can be monitored in real-time, tracking the precursor and reactant gasses as well as the formation of reaction products. By analyzing the composition of gases exiting the reactor, one can determine which reactions have taken place in the reactor, and it would be possible to adjust the process parameters accordingly. A mass spectrum obtained by QMS is usually presented as a bar graph, in which each bar represents an ion having a specific mass-to-charge ratio ( $m/z$ ). The  $m/z$  ratio is in most cases the same as the mass since most ions have charge +1. The mass spectrum obtained from the fragmentation of a particular molecule is referred to as the cracking pattern. The cracking pattern can be used to identify the parent molecules responsible for a measured spectrum. The NIST database contains a wide range of cracking patterns from a variety of sources, and can therefore be used to analyze measured mass spectra.<sup>9</sup> In the mass spectrum of a single molecule, the line produced by the heaviest ion passing through the machine is due to the parent ion.



The highest line in the bar diagram is usually called the base peak. This is the highest peak because it represents the most common fragment ion to be formed (either because there are several ways in which it could be produced during fragmentation of the parent ion, or because it is a particularly stable ion).

### Quadrupole mass spectrometry

A schematic diagram of the mass spectrometer is depicted in Figure 3.8. First, a small fraction of the gas molecules is extracted from the reactor through the orifice into the QMS. The gas molecules are ionized through electron-impact ionization by electrons with an energy of typically  $\sim 70$  eV. In most QMS configurations only stable gas-phase species are detected since plasma radicals will generally recombine while entering the QMS before they can be ionized. When a high energy electron collides with a molecule it often ionizes it:



However, a significant part of the molecules will be dissociated to smaller fragments of the parent molecule:



The species will then enter the quadrupole mass analyzer. Only charged particles will be accelerated, deflected and detected by the mass spectrometer. As the name implies, a quadrupole mass spectrometer consists of four cylindrical rods, set parallel to each other. Ions in the quadrupole are separated based on the stability of their trajectories in the oscillating electric fields that are applied to the rods. The quadrupole mass filter allows only a narrow mass range to pass through. The mass-to-charge-ratio ( $m/z$ ) of the ions that pass through is measured by the detector. Because ions are very reactive and short-lived their formation and manipulation must be conducted in high vacuum.

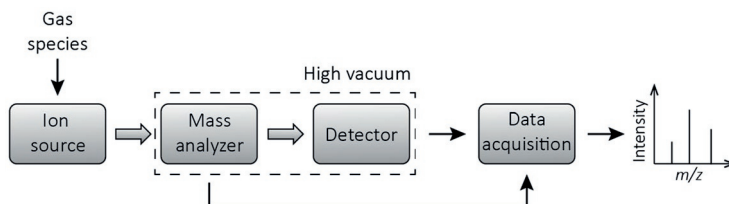


**Figure 3.8** Schematic diagram of a mass spectrometer. The gas species are ionized by the ion source. Ions are sorted and separated according to their mass and charge. The separated ions are then measured by the detector. The results are displayed in a chart.

In this research, the QMS was operated in two different modes. First, a wide mass range ( $m/z = 1 - 100$ ) with low time resolution was measured. This was done for example to measure all reagents. Next, a few selected masses with higher time resolution were measured. This is also referred to as a time-resolved scan. Measuring a large range of masses is desired to attribute changes at certain  $m/z$  values to specific gaseous species. However, to achieve sufficient time resolution, the time resolved measurements should be carried out. The masses should be carefully selected to represent the signals for the complete mass spectrum. Furthermore, the signals of multiple cycles can be used for averaging to improve the signal-to-noise ratio. In addition, reference spectra should be measured to distinguish the signals caused by species not taking place in the ALD process itself. Reaction products will not be formed when the surface reactions are already saturated, so repeating a precursor or reactant exposure will show their cracking patterns and can therefore serve as a reference. For example, a measurement of the coreactant using zero plasma power was obtained to measure only the source gas for the plasma-assisted ALD processes in this work. The specific measurement procedure applied for the different processes is described in the corresponding chapters: Chapter 5 for  $\text{Li}_2\text{CO}_3$ , Chapter 6 for  $\text{LiF}$ , and Chapter 7 for  $\text{AlP}_x\text{O}_y$ .

### 3.3 Characterization of the film properties

Previous section already presented the *in situ* diagnostics used to characterize the ALD process itself. For the research in this thesis, a wide variety of additional characterization tools were used to identify the physical and chemical properties of the films. The commonly used methods and diagnostics of the research described in the following chapters are highlighted.

#### 3.3.1 Additional features of SE

The thickness of the films was monitored by *in situ* spectroscopic ellipsometry, as described in previous section. SE is very sensitive to the change in the optical response of incident radiation that interacts with the material being investigated. Therefore, SE can also be used to characterize various material properties, such as uniformity, roughness and film composition. For example, film thickness and refractive index nonuniformity were measured in this work by *ex situ* SE, to map the surface of wafers up to 200 mm. Surface roughness was measured by *ex situ* SE measurements as well. Moreover, the compositional stability of  $\text{Li}_2\text{O}/\text{Li}_2\text{CO}_3$  films was measured using *in situ* SE by monitoring the phase change ( $\Delta$ ) at a fixed wavelength in Chapter 4. A sudden phase shift indicates that certain films were unstable, and a compositional change takes place at certain temperatures or when dosing  $\text{H}_2\text{O}$  or  $\text{CO}_2$ . In Chapter 6, *ex situ* SE was used to accurately measure the absorption spectra of the films to investigate the influence of the  $\text{SF}_6$  plasma on the absorption behavior.

### 3.3.2 Chemical composition

To ensure the quality of the films it is important that the films have a sufficiently high purity. To gain insight into the chemical composition of the films, X-ray photoelectron spectroscopy (XPS) is a very effective method. XPS is a spectroscopic technique which is able to track the elements that exist within a material or on the material surface and to what other elements they are bonded to. The measurements can be performed both at and across the surface, or in-depth profiling mode when ion-beam etching is adopted. However, in some cases it was found that the stoichiometry of the films changed due to interaction with Ar ions (preferential sputtering). This was the case for  $\text{Li}_2\text{CO}_3$  films which experiences a transition to  $\text{Li}_2\text{O}$  upon chemical decomposition during sputtering (see Chapter 4).

To complement the XPS measurements, a combination of ion beam techniques was used in this work. Ion beam analysis (IBA) involves the use of ion beams to probe the composition and to obtain elemental depth profiles. IBA methods are highly

#### X-ray photoelectron spectroscopy

XPS involves the irradiation of a sample with x-rays of sufficient energy which results in the excitation of electrons in specific bound states. The electron binding energy of each of the emitted electrons can be determined by using the following equation:

$$E_{\text{binding}} = E_{\text{photon}} - (E_{\text{kinetic}} + \varphi) \quad (\text{Eq. 3.4})$$

Here,  $E_{\text{binding}}$  is the energy of an electron attracted to a nucleus,  $E_{\text{photon}}$  is the energy of X-ray photons being used by the spectrometer and  $E_{\text{kinetic}}$  is the energy of the ejected electrons from the sample. The work function  $\varphi$  is a correction factor for the instrument and correlates to the minimum energy required to eject an electron from an atom. The kinetic energy is measured by the detector and the work function and photon energy are known, and therefore the binding energy can be determined.

The composition can be determined because the binding energy depends on the orbital and specific subshell (e.g., 1s, 2s, 2p, 3s, et cetera) where the electron is emitted from. Moreover, the binding energy also depends on the chemical environment (the bonds of the atom) and therefore chemical shifts can be determined using XPS. Typically, XPS plots show the number of electrons detected at a specific binding energy. For each chemical element, electrons are measured at a certain binding energy range, resulting in a set of characteristic XPS peaks. The Atomic percentage values are calculated by taking into account the relative sensitivity factor (RSF) for each element. Hydrogen cannot be detected and is therefore not included in these atomic percentages.

sensitive and the depth resolution is typically in the range of a few nanometers. The analyzed depth ranges from a few ten nanometers to a few ten micrometers. To be specific, Rutherford backscattering spectrometry (RBS), elastic recoil detection (ERD), and elastic backscattering (EBS) were carried out to determine the composition and mass density of the films. The measurements are particularly useful to verify the results obtained by XPS and to be able to probe the hydrogen content in the films.

### Ion beam analysis

Schematics of the set-ups for IBA are depicted in Figure 3.9. During the RBS analysis, an elastic, hard-sphere collision between high-energy (MeV)  $\text{He}^+$  ions from the incident beam and a stationary particle located in the sample takes place. Elastic means that no energy is transferred between the incident particle and the stationary particle during the collision. The measurement is nondestructive since the state of the stationary particle is not changed. The energy distribution and yield of the backscattered  $\text{He}^+$  ions at a given angle is measured. Since the backscattering cross section for each element is known, it is possible to obtain a quantitative compositional depth profile from the RBS spectrum obtained for films that are less than  $1\ \mu\text{m}$  thick. RBS was performed to determine most of the elements in the film. However, back-scattering can only occur from atoms that are heavier than the projectile ion, which means that hydrogen cannot be detected by RBS. Still, it is possible to measure hydrogen that is recoiled out of the sample in a forward-scattering event. ERD was performed to determine the hydrogen. Moreover, EBS was necessary for a more accurate determination of the Li and C contents in the films. This technique is similar to RBS but has the advantage that the cross sections for light elements are enhanced by the use of high energy protons as projectiles instead of  $\text{He}^+$ . The measured experimental IBA data are compared to a simulation for data interpretation. The results of the IBA are the areal density ( $\text{at} \cdot \text{cm}^{-2}$ ) of the atoms present in the film.

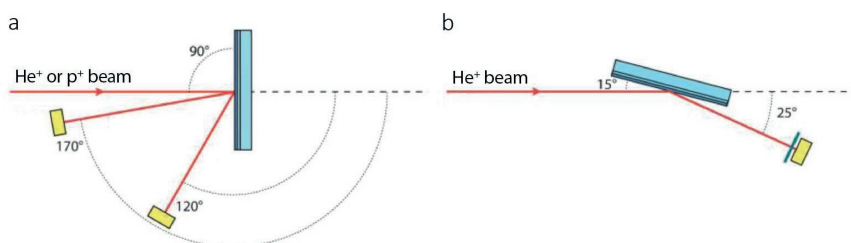


**Figure 3.9** Schematic representation of the set-up for a) RBS and EBS analysis and b) ERD analysis. The scattering and recoil angles and the sample tilt varied slightly among the different samples. The specific details are presented in the corresponding chapters.

### 3.3.3 Surface morphology, uniformity and conformality

To study the morphology of films, scanning electron microscopy (SEM) is a very useful technique. With SEM, the sample is imaged by scanning the surface with a focused beam of electrons. The electrons then interact with the atoms in the sample, producing various signals that contain information about the surface topography and composition of the sample. High resolution SEM can achieve resolutions better than 1 nanometer. In the present work, electronically insulating samples were measured. To prevent accumulation of electrons on the sample surface, the samples were sputter coated with a 5 nm conductive Au/Pd film prior to the SEM measurements. High resolution SEM was not only used to measure the surface morphology, but also to measure the surface uniformity and conformality of the as-deposited films. Uniform and conformal coating of 3D-structures is important for future Li-ion batteries. Moreover, SEM was also used to confirm the thickness measurements by SE. The thickness and conformality measurements were performed by cutting the samples and imaging the cross-sections of the samples. For  $\text{AlP}_x\text{O}_y$ , the conformality was determined by transmission electron microscopy (TEM) measurements. The main difference between SEM and TEM is that SEM creates an image by detecting reflected or knocked-off electrons, while TEM uses transmitted electrons to create an image. The magnification that TEM offers is usually much higher compared to SEM. The TEM analysis could not be performed on the lithium-containing samples, as the measurements appeared to be destructive. It is expected that this has something to do with the use of higher acceleration voltage needed for the TEM measurements.

### 3.3.4 Crystallinity

X-ray diffraction (XRD) is used to determine the crystallinity of the material deposited. During the XRD measurement X-rays are directed at the sample under investigation. Interference patterns are formed depending on the crystal planes present in the material. By collecting these interference patterns, information about the crystal structure, inter-plane distance and lattice constants can be obtained. In the present work, XRD was used to measure the crystallinity in relation to the process parameters and to investigate whether a certain preferential crystal growth orientation is present. Moreover, in combination with SEM results additional information on the crystallite shapes was obtained.

### 3.3.5 Ionic conductivity

To determine the ionic conductivity of the material, impedance spectroscopy is performed. The device used consists of the typical metal-insulator-metal capacitor. During the measurements a sinusoidal AC-signal (generally 30 mV) is applied to the sample in a frequency range from 0.01 Hz to 1 MHz. The resulting impedance and phase response is registered. The impedance ( $Z$ ) of a material equals the ratio of the voltage applied, over the current flowing through the material (Ohm's Law). This

response is generally a mixture of various resistive, capacitive, and inductive elements. The result of such measurement and its analysis differ greatly depending on the system. Commonly, the impedance response is analyzed by fitting to an equivalent circuit. These circuit elements can be mathematically represented in their complex form. The ionic conductivity of thermal and plasma-assisted  $\text{Li}_2\text{CO}_3$  films was evaluated using impedance spectroscopy, as described in Chapter 4.

## References

1. H. B. Profijt, S. E. Potts, M. C. M. van de Sanden, et al. Plasma-assisted atomic layer deposition: basics, opportunities, and challenges. *J. Vac. Sci. Technol. A* **29**, 050801 (2011).
2. M. De Keijser and C. Van Oordorp. Atomic layer epitaxy of gallium arsenide with the use of atomic hydrogen. *Appl. Phys. Lett.* **58**, 1187–1189 (1991).
3. H. C. M. Knoop, T. Faraz, K. Arts, et al. Status and prospects of plasma-assisted atomic layer deposition. *J. Vac. Sci. Technol. A* **37**, 030902 (2019).
4. J. T. Gudmundsson, I. G. Kouznetsov, K. K. Patel, et al. Electronegativity of low-pressure high-density oxygen discharges. *J. Phys. D: Appl. Phys.* **34**, 1100–1109 (2001).
5. T. Faraz, H. C. M. Knoop, M. A. Verheijen, et al. Tuning material properties of oxides and nitrides by substrate biasing during plasma-enhanced atomic layer deposition on planar and 3D substrate topographies. *ACS Appl. Mater. Interfaces* **10**, 13158–13180 (2018).
6. S. E. Potts and W. M. M. Kessels. Energy-enhanced atomic layer deposition for more process and precursor versatility. *Coord. Chem. Rev.* **257**, 3254–3270 (2013).
7. S. E. Potts, W. Keuning, E. Langereis, et al. Low temperature plasma-enhanced atomic layer deposition of metal oxide thin films. *J. Electrochem. Soc.* **157**, P66 (2010).
8. H. C. M. Knoop, S. E. Potts, A. A. Bol, et al. Atomic layer deposition. in *Handbook of crystal growth: thin films and epitaxy* 1101–1134 (Elsevier B.V., 2015).
9. NIST Mass Spectrometry Data Center. Mass spectra. in *NIST Chemistry WebBook, NIST Standard Reference Database Number 69* (eds. Mallard, P. J. & Linstrom, W. G.) (National Institute of Standards and Technology, 2020).







# 4

## Plasma-assisted and thermal ALD of electrochemically active $\text{Li}_2\text{CO}_3$

---

---

Thin-film lithium carbonate ( $\text{Li}_2\text{CO}_3$ ) has applications in various electrochemical devices, like Li-ion batteries, gas sensors and fuel cells. ALD of  $\text{Li}_2\text{CO}_3$  is of interest for these applications as it allows for uniform and conformal coating of high-aspect ratio structures and particles with very precise thickness control. However, there are few studies that focus on its fabrication and characterization. In this work, plasma-assisted and thermal ALD were adopted to grow ultra-thin, conformal  $\text{Li}_2\text{CO}_3$  films between 50 and 300 °C using lithium tert-butoxide as a precursor and  $\text{O}_2$  plasma or  $\text{H}_2\text{O}/\text{CO}_2$  as co-reactants. More specifically, we focus on the plasma-assisted process by film growth, stability and conductivity studies and emphasize the differences from its more extensively adopted thermal counterpart. Plasma-assisted ALD allows for higher growth per cycle values (0.82 vs 0.60 Å), lower substrate temperatures and shorter cycle times. The stoichiometry of the films, ranging from  $\text{Li}_2\text{CO}_3$  to  $\text{Li}_2\text{O}$ , can be controlled by substrate temperature and  $\text{O}_2$  plasma exposure time. The ionic conductivity for both plasma-assisted and thermal ALD is measured for the first time and is in the order of  $10^{-10} \text{ S} \cdot \text{cm}^{-1}$  after normalizing to the different effective surface areas. The Li-ion conductivities found here are in line with literature values predicted by simulation studies.

## 4.1 Introduction

Lithium carbonate is considered a potential electrode passivating film in Li-ion batteries<sup>1</sup> and electrolyte material or sensing layer in electrochemical devices like fuel cells or chemical sensors.<sup>2,3</sup> This is attributed to its purely ionically conductive behavior and good electrochemical stability.<sup>4</sup> In addition, it is widely used as building block for the fabrication of electrodes and electrolytes or as additive to improve electrode performance.<sup>5</sup> Despite its widespread usage there are only few studies in literature focusing on its characterization.

With the trend of manufacturing devices that have smaller size, weight and lower power consumption, thin film fabrication techniques are becoming preferable. This is especially applicable in the field of Li-ion batteries, where thin-film 3D battery architectures are currently being investigated.<sup>6</sup> Nanostructured energy storage systems have demonstrated a substantial increase in power and energy density.<sup>6-8</sup> Key to nanostructured energy storage systems is thin films processing of battery active and passive materials compatible with complex battery design. Conventional deposition techniques, such as physical vapor deposition (PVD) and plasma-enhanced chemical vapor deposition (PE-CVD), do not generally lead to conformal thin layers on high aspect ratio structures. To enable fast charging thin-film batteries, conformality and uniform material composition in extreme aspect ratios are required.<sup>9</sup> Therefore, novel deposition techniques leading to enhanced control in thin film properties and conformality are being presently introduced in the field of Li-ion batteries.<sup>10-12</sup> Atomic layer deposition (ALD), which is based on sequential and self-limiting half-reactions between precursors (co-reactants) and surface, has emerged as a powerful tool since it shows potential towards exceptional conformality on high-aspect ratio structures, thickness control at sub-nanometer level, and tunable film properties.<sup>13</sup> Promising applications of ALD for Li-ion batteries include (surface modification of) particle-based electrodes, 3D-structured electrodes, and 3D all-solid-state microbatteries.<sup>10-12,14,15</sup> Due to the excellent conformality and thickness control of ALD, it is suggested that ALD of lithium carbonate ( $\text{Li}_2\text{CO}_3$ ) is especially beneficial when it is employed as electrode passivating film or as additive to improve electrode performance.

In the present work we focus on the ALD characterization of  $\text{Li}_2\text{CO}_3$ . More specifically, we focus on the plasma-assisted ALD process of  $\text{Li}_2\text{CO}_3$  by (*in situ*) growth studies and emphasize the differences from its more extensively adopted thermal counterpart. This is expected to be generally helpful to assess the opportunities of ALD for Li-ion materials. With plasma-assisted ALD a high reactivity is delivered to the deposition surface by the plasma species and therefore less thermal budget is required at the substrate to drive the ALD surface chemistry than for thermal ALD. The application of plasmas in combination with ALD generally leads to a wider range in substrate temperature and processing conditions and thus enables a larger variety of material properties.<sup>16</sup> The process details of ALD  $\text{Li}_2\text{CO}_3$  as collected from literature are shown in Table 4.1. Although the plasma-assisted ALD process for  $\text{Li}_2\text{CO}_3$  has been

**Table 4.1** Li<sub>2</sub>CO<sub>3</sub> ALD process details collected from earlier publications.

Precursor	Coreactant(s)	T <sub>sub</sub> (°C)	GPC (Å)	Ref.
LiO <sup>t</sup> Bu	H <sub>2</sub> O, CO <sub>2</sub>	225	0.8	17
LiHMDS	H <sub>2</sub> O, CO <sub>2</sub>	89 - 332	0.41 - 0.14	18
LiTMSO	H <sub>2</sub> O, CO <sub>2</sub>	200 - 300	0.5 - 0.3	19
LiO <sup>t</sup> Bu	O <sub>2</sub> plasma	225, 300	0.4	20
LiTMHD	O <sub>3</sub>	185 - 225	0.3 - 0.07	21

already reported in literature, the understanding of the ALD film growth (primarily in terms of developed chemistry during and after deposition) is, so far, insufficient. In addition, the effect of the process parameters on the layer properties was not reported. To the best of our knowledge, we provide the first proper conductivity measurement of thin film Li<sub>2</sub>CO<sub>3</sub>.

Moreover, Li<sub>2</sub>CO<sub>3</sub> ALD represents an attractive model process for incorporating Li into multicomponent (ternary) ALD materials since it is a highly stable compound with respect to process stability and ease of postdeposition analysis of the films. Li<sub>2</sub>O and LiOH often develop simultaneously during processing due to the reversible reaction with H<sub>2</sub>O and CO<sub>2</sub> and are being deposited by ALD as well.<sup>17–23</sup> These materials are also widely used as building block for the fabrication of various other Li-ion battery active materials.<sup>24–26</sup>

## 4.2 Experimental

All depositions presented in this work were carried out using the thermal and remote plasma ALD reactor FlexAL (Oxford Instruments). The reactor consists of a rotary and turbo molecular pump such that it can reach a base pressure of < 10<sup>-6</sup> Torr by overnight pumping. The pump unit as well as the inductively coupled plasma (ICP) source are connected to the deposition chamber trough gate valves.

The ALD processes developed in this work are shown in Figure 4.1. For thermal ALD (Figure 4.1a), the cycle consists of the exposure of the substrate to LiO<sup>t</sup>Bu (97%, Sigma Aldrich) lithium precursor, H<sub>2</sub>O gas and CO<sub>2</sub> gas respectively, alternated by argon purges. The plasma-assisted ALD process (Figure 4.1b) consists of a combination of the substrate exposure to the same lithium precursor and to an O<sub>2</sub>-fed plasma with a plasma power of 100 W, alternated by argon purging steps. To ensure the gas flow and the pressure have stabilized, the reactor was filled with oxygen prior to switching on the plasma source. Air exposure of the fabricated layers was minimized by transporting the samples in an evacuated transport tube.

The LiO<sup>t</sup>Bu precursor was bubbled from the precursor pod with Ar at a reactor pressure of 20 mTorr and the precursor and precursor supply line were heated to 140 °C and 150 °C respectively to avoid precursor condensation. The reactor pressure

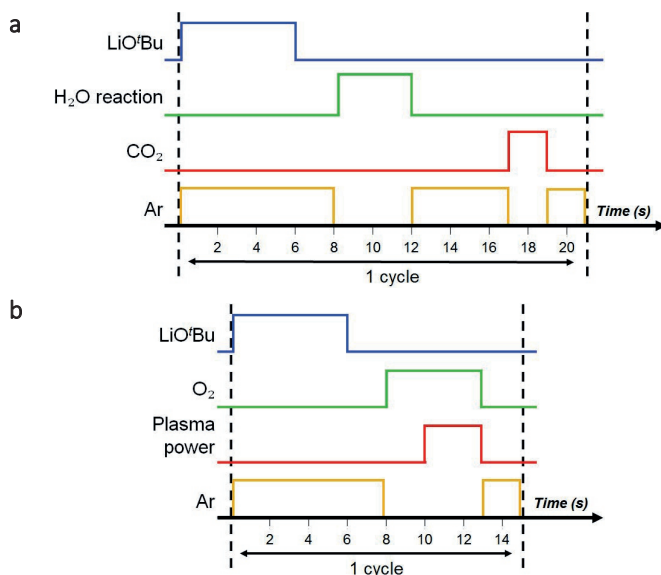


**Figure 4.1** Schematic of the pulsing sequence of the ALD cycle for depositions of  $\text{Li}_2\text{CO}_3$  by a) thermal and b) plasma-assisted ALD. The  $\text{H}_2\text{O}$  dose during the thermal ALD process was only 50 ms, after which all valves were closed for 4 s to allow for the molecules to react. Therefore, this is referred to as “ $\text{H}_2\text{O}$  reaction”.

during the  $\text{O}_2$  plasma generation was 13 mTorr. The process table was heated to 50 - 300 °C, since it is reported that precursor decomposition takes place from 350 °C.<sup>27</sup> The wafers were placed on an aluminum substrate holder. The reactor wall is maintained at a temperature of 120 °C (which is the maximum wall temperature), except for the deposition at 50 or 100 °C, where the reactor wall is kept at 50 or 100 °C, respectively.

As substrate, 60 nm titanium nitride (TiN) sputtered on silicon was used (Endura PVD). TiN is a barrier for Li-ion diffusion, and also functions as current collector for electrochemical testing of the layers. The film thickness and dielectric function were monitored *in situ* by spectroscopic ellipsometry (SE) with a J.A. Woollam, Inc. M2000U (0.75 - 5.0 eV) tool. The dielectric function of  $\text{Li}_2\text{CO}_3$  was parameterized using a mathematical description in the form of B-splines, since this method requires no prior knowledge about the dielectric function of the deposited films. Thickness values were confirmed by high resolution SEM (Zeiss Sigma) operated at 2 kV acceleration voltage.

The entire chemical composition of the samples has been characterized with ion beam analysis methods by Detect99. The hydrogen profiles were determined by Elastic Recoil Detection (ERD) using a 1.9 MeV  $\text{He}^+$  beam impinging on the sample under 15° glancing incidence, and 30° recoil angle. All other elements could be determined in a single run by Elastic Backscattering Spectrometry (EBS) with 2.8 MeV

protons at perpendicular incidence. This technique is similar to Rutherford Backscattering Spectrometry (RBS) but has the advantage that the cross sections for light elements is enhanced by the use of high energy protons as projectiles instead of He. Spectra have been registered at  $170^\circ$  and  $150^\circ$  scattering angle. EBS was in this case necessary for the determination of the Li and C contents, for which the sensitivity of RBS is rather poor. Finally, the O, N and Ti contents have been confirmed by channeling RBS using 1900 keV He ions in the same configuration as for the EBS measurements.

X-ray photoelectron spectroscopy (XPS) spectra were recorded by a Thermo Scientific K-Alpha+ system using monochromatic Al  $K\alpha$  X-rays. The spot size of the beam was 400  $\mu\text{m}$  and the base pressure of the system was  $10^{-8}$  mbar. The depth profile was obtained by an Ar ion gun of 500 eV during 5 s for each sputter step. The crystal structure of the  $\text{Li}_2\text{CO}_3$  layers was determined using a Philips X'Pert MPD diffractometer equipped with a Cu  $K\alpha$  source (1.54  $\text{\AA}$  radiation). The morphology of the deposited layers was investigated by the SEM which was described before.

For electrochemical impedance spectroscopy (EIS) testing an Autolab (Metrohm) potentiostat with a frequency-response analyzer module (frequency range from 0.01 Hz to 1 MHz) was used, operated by Nova software (Metrohm Autolab). A three-electrode Teflon cell was clamped on top of the sample using a Kalrez O-ring. A Luggin capillary was used to connect the cell with the reference-electrode compartment. One molar  $\text{LiClO}_4$  (battery-grade, Sigma-Aldrich) in propylene carbonate was used as the electrolyte. The experiments were carried out in an Ar glovebox ( $\text{O}_2$ ,  $\text{H}_2\text{O} < 1$  ppm). Impedance spectroscopy results were analyzed by fitting an equivalent circuit to the data, using MEISP software (Kumho Chemical Laboratories). The obtained fits had a  $\chi^2$  value in the range from  $10^{-3}$  to  $10^{-5}$ . The relative standard deviation for all fitted values remained below 5%.

## 4.3 Results and discussion

### 4.3.1 ALD process characterization

A deposition temperature of  $150^\circ\text{C}$  was adopted to investigate the saturation behavior of the surface reactions during the sub-cycles of both thermal and plasma ALD  $\text{Li}_2\text{CO}_3$ . Film thickness was monitored every 10 cycles by *in situ* SE measurements while changing precursor or co-reactant dose times. Saturation curves for the thermal ALD process of  $\text{Li}_2\text{CO}_3$  are shown in Figure 4.2a. A  $\text{LiO}^t\text{Bu}$  dose of 6 s, a water dose of 50 ms and a  $\text{CO}_2$  dose of 2 s were chosen as standard conditions for thermal ALD of  $\text{Li}_2\text{CO}_3$ . Without  $\text{H}_2\text{O}$  dosing no film growth occurred and without  $\text{CO}_2$ ,  $\text{LiOH}$  was formed. Due to a slower response speed of the  $\text{CO}_2$  valve, dosing of 0.5 s or less did not deliver any  $\text{CO}_2$  in the chamber (no pressure increase was observed). Purge steps after  $\text{LiO}^t\text{Bu}$  and  $\text{CO}_2$  dose of 2 s are sufficient to remove the reaction products and

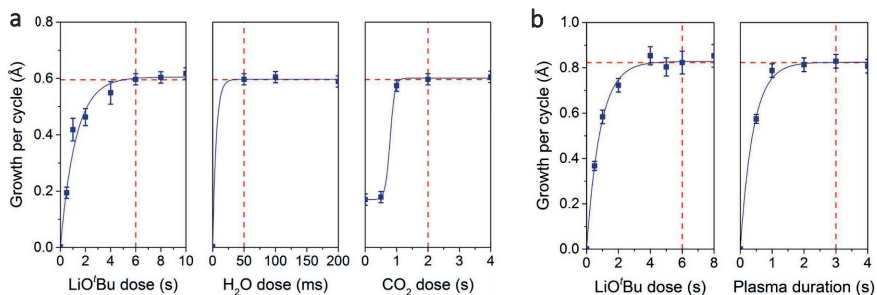


**Figure 4.2** Saturation curves for a) thermal and b) plasma-assisted ALD of  $\text{Li}_2\text{CO}_3$  obtained at  $150\text{ }^\circ\text{C}$  showing the self-limiting growth behavior of the ALD process. The solid line serves as a guide to the eye. Dotted lines indicate the chosen standard values and the corresponding growth per cycle. Note that the reaction time of  $\text{H}_2\text{O}$  after dosing was kept at 4 s.

unreacted species from the processing chamber, although 5 s purge was necessary for  $\text{H}_2\text{O}$ . A growth per cycle of  $0.60\text{ \AA}$  was found for the thermal ALD process.

The saturation behavior of the surface reactions during the two half cycles of the plasma-assisted ALD process, i.e. the exposure to the lithium precursor and  $\text{O}_2$  plasma, is shown in Figure 4.2b: self-limiting growth was verified for both the precursor and the plasma step. For both half-cycles purge steps of 2 s are sufficient to remove the reaction products and unreacted species. A growth per cycle of  $0.82\text{ \AA}$  was obtained for a deposition temperature of  $150\text{ }^\circ\text{C}$ .

The previously reported growth per cycle of  $0.8\text{ \AA}$  for thermal ALD of  $\text{Li}_2\text{CO}_3$ ,<sup>17</sup> differs from our values. The reason for this difference is unclear, yet it is noted that the main difference with our process is a higher reactor pressure. Plasma-assisted ALD using  $\text{LiO}^t\text{Bu}$  on the other hand was reported to have a growth per cycle of  $0.4\text{ \AA}$ ,<sup>20</sup> but the obtained stoichiometry was a mixture of  $\text{Li}_2\text{CO}_3$  and  $\text{Li}_2\text{O}$ . Our films grown at  $150\text{ }^\circ\text{C}$  are found to be pure  $\text{Li}_2\text{CO}_3$ , as shown in the next section. Moreover, no saturation curves were shown in literature to support the data for this particular case. In general, plasma processes often have a higher growth per cycle when compared to thermal processes which is in agreement with our results.<sup>16</sup>

Next, the process window of ALD films was extended to deposition temperatures between  $50$  and  $300\text{ }^\circ\text{C}$ . Figure 4.3a shows the thickness evolution as a function of the number of ALD cycles for various deposition temperatures. For plasma-assisted ALD and  $T_{\text{sub}} \leq 200\text{ }^\circ\text{C}$ , the thickness of the films develops linearly with the number of cycles. For temperatures higher than  $250\text{ }^\circ\text{C}$ , the film thickness develops according to two slopes, which correlates with a transition in film chemical composition, as discussed in the next section. Due to high temperature sensitivity of the reactions and minor temperature fluctuations of the process table, the trends of the thickness as a function of the number of cycles at  $250\text{ }^\circ\text{C}$  varied from occasion to occasion: in some cases they tend to be similar to the growth behavior for  $T \leq 200\text{ }^\circ\text{C}$  and in other

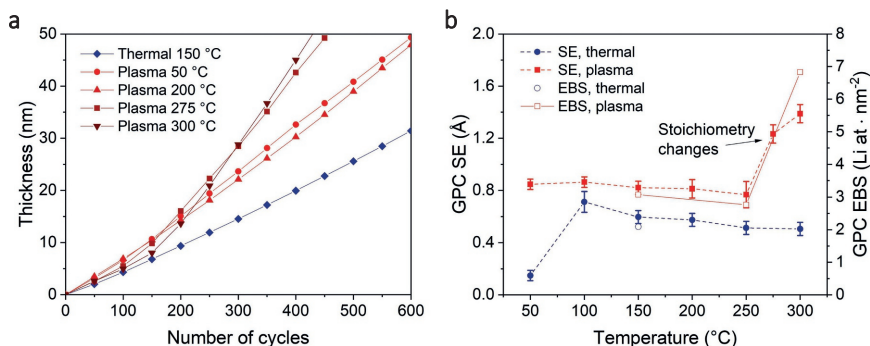


**Figure 4.3** a) *In situ* thickness measurements by SE for plasma-assisted ALD of  $\text{Li}_2\text{CO}_3$  at 50, 200, 275 and 300 °C and thermal ALD of  $\text{Li}_2\text{CO}_3$  at 150 °C. The film growth between 50 and 200 °C with plasma ALD was very similar (see appendix). b) Growth per cycle as a function of process temperature for both plasma-assisted (squares) and thermal (circles) ALD processes.

instances to  $T > 250$  °C. Moreover, films deposited at 250 °C showed large height differences (see SEM images in the next section), which complicated the extraction of the film thickness. For the thermal process, no transition in film chemical composition was observed. However, the growth per cycle increases slightly as function of the number of ALD cycles, which can be explained by crystallization of the films (in Figure S4.1 more growth curves are shown for thermal ALD  $\text{Li}_2\text{CO}_3$ ).

In Figure 4.3b, both the temperature dependency of the growth per cycle for the plasma-assisted, as well as the thermal ALD process is shown. It can be noticed that the growth per cycle of the thermal ALD process strongly decreases at 50 °C, indicating the lower limit of the temperature window. The ALD process window for the plasma-assisted process is extended towards lower temperatures, as it has a similar growth per cycle at 50 °C as at higher temperatures. The overall growth per cycle is higher for the plasma-assisted process as compared to the thermal process. As mentioned before, this is more often observed for plasma processes due to the relatively high reactivity of the plasma species which could create a higher density of reactive surface sites.<sup>16</sup> The differences in growth per cycle between thermal and plasma ALD, but also between different deposition temperatures for plasma-assisted ALD are confirmed by EBS data (see Figure 4.3b). A slight decrease in growth per cycle with increasing temperature was observed for the thermal ALD process. This decrease might be caused by desorption of part of the absorbed precursor monolayer from the surface, by higher purity film growth or by an increase in film crystallinity. The crystallinity of the films will be further discussed in the next paragraph.

To summarize, it is shown that both plasma-assisted and thermal ALD of  $\text{Li}_2\text{CO}_3$  show typical ALD growth behavior within a wide temperature window. Plasma-assisted ALD allows for lower temperature depositions, which results in a wider choice



of (substrate) materials that can be used. This is particularly useful when temperature-sensitive materials are adopted, such as polymers.<sup>16</sup> In addition, the plasma-assisted process allows for higher growth per cycle values and shorter cycle times compared to thermal ALD, without compromising on the quality of the layer. This will enable higher throughputs for ALD reactors.

### 4.3.2 Chemical composition

The stoichiometry of 50 nm thick films was probed using a combination of ERD and EBS. The atomic percentage of all the elements in the film is reported in Table 4.2. For thermal and plasma-assisted ALD films grown up to 250 °C, the results point out a stoichiometry very similar to Li<sub>2</sub>CO<sub>3</sub>. The films are slightly sub-stoichiometric, since the carbon content in the films is relatively low (stoichiometric Li<sub>2</sub>CO<sub>3</sub> contains 33.3 at. % Li, 16.7 at. % C and 50.0 at. % O). Furthermore, the calculated mass density for these samples is slightly lower than the bulk density of 2.11 g · cm<sup>-3</sup>. Only a few at. % of H is found in the films.

Plasma ALD at 300 °C on the other hand shows a high hydrogen content, suggesting the co-presence of LiOH. As mentioned before, air exposure of the fabricated layers was minimized by transporting the samples in an evacuated transport tube, although some degradation of the layers cannot be excluded. The hydrogen content is not constant through the film thickness but is mainly present in the film's depth indicating air reactivity after deposition (a depth profile shown in Figure S4.2). The relatively high carbon content suggests that the film reacted from LiOH towards Li<sub>2</sub>CO<sub>3</sub> upon air exposure. The reactivity of plasma ALD films deposited at 300 °C will be discussed in more detail later in this paragraph.

For all samples, the amount of deposited lithium atoms scales with the growth per cycle obtained by SE (see Figure 4.3b). The surface density in atoms per cm<sup>2</sup> can be calculated *via*  $\left(2 \cdot \frac{\rho \cdot N}{\mu}\right)^{2/3}$ , where  $\rho$  is the mass density,  $N$  Avogadro's number, and  $\mu$  the molecular mass of Li<sub>2</sub>CO<sub>3</sub>. Assuming the mass density of stoichiometric Li<sub>2</sub>CO<sub>3</sub> to

**Table 4.2** Properties of ~ 50 nm films fabricated using the standard thermal ALD process at 150 °C and plasma ALD process at 150, 250 and 300 °C. The growth per cycle in terms of atoms · nm<sup>-2</sup> and the atomic percentages were determined by EBS and ERD. The mass density was obtained by combining EBS and SE results. In the first row the typical error is given for a certain parameter.

Sample	GPC (at. · nm <sup>-2</sup> )	[Li] (at. %)	[C] (at. %)	[O] (at. %)	[H] (at. %)	Mass density (g · cm <sup>-3</sup> )
Thermal 150 °C	2.09 ± 0.1	33.4 ± 1.7	14.6 ± 0.8	50.7 ± 2.0	1.3 ± 0.2	1.95 ± 0.20
Plasma 150 °C	3.08	32.7	15.1	49.6	2.6	2.06
Plasma 250 °C	2.76	30.5	15.8	50.9	2.8	1.97
Plasma 300 °C	6.83	30.9	13.3	44.7	11.1	n.a.

be equal to the bulk density of  $2.11 \text{ g} \cdot \text{cm}^{-3}$ , one monolayer of lithium carbonate contains roughly  $10.58 \text{ Li atoms per nm}^2$ . Based on the EBS growth per cycle of  $2.09 \text{ Li atom per nm}^2$  for the thermal ALD process, in each cycle approximately  $1/5^{\text{th}}$  of a monolayer of  $\text{Li}_2\text{CO}_3$  is deposited. For the plasma-assisted process, about  $1/4^{\text{th}}$  to  $1/3^{\text{rd}}$  of a monolayer is deposited every cycle.

For plasma ALD at  $300 \text{ }^\circ\text{C}$ , the amount of deposited Li atoms deviates strongly from the lower temperature processes. At the same time the SE growth per cycle for this sample, but also for the one prepared at  $275 \text{ }^\circ\text{C}$ , deviates from the lower temperature depositions. The films deposited at higher temperatures changed when they were removed from the reactor as could be observed visually. Furthermore, the ellipsometric data obtained *ex situ* could not be fitted using the same model as during *in situ* measurements. The instability, deviating growth per cycle and increased hydrogen content of these layers suggests that the formed layers were not  $\text{Li}_2\text{CO}_3$  but rather a mixture of  $\text{LiOH}$  and  $\text{Li}_2\text{O}$ . The increased growth per cycle can be explained by the fact that  $\text{LiOH}$  is hygroscopic and easily absorbs  $\text{H}_2\text{O}$  and forms a hydrate.<sup>17,23,28</sup> It is reported for thermal ALD of  $\text{LiOH}$  at  $225 \text{ }^\circ\text{C}$  that long purge times of 2 hours lead to a stable mass measured by QCM as a result of  $\text{H}_2\text{O}$  desorption.<sup>17</sup>

To further investigate the film instability for growth temperatures above  $250 \text{ }^\circ\text{C}$ ,  $50 \text{ nm}$  thick films were fabricated at different deposition temperatures. These were then subsequently exposed to  $\text{CO}_2$  and  $\text{H}_2\text{O}$  pulses inside the ALD reactor. The films were measured by *in situ* SE and the phase change ( $\Delta$ ) was monitored at  $589 \text{ nm}$  after every pulse as shown in Figure 4.4. For plasma depositions at  $250 \text{ }^\circ\text{C}$ ,  $\Delta$  was unaffected

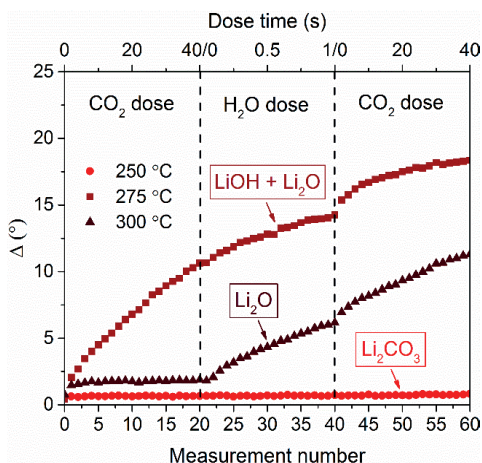


**Figure 4.4** Phase shift of the incident light ( $\Delta$ ) from *in situ* SE measurements of the reaction of  $\text{CO}_2$  and  $\text{H}_2\text{O}$  with  $\sim 50 \text{ nm}$  plasma ALD films grown at  $250$ ,  $275$  and  $300 \text{ }^\circ\text{C}$ . First,  $\text{CO}_2$  was dosed into the reaction chamber 20 times with pulses of  $2 \text{ s}$ , next  $\text{H}_2\text{O}$  was pulsed 20 times for  $50 \text{ ms}$  and afterwards  $\text{CO}_2$  was again pulsed 20 times. SE data was recorded after every pulse and  $\Delta$  is plotted at  $589 \text{ nm}$ .

by CO<sub>2</sub> and H<sub>2</sub>O exposure, pointing out the stability of the film. However, the film deposited at a slightly higher temperature of 275 °C strongly reacted with CO<sub>2</sub>, whereas for the film deposited at 300 °C  $\Delta$  only slightly changes during the first pulse. Both LiOH and Li<sub>2</sub>O could react with CO<sub>2</sub> to form Li<sub>2</sub>CO<sub>3</sub>. However, it is reported in literature that the reaction between Li<sub>2</sub>O and CO<sub>2</sub> for temperatures from 200 - 400 °C only occurs in the top few nanometers of the Li<sub>2</sub>O and then a self-limiting shell of Li<sub>2</sub>CO<sub>3</sub> develops.<sup>29</sup> This in contrast to LiOH, which would be extremely reactive towards CO<sub>2</sub>. Hence, the film at 300 °C most likely consists of Li<sub>2</sub>O as after the first CO<sub>2</sub> pulse  $\Delta$  only slightly changes suggesting that only a surface reaction is occurring. During subsequent exposure steps, the layer does not further react with CO<sub>2</sub>, implying the absence of LiOH. After the CO<sub>2</sub> pulses, the sample was subjected to H<sub>2</sub>O pulses. As observed in Figure 4.4, the 300 °C film consisting of Li<sub>2</sub>O is reacting with the H<sub>2</sub>O forming LiOH. Next, CO<sub>2</sub> is pulsed again, and the layer is again reacting to form Li<sub>2</sub>CO<sub>3</sub>. Unlike the film deposited at 300 °C, the as-deposited 275 °C film was very reactive towards the first CO<sub>2</sub> pulses and therefore (partly) consisted of LiOH. For all other films, which include plasma ALD films deposited at 50 – 250 °C and thermal ALD films deposited at 50 – 300 °C, the change in  $\Delta$  was negligibly small, indicating that almost no reaction with H<sub>2</sub>O or CO<sub>2</sub> occurred. These stable Li<sub>2</sub>CO<sub>3</sub> films were used for *ex situ* XPS analysis which will be discussed later in this section.

The *in situ* SE measurements presented in Figure 4.4 show the formation of LiOH/Li<sub>2</sub>O for plasma-assisted ALD at processing temperatures > 250 °C. For these temperatures it was also shown that the film thickness *versus* number of ALD cycles develops differently. In the first 100 cycles the film growth was significantly different from the rest of the deposition which is correlated with the transition in film chemical composition. Since the use of plasma at processing temperatures > 250 °C has a significant effect on the film growth and composition, also the effect of the plasma duration was investigated. Up to this point, a plasma exposure of 3 s was adopted. Figure 4.5 shows the thickness evolution with number of ALD cycles for various plasma exposure times. As observed from the graph, the bulk growth per cycle for different plasma exposure times is similar. However, for longer plasma exposure times, the growth per cycle requires a lower number of ALD cycles to become linear, compared to shorter plasma exposure times. The formation of LiOH/Li<sub>2</sub>O can thus be further stimulated by prolonging the plasma exposure time.

The chemical composition of the deposited films was further studied by *ex situ* XPS. No sputtering procedure was adopted, as it was found that the stoichiometry of the films changed due to interaction with Ar ions. Upon chemical decomposition during sputtering, Li<sub>2</sub>CO<sub>3</sub> experiences a transition to Li<sub>2</sub>O (see Figure S4.3). In Figure 4.6, the XPS core level spectra of C 1s, Li 1s and O 1s are shown for thermal ALD at 150 °C. The binding energy scale was calibrated by using the hydrocarbon contamination C 1s peak at 285.0 eV. As expected, the C 1s spectrum shows a main peak at ~ 290.1 eV assigned to the carbonate environment in Li<sub>2</sub>CO<sub>3</sub>. The other peaks

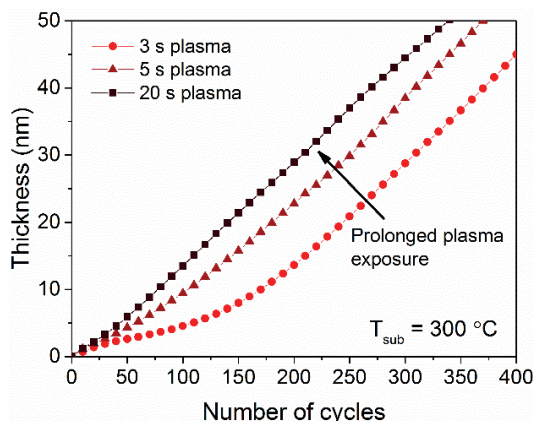


**Figure 4.5** *In situ* SE thickness measurement for plasma-assisted ALD of  $\text{Li}_2\text{CO}_3$  at 300 °C using different  $\text{O}_2$  plasma exposure times.

fitted with a red line are associated with adventitious carbon on the sample surface. In the Li 1s spectrum a peak at  $\sim 55.4$  eV is observed which is associated to  $\text{Li}_2\text{CO}_3$ . The O 1s spectrum consists of a peak with a maximum at  $\sim 531.8$  eV. The shape of the peak is slightly asymmetric. To visualize the asymmetry a second peak is fitted to the data. The asymmetry can be explained by the crystallographic structure of  $\text{Li}_2\text{CO}_3$  in which two oxygen atoms have an identical environment, but the third oxygen has a different environment of surrounding atoms.<sup>30</sup> The obtained stoichiometry for this film was: 33.0 at. % lithium, 17.7 at. % carbon and 49.3 at. % oxygen, corresponding to stoichiometric  $\text{Li}_2\text{CO}_3$ . Proportionate, there is slightly more carbon than obtained by EBS. To some extent, the difference can be explained by the low penetration depth of XPS ( $\sim 10$  nm) and the presence of carbon on the sample surface. All other films (prepared by plasma as well as thermal ALD) are measured and subsequently fitted using the same method and all showed the expected  $\text{Li}_2\text{CO}_3$  stoichiometry. The results are summarized in Table S4.1.

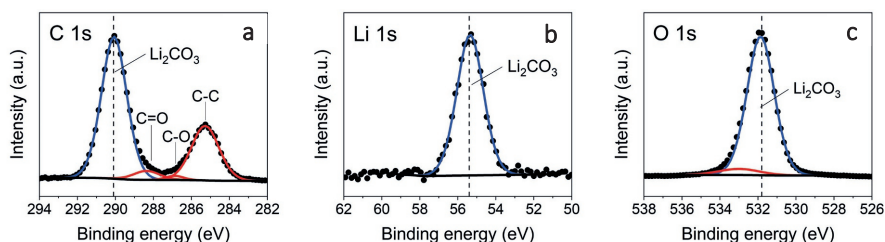


**Figure 4.6** XPS a) C 1s, b) Li 1s and c) O 1s spectra for  $\text{Li}_2\text{CO}_3$  grown by thermal ALD at 150 °C. The measured spectra (black line) and fitted peaks (blue and red) are plotted together. The obtained  $\text{Li}_2\text{CO}_3$  stoichiometry is 33.0 at. % Li, 17.7 at. % C and 49.3 at. % O.

$\text{Li}_2\text{CO}_3$  films which are only slightly sub-stoichiometric can thus be deposited by thermal as well as by plasma ALD. In addition, it is possible to deposit  $\text{Li}_2\text{O}$  at temperatures  $> 250^\circ\text{C}$  using the plasma-assisted process. It has already been shown in literature that this is also possible using thermal ALD for temperatures  $> 250^\circ\text{C}$ , when the  $\text{CO}_2$  step was omitted from the process.<sup>20</sup> Deposition of  $\text{Li}_2\text{O}$  can be beneficial when presence of carbon in the films is undesirable. On the other hand, with thermal ALD it is possible to deposit  $\text{Li}_2\text{CO}_3$  films also at high temperatures of  $300^\circ\text{C}$ . If high temperature  $\text{Li}_2\text{CO}_3$  depositions are preferred, for example when the process is combined in supercycles (to make more complex material structures) also employing precursors or co-reactants which require higher deposition temperatures, the thermal process could be preferred.

### 4.3.3 Crystallinity and morphology

XRD was used to determine the crystallinity of the films deposited at different temperatures. Figure 4.7 shows the X-ray diffractograms for  $\sim 50$  nm thick films. Both plasma and thermal ALD films show a typical diffraction peak originating from crystalline  $\text{Li}_2\text{CO}_3$ . The gonio measurements, which detect periodicity of planes parallel to the surface, show only the peak at  $31.7^\circ$ , meaning the process yields a preferential crystal growth orientation in the  $\langle 002 \rangle$  direction. For thermal ALD films, the crystallinity increases slightly with increasing deposition temperature. A similar trend was observed in literature for thermal ALD of  $\text{Li}_2\text{CO}_3$  on Si (100) substrates using a  $\text{LiN}(\text{SiMe}_3)_2$  precursor,<sup>18</sup> although the crystalline growth started only at  $\sim 180^\circ\text{C}$

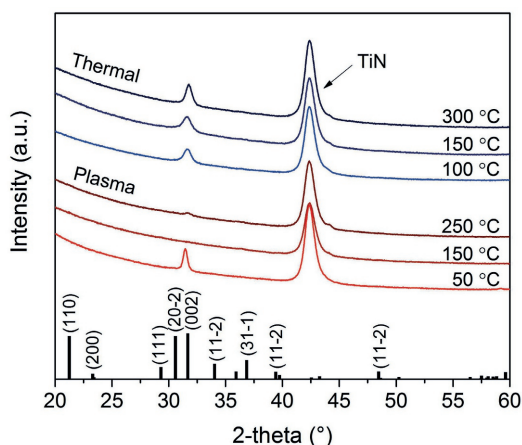


**Figure 4.7** XRD goni scans of  $\sim 50$  nm thick  $\text{Li}_2\text{CO}_3$  films grown on TiN using thermal (blue) and plasma (red) ALD at different processing temperatures. The bars in the lower panel indicate the expected diffraction from a  $\text{Li}_2\text{CO}_3$  powder sample. The reflections at  $\sim 42.5^\circ$  originate from the TiN (200) textured substrate.

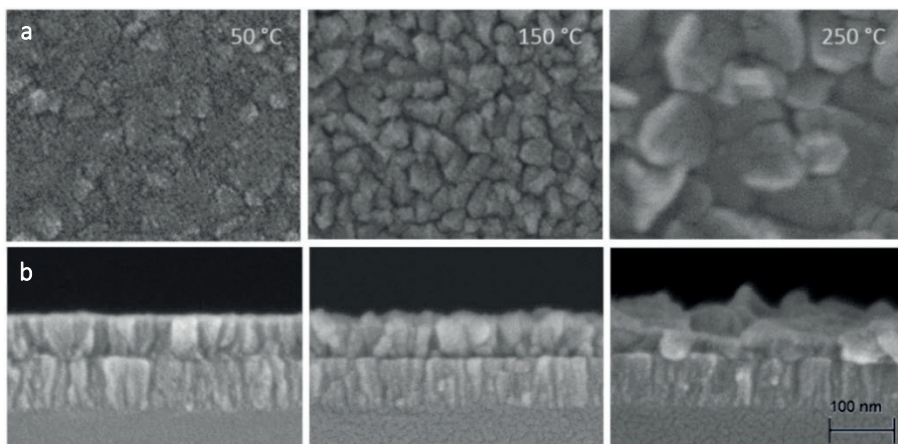


**Figure 4.8** a) High resolution SEM pictures showing the surface topography and b) cross-section of  $\text{Li}_2\text{CO}_3$  deposited with plasma ALD at 50, 150, and 250 °C. The scale bar applies to all the pictures.

according to their XRD spectra. The onset for crystalline growth could thus be influenced by the precursor, the substrate or a combination of both.

When considering the plasma ALD  $\text{Li}_2\text{CO}_3$  films, the layer deposited at 50 °C is highly crystalline and oriented in the  $\langle 002 \rangle$  direction, similar to the thermal process. At higher deposition temperatures, the spectra change significantly and the crystallinity seems to be suppressed. Since the samples are measured by goni XRD, we cannot exclude that there is a crystalline component present in the films because this technique is less sensitive to 50 nm thick films. In Figure 4.8 SEM images of the surfaces and cross-sections are shown corresponding to the samples measured by XRD. The film growth, and resulting topography, change drastically when increasing temperature. Although for lower deposition temperatures highly uniform films are formed, at 250 °C, the films show large thickness variations. We expect that this is related to the combustion of organic ligands and the formation of  $\text{LiOH}/\text{Li}_2\text{O}$  during deposition induced by the  $\text{O}_2$  plasma.

#### 4.3.4 Conformality

The conformality of the deposition was studied using SEM at different positions on high aspect ratio Si pillars. The pillars, which are 50  $\mu\text{m}$  high and have a diameter of 2  $\mu\text{m}$ , are coated with a  $\sim 30$  nm TiN current collector using ALD. On top of the TiN a  $\sim 50$  nm  $\text{Li}_2\text{CO}_3$  layer was deposited using a table temperature of 150 °C. Figure 4.9 shows 6 SEM pictures taken at different heights along the pillar for plasma-assisted as well as thermal ALD. Image a) is taken at the top of the pillars and shows a  $\text{Li}_2\text{CO}_3$  layer of  $\sim 55$  nm for the plasma-assisted deposition. Image b) is taken halfway the pillar and depicts a  $\sim 45$  nm  $\text{Li}_2\text{CO}_3$  layer (82 % of thickness at top). At the bottom c),

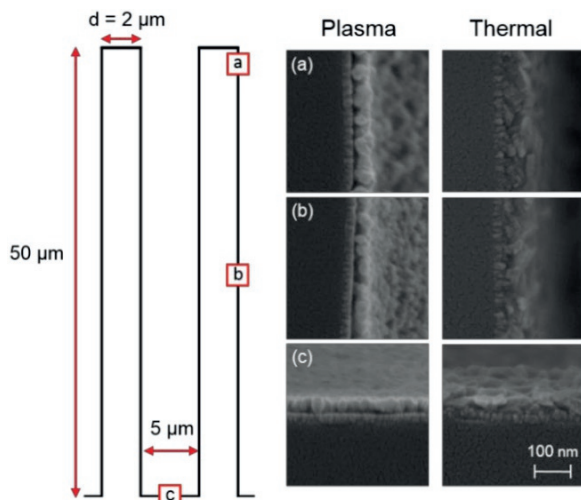


**Figure 4.9** Examination of the conformality of the  $\text{Li}_2\text{CO}_3$  processes at  $150^\circ\text{C}$ . Micropillars of  $50\ \mu\text{m}$  high and a diameter of  $2\ \mu\text{m}$  are used for this purpose. The pillars are coated with a  $30\ \text{nm}$  TiN layer on top of which a  $\sim 50\ \text{nm}$  layer of  $\text{Li}_2\text{CO}_3$  was deposited. Images a), b) and c) show the  $\text{Li}_2\text{CO}_3/\text{TiN}$  layer at respectively the top, middle and bottom of the pillars. Thickness variations from  $40\text{--}55\ \text{nm}$  (plasma) and  $48\text{--}60\ \text{nm}$  (thermal) were observed. For the thermal process a lithium dosing time of  $10\ \text{s}$  was used, whereas for the plasma process the standard dose time of  $6\ \text{s}$  was sufficient. The scale bar applies to all the pictures.

the plasma-assisted  $\text{Li}_2\text{CO}_3$  is  $\sim 40\ \text{nm}$  thick (73 %). For thermal ALD on the other hand, thicknesses of  $\sim 60$ ,  $52$  (87 %) and  $48\ \text{nm}$  (80 %) are measured along the pillars. We can conclude that the conformality on high aspect ratio pillars is rather good. Note that only the lithium exposure time was varied. Elongation of the lithium dosing time drastically improves the conformality of thermal ALD. For example, when thermal ALD was adopted using  $6\ \text{s}$  lithium dosing instead of  $10\ \text{s}$ , the  $\text{Li}_2\text{CO}_3$  layer at the bottom is  $20\ \text{nm}$  instead of  $48\ \text{nm}$ . For plasma ALD the conformality remains similar when varying the lithium dosing time. It is expected that the conformality can still be improved by further optimization of the precursor and plasma exposure steps.

### 4.3.5 Electrochemical analysis

The Li-ion conductivity of plasma and thermal ALD  $\text{Li}_2\text{CO}_3$  layers was investigated using impedance spectroscopy. The measurements were performed at open circuit potential (OCP) on  $50\ \text{nm}$   $\text{Li}_2\text{CO}_3$  films deposited at  $150^\circ\text{C}$  on a TiN current collector. The results are shown in Figure 4.10a on a complex plane plot. Both the measured layers show a behavior characteristic of a solid electrolyte: an intercept with the x-axis at high frequency, a semi-circle at medium frequency and a  $45^\circ$  inclined response at low frequency. Such behavior is typically associated with the ionic conductivity through a solid material.<sup>31</sup> The high frequency intercept with the x-axis is generally

attributed to the resistance of the cables, contacts and liquid electrolyte, the semi-circle originates from the ionic conductivity through the solid material and its capacitive response. The  $45^\circ$  slope is typically associated with a Warburg-like response, here the Li-ion diffusion through the liquid electrolyte. Note that in the measurements performed here electronic leakage through the  $\text{Li}_2\text{CO}_3$  films is not probed.

Further analysis was performed by fitting an equivalent circuit to the measured impedance response (shown in Figure 4.10a). The response of the  $\text{Li}_2\text{CO}_3$  layer deposited by thermal ALD could be adequately fitted using model I shown in Figure 4.10b which is confirmed by the low  $\chi^2$  value of  $5 \cdot 10^{-4}$ . When equivalent circuit model I was tried to fit the response of the plasma deposited  $\text{Li}_2\text{CO}_3$  layer, no adequate fit could be obtained. For this reason, model II was used, resulting in the fit shown in Figure 4.10a. The quality of the fit was again confirmed by the low  $\chi^2$  value of  $2 \cdot 10^{-4}$ .

From the complex non-linear square fitting of the models to the impedance data, different component values are extracted. The  $R_s$  was found to be around  $150 \Omega$  for both thermal and plasma samples. This value corresponds to the resistance of the cables and the electrochemical cell. The other relevant parameters are summarized in Table 4.3. For the thermal sample a resistance ( $R_1$ ) value of  $25 \text{ k}\Omega$  is extracted, corresponding to a Li-ion conductivity of  $4 \cdot 10^{-10} \text{ S} \cdot \text{cm}^{-1}$ , well in accordance values predicted by simulation studies.<sup>32</sup> From the constant phase element ( $\text{CPE}_1$ ), a capacitance value can be extracted according to the following formula<sup>33,34</sup>:

$$C = Q^{1/n} R_1^{(1-n)/n} \quad (\text{Eq. 4. 1})$$

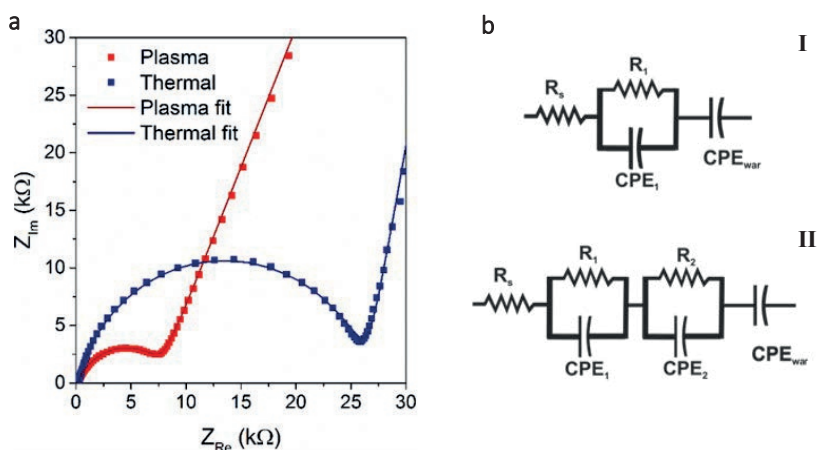


**Figure 4.10** a) Impedance spectroscopy of  $50 \text{ nm}$   $\text{Li}_2\text{CO}_3$  films prepared by thermal (blue) and plasma-assisted (red) ALD at  $150^\circ\text{C}$  and b) equivalent circuit models used to fit the data.



**Table 4.3** Summary of the most relevant circuit model parameters.

Sample	$R_1$ (k $\Omega$ )	$C_1$ (F)	$R_2$ (k $\Omega$ )	$C_2$ (F)	$\chi^2$
Thermal	25	$2 \cdot 10^{-7}$	-	-	$5 \cdot 10^{-4}$
Plasma	2.5	$4 \cdot 10^{-7}$	3	$8 \cdot 10^{-7}$	$2 \cdot 10^{-4}$

Usage of this formula assumes a normal distribution of the time constants associated with the constant phase element. It allows an accurate determination of the capacitance value associated with the CPE even with an  $n$  value around 0.8.<sup>33,34</sup> By using the above formalism, a capacitance value of 200 nF is extracted for CPE<sub>1</sub>, corresponding to a dielectric constant of  $\sim 25$ . This value is higher than what is expected for typical oxide films. However, the large surface roughness of the thermal films must be considered (see appendix Figure S4.4). Such roughness increases the effective contact area of the capacitor which is not included when using the geometrical surface area. For this reason, also the extracted ionic conductivity value will be slightly overestimated and can be adjusted for surface roughness down to a value of  $10^{-10} \text{ S} \cdot \text{cm}^{-1}$ .

The impedance response of the plasma-assisted Li<sub>2</sub>CO<sub>3</sub> sample was also probed. Figure 4.10a shows that the plasma sample has a lower ionic resistance (as indicated from the intercept with the x-axis). This semi-circle consists of two overlapping semi-circles with slightly different time constants which is reflected in the model choice (model II). The capacitance values were again extracted by using Equation 4.1. The values found were 400 and 800 nF for respectively CPE<sub>1</sub> and CPE<sub>2</sub>. These values correspond to dielectric constants of 40 and 80, so significantly higher than the one of the thermal sample and too high for typical oxide films.

Such capacity values can be attributed to a change in dielectric constant or different geometrical dimensions. However, no difference in mass density could be detected between the thermal and plasma Li<sub>2</sub>CO<sub>3</sub> layers (see Table 4.2). Therefore, it is unlikely that a significant difference in dielectric constant exists between the two layers. When considering the morphology of the layers (see Figure 4.8), a columnar structure can be seen. Therefore, the liquid electrolyte may contact the individual grains. Clearly this would lead to a significant increase in contact area and thus an increased capacitance value. The distribution in grain size can in such case lead to a distribution in time constants. The two resistance values extracted from the fitting, each correspond to a Li-ion conductivity value in the order of  $1 \cdot 10^{-9} \text{ S} \cdot \text{cm}^{-1}$ . However, the underestimation of the contact area introduces a significant uncertainty on this value which, based on the increased surface area, will be overestimated. When normalizing the conductivity value found here to the ratio of the different effective surface areas of the thermal and plasma samples, a conductivity value of  $10^{-10} \text{ S} \cdot \text{cm}^{-1}$  is obtained, a value again in line with other literature reports.<sup>32</sup>

## 4.4 Conclusions

A comparison has been made between the remote plasma ALD process and its more extensively adopted thermal counterpart. Self-limiting growth was obtained for both processes within a wide temperature window. This wide temperature window could especially be useful when  $\text{Li}_2\text{CO}_3$  is combined in supercycles to obtain more complex material stoichiometries, since many other precursors or co-reactants have a limited temperature window. Especially the use of plasma allows for the possibility to deposit at lower process temperatures, which would be beneficial for temperature-sensitive substrates. Moreover, plasma-assisted ALD allows for shorter deposition times and higher growth per cycle values leading to an increase in reactor throughput.

Stoichiometric  $\text{Li}_2\text{CO}_3$  films can be deposited with both ALD processes. In addition, it is possible to deposit  $\text{Li}_2\text{O}$  at temperatures  $> 250\text{ }^\circ\text{C}$  through combustion of the organic ligands. This could be beneficial when presence of carbon in the films is undesirable. For thermal ALD it is necessary to also omit the  $\text{CO}_2$  step from the process to obtain  $\text{Li}_2\text{O}$ . For plasma-assisted ALD, introduction of  $\text{Li}_2\text{O}$  in the films is accompanied with suppression of film crystallinity and increases film non-uniformity. The formation of  $\text{Li}_2\text{O}$  can be further promoted by prolonging the plasma exposure time.

Both plasma-assisted and thermal ALD of  $\text{Li}_2\text{CO}_3$  allow for conformal coating of high aspect ratio substrates as can be important for future Li-ion batteries. To the best of our knowledge this paper provides the first proper conductivity measurement of  $\text{Li}_2\text{CO}_3$  ALD films. An ion conductivity in the order of  $10^{-10}\text{ S} \cdot \text{cm}^{-1}$  was obtained for both plasma and thermal ALD after normalizing the fitted conductivity values to the ratio of the different effective surface areas. Studies are ongoing to characterize the electrochemical properties of the  $\text{Li}_2\text{CO}_3$  films in more depth.

## Acknowledgements

The authors gratefully acknowledge dr. Marcel Verheijen for fruitful discussion and Cristian van Helvoirt and Jeroen van Gerwen for technical assistance. This project is financially supported by the Dutch program “A green Deal in Energy Materials” ADEM Innovation Lab.

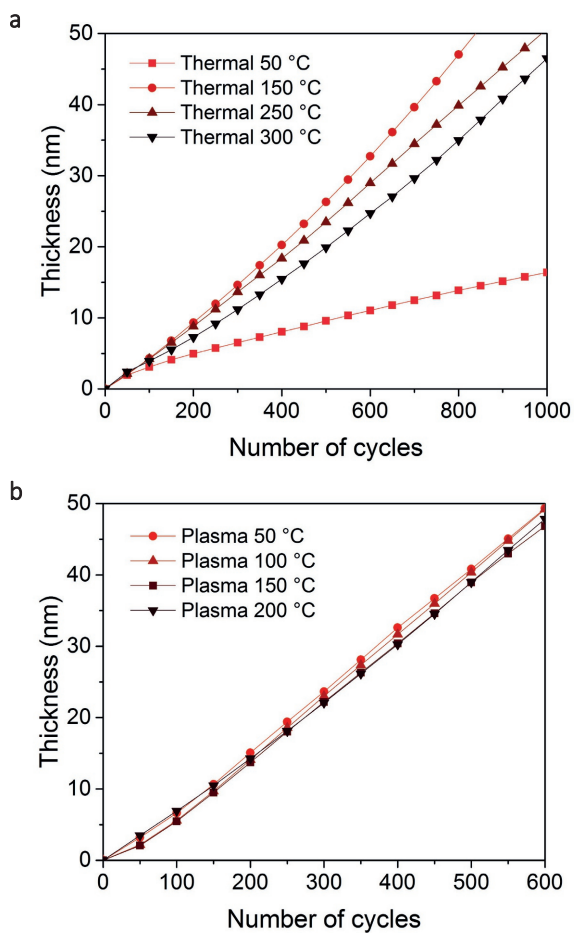
## References

1. K. Chung, J.-D. Lee, E.-J. Kim, et al. Studies on the effects of coated Li<sub>2</sub>CO<sub>3</sub> on lithium electrode. *Microchem. J.* **75**, 71–77 (2003).
2. Y. C. Zhang, H. Tagawa, S. Asakura, et al. Solid-state electrochemical CO<sub>2</sub> sensor by coupling lithium ion conductor (Li<sub>2</sub>CO<sub>3</sub>-Li<sub>3</sub>PO<sub>4</sub>-Al<sub>2</sub>O<sub>3</sub>) with oxide ion-electron mixed conductor (La<sub>0.9</sub>Sr<sub>0.1</sub>MnO<sub>3</sub>). *Solid State Ionics* **100**, 275–281 (1997).
3. Y. Shimamoto, T. Okamoto, Y. Itagaki, et al. Performance and stability of potentiometric CO<sub>2</sub> gas sensor based on the Pt, Li<sub>2</sub>CO<sub>3</sub>/Na<sub>2</sub>O-Al<sub>2</sub>O<sub>3</sub>-4SiO<sub>2</sub>/YSZ/Pt electrochemical cell. *Sensors Actuators B Chem.* **99**, 113–117 (2004).
4. J. Mizusaki and H. Tagawa. Lithium carbonate as a solid electrolyte. *Solid State Ionics* **53–56**, 791–797 (1992).
5. S. Bhattacharya, A. R. Riahi and A. T. Alpas. Electrochemical cycling behaviour of lithium carbonate (Li<sub>2</sub>CO<sub>3</sub>) pre-treated graphite anodes - SEI formation and graphite damage mechanisms. *Carbon N. Y.* **77**, 99–112 (2014).
6. J. W. Long, B. Dunn, D. R. Rolison, et al. Three-dimensional battery architectures. *Chem. Rev.* **104**, 4463–4492 (2004).
7. J. F. M. Oudenhoven, L. Baggetto and P. H. L. Notten. All-solid-state lithium-ion microbatteries: A review of various three-dimensional concepts. *Adv. Energy Mater.* **1**, 10–33 (2011).
8. G. W. Rubloff, A. C. Kozen and S. B. Lee. From nanoscience to solutions in electrochemical energy storage. *J. Vac. Sci. Technol. A Vacuum, Surfaces, Film.* **31**, 058503 (2013).
9. P. M. Vereecken and C. Huyghebaert. Conformal deposition for 3D thin-film batteries. *ECS Trans.* **58**, 111–118 (2013).
10. H. C. M. Knoops, M. E. Donders, M. C. M. van de Sanden, et al. Atomic layer deposition for nanostructured Li-ion batteries. *J. Vac. Sci. Technol., A* **30**, 010801 (2012).
11. X. Meng, X.-Q. Yang and X. Sun. Emerging applications of atomic layer deposition for lithium-ion battery studies. *Adv. Mater.* **24**, 3589–3615 (2012).
12. O. Nilsen, V. Miikkulainen, K. B. Gandrud, et al. Atomic layer deposition of functional films for Li-ion microbatteries. *Phys. Status Solidi Appl. Mater. Sci.* **211**, 357–367 (2014).
13. S. M. George. Atomic layer deposition: An overview. *Chem. Rev.* **110**, 111–131 (2010).
14. C. Guan and J. Wang. Recent development of advanced electrode materials by atomic layer deposition for electrochemical energy storage. *Adv. Sci.* **3**, 1–23 (2016).

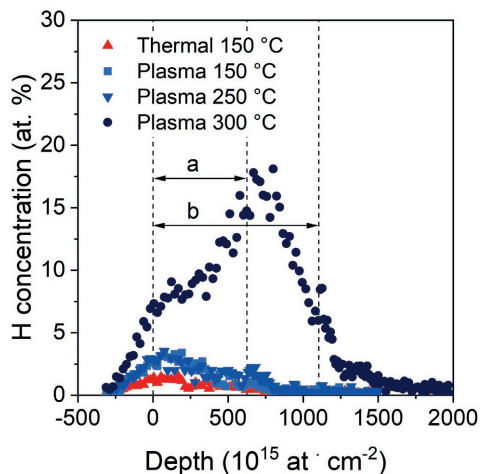
15. C. Guan, X. Qian, X. Wang, et al. Atomic layer deposition of  $\text{Co}_3\text{O}_4$  on carbon nanotubes/carbon cloth for high-capacitance and ultrastable supercapacitor electrode. *Nanotechnology* **26**, 094001 (2015).
16. H. B. Profijt, S. E. Potts, M. C. M. van de Sanden, et al. Plasma-assisted atomic layer deposition: basics, opportunities, and challenges. *J. Vac. Sci. Technol. A* **29**, 050801 (2011).
17. A. S. Cavanagh, Y. Lee, B. Yoon, et al. Atomic Layer Deposition of  $\text{LiOH}$  and  $\text{Li}_2\text{CO}_3$  Using Lithium t-butoxide as the Lithium Source. *ECS Trans.* **33**, 223–229 (2010).
18. E. Østreng, P. Vajeeston, O. Nilsen, et al. Atomic layer deposition of lithium nitride and carbonate using lithium silylamide. *RSC Adv.* **2**, 6315–6322 (2012).
19. A. Ruud, V. Miikkulainen, K. Mizohata, et al. Enhanced process and composition control for atomic layer deposition with lithium trimethylsilylanolate. *J. Vac. Sci. Technol., A* **35**, 01B133 (2017).
20. A. C. Kozen, A. J. Pearse, C. Lin, et al. Atomic layer deposition and in situ characterization of ultraclean lithium oxide and lithium hydroxide. *J. Phys. Chem. C* **118**, 27749–27753 (2014).
21. M. Putkonen, T. Aaltonen, M. Alnes, et al. Atomic layer deposition of lithium containing thin films. *J. Mater. Chem.* **19**, 8767–8771 (2009).
22. T. Aaltonen, O. Nilsen, A. Magrasó, et al. Atomic layer deposition of  $\text{Li}_2\text{O}-\text{Al}_2\text{O}_3$  thin films. *Chem. Mater.* **23**, 4669–4675 (2011).
23. D. J. Comstock and J. W. Elam. Mechanistic study of lithium aluminum oxide atomic layer deposition. *J. Phys. Chem. C* **117**, 1677–1683 (2013).
24. M. E. Donders, W. M. Arnoldbik, H. C. M. Knoop, et al. Atomic layer deposition of  $\text{LiCoO}_2$  thin-film electrodes for all-solid-state Li-ion micro-batteries. *J. Electrochem. Soc.* **160**, A3066–A3071 (2013).
25. T. Aaltonen, M. Alnes, O. Nilsen, et al. Lanthanum titanate and lithium lanthanum titanate thin films grown by atomic layer deposition. *J. Mater. Chem.* **20**, 2877–2881 (2010).
26. X. Meng, J. Liu, X. Li, et al. Atomic layer deposited  $\text{Li}_4\text{Ti}_5\text{O}_{12}$  on nitrogen-doped carbon nanotubes. *RSC Adv.* **3**, 7285–7288 (2013).
27. J. Hämäläinen, J. Holopainen, F. Munnik, et al. Lithium phosphate thin films grown by atomic layer deposition. *J. Electrochem. Soc.* **159**, A259–A263 (2012).
28. D. D. Williams and R. R. Miller. Effect of water vapor on the  $\text{LiOH}-\text{CO}_2$  reaction. Dynamic isothermal system. *Ind. Eng. Chem. Fundam.* **9**, 454–457 (1970).
29. H. A. Mosqueda, C. Vazquez, P. Bosch, et al. Chemical sorption of carbon dioxide ( $\text{CO}_2$ ) on lithium oxide ( $\text{Li}_2\text{O}$ ). *Chem. Mater.* **18**, 2307–2310 (2006).
30. R. Dedryvere, L. Gireaud, S. Grugeon, et al. Characterization of lithium alkyl carbonates by X-ray photoelectron spectroscopy: Experimental and theoretical study. *J. Phys. Chem. B* **109**, 15868–15875 (2005).

31. B. Put, P. M. Vereecken, J. Meersschaut, et al. Electrical characterization of ultrathin RF-sputtered LiPON layers for nanoscale batteries. *ACS Appl. Mater. Interfaces* **8**, 7060–7069 (2016).
32. S. Shi, Y. Qi, H. Li, et al. Defect thermodynamics and diffusion mechanisms in Li<sub>2</sub>CO<sub>3</sub> and implications for the solid electrolyte interphase in Li-ion batteries. *J. Phys. Chem. C* **117**, 8579–8593 (2013).
33. M. E. Orazem, I. Frateur, B. Tribollet, et al. Dielectric properties of materials showing constant-phase-element (CPE) impedance response. *J. Electrochem. Soc.* **160**, C215–C225 (2013).
34. B. Hirschorn, M. E. Orazem, B. Tribollet, et al. Determination of effective capacitance and film thickness from constant-phase-element parameters. *Electrochim. Acta* **55**, 6218–6227 (2010).

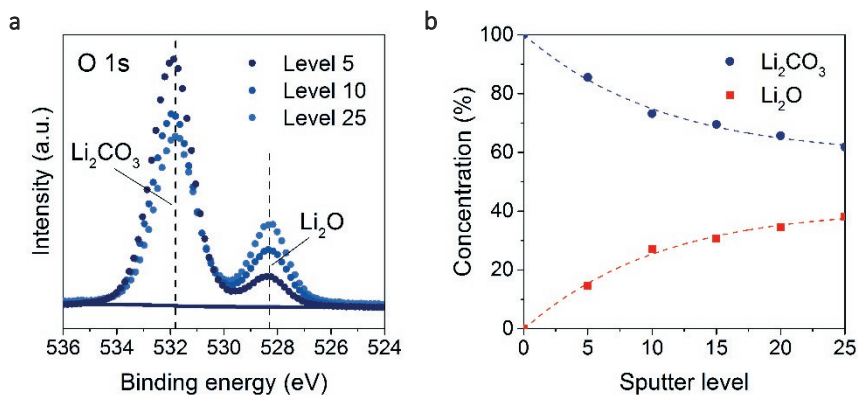
## Appendix



**Figure S4.1** a) *In situ* SE thickness measurement for thermal ALD of  $\text{Li}_2\text{CO}_3$  at 50, 150, 250 and 300 °C. b) *In situ* SE film growth of  $\text{Li}_2\text{CO}_3$  plasma ALD between 50 and 200 °C showing similar growth.



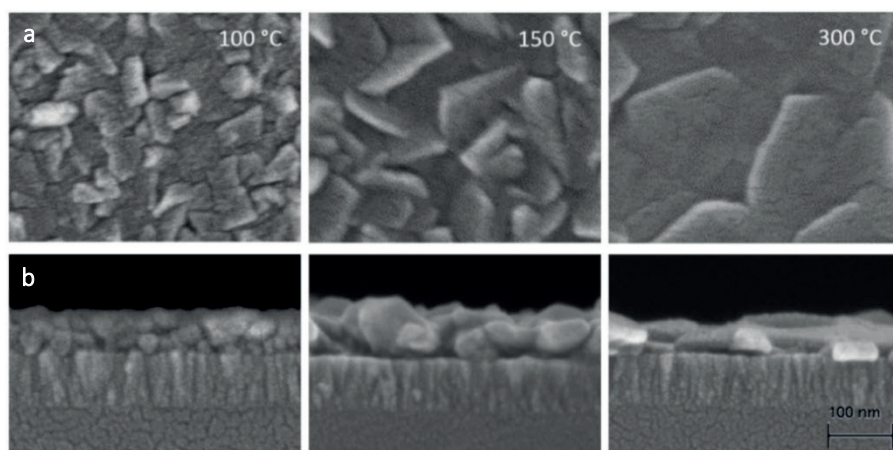
**Figure S4.2** Hydrogen concentration as a function of film depth measured by ERD for thermal ALD at 150 °C and plasma ALD at 150, 250 and 300 °C. As deposited, the film thickness was  $\sim 50$  nm. The total number of measured at  $\cdot \text{cm}^{-2}$  was similar for the first three samples and is indicated by (a). The thickness of the plasma film deposited at 300 °C increases due to air reactivity. Therefore, the thickness of this film prior to the ERD measurement was unclear. The total number of measured atoms for this sample is indicated by (b).



**Figure S4.3** a) XPS O 1s spectrum for an ALD  $\text{Li}_2\text{CO}_3$  film subject to  $\text{Ar}^+$  sputtering. As a result of chemical decomposition, a peak at  $\sim 528.3$  eV appears originating from  $\text{Li}_2\text{O}$ . 25 sputter levels corresponds to removing approximately 30 nm  $\text{Li}_2\text{CO}_3$ . b) Decrease in amount of  $\text{Li}_2\text{CO}_3$  as a function of sputter level obtained from the XPS fitting.

**Table S4.1** *Ex situ* XPS stoichiometry results for both plasma and thermal ALD  $\text{Li}_2\text{CO}_3$  films.

Sample	O (at. %)	Li (at. %)	C (at. %)
Stoichiometric $\text{Li}_2\text{CO}_3$	50.0	33.3	16.7
Plasma 50	47.7	33.5	18.8
Plasma 150	49.1	33.0	18.0
Plasma 250	48.0	33.7	18.4
Thermal 100	48.1	33.3	18.6
Thermal 150	49.3	33.0	17.7
Thermal 300	48.5	33.8	17.7

**Figure S4.4** a) High resolution SEM topography and b) cross-section images of  $\text{Li}_2\text{CO}_3$  deposited with thermal ALD at 100, 150, and 300 °C. The scale bar applies to all of the pictures.





# 5

## QMS of $\text{Li}_2\text{CO}_3$ film growth by thermal and plasma-assisted ALD

---

---

Quadrupole mass spectrometry (QMS) was carried out to detect and identify the reaction products during atomic layer deposition (ALD) of lithium carbonate ( $\text{Li}_2\text{CO}_3$ ). We examined gas phase species for thermal ALD using a  $\text{LiO}^t\text{Bu}$  precursor together with  $\text{H}_2\text{O}$  and  $\text{CO}_2$  and plasma-assisted ALD using the same lithium precursor combined with an  $\text{O}_2$  plasma. For both processes it was concluded that in the first half cycle the  $\text{LiO}^t\text{Bu}$  chemisorbs on the surface by an association reaction of the complete precursor whereas in the second half-cycle the organic ligand is abstracted as *tert*-butanol. The differences between the two processes lie mainly in the formation of  $\text{CO}_2$  and  $\text{H}_2\text{O}$  reaction byproducts in the second half-cycle when an  $\text{O}_2$  plasma is used as coreactant instead of  $\text{H}_2\text{O}$ . The generation of  $\text{CO}_2$  supports the fact that it is possible to deposit  $\text{Li}_2\text{CO}_3$  films directly by plasma-assisted ALD. Instead, in the case of thermal ALD, an additional  $\text{CO}_2$  dose step is required to deposit  $\text{Li}_2\text{CO}_3$  and suppress  $\text{LiOH}$  or  $\text{Li}_2\text{O}$  formation. The reaction with  $\text{CO}_2$  appears to be reversible at higher deposition temperatures ( $T \geq 250$  °C) and by using extended plasma exposure times and therefore the composition of the plasma-assisted ALD films can be varied between  $\text{Li}_2\text{CO}_3$  and  $\text{Li}_2\text{O}$ .

## 5.1 Introduction

Lithium carbonate is the most widely studied model system in atomic layer deposition (ALD) of Li-compounds.<sup>1–3</sup> Specifically, it is considered an essential step for incorporating Li into multicomponent ALD electrode and electrolyte material. Furthermore, it is an electrochemically stable, pure ionic conductor on its own and therefore interesting as protective coating/electron barrier on electrode materials. In several studies the stoichiometry of atomic layer deposited  $\text{Li}_2\text{CO}_3$  as well as  $\text{LiOH}$  and  $\text{Li}_2\text{O}$  have been investigated by e.g. time of flight secondary ion mass spectrometry (ToF-SIMS) or X-ray photoelectron spectroscopy (XPS).<sup>1–7</sup> From these studies it is known that if an ALD process is employed with two half cycles using a lithium precursor and  $\text{H}_2\text{O}$ , either  $\text{LiOH}$  or  $\text{Li}_2\text{O}$  is formed depending on the deposition temperature.  $\text{Li}_2\text{CO}_3$  can be deposited by adding an extra  $\text{CO}_2$  subcycle to the ALD process. In previous chapter, it was found that if an  $\text{O}_2$  plasma is used as coreactant instead of  $\text{H}_2\text{O}$  and  $\text{CO}_2$ , the stoichiometry of the films can be varied between  $\text{Li}_2\text{CO}_3$  and  $\text{Li}_2\text{O}$ , with deposition temperature playing an important role.<sup>7</sup>

Cavanagh et al. postulated a reaction scheme for  $\text{LiOH}$  and  $\text{Li}_2\text{CO}_3$  thermal ALD and used a quartz crystal microbalance (QCM) to strengthen their hypothesis based on the measured mass gains and losses during different steps of the ALD process.<sup>8</sup> It was proposed that in the first ALD subcycle,  $\text{LiO}^t\text{Bu}$  precursor chemically adsorbs on the surface and remains intact. In the second subcycle  $\text{LiOH}$  is formed upon  $\text{H}_2\text{O}$  exposure, releasing *tert*-butanol as reaction product. In the last process step  $\text{CO}_2$  is dosed, resulting in a  $\text{Li}_2\text{CO}_3$  film and releasing  $\text{H}_2\text{O}$  as reaction byproduct. The mass changes obtained by QCM were close to the values calculated using the molecular mass ratios of the reaction products following from the proposed reactions. So far, the reaction products during the ALD process have not been experimentally confirmed by direct measurements. Moreover, reaction mechanism studies for the plasma-assisted ALD process are still lacking and it is not known what the differences between plasma-assisted and thermal ALD are in terms of surface reactions. Thermal ALD processes are generally exploiting ligand exchange reactions, where the ligands of the metal precursor are eliminated by bonding to the Lewis acid groups, most commonly hydrogen, provided by the nonmetal coreactant. ALD processes using oxygen, oxygen plasma or ozone as a coreactant typically involve a different chemistry often leading to combustion reactions.<sup>9</sup> With plasma-assisted ALD, a high reactivity is delivered to the deposition surface by the plasma species and therefore less thermal energy is required at the substrate to drive the ALD surface chemistry.<sup>10</sup> In previous studies we found that the use of plasma species as reactants for the  $\text{Li}_2\text{CO}_3$  process allows for deposition at temperatures as low as 50 °C, higher growth per cycle values, and shorter cycle times due to the possibility to deposit  $\text{Li}_2\text{CO}_3$  with less process steps.<sup>7</sup>

In this work, a quadrupole mass spectrometry (QMS) study was carried out to detect and identify the reaction products during ALD of  $\text{Li}_2\text{CO}_3$ . QMS gives direct insight into the gas species present in the chamber and can therefore give useful

information on the surface reactions. The influence of temperature and plasma exposure time was also investigated.  $\text{Li}_2\text{CO}_3$  films were deposited by thermal ALD using a  $\text{LiO}^t\text{Bu}$  precursor combined with  $\text{H}_2\text{O}$  and  $\text{CO}_2$  and by plasma-assisted ALD using  $\text{LiO}^t\text{Bu}$  together with an  $\text{O}_2$  plasma. By investigating the thermal ALD process, previously proposed reaction mechanisms were experimentally confirmed and knowledge on QMS of lithium materials was obtained, useful for understanding the more complex plasma-assisted ALD process. Knowledge on the reaction products can provide new insights which can be useful for preparing better quality ALD films for Li-ion battery applications.

## 5.2 Experimental

The ALD processes presented in this work were carried out using the thermal and remote plasma ALD reactor FlexAL of Oxford Instruments. The reactor is equipped with an inductively coupled plasma source and it has a turbo and rotary molecular pump such that it can reach a base pressure of  $< 10^{-6}$  Torr by overnight pumping. For thermal ALD, the cycle consists of the exposure of the substrate to  $\text{LiO}^t\text{Bu}$  lithium precursor (97%, Sigma Aldrich),  $\text{H}_2\text{O}$  gas, and  $\text{CO}_2$  gas, respectively. The plasma-assisted ALD process consists of a combination of exposure of the substrate to the same lithium precursor and to an  $\text{O}_2$ -fed plasma generated with a plasma power of 100 W. The lithium precursor is bubbled from a precursor pod with argon. To reduce possible clogging, the lithium line is equipped with a stainless-steel VCR (vacuum coupling radiation) face seal fitting including a silver-plated gasket with 20  $\mu\text{m}$  pores.

The precursor dosing steps are alternated by argon purging steps. The purge time is kept at 6 s for consistency and to clearly separate the process steps. The table and wall temperature were kept at 150 and 120  $^\circ\text{C}$ , respectively, unless specified differently. The processing pressure was in the range of 7 - 200 mTorr and is specified in the time-resolved measurement section. All the ALD process parameters are summarized in Table 5.1. More details are presented in earlier work.<sup>7</sup>

A Pfeiffer Vacuum mass spectrometer with a mass-to-charge ( $m/z$ ) range of 100 atomic mass units (amu) was connected to the deposition chamber through a pipeline and a 150  $\mu\text{m}$  diameter pinhole. The system is equipped with a Channeltron detector and the energy of the electrons in the ionizer was set to 70 eV. The pressure in the QMS was maintained below  $10^{-6}$  Torr using differential pumping with a turbomolecular pump. Prior to every measurement the reactor was conditioned with a  $\text{Li}_2\text{CO}_3$  film and the background signal of the reactor was measured as a reference.

The QMS used measures only stable neutral species which are then ionized in the mass spectrometer. To learn about the species present in the reactor during processing, first the total  $m/z$  range was measured. The measuring time per atomic mass unit (amu) was set to 200 ms. Only  $m/z$  values of 0 to 60 are plotted in this work, since for higher values only peaks with a very low ion current were found, which were

**Table 5.1** ALD process parameters used for the measurements.

Parameter	Setting	Unit
Base pressure	< 10 <sup>-6</sup>	Torr
Processing pressure	7 - 200	mTorr
Process table temperature	150	°C
Reactor wall temperature	120	°C
Precursor pod temperature	140	°C
Precursor lines and valves	150	°C
Lithium precursor dosing time	6	s
Thermal process		
H <sub>2</sub> O dose	50	ms
H <sub>2</sub> O reaction step	4	s
CO <sub>2</sub> dose	2	s
Plasma process		
O <sub>2</sub> dose time	5	s
Plasma exposure time	3	s
Plasma power	100	W
Ar purge times	6	s

difficult to distinguish from the background signal. The cracking patterns for each of the reagents were recorded. From these results the relevant  $m/z$  ratios were selected for further analysis.

For the time-resolved measurements, the selected  $m/z$  values were tracked per channel using a dwell time (or integration time) of 50 ms. The QMS data of at least 10 ALD cycles were monitored to verify that steady-state values were achieved. Moreover, all measurements were repeated at least three times to verify reproducibility. The pressure in the system was monitored to distinguish pressure-related fluctuations in the signal from variations in the gas composition unrelated to the pressure changes. This allows for distinguishing the signals originating from species potentially involved in the reactions. Also, to distinguish reaction products from other species in the chamber, reference measurements were carried out. In the reference measurements one or more of the reagents are excluded from the standard ALD sequence. A similar procedure was used by Knoops et al. for ALD of TaN<sub>x</sub>.<sup>11</sup>

## 5.3 Results and discussion

### 5.3.1 Mass spectra of all reagents

The mass spectrum obtained during LiO<sup>t</sup>Bu precursor dose is shown in Figure 5.1. Several peaks associated with Ar used to bubble the precursor are also present. Therefore, the ionization pattern originating from only the Ar flow is plotted in the same figure for comparison. In addition, a measurement without injection of gas at a

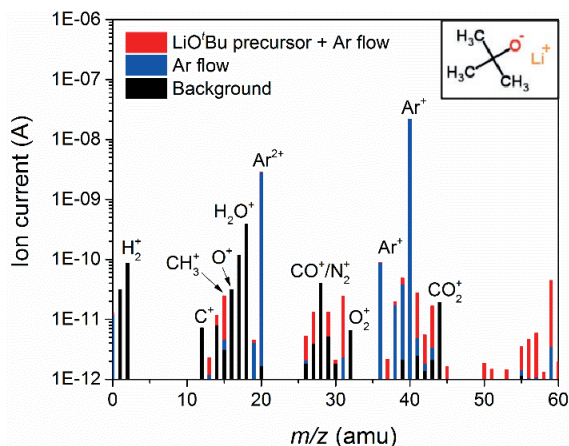


**Figure 5.1** The cracking pattern obtained by mass spectrometry during  $\text{LiO}^t\text{Bu}$  precursor dose. The patterns from the reactor background and Ar flow are plotted in the same figure for comparison. The insert shows the chemical structure of the  $\text{LiO}^t\text{Bu}$  precursor molecule.

reactor pressure in the range of  $10^{-6}$  Torr is shown. This allows one to discern between precursor species, the Ar signal and the background signal. Peaks are found at  $m/z = 15$  from  $\text{CH}_3^+$ , 31 most likely from  $\text{CH}_3\text{O}^+$ , 41 from  $\text{C}_2\text{HO}^+$  or  $\text{C}_3\text{H}_5^+$ , 43 from  $\text{C}_2\text{H}_3\text{O}^+$  or  $\text{C}_3\text{H}_7^+$ , 57 from  $\text{C}_3\text{H}_5\text{O}^+$  or  $\text{C}_4\text{H}_9^+$  and 59 amu from  $\text{C}_3\text{H}_7\text{O}^+$ . The cracking pattern of  $\text{LiO}^t\text{Bu}$  is very similar to the one of *tert*-butanol from the NIST database,<sup>12</sup> except that the peak distribution is slightly different. However, this discrepancy could also be due to instrumental differences in sensitivity of the mass spectrometers used.

For the thermal ALD process, the  $\text{LiO}^t\text{Bu}$  precursor is combined with  $\text{H}_2\text{O}$  and  $\text{CO}_2$  gas steps, respectively. The cracking patterns for  $\text{H}_2\text{O}$  and  $\text{CO}_2$  gas dose together with the background signal of the reactor are shown in Figure S5.1 in the appendix. Peaks originating from  $\text{H}_2\text{O}^+$ ,  $\text{H}^+$ ,  $\text{OH}^+$ , and  $\text{O}^+$  can be recognized in mass spectrum of  $\text{H}_2\text{O}$ . The pattern of  $\text{CO}_2$  predominantly consists of  $\text{CO}_2^+$ ,  $\text{CO}^+$ , and  $\text{C}^+$  species, as expected. In the plasma-assisted ALD process of  $\text{Li}_2\text{CO}_3$ , the  $\text{H}_2\text{O}$  and  $\text{CO}_2$  gas are replaced by an  $\text{O}_2$  plasma. During the  $\text{O}_2$  plasma exposure step, mainly  $\text{O}^+$  and  $\text{O}_2^+$  species are identified in the cracking pattern as shown in Figure S5.2 in the appendix.

### 5.3.2 Time-resolved measurements for thermal ALD $\text{Li}_2\text{CO}_3$

To obtain information on the reaction products formed during the thermal ALD process, time-resolved mass spectrometry was carried out. From the ionization patterns shown in previous section, it was concluded that the  $\text{LiO}^t\text{Bu}$  precursor can be tracked by following  $m/z = 15$  and 59.  $\text{H}_2\text{O}$  and  $\text{CO}_2$  can be tracked by following  $m/z$  values 18 and 44, respectively. Hence, we started the investigations by tracking the changes in ion current for  $m/z = 15, 18, 44,$  and 59. The results for other common  $m/z$  values will be discussed later in this section.

In Figure 5.2, the time resolved QMS data are plotted for one ALD cycle of  $\text{Li}_2\text{CO}_3$ . The graph is divided into several sections representing the different ALD process steps (i.e.  $\text{LiO}^t\text{Bu}$ ,  $\text{H}_2\text{O}$  and  $\text{CO}_2$  dosing, respectively), which are alternated by Ar purging. In addition to the standard ALD recipe, also the curves are plotted for conditions when only one or two of the reagents are used in the recipe. In this way it is possible to distinguish the reaction products from other species present in the reactor. In every plot four different curves are shown, corresponding to the following recipes: the

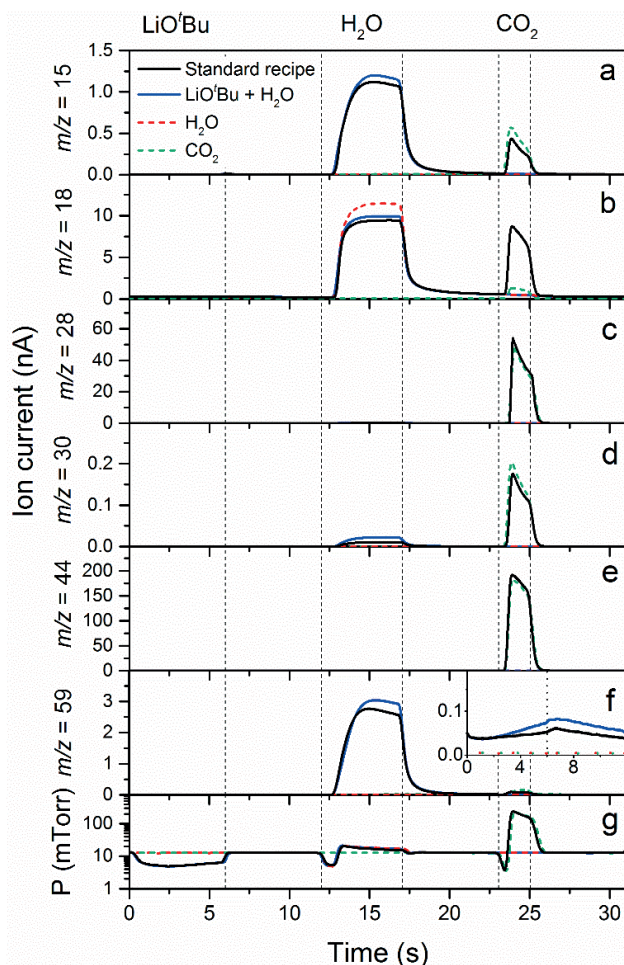


**Figure 5.2** Time-resolved QMS data of  $m/z = 15$  ( $\text{CH}_3^+$ , from *tert*-butanol or  $\text{LiO}^t\text{Bu}$ ), 18 ( $\text{H}_2\text{O}^+$  from  $\text{H}_2\text{O}$ ), 28 ( $\text{CO}^+$  from  $\text{CO}$  and  $\text{CO}_2$ ), 30, 44 ( $\text{CO}_2^+$  from  $\text{CO}_2$ ), and 59 ( $\text{C}_3\text{H}_7\text{O}^+$  from *tert*-butanol or  $\text{LiO}^t\text{Bu}$ ) for thermal ALD of  $\text{Li}_2\text{CO}_3$ . The standard ALD recipe (black) is compared to the recipe with only  $\text{LiO}^t\text{Bu}$  and  $\text{H}_2\text{O}$  (blue), the recipe with only  $\text{H}_2\text{O}$  (red) and the recipe with only  $\text{CO}_2$  (green). The precursor dosing steps are alternated by argon purge steps of 6 s.

standard recipe, the recipe with only LiO<sup>t</sup>Bu and H<sub>2</sub>O (corresponding to the ALD process of LiOH),<sup>6</sup> the recipe with only H<sub>2</sub>O, and the recipe with only CO<sub>2</sub>.

Before discussing the trends of the different fragments, we report on the variation in pressure according to the different recipes. In Figure 5.2g, the pressure curves are plotted. The pressure during the lithium precursor dose was around 7 mTorr. During the Ar purge step Ar gas was injected from a different line and the pressure increases and stays constant around 12 mTorr, as observed from the graph. In the first second of the following subcycle the automated pressure control (APC) gate valve is closed to promote the distribution of H<sub>2</sub>O in the chamber and limit the exposure time necessary to saturate the reaction with a dosing time of 50 ms. In this way also the purge time is kept relatively short. The Ar flow is stopped and therefore the pressure decreases. When H<sub>2</sub>O is dosed, the pressure reaches 20 mTorr. During the CO<sub>2</sub> dose step, another small pressure drop is observed due to a slight delay of the CO<sub>2</sub> flow caused by the geometry of the gas dosing system. When the CO<sub>2</sub> reaches the chamber, the pressure increases to about 200 mTorr. Note that the pressure curves are plotted on a logarithmic scale for clarity, since the pressure during the CO<sub>2</sub> dosing was relatively high, compared to the pressure when dosing other reagents.

In the first ALD subcycle the LiO<sup>t</sup>Bu precursor is introduced in the chamber. During this subcycle hardly any change in the signals is observed. However, on a much smaller ion current scale it is possible to observe a slight signal increase at all the  $m/z$  values related to the precursor (e.g. 15, 31, 41 and 59 amu). This is shown in the inset of Figure 5.2f. The intensity of this signal is much lower compared to the signal obtained in the next subcycle, as will be discussed later. This suggests that the increase originates from dissociation of residual, unreacted LiO<sup>t</sup>Bu molecules in the mass spectrometer or negligible abstraction of *tert*-butanol during the LiO<sup>t</sup>Bu surface reaction. As addressed in the introduction, it was postulated by Cavanagh et al. that LiO<sup>t</sup>Bu molecularly adsorbs on the sample surface.<sup>8</sup> The current QMS data is in line with this postulation, because the signal at  $m/z = 59$  is definitely negligible with respect to the signal obtained in the next subcycle. The LiO<sup>t</sup>Bu most likely chemisorbs on the sample surface with an association reaction of the complete precursor. In such an association reaction, the precursor remains intact when it chemically adsorbs without the release of reaction products into the gas phase.<sup>13</sup>

In the next subcycle H<sub>2</sub>O is dosed, and large signals at  $m/z = 15$ , 18 and 59 are detected instantly. The signals are now much larger as compared to the first subcycle, which suggests the presence of surface reactions. After dosing, the APC is kept closed for 4 s meaning the reactor is not being pumped and therefore the signals only decrease very slowly. The increase for  $m/z = 59$  indicates that a precursor fragment was released during this subcycle, since this is the main peak of the LiO<sup>t</sup>Bu cracking pattern. This is supported by the increase in ion current for  $m/z = 31$  and 41 amu, as shown in the appendix (Figure S5.3). The presence of these mass values also indicates

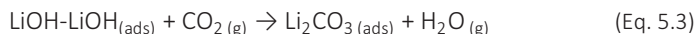
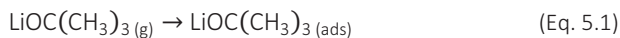


that the precursor ligand is most likely released in the form of *tert*-butanol since 31, 41 and 59 amu are the three major peaks in the *tert*-butanol mass spectrum.

H<sub>2</sub>O is difficult to pump and in the purge step after H<sub>2</sub>O dose, it seems as if not all the H<sub>2</sub>O is removed from the chamber. However, it was shown in previous chapter that the purge times are sufficient to suppress a significant CVD contribution to film growth.<sup>7</sup> As mentioned in the introduction, it is known from previous studies that H<sub>2</sub>O dosing initiates the reaction towards LiOH.<sup>6</sup> LiOH is hygroscopic and can easily adsorb H<sub>2</sub>O and form a hydrate.<sup>14</sup> The hygroscopic character is reversible and H<sub>2</sub>O can desorb from the LiOH-hydrate during the purge times, which might be the reason for the slow decay of the signal during the purge step.

In the third subcycle, CO<sub>2</sub> was introduced in the chamber and the reaction towards Li<sub>2</sub>CO<sub>3</sub> took place.<sup>7</sup> As observed from Figure 5.2b, it is established that H<sub>2</sub>O is a reaction byproduct. Moreover, no precursor-related reaction products were observed.

Based on these observations, a reaction sequence during Li<sub>2</sub>CO<sub>3</sub> thermal ALD can be proposed. Our reaction mechanism is in line with findings from literature, and therefore confirms earlier data.<sup>8</sup> In summary, in the first subcycle the LiO<sup>t</sup>Bu precursor chemically adsorbs without the significant release of reaction products into the gas phase (Equation 5.1). In the second subcycle LiOH is formed upon H<sub>2</sub>O dosing and the ligand is released in the form of *tert*-butanol (Equation 5.2).



The first two equations also describe the binary reaction of LiOH ALD. In previous chapter it was shown that the introduction of CO<sub>2</sub> in the chamber initiates the reaction towards Li<sub>2</sub>CO<sub>3</sub>.<sup>7</sup> As preliminary conclusion, we have demonstrated that upon CO<sub>2</sub> dosing, H<sub>2</sub>O was released in the gas phase and is therefore a reaction byproduct, according to Equation 5.3.

### 5.3.3 Time-resolved measurements for plasma-assisted ALD Li<sub>2</sub>CO<sub>3</sub>

The plasma-assisted ALD process of Li<sub>2</sub>CO<sub>3</sub> consists of two half cycles: in the first half-cycle the lithium precursor is dosed in the chamber and in the second half cycle the O<sub>2</sub> plasma is ignited (see Figure 5.3). The pressure in the chamber, which is plotted in Figure 5.3g, shows a similar behavior for the precursor injection and purging as was the case for the thermal ALD process. The pressure is now slightly higher, because there is an additional Ar flow from the ICP gate valve to prevent a backflow of species into the plasma source when the O<sub>2</sub> plasma is not used (for the thermal ALD process

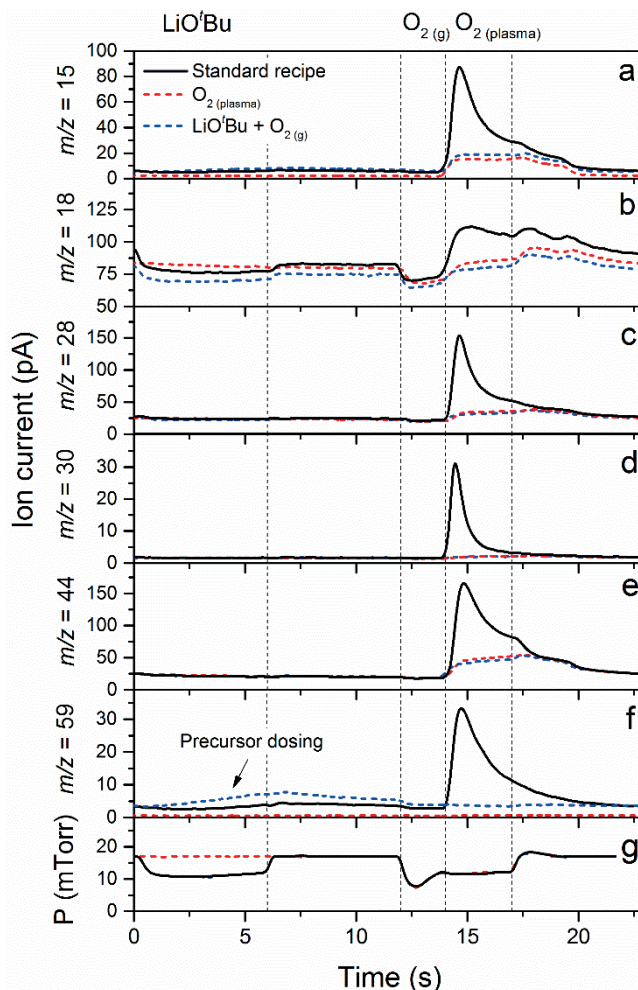


**Figure 5.3** Time-resolved QMS data following  $m/z = 15$  ( $\text{CH}_3^+$ ), 18 ( $\text{H}_2\text{O}^+$  from  $\text{H}_2\text{O}$ ), 28 ( $\text{CO}^+$  from  $\text{CO}$  and  $\text{CO}_2$ ), 30 (most likely  $\text{CH}_2\text{O}^+$ ), 44 ( $\text{CO}_2^+$  from  $\text{CO}_2$ ), and 59 ( $\text{C}_3\text{H}_7\text{O}^+$  from *tert*-butanol or  $\text{LiO}^i\text{Bu}$ ) for plasma-assisted ALD of  $\text{Li}_2\text{CO}_3$ . The standard ALD recipe (black) is compared to the recipe with only  $\text{O}_2$  plasma (red) and the recipe with only  $\text{LiO}^i\text{Bu}$  and  $\text{O}_2$  gas (blue).  $\text{O}_2(\text{g})$  and  $\text{O}_2(\text{plasma})$  represent  $\text{O}_2$  gas and plasma exited  $\text{O}_2$ , respectively. The precursor dosing steps are alternated by argon purge steps of 6 s.

the ICP gate valve was closed). During the  $\text{O}_2$  gas dose the pressure slightly drops to 10 mTorr and increases again during the Ar purge step.

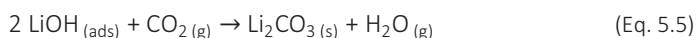
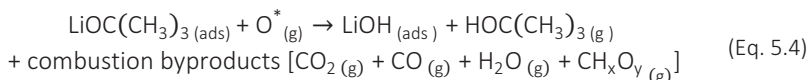
The introduction of  $\text{LiO}^i\text{Bu}$  in the first half-cycle leads to a small increase in signal for  $m/z = 15$  and 59 (Figure 5.3a and Figure 5.3f), but also for 31 and 41 amu (appendix Figure S5.4). All masses related to the precursor show a small increase in ion current,

most likely originating from dissociation of unreacted  $\text{LiO}^t\text{Bu}$  molecules in the mass spectrometer. During the Ar purge, the signal decreases slowly again. The  $\text{H}_2\text{O}$  ( $m/z = 18$ ) and  $\text{CO}_2$  ( $m/z = 44$ ) level are not altered when  $\text{LiO}^t\text{Bu}$  is injected into the chamber. Similar to the thermal ALD process, also for plasma-assisted ALD no significant release of reaction products into the gas phase was observed in the first subcycle. Therefore, it is expected that the precursor chemisorbs by an association reaction as well.

As was reported in previous chapter, no surface-reaction takes place when  $\text{O}_2$  gas is introduced in the chamber without ignition of plasma.<sup>7</sup> This is confirmed by the mass spectrometry data in Figure 5.3. If we only use  $\text{LiO}^t\text{Bu}$  and  $\text{O}_2$  gas, the curve follows the same trend as when there is no lithium precursor (as indicated by the blue and red line). However, if the plasma is switched on, we observe a large signal increase for all the masses shown in Figure 5.3. The increased ion current for  $m/z = 15, 31, 41$  and  $59$  amu during the plasma step indicates a reaction of the precursor ligand. In addition, volatile byproducts such as  $\text{CO}_2$  and  $\text{H}_2\text{O}$  were detected (Figure 5.3b and Figure 5.3e), attributed to the combustion of the absorbed ligand by O radicals.<sup>15,16</sup> By comparing the measured  $\text{CO}_2$  cracking pattern shown in appendix Figure S5.2 (parent ion at  $m/z = 44$ : 100 % and at  $m/z = 28$ :  $\pm 25$  % of normalized peak height) to the measurements shown in Figure 5.3, it can be concluded that also CO is present in the deposition chamber during the  $\text{O}_2$  plasma step. As observed from the time-resolved measurements, the  $\text{CO}^+$  signal (Figure 5.3c) has a comparable intensity during the plasma exposure step as the  $\text{CO}_2^+$  signal (Figure 5.3e). The origin of CO could either be through incomplete combustion of the ligands or through dissociation of  $\text{CO}_2$  in the plasma. Although the signals are decreasing, the detection of  $\text{H}_2\text{O}$ ,  $\text{CO}_2$  and CO continues for the whole plasma duration. Moreover, the presence of high signals at  $m/z = 15$  ( $\text{CH}_3^+$ ), 29 ( $\text{CHO}^+$ , shown in appendix Figure S5.4) and 30 (most likely  $\text{CH}_2\text{O}^+$ ) during the  $\text{O}_2$  plasma exposure step suggests additional surface reactions. The peaks are similar in height with respect to the fragments of *tert*-butanol, different from the thermal ALD process, where  $m/z = 15$  is relatively small and  $m/z = 29$  and  $m/z = 30$  are much smaller. Therefore, it is expected that other surface reactions occur, for which only a fraction of the precursor is converted to combustion byproducts.

Another finding concerns the deposition of  $\text{Li}_2\text{CO}_3$  directly using the plasma-assisted ALD route.<sup>7</sup> It is shown in Figure 5.3 that a high amount of  $\text{CO}_2$  is formed during the  $\text{O}_2$  plasma exposure step. Therefore, it is expected that a secondary reaction by  $\text{CO}_2$  produced at the surface takes place and leads to  $\text{Li}_2\text{CO}_3$ . We hypothesize the following reaction sequence  $\text{Li}_2\text{CO}_3$  plasma-assisted ALD accordingly: The first subcycle is expected to be similar to what was found for thermal ALD (Equation 5.1). The second subcycle however is expected to be more complex and proposed to consist out of two elementary steps. Next to the typical combustion reactions induced by the  $\text{O}_2$  plasma (Equation 5.4), a reaction with the  $\text{CO}_2$  produced at the surface is taking place, leading to the formation of  $\text{Li}_2\text{CO}_3$  (Equation 5.5). Note

that the combustion byproducts are written in brackets in these equations since the exact number of each byproduct formed is unknown at this point.



The reaction mechanism was proposed for plasma-assisted ALD of Li<sub>2</sub>CO<sub>3</sub> on the basis of experimental data obtained for a deposition temperature of 150 °C and a plasma exposure time of 3 s. Now the influence of substrate temperature and plasma exposure time will be discussed since it was found in previous work that the stoichiometry of the plasma-assisted ALD process is temperature and plasma exposure dependent.<sup>7</sup> By using a short O<sub>2</sub> exposure time and a substrate temperature of ≤ 200 °C, stoichiometric Li<sub>2</sub>CO<sub>3</sub> was formed. At higher temperatures Li<sub>2</sub>O is formed and it was proposed that this is further promoted by prolonging the O<sub>2</sub> plasma exposure. However, when changing the temperature we do not observe clear differences from QMS. Likely, this is related to the fact that the QMS will only measure a small part of the reaction products coming from the heated table and substrates surfaces. The reactor wall surface is heated to a maximum of 120 °C only, and comprises the largest part of the reactor. All internal surfaces of the reactor (i.e., also the reactor walls) contribute to the reaction since the process window of plasma-assisted ALD extends down to 50 °C. This means that even at high deposition temperatures ( $T \geq 250$  °C), the largest part of the measured reaction products originates from the formation of Li<sub>2</sub>CO<sub>3</sub> instead of Li<sub>2</sub>O. Another probable reason for the minimal change in QMS signal is that the difference in obtained reaction products we expect to see in the reaction is quite small. If we replace Li<sub>2</sub>CO<sub>3</sub> by Li<sub>2</sub>O in Equation 5.5, essentially only the relative amount of CO<sub>2</sub> byproducts would slightly increase.

It was shown in previous studies that a plasma duration of 1 s was already sufficient to obtain stoichiometric Li<sub>2</sub>CO<sub>3</sub>, which (partly) shifts towards Li<sub>2</sub>O at elevated temperatures ( $T \geq 250$  °C). It was postulated that the extended plasma exposure promotes the development of Li<sub>2</sub>O at  $T \geq 250$  °C, since higher growth rates were observed for longer plasma exposure times and the higher growth rates were typical for LiOH/Li<sub>2</sub>O growth (probably related to the hygroscopic nature of the films).<sup>7</sup> We now take a closer look into the CO<sub>2</sub> combustion byproduct. In Figure 5.4, QMS data for 15 and 44 amu are plotted for a plasma exposure time of 10 s and table temperature of set point of 300 °C. As observed in the graph, the detection of CO<sub>2</sub> continues for a long time when the plasma duration is extended whereas the CH<sub>3</sub><sup>+</sup> signal saturates. CO<sub>2</sub> is formed by the combustion of precursor ligands (Equation 5.4), and expected to be simultaneously used in the reaction towards Li<sub>2</sub>CO<sub>3</sub> (Equation 5.5). Since only 1 s plasma duration is sufficient to obtain Li<sub>2</sub>CO<sub>3</sub> films, we know from

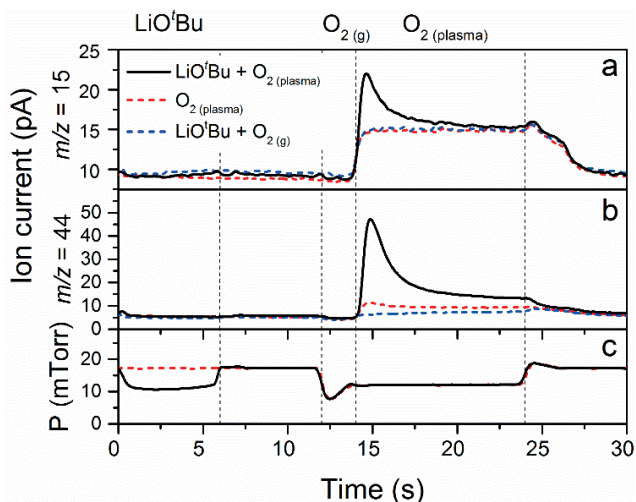


**Figure 5.4** QMS data for a long plasma exposure time of 10 s and substrate temperature of 300 °C following  $m/z = 15$  ( $\text{CH}_3^+$ ) and  $m/z = 44$  ( $\text{CO}_2^+$ ). The standard ALD recipe (black) is compared to the recipe with only  $\text{O}_2$  plasma (red) and the recipe with only  $\text{LiO}^t\text{Bu}$  and  $\text{O}_2$  gas (blue).  $\text{O}_2(\text{g})$  and  $\text{O}_2(\text{plasma})$  represent  $\text{O}_2$  gas and plasma exited  $\text{O}_2$ , respectively. The precursor dosing steps are alternated by argon purge steps of 6 s.

Figure 5.4b that an excess of  $\text{CO}_2$  is present. However, the source of precursor ligands (and therefore  $\text{CO}_2$ ) will eventually be released in the gas phase and pumped away from the reactor. This is confirmed by the graphs in Figure 5.4a, as the  $\text{CH}_3^+$  signal (which is directly related to the combustion of precursor ligands) saturates. However, since the detection of  $\text{CO}_2$  continues, it is expected that a longer  $\text{O}_2$  plasma exposure leads to  $\text{CO}_2$  desorption from the  $\text{Li}_2\text{CO}_3$  film. This will eventually reduce the  $\text{CO}_2$  in the surface region of the film, which allows for  $\text{LiOH}/\text{Li}_2\text{O}$  to form.

## 5.4 Conclusions

The reaction mechanism of thermal and plasma-assisted  $\text{Li}_2\text{CO}_3$  ALD has been investigated using time-resolved QMS. It was concluded that for both processes the  $\text{LiO}^t\text{Bu}$  precursor ligand chemisorbs on the surface with an association reaction of the complete precursor. By introducing the coreactant in the following subcycle, the organic part is released in the form of *tert*-butanol. This provides proof for the previously proposed reaction mechanism of thermal ALD  $\text{LiOH}/\text{Li}_2\text{O}$ .<sup>8</sup> When an  $\text{O}_2$  plasma is used instead of  $\text{H}_2\text{O}$  to undergo this reaction, also  $\text{H}_2\text{O}$ ,  $\text{CO}_2$ ,  $\text{CO}$ , and (oxidized) hydrocarbon reaction products are formed. The presence of (oxidized) hydrocarbon reaction products indicate that additional surface reactions occur for plasma-assisted ALD, where only a fraction of the precursor is converted to combustion products. The formation of  $\text{CO}_2$  in the plasma is especially interesting as

it allows to produce  $\text{Li}_2\text{CO}_3$  films directly: it is possible to deposit  $\text{Li}_2\text{CO}_3$  with less process steps since we do not need to add  $\text{CO}_2$  intentionally as is the case for thermal ALD. Moreover, we propose that for extended plasma exposure times,  $\text{CO}_2$  is removed from the  $\text{Li}_2\text{CO}_3$  film leading to formation of  $\text{Li}_2\text{O}$ . Experimental evidence was given that  $\text{CO}_2$  detection continues when the plasma exposure time is extended, while at the same time the source of precursor ligands, and thus  $\text{CO}_2$ , is released in the gas phase and pumped from the reactor. This will eventually lead to the formation of  $\text{Li}_2\text{O}$ , in line with observations in previous chapter.<sup>7</sup> The insights achieved by QMS studies into the reaction mechanisms of lithium ALD processes stimulates the future application of this diagnostic tool to more complex lithium (plasma-assisted) ALD processes.

### **Acknowledgements**

This project is financially supported by ADEM, A green Deal in Energy Materials of the Ministry of Economic Affairs of The Netherlands. We gratefully acknowledge C.A.A. van Helvoirt and J. van Gerwen for their technical assistance.

## References

1. M. Putkonen, T. Aaltonen, M. Alnes, et al. Atomic layer deposition of lithium containing thin films. *J. Mater. Chem.* **19**, 8767–8771 (2009).
2. E. Østreng, P. Vajeeston, O. Nilsen, et al. Atomic layer deposition of lithium nitride and carbonate using lithium silylamide. *RSC Adv.* **2**, 6315–6322 (2012).
3. A. Ruud, V. Miikkulainen, K. Mizohata, et al. Enhanced process and composition control for atomic layer deposition with lithium trimethylsilylanolate. *J. Vac. Sci. Technol., A* **35**, 01B133 (2017).
4. D. J. Comstock and J. W. Elam. Mechanistic study of lithium aluminum oxide atomic layer deposition. *J. Phys. Chem. C* **117**, 1677–1683 (2013).
5. T. Aaltonen, O. Nilsen, A. Magrasó, et al. Atomic layer deposition of Li<sub>2</sub>O–Al<sub>2</sub>O<sub>3</sub> thin films. *Chem. Mater.* **23**, 4669–4675 (2011).
6. A. C. Kozen, A. J. Pearse, C. Lin, et al. Atomic layer deposition and in situ characterization of ultraclean lithium oxide and lithium hydroxide. *J. Phys. Chem. C* **118**, 27749–27753 (2014).
7. N. Hornsveld, B. Put, W. M. M. Kessels, et al. Plasma-assisted and thermal atomic layer deposition of electrochemically active Li<sub>2</sub>CO<sub>3</sub>. *RSC Adv.* **7**, 41359–41368 (2017).
8. A. S. Cavanagh, Y. Lee, B. Yoon, et al. Atomic layer deposition of LiOH and Li<sub>2</sub>CO<sub>3</sub> using lithium t-butoxide as the lithium source. *ECS Trans.* **33**, 223–229 (2010).
9. K. Knapas and M. Ritala. In situ studies on reaction mechanisms in atomic layer deposition. *Crit. Rev. Solid State Mater. Sci.* **38**, 167–202 (2013).
10. H. B. Profijt, S. E. Potts, M. C. M. van de Sanden, et al. Plasma-assisted atomic layer deposition: basics, opportunities, and challenges. *J. Vac. Sci. Technol. A* **29**, 050801 (2011).
11. H. C. M. Knoop, E. Langereis, M. C. M. van de Sanden, et al. Reaction mechanisms of atomic layer deposition of TaN<sub>x</sub> from Ta(NMe<sub>2</sub>)<sub>5</sub> precursor and H<sub>2</sub>-based plasmas. *J. Vac. Sci. Technol., A* **30**, 01A101 (2012).
12. NIST Mass Spectrometry Data Center. Mass spectra. in *NIST Chemistry WebBook, NIST Standard Reference Database Number 69* (eds. Mallard, P. J. & Linstrom, W. G.) (National Institute of Standards and Technology, 2020).
13. R. L. Puurunen. Surface chemistry of atomic layer deposition: A case study for the trimethylaluminum/water process. *J. Appl. Phys.* **97**, 121301 (2005).
14. D. D. Williams and R. R. Miller. Effect of water vapor on the LiOH-CO<sub>2</sub> reaction. Dynamic isothermal system. *Ind. Eng. Chem. Fundam.* **9**, 454–457 (1970).
15. I. J. M. Erkens, A. J. M. Mackus, H. C. M. Knoop, et al. Mass spectrometry study of the temperature dependence of Pt film growth by atomic layer deposition. *ECS J. Solid State Sci. Technol.* **1**, P255–P262 (2012).

16. S. B. S. Heil, J. L. van Hemmen, M. C. M. van de Sanden, et al. Reaction mechanisms during plasma-assisted atomic layer deposition of metal oxides: A case study for  $\text{Al}_2\text{O}_3$ . *J. Appl. Phys.* **103**, (2008).



## Appendix

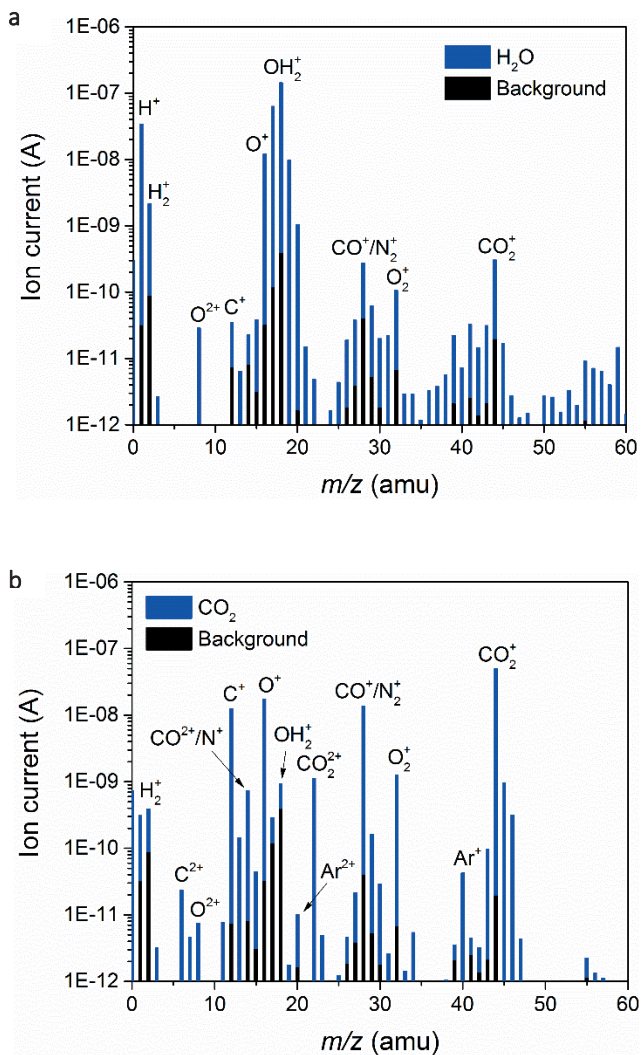
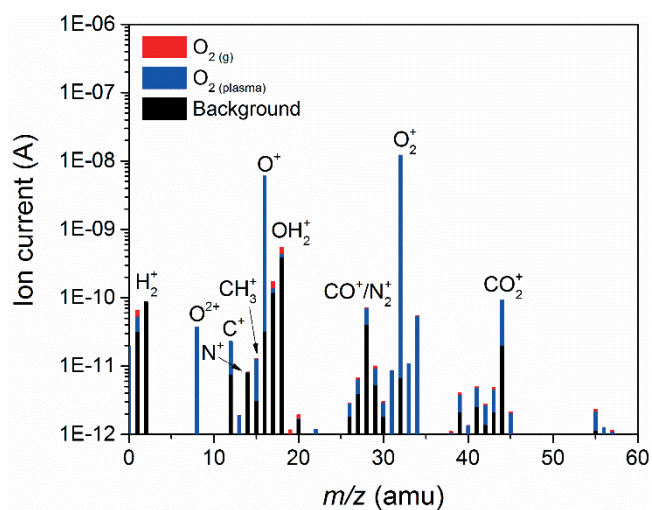
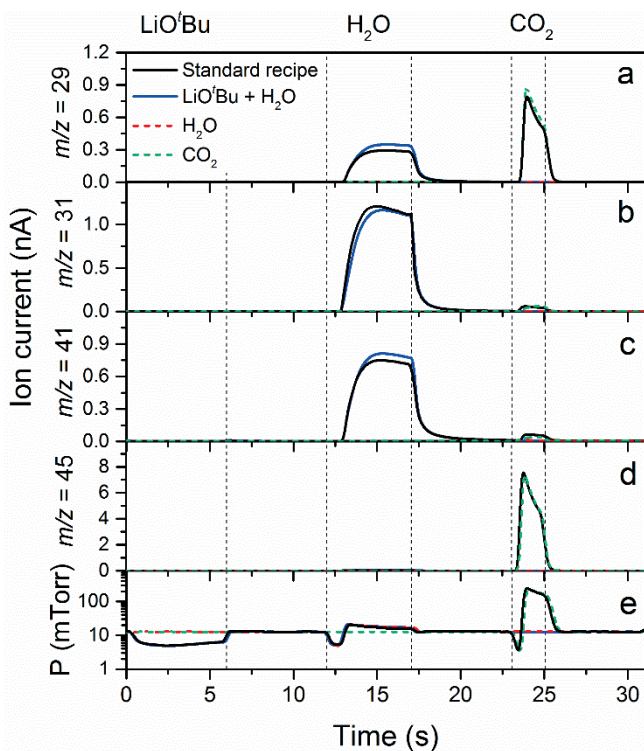


Figure S5.1 Cracking patterns obtained by mass spectrometry during a)  $\text{H}_2\text{O}$  and b)  $\text{CO}_2$  gas dose. The patterns from the reactor background are plotted in the figures for comparison.



**Figure S5.2** Cracking pattern obtained by mass spectrometry during  $\text{O}_2$  plasma ignition used for plasma-assisted ALD of  $\text{Li}_2\text{CO}_3$ . The patterns from  $\text{O}_2$  gas and the reactor background are plotted in the figure for comparison.  $\text{O}_2$  (g) and  $\text{O}_2$  (plasma) represent  $\text{O}_2$  gas and plasma excited  $\text{O}_2$ , respectively.



**Figure S5.3** Time-resolved QMS data of  $m/z = 29$  ( $\text{CHO}^+$ ), 31 (most likely  $\text{CH}_3\text{O}^+$  from *tert*-butanol or  $\text{LiO}^t\text{Bu}$ ), 41 ( $\text{C}_2\text{HO}^+$  or  $\text{C}_3\text{H}_5^+$  from *tert*-butanol or  $\text{LiO}^t\text{Bu}$ ) and 45 ( $\text{CHO}_2^+$ ) amu for thermal ALD of  $\text{Li}_2\text{CO}_3$ . The standard ALD recipe (black) is compared to the recipe with only  $\text{LiO}^t\text{Bu}$  and  $\text{H}_2\text{O}$  (blue), the recipe with only  $\text{H}_2\text{O}$  (red), and the recipe with only  $\text{CO}_2$  (green). The precursor dosing steps are alternated by argon purge steps of 6 s.

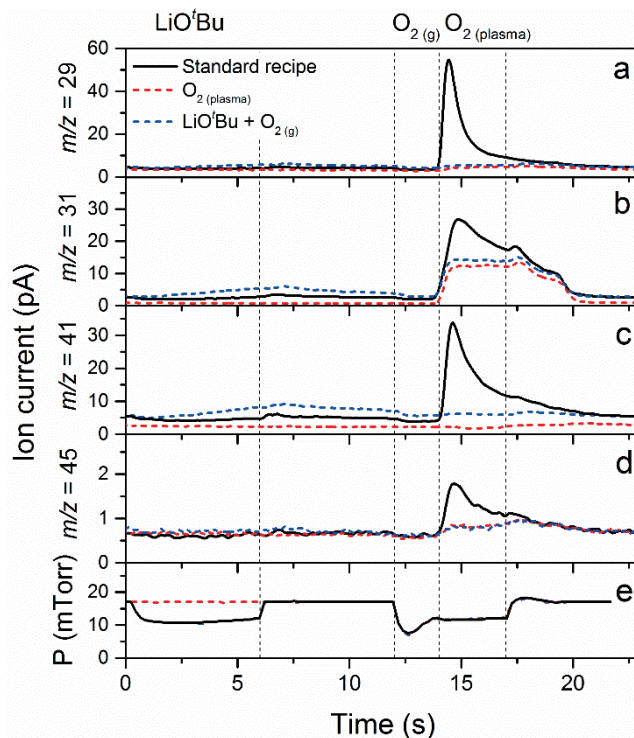


**Figure S5.4** Time-resolved QMS data for plasma-assisted ALD of  $\text{Li}_2\text{CO}_3$  following  $m/z = 29$  ( $\text{CHO}^+$ ), 31 (most likely  $\text{CH}_3\text{O}^+$  from *tert*-butanol or  $\text{LiO}^+\text{Bu}$ ), 41 ( $\text{C}_2\text{HO}^+$  or  $\text{C}_3\text{H}_5^+$  from *tert*-butanol or  $\text{LiO}^+\text{Bu}$ ) and 45 ( $\text{CHO}_2^+$ ) amu. The standard ALD recipe (black) is compared to the recipe with only  $\text{O}_2$  plasma (red), and the recipe with only  $\text{LiO}^+\text{Bu}$  and  $\text{O}_2$  gas (blue).  $\text{O}_2(\text{g})$  and  $\text{O}_2(\text{plasma})$  represent  $\text{O}_2$  gas and plasma excited  $\text{O}_2$ , respectively. The precursor dosing steps are alternated by argon purge steps of 6 s.



# 6

## ALD of LiF using $\text{LiN}(\text{SiMe}_3)_2$ and $\text{SF}_6$ plasma

---

---

Lithium fluoride films were prepared by atomic layer deposition (ALD) using a new route in which  $\text{LiN}(\text{SiMe}_3)_2$  is used as precursor and  $\text{SF}_6$  plasma as coreactant. Conformal LiF films were deposited at 150 °C at a growth rate of  $\sim 0.4 \text{ \AA}$  per cycle. All deposited films were polycrystalline and slightly lithium-rich with a composition of  $\text{LiF}_{0.8}$ , independently of the plasma conditions (e.g. exposure time, pressure and power). The levels of H, C, N, O, Si, and S were all  $< 1 \text{ at. \%}$ . Spectroscopic ellipsometry measurements were carried out over the wavelength range of 140–2480 nm and showed a refractive index of 1.37 at 633 nm for films deposited using 1 s plasma exposure time. It can be concluded that short plasma exposures are preferred, since a prolonged exposure time leads to an increase in optical absorption and lower growth per cycle values. Furthermore, mass spectrometry measurements revealed the formation of  $\text{SiMe}_3\text{F}$  species during both half-cycles, originating from the reaction between the precursor ligands and fluorine species present either at the surface or in the plasma. Moreover, the  $\text{SF}_6$  plasma step led to the formation of fluorocarbon species, suggesting that dissociation and recombination in the plasma takes place. Overall, the work in this chapter demonstrates that  $\text{SF}_6$  plasma offers a promising alternative to other coreactants for ALD of high purity lithium fluoride.

## 6.1 Introduction

Lithium fluoride (LiF) is of large scientific and technological interest because of several emerging applications. LiF films have a large electrochemical stability window of 0 - 6.4 V vs Li<sup>+</sup>/Li,<sup>1</sup> a good chemical stability,<sup>2,3</sup> and a high mechanical strength.<sup>4-6</sup> LiF has therefore gained attention for its role as an electrode protective/passivating film or as an additive to improve electrode performance in lithium ion batteries.<sup>5-7</sup> Moreover, LiF has one of the largest optical band gaps,<sup>8</sup> and has a low refractive index of 1.39 at 633 nm.<sup>9</sup> Due to these properties, LiF is useful as a protective transparent optical coating to preserve performance in the ultraviolet region of e.g. aluminum mirrors for space applications.<sup>10,11</sup> LiF has also been employed as the electron injection layer of organic light-emitting diodes.<sup>12,13</sup> Moreover, LiF has been explored as a promising electron contact layer in solar cells.<sup>14,15</sup>

So far, lithium fluoride based thin films have been deposited with various physical vapor deposition methods, including thermal and electron beam evaporation and pulsed laser deposition.<sup>3,16-18</sup> In recent years, atomic layer deposition (ALD) of LiF was demonstrated.<sup>2,5,10,19-22</sup> ALD is a thin film growth technique based on sequential and self-limiting half reactions. Its benefits of precise thickness control at sub-nanometer level and ability to deposit uniform and conformal films on high-aspect ratio and large-area substrates, are widely recognized.<sup>23</sup> These merits will enable applications of LiF such as 3D-nanostructured batteries or solar cells with a demanding surface topology. Moreover, LiF ALD cycles can be combined with ALD cycles of other materials to tune the film properties. This is the case of LiF combined with AlF<sub>3</sub> to deliver lithium aluminum fluoride, serving as e.g. solid-state Li-ion electrolyte. A literature overview of LiF ALD is presented in Table 6.1. LiF has for example been deposited using LiTMHD or LiO<sup>t</sup>Bu as lithium precursor and TiF<sub>4</sub> as coreactant (the latter also in combination with Mg(TMHD)<sub>2</sub>). Otherwise, anhydrous HF and HF-pyridine have also been adopted as the fluorine source. The combination of LiTMHD with TiF<sub>4</sub> lead to high growth per

**Table 6.1** Overview of process details collected from earlier and the present work on the ALD of lithium fluoride.

Precursor	Coreactant(s)	$T_{sub}$ (°C)	GPC (Å)	Ref.
LiTMHD <sup>a</sup>	TiF <sub>4</sub>	250 - 350	1.5 - 1.0	19
LiTMHD <sup>a</sup>	TiF <sub>4</sub> + Mg(TMHD) <sub>2</sub> <sup>a</sup>	300 - 350	1.6 - 1.4	20
LiO <sup>t</sup> Bu	TiF <sub>4</sub>	200 - 300	0.35 - 0.48	2
LiO <sup>t</sup> Bu	HF-pyridine	150	0.8	5
LiO <sup>t</sup> Bu	NH <sub>4</sub> F	150 - 300	0.35 - 0.65	22
LiN(SiMe <sub>3</sub> ) <sub>2</sub>	HF-pyridine	125 - 250	0.2 - 0.6	21
LiN(SiMe <sub>3</sub> ) <sub>2</sub>	Anhydrous HF	150	0.15	10
LiN(SiMe <sub>3</sub> ) <sub>2</sub>	SF <sub>6</sub> plasma	150	0.37	This work

<sup>a</sup>TMHD = 2,2,6,6-tetramethyl-3,5-heptanedionate.

cycle values and nearly stoichiometric films with impurity levels < 1 at. %.<sup>19</sup> However, the deposition has proven challenging, as the growth was highly dependent on the temperature gradient inside the reactor and required a relatively large LiTMHD dose to deliver uniform films. Furthermore, the films were often characterized by poor adhesion to the substrate. Although these drawbacks can be partially overcome by introducing an additional Mg(TMHD)<sub>2</sub> dose step,<sup>20</sup> the process becomes complicated. The combination of LiO<sup>t</sup>Bu and TiF<sub>4</sub> delivered much better film uniformity,<sup>2</sup> yet no ALD saturation behavior was reported. More recently, LiF has been deposited using anhydrous HF,<sup>10</sup> or a HF-pyridine solution,<sup>5,21</sup> leading to lower deposition temperatures and films with good uniformity. However, the HF precursor is potentially dangerous and corrosive, and although HF-pyridine solutions provide a safer alternative to anhydrous HF and the use of compressed gas cylinders is avoided, strict safety precautions are still required. Very recently, ALD LiF based on a less harmful chemistry, i.e. LiO<sup>t</sup>Bu and NH<sub>4</sub>F, has been reported.<sup>22</sup>

In our present work, an SF<sub>6</sub>-fed plasma is exploited as fluorine source for ALD of LiF films. SF<sub>6</sub> plasmas, as well as other F-containing plasmas such as CF<sub>4</sub> and NF<sub>3</sub>, are extensively used for etching of Si-based materials (Si, SiO<sub>2</sub>, Si<sub>3</sub>N<sub>4</sub>, etc.) and chamber cleaning. For the latter purpose, fluorine plasmas are readily available in many plasma operated ALD reactors. The use of a SF<sub>6</sub> plasma as coreactant has so far only been investigated for the deposition of AlF<sub>3</sub>.<sup>24</sup> It was demonstrated that this approach is a promising alternative to the more commonly used anhydrous HF and HF-pyridine as the F-source for ALD of AlF<sub>3</sub>. SF<sub>6</sub> is a stable, non-toxic gas which is easy to handle. Here, we combine SF<sub>6</sub> plasma with LiN(SiMe<sub>3</sub>)<sub>2</sub> as the lithium precursor. LiN(SiMe<sub>3</sub>)<sub>2</sub> has a relatively low melting point of 70 °C and it can be used in vapor draw mode. Therefore, the temperature of the precursor delivery line as well as of the walls of the vacuum chamber can be kept relatively low and line clogging is less probable. We examined the growth, film properties as well as surface reactions involved in the LiF plasma-ALD process. ALD behavior was confirmed at 150 °C and the growth rate of the films was approximately 0.4 Å per cycle. All investigated films were found slightly lithium-rich (LiF<sub>0.8</sub>) with negligible levels of impurities. From spectroscopic ellipsometry measurements it followed that films were characterized by optical absorption in the shorter wavelength range. The latter increased with the plasma exposure time. To gain more insight into the ALD growth of LiF, quadrupole mass spectrometry (QMS) studies were carried out to identify the reaction mechanisms during the two half-cycles and the similarities and differences with the thermal ALD process of LiF are highlighted.

## 6.2 Experimental

The LiF films were fabricated using the Oxford Instruments FlexAL™ thermal and remote plasma ALD reactor. The reactor consists of a rotary and turbo molecular



pump such that it can reach a base pressure of  $< 10^{-6}$  Torr by overnight pumping. The pump unit as well as the inductively coupled plasma (ICP) source are connected to the deposition chamber through gate valves.

In Figure 6.1, the ALD process developed in this work is shown. The LiF ALD cycle consists of the exposure of the substrate to  $\text{LiN}(\text{SiMe}_3)_2$  (97 %, Pegasus Chemicals) as precursor and a  $\text{SF}_6$  (99.995 %) fed plasma as coreactant. Note that in the gas phase,  $\text{LiN}(\text{SiMe}_3)_2$  is mainly present as a dimer but also a small percentage of monomers are observed.<sup>25</sup> Because of their lower coordination, monomers are expected to be more reactive than dimers and can dominate the ALD reaction mechanism. In line with previous ALD studies, only monomers are considered in this work.<sup>21,26</sup> The  $\text{LiN}(\text{SiMe}_3)_2$  dose and  $\text{SF}_6$  plasma step are alternated by Ar purges to remove all the unreacted species and reaction products from the chamber. The  $\text{LiN}(\text{SiMe}_3)_2$  precursor was kept in a stainless steel container and inserted into the chamber by vapor draw for the standard process. Also, the option to bubble the precursor with Ar carrier gas was investigated and is discussed in next section. The  $\text{LiN}(\text{SiMe}_3)_2$  precursor pod was kept at 85 °C and the supply line was heated to 120 °C to prevent precursor condensation. The power for the  $\text{SF}_6$  plasma was set to 300 W. The pressure during processing was kept constant at 50 mTorr and a 100 sccm  $\text{SF}_6$  gas flow was continuously injected from the top *via* the inductively coupled plasma (ICP) valve. It was confirmed that no film growth occurs without ignition of the plasma, indicating that  $\text{LiN}(\text{SiMe}_3)_2$  does not react with  $\text{SF}_6$  gas. The wall temperature was set to the maximum temperature of 120 °C.

Depositions were performed on a Si (100) wafer with native oxide (Siegert Wafer, 10-20 Ohm-cm) and on a Si wafer with micropillars which are 50  $\mu\text{m}$  high and have a diameter of 3  $\mu\text{m}$  and 5  $\mu\text{m}$  spacing. Since  $\text{SF}_6$  plasmas can be used for etching of Si-based materials, 10  $\text{Al}_2\text{O}_3$  ALD cycles ( $\sim 1.5$  nm) were used as a protective layer prior to LiF processing. Substrates were placed on a 200 mm carrier wafer and the table temperature was set to 150 °C.

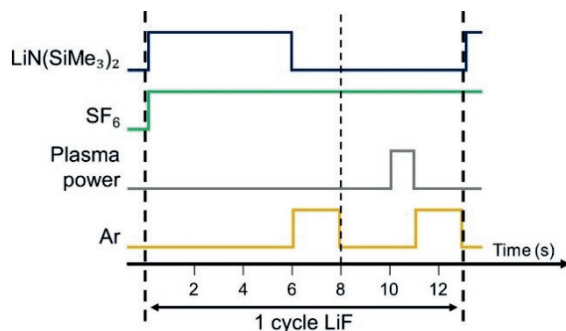


**Figure 6.1** Schematic of the pulsing sequence of the ALD cycles for LiF.

To obtain the optical properties of the LiF films over the wavelength range of 140 - 2480 nm, *ex situ* spectroscopic ellipsometry (SE) measurements were performed using vacuum ultraviolet variable angle SE (VUV-VASE) at J.A. Woollam Co., Inc. *Ex situ* measurements were performed at angles of incidence from 55–75° with steps of 5°, and photon energy steps of 0.05 eV. The SE model consisted of a combination of one Sellmeier function and Gaussian oscillator functions. The number of Gaussian oscillators needed to describe the dielectric function increased for longer plasma exposure times. The surface roughness layer was fitted using a Bruggeman effective medium approximation (EMA). Herein, the roughness layer refractive index is described as a mixture of 50 % film and 50 % voids. *Ex situ* SE was also used to probe thickness uniformity over 200 mm Si wafers. The film thickness was monitored by *in situ* SE with a J.A. Woollam, Inc. M-2000F (250 - 1000 nm) system. The results from the *ex situ* SE data were used to fit the data obtained *in situ* but without taking the surface roughness layer into account as it lead to correlation between fitting parameters. This simplification hardly affected the variation in thickness which was the only parameter extracted.

Thickness values were confirmed by high resolution SEM (Zeiss Sigma) operated at 2 kV acceleration voltage. An average of at least five measurements was taken to determine the uncertainty. SEM was also used to investigate the morphology of the deposited layers. The samples were sputter coated with a 5 nm conductive Au/Pd film prior to the SEM measurements to prevent accumulation of electrons on the sample surface.

The LiF films were also investigated by X-ray photoelectron spectroscopy (XPS).<sup>27</sup> XPS spectra were recorded by a Thermo Scientific K-Alpha+ system using monochromatic Al K $\alpha$  X-rays. The spot size of the beam was 400  $\mu$ m and the base pressure of the system was 10<sup>-6</sup> mTorr. Sensitivity values of 0.06 and 4.43 were used for composition analysis of the Li 1s and F 1s regions, respectively. These are the standard values from the database associated with the instrumentation of the Avantage XPS software. The background used to analyze the peaks is a Smart background. The Smart background is an iterative Shirley background to which a constraint has been added such that at no point a background will have a greater intensity than the actual data.<sup>28</sup>

Elastic backscattering (EBS), elastic recoil detection (ERD) and Rutherford backscattering spectroscopy (RBS) were carried out by Detect99 to determine the composition and mass density of the films. A 2000 keV He<sup>+</sup> beam was applied for both ERD and RBS. ERD was performed to determine the hydrogen content using 75° sample tilt and the detector at a recoil angle of 25°. For determination of the other elements, RBS was performed with perpendicular incidence and in channeling mode to reduce the background under the Li, C and O features and with two detectors, at scattering angles of 170° and 107°. EBS was necessary for a more accurate determination of the Li content in the films. Here, a 2800 keV proton beam was used

in combination with glancing angle geometry to enhance the Li peak area to (Si) background height; also here the sample was tilted by 75°. The scattering angle was 170° in Cornell geometry. For all ion beam techniques, the product of the number of incident particles with the opening angle of the detector has been determined using a beam chopper. The product was calibrated using a reference sample of known composition and thickness. In the case of EBS and RBS, the reference sample was a 100 nm Ni layer on c-Si. For ERD it was a 180 nm Si<sub>3</sub>N<sub>4</sub> layer containing 3.4 at. % H. For each sample, the two RBS spectra were simulated simultaneously with the EBS spectrum by NDF (Nuno's DataFurnace), a computer code for IBA data fitting.<sup>29</sup> For the EBS simulations, <sup>7</sup>Li and <sup>19</sup>F cross sections of Paneta et al. have been used.<sup>30</sup> In the rest of the paper we refer to the combination of RBS, EBS and ERD as ion beam analysis (IBA). The crystal structure of the layers was determined using a Philips X'Pert MPD diffractometer equipped with a Cu K $\alpha$  source (1.54 Å radiation).

A Pfeiffer Vacuum mass spectrometer with a mass-to-charge ( $m/z$ ) range of 100 atomic mass units (amu) was connected to the deposition chamber through a pipeline and a 150  $\mu$ m diameter pinhole. The system is equipped with a Channeltron detector and the energy of the electrons in the ionizer was set to 70 eV. The pressure in the QMS was maintained below 10<sup>-6</sup> Torr using differential pumping with a turbomolecular pump. Prior to every measurement the background signal and pressure of the reactor were measured as a reference. The measuring time per atomic mass unit (amu) was set to 200 ms. For the time-resolved measurements, the selected  $m/z$  values were tracked per channel using a dwell time of 50 ms. The QMS data of at least 10 cycles were monitored to verify that steady-state values were achieved. The measurement procedure is explained more extensively in previous chapter.<sup>31</sup>

## 6.3 Results and discussion

### 6.3.1 ALD process

Film growth of ALD LiF was examined by *in situ* SE using a deposition temperature of 150 °C. In Figure 6.2 the film thickness is shown as a function of the number of cycles. The first 50 cycles show a slightly enhanced growth compared to the steady growth regime. This can be due to an initial growth effect, but it can also originate from the fitting procedure to extract the thickness from the ellipsometry data. In the fit, the optical properties of the film have been assumed constant throughout the whole thickness but this assumption is not necessarily accurate. The growth per cycle is  $\sim 0.4$  Å, which is in the range of reported literature values for processes which use LiN(SiMe<sub>3</sub>)<sub>2</sub> as the lithium precursor.<sup>10,21</sup> The growth was also monitored after each half-cycle, as shown in the inset of Figure 6.2. The magnitude of the changes in this “apparent” thickness after the precursor and SF<sub>6</sub> plasma steps do not necessarily reflect the real change in physical thickness because the top surface is not included in the model. The inset shows that, after the LiN(SiMe<sub>3</sub>)<sub>2</sub> dosing, the apparent thickness

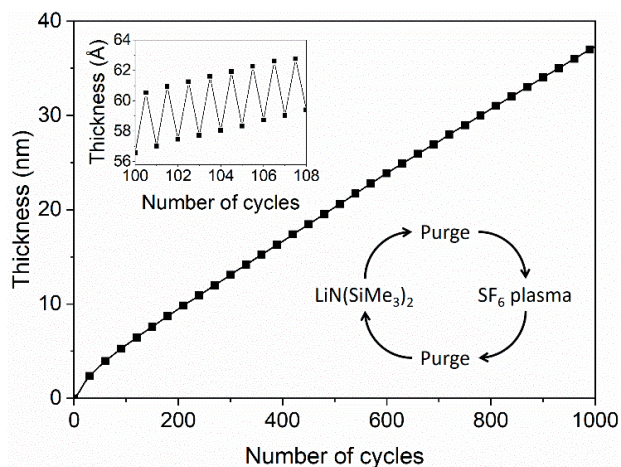


**Figure 6.2** Film thickness as a function of the number of cycles measured by *in situ* spectroscopic ellipsometry for ALD of lithium fluoride using a 6 s  $\text{LiN}(\text{SiMe}_3)_2$  dose and 1 s plasma exposure at 150 °C. The inset shows the apparent thickness measured every half-cycle.

increases by several angstroms, because of the chemisorption of the precursor on the surface. After the  $\text{SF}_6$  plasma step, the apparent thickness decreases, because of the removal of the organic ligands. It can be expected that the precursor ligands are abstracted, and the surface is then terminated with fluorine. The reaction mechanism is further discussed in Section 6.3.3.

In Figure 6.3, the saturation curves for the ALD process of LiF are shown. The growth per cycle was determined as a function of the  $\text{LiN}(\text{SiMe}_3)_2$  dosing time,  $\text{SF}_6$  plasma exposure time and purge times. The saturation of the pressure during the  $\text{LiN}(\text{SiMe}_3)_2$  dose and plasma power are reported in Figure S6.1. To extract the growth per cycle, the film thickness was monitored every 10 cycles while changing the dose time of the reagents, pressure or argon purge. The self-limiting behavior of the  $\text{LiN}(\text{SiMe}_3)_2$  dosing time was tested with and without the use of an Ar carrier gas Figure 6.3a). In some cases, the use of an Ar carrier gas could lead to the decrease of the precursor saturation time. However, no difference was observed for our process, meaning that the vapor pressure of the precursor is high enough to dose a sufficient amount of precursor in the reactor and avoid the use of a carrier gas. The growth per cycle *versus*  $\text{LiN}(\text{SiMe}_3)_2$  dosing time shows a so-called soft saturation behavior. A  $\text{LiN}(\text{SiMe}_3)_2$  dosing time of 6 s was selected for the recipe. A purge step of 2 s was enough to remove the reaction products and unreacted precursor molecules from the chamber. Extending the purge time did not change the growth per cycle value. Figure 6.3b reports the growth per cycle as a function of the plasma exposure time. After an initial increase, the growth per cycle decreases again for extended plasma exposure times. Such a particular trend, which was confirmed by SEM analysis (the

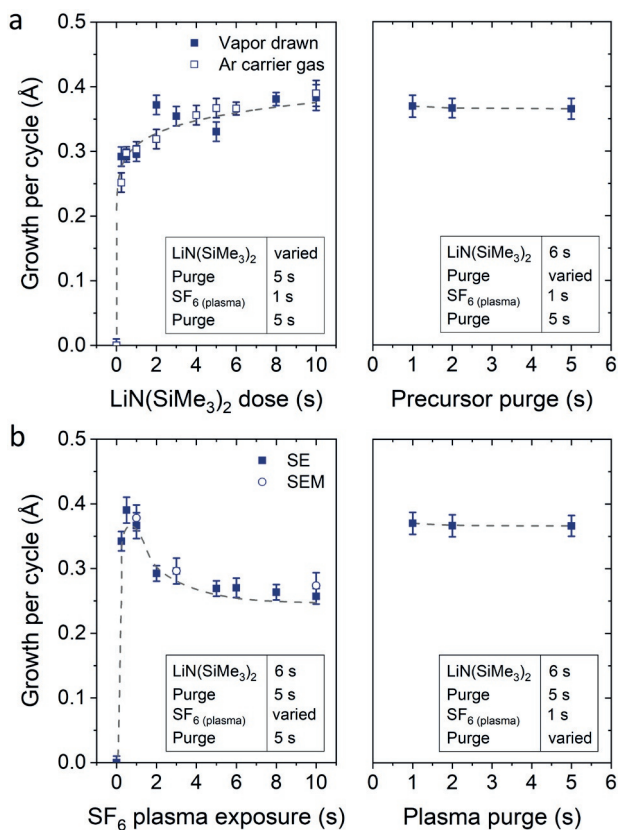


**Figure 6.3** Growth per cycle obtained by SE as a function of a) precursor dose and purge and b) plasma exposure and purge for ALD of LiF obtained at 150 °C. The precursor dose was investigated with and without the use of Ar carrier gas. The SE data in b) were compared to SEM data (diamond symbols). The dotted lines serve as a guide to the eye.

corresponding SE measurements and SEM images can be found in Figure S6.2 and Figure S6.3, respectively) has been observed more often for plasma-ALD processes.<sup>32</sup> It can be attributed to several potential causes such as an etching effect playing a role for long plasma exposure times or inhibition of precursor adsorption after exposing the surface for a longer time to F radicals. Another likely cause is that the film properties are affected by the length of the plasma exposure time which has subsequently an effect on the growth itself. As will be addressed in the next section, the optical absorption of the films changes quite significantly for long exposure times showing that the film properties are affected. For the standard recipe, 1 s plasma exposure was selected. Also for the plasma half-cycle a purge step of 2 s was sufficient to remove the reaction products and unreacted molecules from the chamber. Relatively short cycle times of 13 s were defined for the standard process of LiF ALD

films (Figure 6.1). It is worth reporting that the effect of pressure during the precursor and plasma exposure steps and the effect of plasma power were also investigated. A pressure increase above 50 mTorr during precursor exposure did not lead to any increase in growth per cycle (Figure S6.1). Moreover, the  $\text{SF}_6$  plasma was only stable when the pressure was 50 mTorr or higher. Therefore, a pressure of 50 mTorr was selected for the process. Adjusting the plasma power did not affect the growth per cycle (Figure S6.1).

To further demonstrate the ALD behavior of the LiF process, the uniformity and conformality were investigated. For both studies the standard recipe was used. Film thickness and refractive index uniformity were determined for a  $\sim 90$  nm thick film using *ex situ* SE on various points of films deposited on a 200 mm wafer. The measured thicknesses and refractive indices are presented in Table S6.1. The non-uniformity (standard deviation, 1 sigma) of the thickness and refractive indices were determined to be 4.4 % and 0.2 %, respectively. This points to rather good uniformity of film

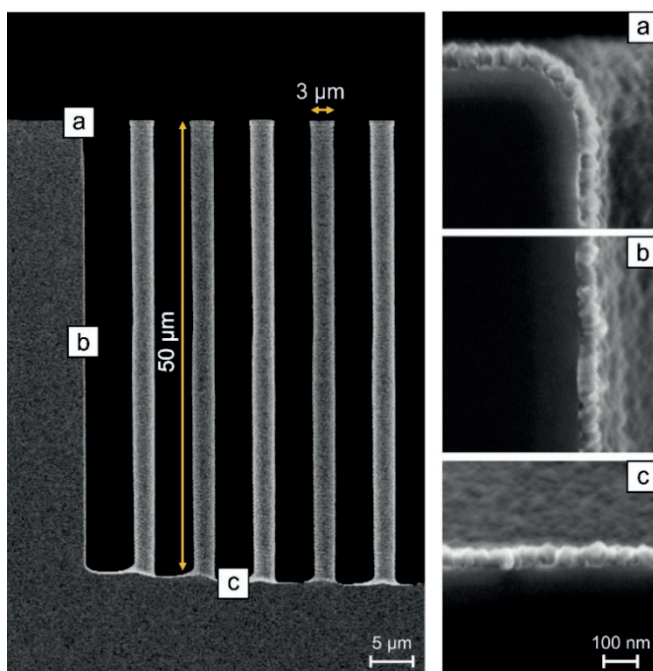


**Figure 6.4** Analysis of the conformality of the LiF ALD process. Micropillars of 50  $\mu\text{m}$  high and a diameter of 3  $\mu\text{m}$  are used for this purpose. On top of the pillars a 60 nm layer of LiF was deposited. Images a), b) and c) show the LiF layer at respectively the top, middle and bottom of the pillars. Thickness variations from 57–62 nm were observed. The scale bar of 100 nm applies to all insets.

thickness and excellent uniformity of the refractive index. However, the process parameters were optimized for the growth per cycle value and not for film uniformity. Therefore, the thickness uniformity can probably still be improved. The conformality of the deposition was studied using SEM at different positions on high aspect ratio Si pillars. The Si pillars were covered with a LiF layer of approximately 60 nm. Figure 6.4 shows three SEM pictures taken at different heights along the pillar. Image “a” is taken at the top of the pillars and shows a LiF layer of  $62 \pm 2$  nm. Image “b” is taken at half-length of the pillar and depicts a  $60 \pm 2$  nm LiF layer (96 % of thickness at top). At the bottom (c), the LiF film is  $57 \pm 2$  nm thick (93 %). From these measurements we can conclude that a conformal coating on high aspect ratio pillars was achieved.

### 6.3.2 Film properties

XPS measurements were carried out to analyze the chemical composition of the LiF films. A survey spectrum can be found in the appendix (Figure S6.4). In Figure 6.5, the XPS core level spectra of C 1s, Li 1s, and F 1s are shown for 40 nm thick films prepared at 150 °C using 1 s plasma exposure time. The spectra for different plasma exposures are very similar and therefore not shown here. The binding energy scale was calibrated using the C 1s peak at 284.8 eV, associated with adventitious carbon on the sample surface. The Li 1s peak and F 1s peak are observed at 55.5 eV and 685.1 eV, respectively, both in close agreement with literature reports for LiF films.<sup>33</sup> A sputtering procedure was adopted to investigate the stoichiometry of the film. In contrast to our previous XPS studies of  $\text{Li}_2\text{CO}_3$ ,<sup>34</sup> the stoichiometry of the films did not change during depth profiling. The obtained LiF stoichiometry of the film is 54.4 at. % Li, 44.3 at. % F, 0.3 at. % C and 0.4 at. % O. Hence, the films deposited in this work are found to be lithium-rich with a stoichiometry of  $\text{LiF}_{0.8}$ . The obtained stoichiometry falls in the range of values reported for ALD LiF films, which have a F/Li ratio of 0.73 to 1.23.<sup>5,10,19–22</sup> Carbon and oxygen were only found at the surface of the films. The atomic percentages of Si, N and S were below the detection limit of the XPS. Literature

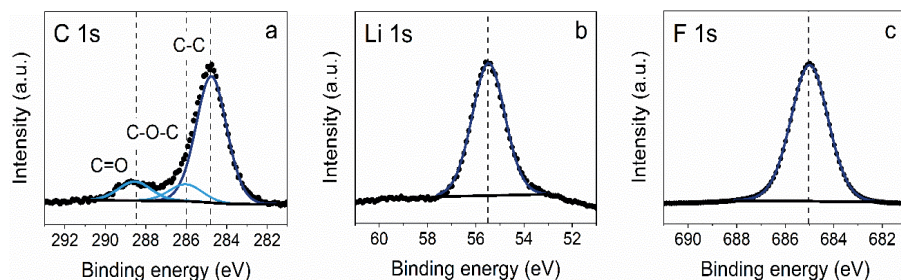


**Figure 6.5** a) C 1s, b) Li 1s, and c) F 1s spectra of a 40 nm thick lithium fluoride film grown at 150 °C using 1 s plasma exposure time. The measured data (black dotted lines) and fitted peaks (blue lines) are reported. Carbon is detected only at the surface of the films.

has also reported the absence of impurities originating from the selected precursor or coreactant. However, in some cases the presence of traces of oxygen or hydrogen was reported.<sup>2,5</sup> In addition, LiF films deposited using longer plasma exposure times were probed by XPS, since these films differ in terms of film growth as shown in the previous section. It was found that the stoichiometry of the films is rather independent of plasma exposure time. These results and a comparison of the stoichiometry of the films for surface scans and during depth profiling can be found in Table S6.2 in the appendix. The influence of pressure and plasma power on the film stoichiometry were also investigated, but no changes in stoichiometry were observed (not shown here). Moreover, film composition did not show noticeable changes after storage in atmosphere for one month (see appendix, Figure S6.5). This also holds for the film thickness as well as the mass density and roughness which will be discussed later. These results suggest that LiF grown by ALD is stable under ambient conditions.

A combination of ion beam techniques, which are nondestructive and give accurate quantitative information, was used to complement the aforementioned XPS data.<sup>35</sup> In addition, these techniques allow to probe also the hydrogen content in the film. LiF films deposited using different SF<sub>6</sub> plasma exposure times were studied and the results are shown in Table 6.2. The original experimental and simulated data are reported in the appendix (Figure S6.6). The films are lithium rich and of high purity, in line with previous XPS studies. The IBA data also show that the total number of deposited atoms per cycle in a nm<sup>2</sup> decreases for longer plasma exposure times. Previously, in Figure 6.3b, it was shown that the growth per cycle in terms of thickness also decreases for longer plasma exposure times. This means that the thickness decrease observed for longer plasma exposure times is caused by an actual decrease in deposited LiF per cycle. According to the trend in the SE and SEM data, a further decrease in growth per cycle would be expected when prolonging the plasma exposure to 3 and 10 s. From the IBA data this decrease is not confirmed.

A combination of the IBA and SE data was used to calculate the mass density of the samples. From IBA measurements the areal number density of a specific atom (atoms per nm<sup>2</sup>) was extracted. The areal densities were multiplied with the mass of the atoms under consideration and after summation the mass density was obtained

**Table 6.2** Properties of 40 nm thick LiF films prepared using plasma exposure times of 1, 3 and 10 s. The stoichiometry was calculated from IBA results. The mass density was obtained by combining IBA and SE results. In the first row the typical error is given for a certain parameter.

Sample	Li at. nm <sup>-2</sup> · cycle <sup>-1</sup>	F at. nm <sup>-2</sup> · cycle <sup>-1</sup>	F/Li	[H] (at. %)	[O] (at. %)	[C] (at. %)	Density (g · cm <sup>-3</sup> )
1 s plasma	2.0 ± 0.1	1.6 ± 0.1	0.78	1.0 ± 0.1	0.8 ± 0.1	0.1 ± 0.1	2.3 ± 0.1
3 s plasma	1.6	1.3	0.83	0.8	1.1	0.9	2.3
10 s plasma	1.6	1.2	0.75	1.1	0.9	1.3	2.3



by dividing by the film thickness. The mass density for all LiF films was found to be  $\sim 2.3 \text{ g} \cdot \text{cm}^{-3}$ . The bulk value of the mass density of stoichiometric LiF reported in the literature is  $2.6 \text{ g} \cdot \text{cm}^{-3}$ .<sup>36</sup> Typically, thin films prepared by ALD or other techniques are reported to have a somewhat lower mass density compared to the bulk material. Differences in mass density probably also exist due to the sub-stoichiometric nature measured for our LiF films.

The deposited films were studied by XRD for various plasma exposure times. Figure 6.6 shows the X-ray diffractograms of  $\sim 40 \text{ nm}$  thick films obtained using a  $\theta$ - $2\theta$  Bragg-Brentano geometry. The  $\theta$ - $2\theta$  measurements, which detect periodicity of planes parallel to the surface, show only the typical diffraction peak of crystalline LiF at  $38.7^\circ$ .<sup>37</sup> The small peak near  $44^\circ$  originates from the sample holder. This means that the process yields a preferential crystal growth orientation in the  $\langle 111 \rangle$  direction. The FWHM and intensity of the peak at  $38.7^\circ$  do not change for different plasma exposure times within the measurement error. This means that film crystallinity does not significantly depend on the plasma exposure time. The LiF films prepared by thermal ALD reported in the literature also showed crystalline features, although in most studies no preferential growth orientation was reported.<sup>2,5,10,19–21</sup> There is only one study on thermal ALD LiF reporting on a preferential crystal growth orientation in the  $\langle 200 \rangle$  direction.<sup>22</sup> The origin of the preferential crystal growth orientation and therefore also the difference between the preferential crystal growth orientation of the thermal LiF process and our plasma based process is unclear.

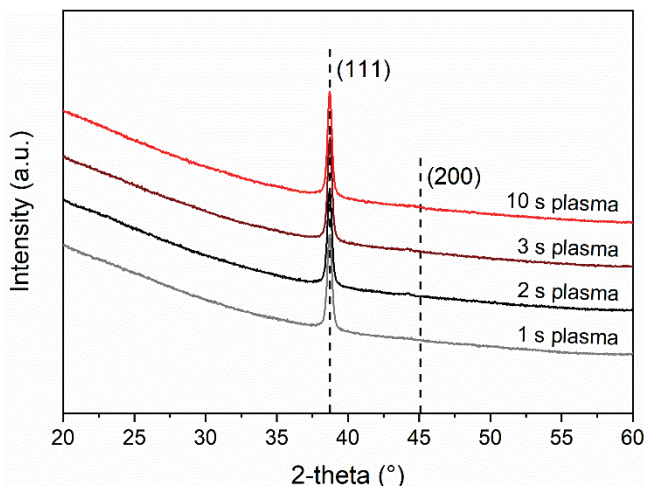
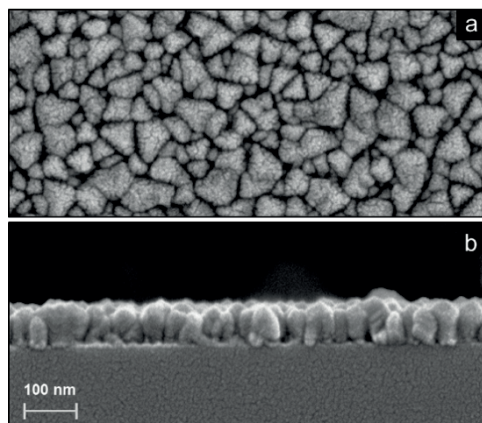


**Figure 6.6** XRD  $\theta$ - $2\theta$  scans of  $\sim 40 \text{ nm}$  thick LiF films grown on Si. LiF films are deposited using plasma exposure times of 1, 2, 3 and 10 s. The dotted lines indicate the positions of the expected diffraction for LiF powder samples.

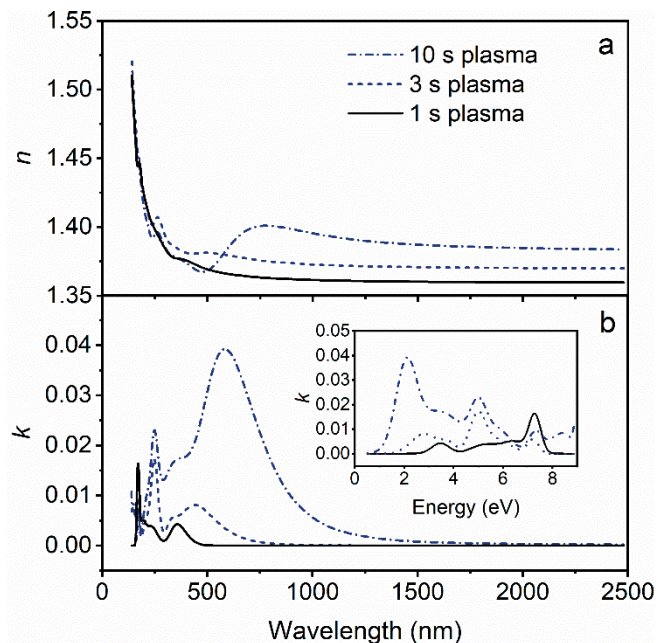
Figure 6.7 shows high resolution SEM images of a 70 nm LiF film deposited using a 1 s plasma dose on top of a Si substrate. The crystallites exhibit a size comparable to the sample thickness and seem to have a triangular shape. Longer plasma exposure times lead to similar results. From the height difference observed in the cross sectional image in Figure 6.7b, it can be concluded that there is significant surface roughness. The presence of surface roughness was confirmed by *ex situ* SE measurements. The surface roughness was relatively high, being  $\sim 10$  nm for each of the films.

Figure 6.8 shows the optical properties as obtained from vacuum ultraviolet (VUV) SE measurements for LiF films deposited at 150 °C using different plasma dosing times. As shown in Figure 6.8a, the refractive index ( $n$ ) is 1.37 at 633 nm and shows a relatively low dispersion for the film deposited using 1 s plasma exposure. At 633 nm the refractive indices are 1.38 and 1.39 for 3 s and 10 s plasma exposure, respectively. The refractive index values for LiF films prepared by thermal ALD using HF and  $\text{TiF}_4$  as coreactants vary from 1.37-1.39 and are thus in agreement with our findings.<sup>5,19,21</sup>

As observed from Figure 6.8b, absorption occurs in a rather broad range of wavelength. However, LiF films are well known for their large optical band gap and high transparency. The LiF films deposited in this work are slightly sub-stoichiometric ( $\text{LiF}_{0.8}$ ). Anionic vacancies can lead to the formation of lattice defects. DFT studies in the literature show that when F vacancies occur, new energy levels develop which may affect the band-gap.<sup>38</sup> However, valence band XPS spectrum analysis (Figure S6.7) shows features at 29-30 eV and 8-10 eV, independent of the plasma exposure time, and in line with literature of stoichiometric LiF.<sup>39</sup> It should be noted that



**Figure 6.7** a) High resolution SEM images showing the surface topography and b) cross-section of a LiF film deposited on Si using a 1 s  $\text{SF}_6$  plasma exposure. The scale bar applies to both images.



**Figure 6.8** Refractive index ( $n$ ) and extinction coefficient ( $k$ ) as a function of wavelength as determined from VUV-SE for 40 nm thick films deposited using 1, 3 and 10 s  $\text{SF}_6$  plasma exposure. The inset shows the extinction coefficient as a function of photon energy.

the band gap itself cannot be determined from the VUV-SE data since it lies outside the measured energy range of 8.8 eV. Finally, we consider the possibility that the plasma environment can play a role in the formation of this absorption features. Specifically, it has been shown that when LiF is irradiated with ions,<sup>40,41</sup> electrons,<sup>42</sup> or even (V)UV radiation emitted from discharges,<sup>43</sup> color centers can be produced. The most dominant defects which can be created in LiF are F centers (an electron localized at a fluorine vacancy).<sup>41</sup> As observed from the absorption spectra Figure 6.8b, the absorption features become dominant and extend to longer wavelengths upon increasing the  $\text{SF}_6$  plasma exposure time from 1 to 10 s. Since the film stoichiometry is the same, independently of the plasma exposure time, we consider it plausible to attribute the presence of the absorption features to changes caused by plasma radiation. This conclusion is also supported by the fact that no absorption features are reported for thermal ALD of LiF.<sup>2,19–21</sup> Instead, literature studies of  $\text{AlF}_3$  films prepared by ALD using an  $\text{SF}_6$  plasma also show absorption features in the lower wavelength range.<sup>24</sup>

### 6.3.3 Surface reactions

The gas phase reaction products were analyzed by mass spectrometry to gain insight into the surface reactions occurring during the ALD process. Specifically, we would like to highlight the similarities and differences between the thermal ALD process when using HF, and the SF<sub>6</sub> plasma based LiF ALD process developed in this work. A study on the surface reactions of thermal ALD of LiF with LiN(SiMe<sub>3</sub>)<sub>2</sub> as precursor and HF-pyridine as coreactant was already presented in the literature.<sup>21</sup> Herein, it was reported that LiN(SiMe<sub>3</sub>)<sub>2</sub> molecules can either physisorb or chemisorb during the first half-cycle. Physisorption of LiN(SiMe<sub>3</sub>)<sub>2</sub> on LiF was attributed to strong interactions of Si and N in LiN(SiMe<sub>3</sub>)<sub>2</sub> with F and Li in LiF, respectively. During the second half-cycle, the surface is exposed to HF to promote ligand abstraction from the physisorbed LiN(SiMe<sub>3</sub>)<sub>2</sub> molecules and form LiF. Specifically, the precursor ligands on the surface were abstracted in the form of SiMe<sub>3</sub>F and NH<sub>3</sub>. However, it was reported that if physisorbed HF is present, the precursor ligand could instead chemisorb and already lose its ligands, i.e. LiF would be formed already during the precursor dosing step.<sup>21,44</sup> Compared to other metal fluorides, which are shown to adsorb a significant amount of HF after HF exposure, the amount of adsorbed HF on LiF is expected to be limited because of the Lewis base nature of LiF.<sup>44</sup> LiF would rather act as a F<sup>-</sup> ion donor. Despite the presence of peaks at  $m/z = 77$  (SiMe<sub>2</sub>F<sup>+</sup> from SiMe<sub>3</sub>F) and  $m/z = 17$  (NH<sub>3</sub><sup>+</sup> from NH<sub>3</sub>) in the mass spectrometer at the end of the precursor step, the authors concluded with a complementary quartz crystal microbalance (QCM) study that the precursor ligands are indeed primarily abstracted during the HF exposure. Moreover, they concluded that at higher deposition temperatures (> 200 °C) the ligand abstraction during the precursor step is suppressed because of the limited physisorbed HF on the LiF surface.

To gain insight into the species present in the reactor during the LiF plasma-ALD process, the spectra during precursor dosing and SF<sub>6</sub> plasma ignition were measured in the range of  $m/z = 1-100$  as shown in Figure 6.9. In Figure 6.9a the cracking pattern of the LiN(SiMe<sub>3</sub>)<sub>2</sub> precursor is shown. Note that the peak from the parent molecule itself and the peaks with the highest expected intensity (146, 130, and 147 amu, respectively) could not be measured since they lie outside the range of the mass spectrometer.<sup>45,46</sup> The peak with the highest intensity within the explored mass range is located at 65.5 amu, and its width would suggest there are multiple contributions to it.<sup>26,45</sup> We expect that the  $m/z$  of 65 amu corresponds with the double ionized species from  $m/z = 130$  (N(SiMe<sub>2</sub>)<sub>2</sub><sup>+</sup>), and the  $m/z$  of 65.5 corresponds with the double ionized species from  $m/z = 131$  (HN(SiMe<sub>2</sub>)<sub>2</sub><sup>+</sup>).<sup>26,47</sup> Figure 6.9b shows the spectra of SF<sub>6</sub> plasma and SF<sub>6</sub> gas, which are essentially identical in terms of detected species. As expected, the peaks during SF<sub>6</sub> plasma exposure are lower than the SF<sub>6</sub> gas spectrum due to dissociation in the plasma. All measured species are ion fragments of SF<sub>6</sub>. Note that again the parent molecule itself (SF<sub>6</sub>) could not be measured since it lies at  $m/z = 146$ . Instead, SF<sub>3</sub><sup>+</sup> at  $m/z = 89$  was tracked to measure SF<sub>6</sub>.

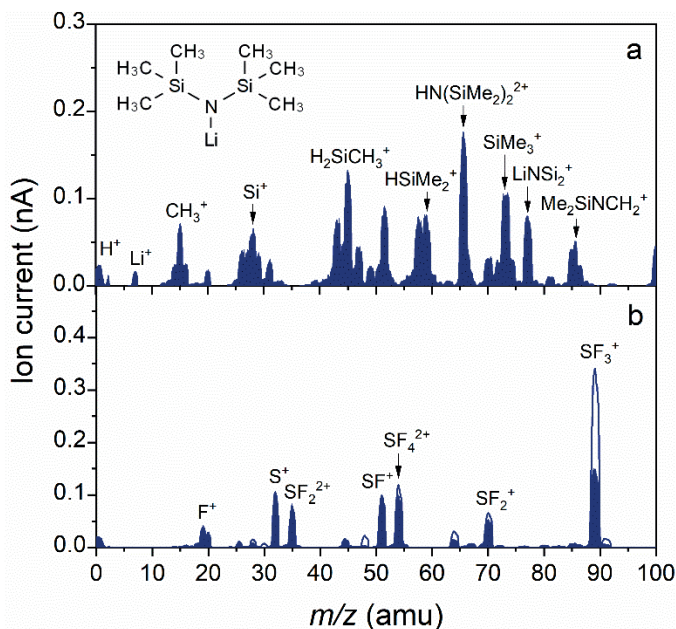


**Figure 6.9** Ionization pattern obtained by mass spectrometry during a) LiN(SiMe<sub>3</sub>)<sub>2</sub> precursor dosing, and b) SF<sub>6</sub> plasma ignition (filled curves). In a) also the LiN(SiMe<sub>3</sub>)<sub>2</sub> precursor molecule is depicted. The ionization pattern for the SF<sub>6</sub> gas (plasma off) is also added (open curve).

A complete overview of the measured species is presented in Table S6.3 in the appendix. Figure 6.10 presents a selection of these species, which are followed during one cycle of LiF. In Figure 6.10a-e, the following masses are considered:  $m/z = 17$  (NH<sub>3</sub><sup>+</sup> from NH<sub>3</sub>), 65.5 (from LiN(SiMe<sub>3</sub>)<sub>2</sub> or HN(SiMe<sub>3</sub>)<sub>2</sub>), 69 (CF<sub>3</sub><sup>+</sup> from CF<sub>4</sub> or CHF<sub>3</sub>), 77 (SiMe<sub>2</sub>F<sup>+</sup> from SiMe<sub>3</sub>F or SiMe<sub>2</sub>F<sub>2</sub> and LiNSi<sub>2</sub><sup>+</sup> from LiN(SiMe<sub>3</sub>)<sub>2</sub>) and 85 (SiF<sub>3</sub><sup>+</sup> from SiF<sub>4</sub> or SiMeF<sub>3</sub> and Me<sub>2</sub>SiNCH<sup>+</sup> from LiN(SiMe<sub>3</sub>)<sub>2</sub>). Note that  $m/z = 77$  is the largest peak in the mass spectrum of SiMe<sub>3</sub>F, whereas the peak at  $m/z = 92$  (SiMe<sub>3</sub>F<sup>+</sup>) has negligible intensity.<sup>46</sup> Additional mass-to-charge ratios 15 (CH<sub>3</sub><sup>+</sup>), 31 (CF<sup>+</sup>), 33 (CH<sub>2</sub>F<sup>+</sup> or SH<sup>+</sup>), 34 (CH<sub>3</sub>F<sup>+</sup> or H<sub>2</sub>S<sup>+</sup>), 50 (CF<sub>2</sub><sup>+</sup>), 51 (CHF<sub>2</sub><sup>+</sup>), and 81 (SiMeF<sub>2</sub><sup>+</sup> from SiMeF<sub>3</sub> or SiMe<sub>2</sub>F<sub>2</sub>) amu can be found in the appendix in Figure S6.8. Also, the pressure in the system was monitored and reported in Figure 6.10f. The graph is divided into several sections representing the different ALD process steps, i.e., LiN(SiMe<sub>3</sub>)<sub>2</sub> dose and SF<sub>6</sub> plasma exposure, which are alternated by Ar purging. Compared to the ALD recipe for LiF described earlier, all purge steps are now extended to 5 s to clearly separate the process steps and facilitate data interpretation. (As shown in Figure 6.3, extended purge times did not influence the process.) In addition to the standard ALD recipe, in Figure 6.10 the data are also reported for recipes where one of the reagents is omitted from the recipe. For these recipes no ALD growth occurred, and the data is

reported after 10 cycles so that steady-state values were achieved. Therefore, it is possible to distinguish the reaction products from other species present in the reactor and fragmentation and ionization occurring in the mass spectrometer. In every plot three different curves are shown, corresponding with the following recipes: the standard recipe, the recipe with only  $\text{LiN}(\text{SiMe}_3)_2$  and  $\text{SF}_6$  gas (no plasma), and the recipe with only  $\text{SF}_6$  plasma.

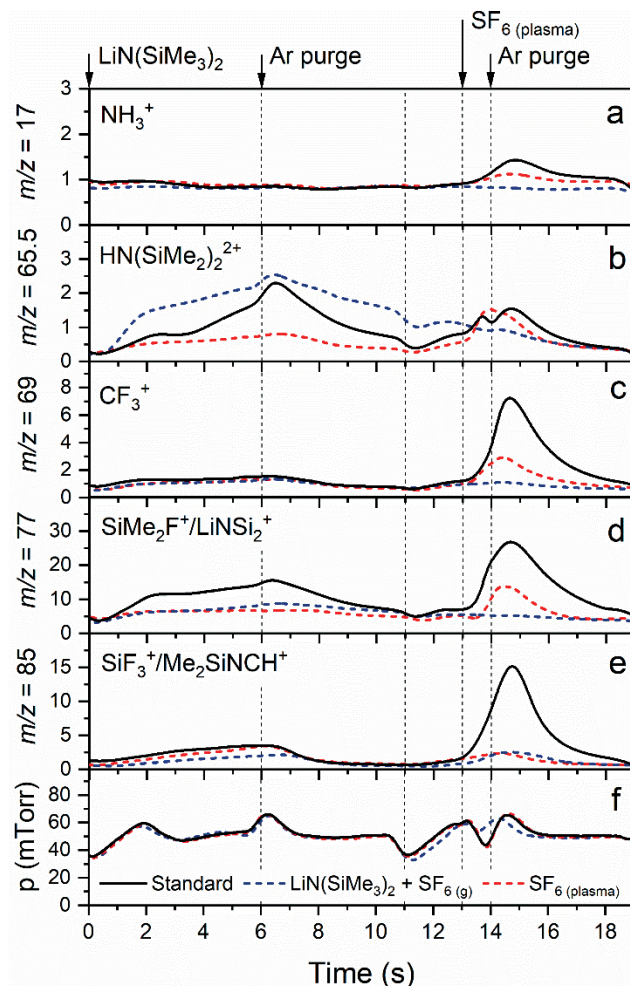
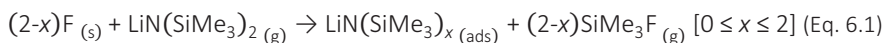


**Figure 6.10** Time-resolved QMS data of  $m/z = 17$ , 65.5, 69, 77 and 85 amu after 10 cycles. Only the ion with the highest intensity contribution is indicated in the figure. The standard ALD recipe (black) is compared to the  $\text{LiN}(\text{SiMe}_3)_2 + \text{SF}_6$  recipe (blue dotted) and  $\text{SF}_6$  plasma recipe (red dotted). The precursor and coreactant dosing steps are alternated by argon purge steps of 5 s.

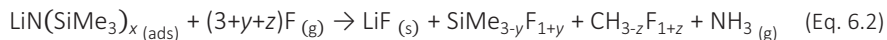
In the first half-cycle the lithium precursor was introduced in the chamber which led to an increase in signal at  $m/z = 65.5$  for the standard recipe as well as for the  $\text{LiN}(\text{SiMe}_3)_2 + \text{SF}_6$  (g) recipe, as expected. The peak at  $m/z = 65.5$  is smaller in the case of the ALD process compared to the  $\text{LiN}(\text{SiMe}_3)_2 + \text{SF}_6$  (g) recipe. We attribute this observation to precursor adsorption and reaction with the surface in the case of the ALD process, whereas for the  $\text{LiN}(\text{SiMe}_3)_2 + \text{SF}_6$  (g) recipe the surface was already saturated with Li-precursor. Also a signal at  $m/z = 77$  was observed during the  $\text{LiN}(\text{SiMe}_3)_2$  dose. The standard ALD recipe has a higher signal compared to the other recipes, pointing out that this is a reaction product of the Li-precursor with the surface, promoted by the presence of F- species on the LiF surface. As mentioned before, this reaction product was also found in the mass spectrometer for the thermal ALD LiF process at 150 °C, although in combination with  $\text{NH}_3$ .<sup>21</sup>

In the second half-cycle the surface is exposed to  $\text{SF}_6$  plasma. Note that from the QMS measurements no clear evidence of sulfur-containing reaction products was observed. The signal at  $m/z = 34$  (Figure S6.8) could however also originate from  $\text{H}_2\text{S}$  species formed in the plasma. Furthermore, no S is detected in the film. The dominant neutral species in an inductively coupled  $\text{SF}_6$  plasma are known to be  $\text{SF}_6$ , F,  $\text{F}_2$ , and  $\text{SF}_4$ , while the dominations are  $\text{SF}_5^+$  and  $\text{F}^+$ .<sup>48–50</sup> The concentration of S and  $\text{S}^+$  is typically a factor  $10^3$  lower than the concentration of F and  $\text{F}^+$ .<sup>50</sup> Moreover, it is known that F is very reactive due to its very high electronegativity and electron affinity.<sup>51</sup> Therefore, it is reasonable to assume that only F takes part in the surface reactions. During this half-cycle again peaks at  $m/z = 65.5$  and 77 were observed, as well as a peak at  $m/z = 17$  ( $\text{NH}_3^+$ ). Also other fluoromethylsilane species and fluorocarbons were found. Specifically, reaction products at  $m/z = 85$  ( $\text{SiF}_3^+$  from  $\text{SiF}_4$  or  $\text{SiMeF}_3$ ) and  $m/z = 69$  ( $\text{CF}_3^+$  from  $\text{CF}_4$  or  $\text{CHF}_3$ ) were observed. As shown in Figure S6.8 in the appendix, reaction products at  $m/z = 81$  ( $\text{SiMeF}_2^+$  from  $\text{SiMeF}_3$  or  $\text{SiMe}_2\text{F}_2$ ),  $m/z = 50$  ( $\text{CF}_2^+$ ) and  $m/z = 31$  ( $\text{CF}^+$ ) were observed. Moreover, relatively small peaks at  $m/z = 33$  and 34 assigned to  $\text{CH}_2\text{F}^+$  and  $\text{CH}_3\text{F}^+$  were found. It can be observed that all masses reported in Figure 6.10 (except 65.5 amu, which corresponds with the precursor molecule) show a higher intensity during the second half-cycle with respect to the first half-cycle. This indicates that ALD surface reaction products are primarily generated during the plasma exposure.

To summarize the findings from the QMS studies in the first and second half-cycles: a fraction of the precursor molecules that adsorb at the surface already loses one of its ligands during the  $\text{LiN}(\text{SiMe}_3)_2$  dose step. The remaining Li-precursor ligands are abstracted during the plasma step. Moreover, the reaction products can be further dissociated in the plasma leading to e.g. fluorocarbon species. The following reaction is proposed for the precursor dose, where the adsorbed precursor can undergo partial loss of ligands:



During the SF<sub>6</sub> plasma exposure step, the fluorine plasma species remove the remaining precursor ligands to form LiF. The equation is unbalanced for simplicity as the surface species and the ratio of the reaction products are unknown at this point:



Our results seem to differ from those of thermal ALD of LiF reported in literature. Unlike thermal ALD, a reasonable fraction of the precursor molecules already loses ligands during the first half-cycle. Moreover, in the case of thermal ALD, the reaction during the first half-cycle was explained by the presence of surface adsorbed HF. As mentioned before, LiF is a Lewis base that can share the lone pairs on F. Therefore, we consider it more likely that F from LiF would be partly consumed in the ALD reaction during the first half-cycle. This could also explain why our films are slightly F-deficient. Moreover, unlike thermal ALD LiF, additional fluoromethylsilane and fluorocarbons are detected in the second half-cycle. Most likely dissociation and recombination in the SF<sub>6</sub> plasma takes place.

## 6.4 Conclusions

A new ALD chemistry has been demonstrated to prepare LiF films using LiN(SiMe<sub>3</sub>)<sub>2</sub> and SF<sub>6</sub> plasma. Self-limiting growth was obtained at ~ 0.4 Å per cycle and conformal coverage of high aspect ratio pillars was achieved for deposition at 150 °C. Moreover, high purity films were obtained with contamination levels < 1 at. %. The obtained stoichiometry of the films was LiF<sub>0.8</sub> as determined by IBA and XPS measurements. Furthermore, the ALD process yields polycrystalline films with preferential growth in the <111> direction. The film density was 2.3 g · cm<sup>-3</sup>. Within the measurement error, no deviation in film stoichiometry, crystallinity or density was found for the plasma conditions studied. When a plasma exposure of 1 s was used, the refractive index at 633 nm was 1.37. Despite the fact that LiF is well-known to be transparent, some optical absorption was found in the films. Prolongation of the plasma exposure time leads to an increase in optical absorption while the stoichiometry is unchanged. We therefore consider it plausible to attribute the presence of the absorption features to the interaction of the SF<sub>6</sub> plasma with the film. Also lower growth per cycle values were obtained for longer plasma exposure times, and therefore short plasma exposure times are preferred. It is expected that the optical properties can be further optimized by modifying the plasma conditions. To gain more insight into the deposition process, also QMS measurements were performed. From the detected species it could be concluded the LiN(SiMe<sub>3</sub>)<sub>2</sub> ligand already partly dissociates during the precursor dosing step. In contrast to thermal ALD, additional formation of different fluoromethylsilane and fluorocarbon species was observed during the SF<sub>6</sub> plasma exposure step. Most likely the SF<sub>6</sub> plasma species promote the abstraction of the remaining ligands and their subsequent dissociation in the plasma. Overall, this



work demonstrates that the easy-to-handle and readily-available SF<sub>6</sub> plasma is a promising alternative to coreactants such as TiF<sub>4</sub>, or HF-pyridine for ALD of lithium fluorides.

## **Acknowledgements**

This project is financially supported by ADEM, A green Deal in Energy Materials of the Ministry of Economic Affairs of The Netherlands. We gratefully acknowledge Cristian van Helvoirt for technical assistance. In addition, the authors would like to thank Pegasus Chemicals for providing the lithium precursor. Moreover, M.C. acknowledges the NWO Aspasia program.

## References

1. W. D. Richards, L. J. Miara, Y. Wang, et al. Interface stability in solid-state batteries. *Chem. Mater.* **28**, 266–273 (2016).
2. J. Xie, A. D. Sendek, E. D. Cubuk, et al. Atomic layer deposition of stable LiAlF<sub>4</sub> lithium ion conductive interfacial layer for stable cathode cycling. *ACS Nano* **11**, 7019–7027 (2017).
3. M. Kumar, S. A. Khan, P. Rajput, et al. Size effect on electronic sputtering of LiF thin films. *J. Appl. Phys.* **102**, 083510 (2007).
4. L. S. Combes, S. S. Ballard and K. A. McCarthy. Mechanical and thermal properties of certain optical crystalline materials. *J. Opt. Soc. Am.* **41**, 215–222 (1951).
5. L. Chen, K. S. Chen, X. Chen, et al. Novel ALD chemistry enabled low-temperature synthesis of lithium fluoride coatings for durable lithium anodes. *ACS Appl. Mater. Interfaces* **10**, 26972–26981 (2018).
6. J. Xie, L. Liao, Y. Gong, et al. Stitching h-BN by atomic layer deposition of LiF as a stable interface for lithium metal anode. *Sci. Adv.* **3**, eaao3170 (2017).
7. S. Choudhury and L. A. Archer. Lithium fluoride additives for stable cycling of lithium batteries at high current densities. *Adv. Electron. Mater.* **2**, 1500246 (2016).
8. D. M. Roessler and W. C. Walker. Electronic spectrum of crystalline lithium fluoride. *J. Phys. Chem. Solids* **28**, 1507–1515 (1967).
9. H. H. Li. Refractive index of alkali halides and its wavelength and temperature derivatives. *J. Phys. Chem. Ref. Data* **5**, 329–528 (1976).
10. J. Hennessy and S. Nikzad. Atomic layer deposition of lithium fluoride optical coatings for the ultraviolet. *Inorganics* **6**, 46 (2018).
11. B. Fleming, M. Quijada, J. Hennessy, et al. Advanced environmentally resistant lithium fluoride mirror coatings for the next generation of broadband space observatories. *Appl. Opt.* **56**, 9941–9950 (2017).
12. Y. Kim. Power-law-type electron injection through lithium fluoride nanolayers in phosphorescence organic light-emitting devices. *Nanotechnology* **19**, 355207 (2008).
13. L. S. Hung, C. W. Tang and M. G. Mason. Enhanced electron injection in organic electroluminescence devices using an Al/LiF electrode. *Appl. Phys. Lett.* **70**, 152–154 (1997).
14. S. E. Shaheen, C. J. Brabec, N. S. Sariciftci, et al. 2.5% efficient organic plastic solar cells. *Appl. Phys. Lett.* **78**, 841–843 (2001).
15. J. Bullock, P. Zheng, Q. Jeangros, et al. Lithium fluoride based electron contacts for high efficiency n-type crystalline silicon solar cells. *Adv. Energy Mater.* **6**, 1600241 (2016).

16. T. Oi and K. Miyauchi. Amorphous thin film ionic conductors of  $m\text{LiF}\cdot n\text{AlF}_3$ . *Mater. Res. Bull.* **16**, 1281–1289 (1981).
17. L. G. Schulz. The structure and growth of evaporation LiF and NaCl films on amorphous substrates. *J. Chem. Phys.* **17**, 1153–1162 (1949).
18. S. J. Henley, M. N. R. Ashfold and S. R. J. Pearce. The structure and composition of lithium fluoride films grown by off-axis pulsed laser ablation. *Appl. Surf. Sci.* **217**, 68–77 (2003).
19. M. Mantymaki, J. Hamalainen, E. Puukilainen, et al. Atomic layer deposition of LiF thin films from Lithd and TiF4 precursors. *Chem. Vap. Depos.* **19**, 111–116 (2013).
20. M. Mantymaki, J. Hamalainen, E. Puukilainen, et al. Atomic layer deposition of LiF thin films from Lithd, Mg(thd)<sub>2</sub>, and TiF4 precursors. *Chem. Mater.* **25**, 1656–1663 (2013).
21. Y. Lee, D. M. Piper, A. S. Cavanagh, et al. Atomic layer deposition of LiF and lithium ion conducting (AlF<sub>3</sub>)(LiF)<sub>x</sub> alloys using trimethylaluminum, lithium hexamethyldisilazide and hydrogen fluoride. *ChemRxiv* 1–37 (2017).
22. J. N. Kvalvik, K. B. Kvamme, K. Almaas, et al. LiF by atomic layer deposition—Made easy. *J. Vac. Sci. Technol. A* **38**, 050401 (2020).
23. S. M. George. Atomic layer deposition: An overview. *Chem. Rev.* **110**, 111–131 (2010).
24. M. F. J. Vos, H. C. M. Knoop, R. A. Synowicki, et al. Atomic layer deposition of aluminum fluoride using Al(CH<sub>3</sub>)<sub>3</sub> and SF<sub>6</sub> plasma. *Appl. Phys. Lett.* **111**, 113105 (2017).
25. T. Fjeldberg, M. F. Lappert and A. J. Thorne. The molecular structure of dimeric bis(trimethylsilyl)amidolithium, [LiN(Si(CH<sub>3</sub>)<sub>3</sub>)<sub>2</sub>]<sub>2</sub>, as determined by gas-phase electron diffraction. *J. Mol. Struct.* **125**, 265–275 (1984).
26. Y. Tomczak, K. Knapas, M. Sundberg, et al. In situ reaction mechanism studies on lithium hexadimethyldisilazide and ozone atomic layer deposition process for lithium silicate. *J. Phys. Chem. C* **117**, 14241–14246 (2013).
27. C. R. Brundle, B. V. Crist and P. S. Bagus. Accuracy limitations for composition analysis by XPS using relative peak intensities: LiF as an example. *J. Vac. Sci. Technol. A* **39**, 013202 (2021).
28. M. H. Engelhard, D. R. Baer, A. Herrera-Gomez, et al. Introductory guide to backgrounds in XPS spectra and their impact on determining peak intensities. *J. Vac. Sci. Technol. A* **38**, 063203 (2020).
29. N. P. Barradas and C. Jeynes. Advanced physics and algorithms in the IBA DataFurnace. *Nucl. Instruments Methods Phys. Res. B* **266**, 1875–1879 (2008).
30. V. Paneta, A. Kafkarkou, M. Kokkoris, et al. Differential cross-section measurements for the <sup>7</sup>Li(p,p 0) <sup>7</sup>Li, <sup>7</sup>Li(p,p 1) <sup>7</sup>Li, <sup>7</sup>Li(p,α 0) <sup>4</sup>He, <sup>19</sup>F(p,p 0) <sup>19</sup>F, <sup>19</sup>F(p,α 0) <sup>16</sup>O and <sup>19</sup>F(p,α 1,2) <sup>16</sup>O reactions. *Nucl. Instruments Methods Phys. Res. B* **288**, 53–59 (2012).

31. N. Hornsveld, W. M. M. Kessels and M. Creatore. Mass spectrometry study of Li<sub>2</sub>CO<sub>3</sub> film growth by thermal and plasma-assisted atomic layer deposition. *J. Phys. Chem. C* **123**, 4109–4115 (2019).
32. H. C. M. Knoop, E. M. J. Braeken, K. de Peuter, et al. Atomic layer deposition of silicon nitride from bis(tert-butylamino)silane and N<sub>2</sub> plasma. *ACS Appl. Mater. Interfaces* **7**, 19857–19862 (2015).
33. W. E. Morgan, J. R. Van Wazer and W. J. Stec. Inner-orbital photoelectron spectroscopy of the alkali metal halides, perchlorates, phosphates, and pyrophosphates. *J. Am. Chem. Soc.* **95**, 751–755 (1973).
34. N. Hornsveld, B. Put, W. M. M. Kessels, et al. Plasma-assisted and thermal atomic layer deposition of electrochemically active Li<sub>2</sub>CO<sub>3</sub>. *RSC Adv.* **7**, 41359–41368 (2017).
35. C. Jeynes, N. P. Barradas and E. Szilágyi. Accurate determination of quantity of material in thin films by Rutherford backscattering spectrometry. *Anal. Chem.* **84**, 6061–6069 (2012).
36. D. R. Lide. *CRC Handbook of Chemistry and Physics*. (CRC Press, 2005).
37. M. E. Straumanis. The precision determination of lattice constants by the powder and rotating crystal methods and applications. *J. Appl. Phys.* **20**, 726–734 (1949).
38. H. Sadeghi, M. R. Jalali, S. Mohammadi, et al. The electronic structure properties of defect centers in LiF and LiF:Mg quantum dot and thermo-luminescent process. *J. Basic Appl. Sci. Res.* **3**, 806–814 (2013).
39. S. Leroy, H. Martinez, R. Dedryvère, et al. Influence of the lithium salt nature over the surface film formation on a graphite electrode in Li-ion batteries: An XPS study. *Appl. Surf. Sci.* **253**, 4895–4905 (2007).
40. L. H. Abu-Hassan and P. D. Townsend. Ion implantation in LiF to form F and F<sub>2</sub> centres. *J. Phys. C Solid State Phys.* **19**, 99–110 (1986).
41. K. Schwartz, C. Trautmann, A. S. El-Said, et al. Color-center creation in LiF under irradiation with swift heavy ions: Dependence on energy loss and fluence. *Phys. Rev. B* **70**, 184104 (2004).
42. G. Baldacchini, G. d’Auria, R. M. Montecali, et al. Colour centres induced in LiF by low-energy electrons. *J. Phys. Condens. Matter* **10**, 857–867 (1998).
43. P. Warneck. LiF color-center formation and uv transmission losses from argon and hydrogen discharges. *J. Opt. Soc. Am.* **55**, 921–925 (1965).
44. Y. Lee, H. Sun, M. J. Young, et al. Atomic layer deposition of metal fluorides using HF-pyridine as the fluorine precursor. *Chem. Mater.* **28**, 2022–2032 (2016).
45. A. G. Sharkey, R. A. Friedel and S. H. Langer. Mass spectra of trimethylsilyl derivatives. *Anal. Chem.* **29**, 770–776 (1957).
46. NIST Mass Spectrometry Data Center. Mass spectra. in *NIST Chemistry WebBook, NIST Standard Reference Database Number 69* (eds. Mallard, P. J. & Linstrom, W. G.) (National Institute of Standards and Technology, 2020).

47. J. Tamás and P. Miklós. Mass spectrometric study of hexamethyldisilazane and some of its N-substituted derivatives. *Org. Mass Spectrom.* **10**, 859–866 (1975).
48. S.-J. Oh, H.-C. Lee and C.-W. Chung. A study on plasma parameters in Ar/SF6 inductively coupled plasma. *Phys. Plasmas* **24**, 013512 (2017).
49. G. Kokkoris, A. Panagiotopoulos, A. Goodyear, et al. A global model for SF6 plasmas coupling reaction kinetics in the gas phase and on the surface of the reactor walls. *J. Phys. D. Appl. Phys.* **42**, 055209 (2009).
50. M. Mao, Y. N. Wang and A. Bogaerts. Numerical study of the plasma chemistry in inductively coupled SF6 and SF6/Ar plasmas used for deep silicon etching applications. *J. Phys. D. Appl. Phys.* **44**, 435202 (2011).
51. Y.-R. Luo. *Comprehensive Handbook of Chemical Bond Energies*. (CRC Press, 2007).

## Appendix

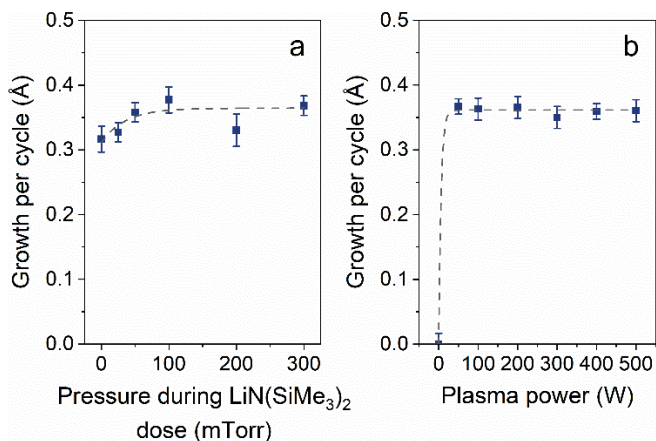


**Figure S6.1** Growth per cycle obtained by *in situ* SE as a function of a) pressure during  $\text{LiN}(\text{SiMe}_3)_2$  dose and b)  $\text{SF}_6$  plasma power for ALD of LiF obtained at 150 °C. The precursor dose time was set to 6 s and the plasma exposure time was set to 1 s. The plasma power was set to 300 W when the pressure during  $\text{LiN}(\text{SiMe}_3)_2$  dose was varied and the pressure during  $\text{LiN}(\text{SiMe}_3)_2$  dose was set to 50 mTorr when the plasma power was varied. The dotted lines serves as a guide to the eye.

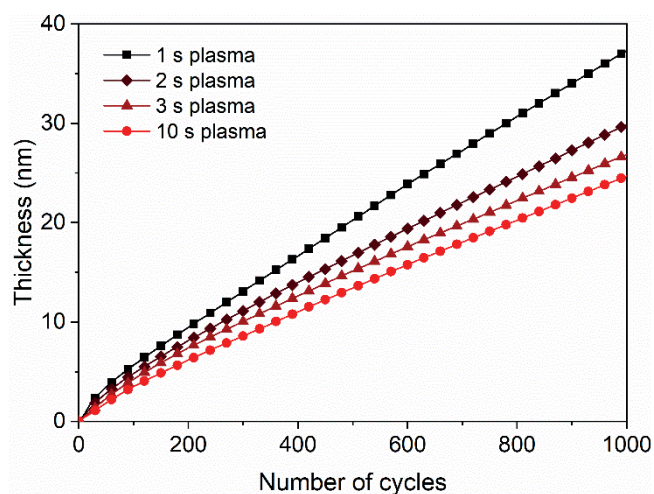


**Figure S6.2** Film thickness as a function of cycle number for different plasma exposure times measured by *in situ* SE. The dosing time of the  $\text{LiN}(\text{SiMe}_3)_2$  precursor was set to 6 s.

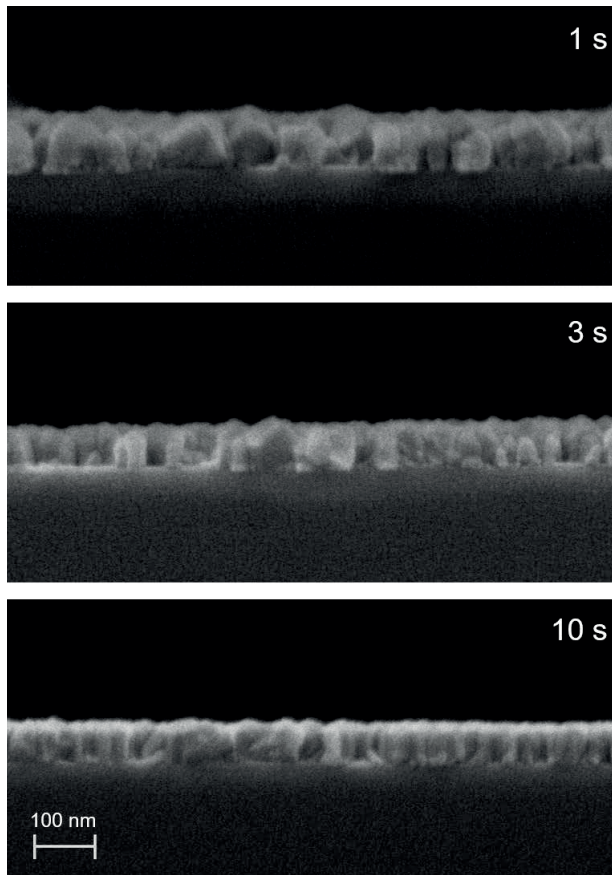


**Figure S6.3** High resolution SEM images showing the cross-section of LiF films deposited on Si using 2200 cycles and a 1 s, 3 s and 10 s  $\text{SF}_6$  plasma exposure, respectively. The scale bar applies to all images.

**Table S6.1** Thicknesses and refractive index values on various locations of a 200 mm wafer with a 90 nm LiF film prepared using a plasma exposure time of 1 s. The centre of the wafer is defined as (0,0). In the first row the typical error is given for the thickness and refractive index.

Position		Thickness (nm)	Refractive index $n$ at 633 nm
$x$ (mm)	$y$ (mm)		
-100	0	$92.0 \pm 0.5$	$1.375 \pm 0.005$
-50	0	89.5	1.370
0	0	90.0	1.375
50	0	85.5	1.375
100	0	80.0	1.375
0	100	85.0	1.375
0	50	88.5	1.380
0	-50	87.0	1.370
0	-100	85.5	1.370

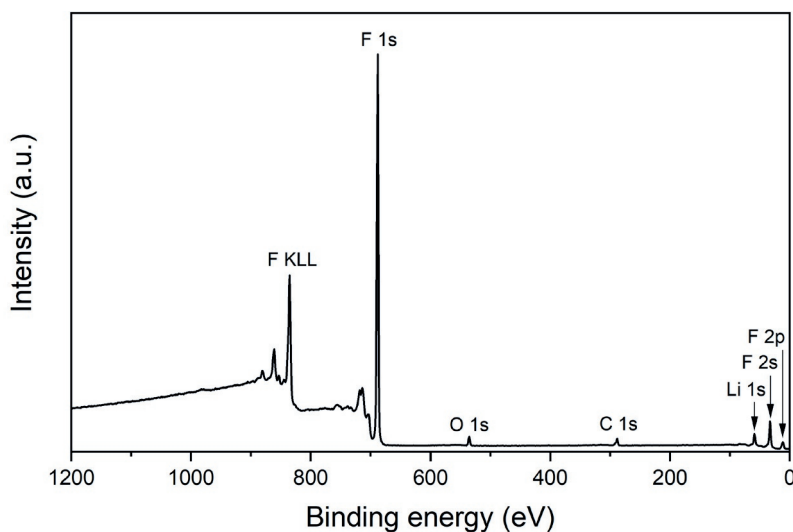
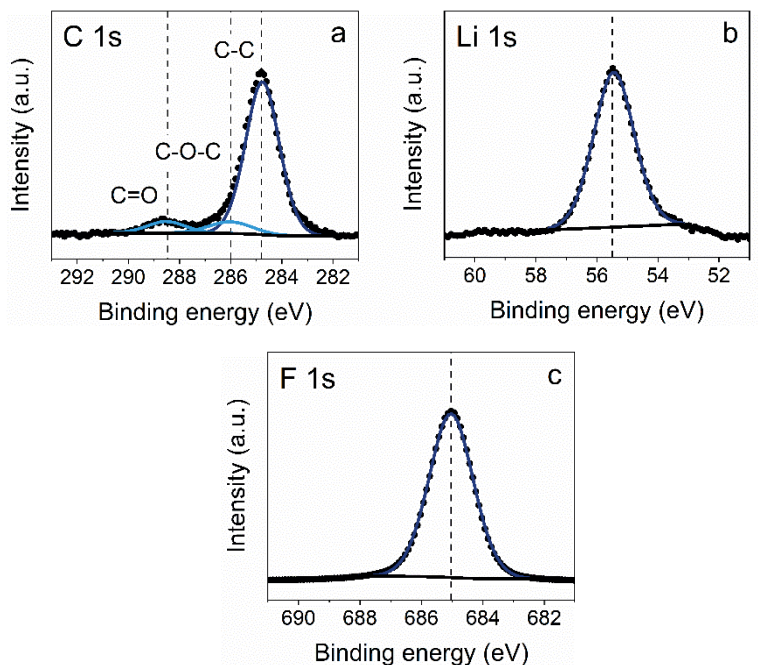


**Figure S6.4** XPS survey spectrum of a lithium fluoride film grown at 150 °C using 1 s plasma exposure. The spectra for 3 s and 10 s plasma exposure are very similar and are therefore not shown.

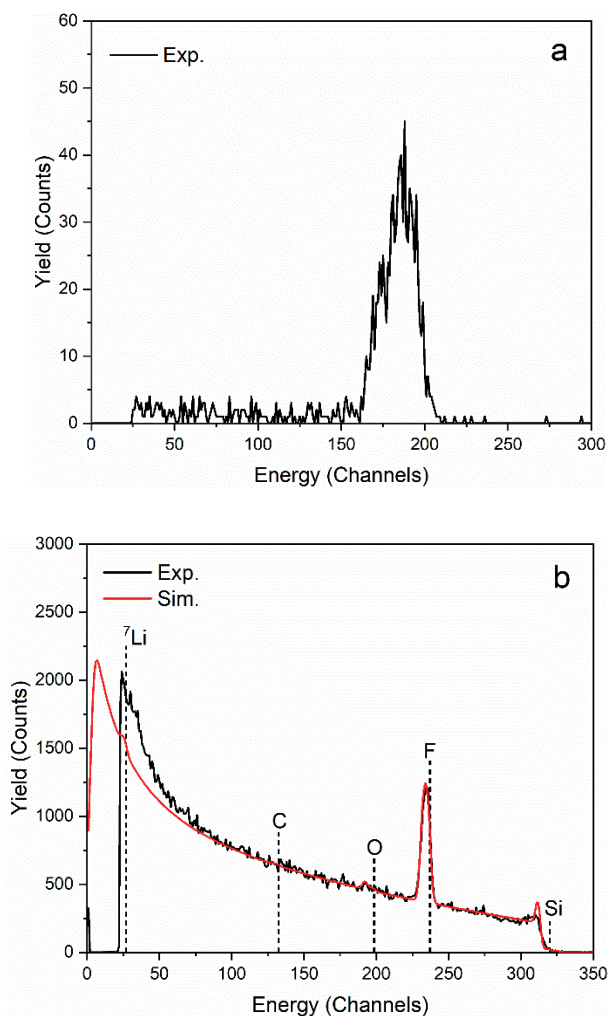


**Table S6.2** Stoichiometry of LiF films deposited at 150 °C using different plasma exposure

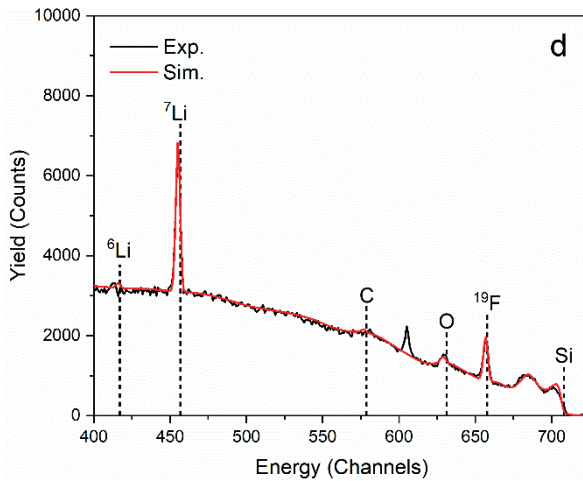
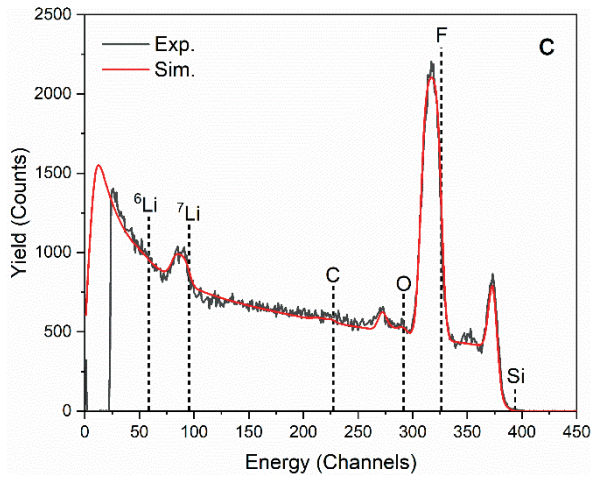
Sample	F/Li	C (at%)	O (at%)	H (at%)
1 s plasma duration				
XPS surface	0.80	9.0 ± 0.5	4.5 ± 0.5	-
XPS depth profiling	0.81	0.5 ± 0.5	0.5 ± 0.5	-
RBS/ERD	0.78	0.8 ± 0.1	1.1 ± 0.1	0.9 ± 0.1
3 s plasma duration				
XPS surface	0.80	6.0 ± 0.5	4.0 ± 0.5	-
XPS depth profiling	0.82	0.5 ± 0.5	0.5 ± 0.5	-
RBS/ERD	0.83	0.9 ± 0.1	1.1 ± 0.1	0.8 ± 0.1
10 s plasma duration				
XPS surface	0.80	6.5 ± 0.5	7.0 ± 0.5	-
XPS depth profiling	0.80	0.5 ± 0.5	0.5 ± 0.5	-
RBS/ERD	0.75	1.3 ± 0.1	0.9 ± 0.1	0.7 ± 0.1

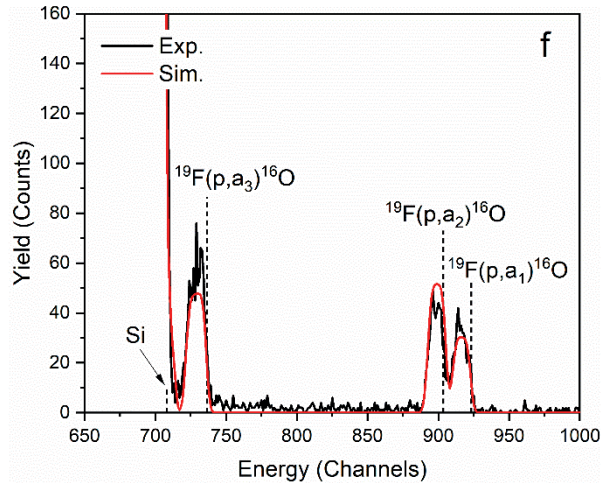
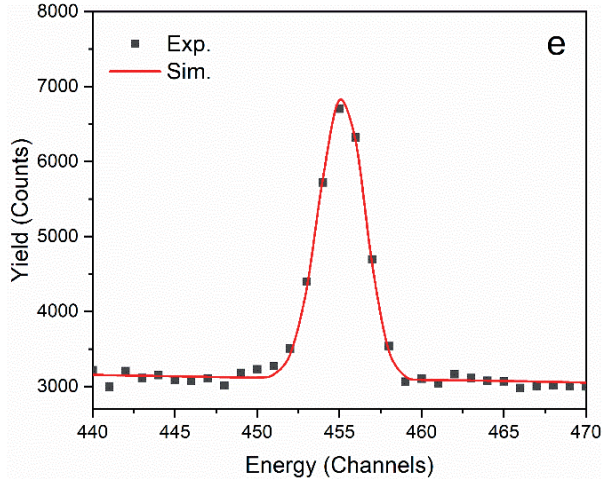


**Figure S6.5** a) C 1s, b) Li 1s, and c) F 1s spectra of a 40 nm thick lithium fluoride film grown at 150 °C using 1 s plasma exposure time after storage in atmosphere for one month. The measured data (black dotted lines) and fitted peaks (blue lines) are reported. Carbon is detected only at the surface of the films.



**Figure S6.6** Spectra from 40 nm LiF deposited at 150 °C using 3 s plasma exposure as measured with a) Elastic Recoil Detection (ERD), b-c) Rutherford Backscattering Spectrometry (RBS) at 170° and 107° respectively, and d-f) Elastic Backscattering Spectrometry (EBS). The experimental spectra are plotted in black and the simulated spectra in red. Figure e) shows the  $^7\text{Li}$  peak in detail and f) zooms in on three peaks originating from nuclear reactions with  $^{19}\text{F}$ . The 107° RBS spectrum c) also shows a significant Li peak which is in line with the EBS result. The EBS spectrum shows a peak between the C and O peak which is not simulated. The origin of this peak is unclear, although its position is close to the nitrogen surface channel. RBS clearly shows the absence of N in the films. Note that the spectra for 1 s and 10 s plasma exposure are very similar and are therefore not shown.





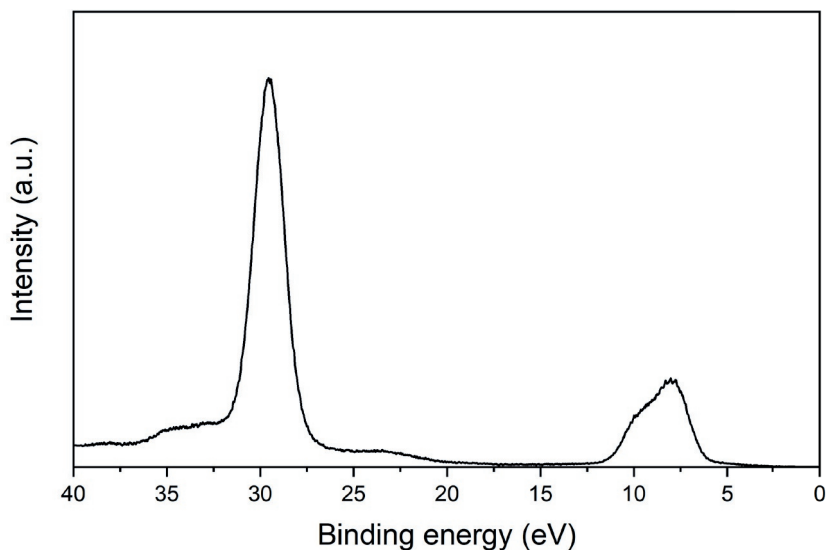


**Figure S6.7** XPS valence band spectrum of a LiF film grown at 150 °C using 1 s plasma exposure. The spectra for 3 s and 10 s plasma exposure are very similar and are therefore not shown.

**Table S6.3** Relevant  $m/z$  ratios, their assigned ions and their (main) assigned parent molecules.

$m/z$	Assigned ions	Assigned parent species
15	$\text{CH}_3^+$	$\text{CH}_3\text{F}$ , $\text{CH}_4$
16	$\text{CH}_4^+$	$\text{CH}_4$
17	$\text{NH}_3^+$	$\text{NH}_3$
20	$\text{HF}^+$ , $\text{Ar}^{++}$	$\text{HF}$ , $\text{Ar}$
31	$\text{CF}^+$	$\text{CF}_4$ , $\text{CH}_x\text{F}_y$
32	$\text{S}^+$ , $\text{CHF}^+$	$\text{SF}_6$ , $\text{H}_2\text{S}$ , $\text{CH}_x\text{F}_y$
33	$\text{CH}_2\text{F}^+$ , $\text{HS}^+$	$\text{CH}_2\text{F}_2$ , $\text{CH}_3\text{F}$ , $\text{H}_2\text{S}$
34	$\text{CH}_3\text{F}^+$ , $\text{H}_2\text{S}^+$	$\text{CH}_3\text{F}$ , $\text{H}_2\text{S}$
50	$\text{CF}_2^+$	$\text{CF}_4$ , $\text{CHF}_3$ , $\text{CH}_2\text{F}_2$
51	$\text{CHF}_2^+$ , $\text{SF}^+$	$\text{CH}_2\text{F}_2$ , $\text{CHF}_3$ , $\text{SF}_6$
52	$\text{NF}_2^+$	$\text{NF}_3$
65.5	$\text{HN}(\text{SiMe}_2)_2^{2+}$	$\text{LiN}(\text{SiMe}_3)_2$ , $\text{HN}(\text{SiMe}_3)_2$
69	$\text{CF}_3^+$	$\text{CF}_4$ , $\text{CHF}_3$
73	$\text{SiMe}_3^+$	$\text{LiN}(\text{SiMe}_3)_2$ , $\text{HN}(\text{SiMe}_3)_2$ , $\text{SiMe}_3\text{F}$ , $\text{SiMe}_3\text{H}$
77	$\text{SiMe}_2\text{F}^+$ , $\text{LiNSi}_2^+$	$\text{SiMe}_3\text{F}$ , $\text{SiMe}_2\text{F}_2$ , $\text{LiN}(\text{SiMe}_3)_2$
81	$\text{SiMeF}_2^+$	$\text{SiMe}_2\text{F}_2$ , $\text{SiMeF}_3$
85	$\text{SiF}_3^+$ , $\text{Me}_2\text{SiNCH}^+$	$\text{SiF}_4^+$ , $\text{SiMeF}_3^+$ , $\text{LiN}(\text{SiMe}_3)_2$
89	$\text{SF}_3^+$	$\text{SF}_6$

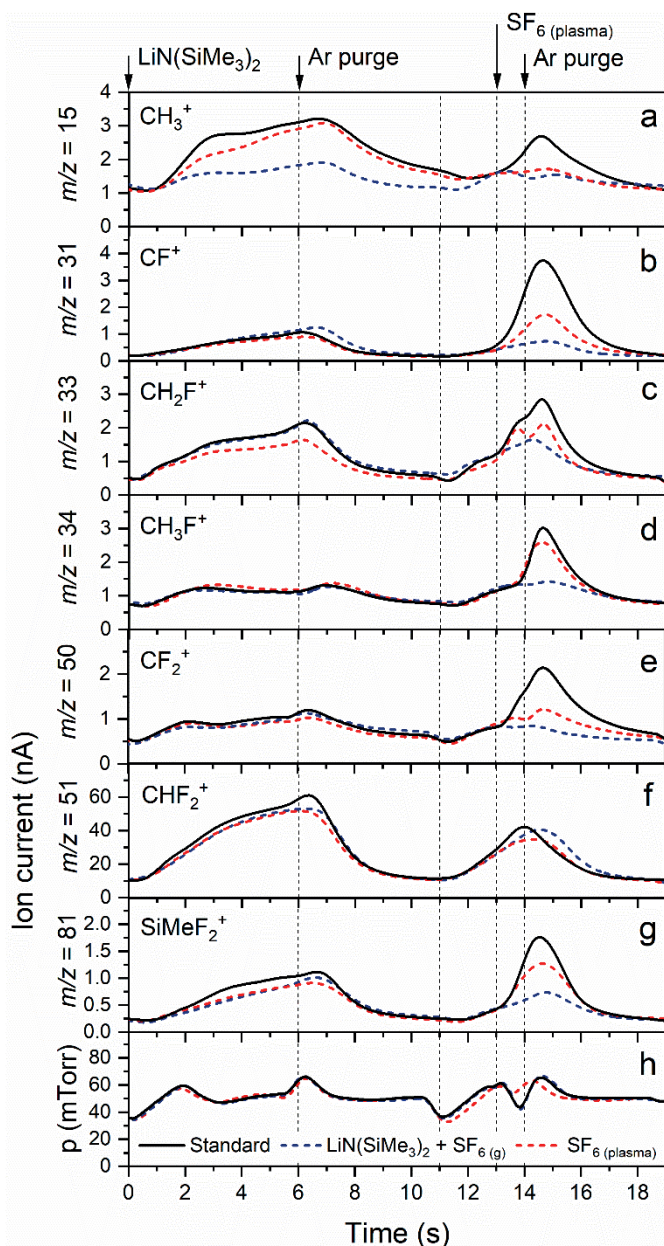


**Figure S6.8** Time-resolved QMS data of  $m/z = 15, 31, 33, 34, 50, 51,$  and  $81$ . The standard ALD recipe (black) is compared to the  $\text{LiN}(\text{SiMe}_3)_2 + \text{SF}_6$  recipe (blue dotted) and  $\text{SF}_6$  plasma recipe (red dotted). The precursor and coreactant dosing steps are alternated by argon purge steps of 5 s.



## ALD of aluminum phosphate using $\text{AlMe}_3$ , $\text{PO}(\text{OMe})_3$ and $\text{O}_2$ plasma

---

---

High purity, uniform, and conformal aluminum phosphate ( $\text{AlP}_x\text{O}_y$ ) thin films were deposited by atomic layer deposition (ALD) between 25 and 300 °C using supercycles consisting of (i)  $\text{PO}(\text{OMe})_3$  dosing combined with  $\text{O}_2$  plasma exposure and (ii)  $\text{AlMe}_3$  dosing followed by  $\text{O}_2$  plasma exposure. *In situ* spectroscopic ellipsometry and mass spectrometry were applied to demonstrate the ALD self-limiting behavior and to gain insight into the surface reactions during the precursor and coreactant exposures, respectively. Compared to earlier reported  $\text{AlP}_x\text{O}_y$  ALD studies using  $\text{H}_2\text{O}$  and  $\text{O}_3$  as coreactants, the use of an oxygen plasma generally leads to higher growth per cycle values and promotes phosphorus incorporation in the film. Specifically, when using a 1:1  $\text{PO}_x:\text{Al}_2\text{O}_3$  cycle ratio and a substrate temperature of 150 °C, the growth per supercycle is found to be 1.8 Å. The [P]:[Al] atomic ratio for this process is approximately 0.5 ( $\sim \text{AlP}_{0.5}\text{O}_{2.9}$ ) and can be tailored by changing the ratio between the two cycles or the substrate temperature. In literature reports where the same aluminum precursor was used, the [P]:[Al] atomic ratio was limited to 0.2 or a very high number of phosphorus cycles was needed in order to increase the phosphorus content. Instead, we demonstrate deposition of films with a composition close to  $\text{AlPO}_4$  by using a 2:1  $\text{PO}_x:\text{Al}_2\text{O}_3$  cycle ratio. The limited incorporation of P in the film is suspected to derive from the steric hindrance of the relatively bulky phosphorous precursor. Mass spectrometry suggests that the  $\text{PO}(\text{OMe})_3$  precursor chemisorbs on the surface without the release of reaction products into the gas phase, whereas  $\text{Al}(\text{Me})_3$  already undergoes methyl ligand abstraction upon chemisorption.



## 7.1 Introduction

Aluminum phosphate ( $\text{AlP}_x\text{O}_y$ ) thin films have been explored for a wide variety of applications such as catalyst support,<sup>1,2</sup> electrode coating to improve both safety and cycle performance of Li-ion battery cathodes,<sup>3-7</sup> thin film dielectric,<sup>8-10</sup> and oxidation resistant coating for carbonaceous materials.<sup>11,12</sup> Film uniformity and conformality are highly relevant for the practical application of aluminum phosphate, especially when deposition on 3D structures is required. The latter applies, for example, to the field of 3D Li-ion batteries where  $\text{AlP}_x\text{O}_y$  is used to coat cathode particles,<sup>4,5</sup> or in case of oxidation resistant coatings on fibers or carbon nanotubes.<sup>11,12</sup> In addition, the ability to tune the composition has been shown to play a critical role for aluminum phosphate thin films. The stoichiometry of the films determines film properties such as catalytic activity, permittivity, leakage current and breakdown fields, and (thermal) stability.<sup>2,4,8,13</sup>

Atomic layer deposition (ALD) is a powerful technique to meet the above-mentioned requirements in thin film deposition.<sup>14</sup> ALD is based on sequential and self-limiting half-reactions between precursors and coreactants with the surface leading to exceptional conformality and thickness control. For multicomponent oxides, the composition of the films and other related film properties, can be tuned by adjusting the number of ALD cycles for each oxide, in a so-defined ALD supercycle.<sup>15</sup>

So far, several studies on the synthesis of aluminum phosphate by ALD have been published. The results and most important process details have been summarized in Table 7.1. In earlier studies, aluminum phosphate films were deposited using  $\text{AlCl}_3$  or  $\text{Al}(\text{O}^i\text{Pr})_3$  together with  $\text{P}_2\text{O}_5$  or  $\text{PO}(\text{OMe})_3$  precursors and  $\text{H}_2\text{O}$  or  $t\text{-C}_4\text{H}_9\text{OH}$  coreactants at fairly high deposition temperatures (450 - 500 °C).<sup>9,16</sup> A wide compositional range could be obtained. Yet for some applications, specifically when using temperature sensitive substrates, a high substrate temperature may be unsuitable (see e.g. ref. 12). Moreover, the usage of chlorides ( $\text{AlCl}_3$ ) might be undesirable in some cases, because it may lead to Cl impurities in the deposited films and can cause corrosion of the process chamber.<sup>17</sup> More recently, a process using the chlorine free precursor  $\text{AlMe}_3$ , a deposition temperature down to 150 °C, and a controllable stoichiometry were demonstrated.<sup>12</sup> Also, ALD without the use of a coreactant after the precursors exposures was reported.<sup>11,17</sup> Despite these advantages, it has been shown difficult to incorporate a sufficiently large atomic content of phosphorus in the film for the processes where  $\text{AlMe}_3$  was used. For the reported ALD process using  $\text{H}_2\text{O}$  after  $\text{AlMe}_3$  and  $\text{O}_3$  after  $\text{PO}(\text{OMe})_3$ ,<sup>12</sup> or without the use of coreactants,<sup>11</sup> the [P]:[Al] atomic ratio was limited to 0.2. A very high number of  $\text{PO}_x$  cycles (> 20) was needed to increase the phosphorus content in the films to 0.8.<sup>11,12</sup> This is likely to be caused by steric hindrance of the  $\text{PO}(\text{OMe})_3$  precursor. Moreover, the use of a high number of  $\text{PO}_x$  cycles considerably extends the cycle time of the process. In a more recent study, it was shown that the use of  $\text{PO}(\text{OMe})_3$  plasma polymerization greatly increases the reactivity of  $\text{PO}(\text{OMe})_3$  precursor, therefore increasing the phosphorus content in the

**Table 7.1** Overview of process details collected from earlier work on ALD of aluminum phosphate.

Al source	Coreactant	P source	Coreactant	Tsub (°C)	P:Al cycle ratio	GPSC (Å)	[P]:[Al] ratio	Ref.
$\text{AlCl}_3$	$\text{H}_2\text{O}$	$\text{P}_2\text{O}_5/\text{PO}(\text{OMe})_3$	$\text{H}_2\text{O}$	500	1:60 - 1:5	N.A.	0.06 - 1.3 <sup>e</sup>	16
$\text{AlCl}_3/\text{Al}(\text{OPr})_3$	$\text{H}_2\text{O}/\text{C}_4\text{H}_9\text{OH}$	$\text{P}_2\text{O}_5$	$\text{H}_2\text{O}/\text{C}_4\text{H}_9\text{OH}$	450 - 500	1:30 - 1:5	1.3/1.1 <sup>a</sup>	0.04 - 1.4 <sup>e</sup>	9
$\text{AlCl}_3$	-	$\text{PO}(\text{OMe})_3$	-	150 - 400	1:1	1.4 - 2.4 <sup>b</sup>	0.4 - 0.6 <sup>e</sup>	17
$\text{AlMe}_3$	$\text{H}_2\text{O}$	$\text{P}(\text{OMe})_3$	$\text{O}_3$	150	5:1 - 20:1	1.7 <sup>c</sup>	0.2 - 0.8 <sup>f</sup>	12
$\text{AlMe}_3$	-	$\text{PO}(\text{OEt})_3$	-	250	1:1	1.4 <sup>d</sup>	0.2 - 0.3 <sup>g</sup>	11
$\text{AlMe}_3$	-	$\text{PO}(\text{OMe})_3$ plasma	$\text{O}_2$ plasma	320	1:1	3.7 <sup>d</sup>	1.8 <sup>e,h</sup>	18
$\text{AlMe}_3$	$\text{O}_2$ plasma	$\text{PO}(\text{OMe})_3$	$\text{O}_2$ plasma	25 - 300	1:1 - 10:1	1.8 - 4.6 <sup>d</sup>	0.5 - 3.3 <sup>e,h</sup>	This work

The GPSC refers to the growth per  $\text{AlP}_x\text{O}_y$  supercycle which depends on the number of phosphorus and aluminum cycles and temperature used, specified in the columns to the left. The same holds for the range of deposited [P]:[Al] atomic ratio. <sup>a</sup>GPSC measured by profilometry, <sup>b</sup>GPSC measured by spectrophotometry. <sup>c</sup>GPSC measured by transmission electron microscopy. <sup>d</sup>GPSC measured by spectroscopic ellipsometry. <sup>e</sup>Film composition determined by Rutherford backscattering spectrometry and/or elastic recoil detection. <sup>f</sup>Film composition determined by energy-dispersive X-ray spectroscopy. <sup>g</sup>Film composition determined by solid-state nuclear magnetic resonance. <sup>h</sup>Film composition determined by X-ray photoelectron spectroscopy.

film.<sup>18</sup> For films deposited at 320 °C, the phosphorus atomic content was found to be twice as much as the aluminum content. This process is however not strictly ALD, since saturation of the plasma polymerization step was not shown and for deposition temperatures below 320 °C, continuous and unsaturated growth occurred.

In this work, we report on a new process to synthesize aluminum phosphate thin films using plasma-assisted ALD in which an O<sub>2</sub> plasma is applied after each precursor step. It is generally known that with plasma-assisted ALD a high reactivity is delivered to the surface by the plasma species and therefore less thermal budget is required at the substrate to drive the ALD surface chemistry than in the case of thermal ALD. PO(OMe)<sub>3</sub> and AlMe<sub>3</sub> were used as precursors as it was proven in different studies these lead to successful deposition of AlP<sub>x</sub>O<sub>y</sub> (see Table 7.1). Moreover, in this way a fair comparison could be made to already existing AlP<sub>x</sub>O<sub>y</sub> ALD processes. We demonstrated ALD growth occurring for a wide temperature range of 25 - 300 °C. ALD saturation behavior and the ability to tune film composition were extensively studied. When using a 1:1 PO<sub>x</sub>:Al<sub>2</sub>O<sub>3</sub> cycle ratio, the growth per supercycle is found to saturate at 1.78 Å. Compared to AlP<sub>x</sub>O<sub>y</sub> ALD studies using a AlMe<sub>3</sub> precursor in combination with H<sub>2</sub>O and O<sub>3</sub>,<sup>12</sup> or without the use of coreactants,<sup>11</sup> the use of an oxygen plasma increased the ability to incorporate phosphorus in the film. The [P]:[Al] atomic ratio for the saturated process at 150 °C is approximately 0.5 (~ Al<sub>2</sub>PO<sub>6</sub>) compared to 0.2 in literature reports. The phosphorus content can be further enhanced by increasing the number of PO<sub>x</sub> cycles or substrate temperature. When using a deposition temperature of 150 °C, only 2 PO<sub>x</sub> cycles per Al<sub>2</sub>O<sub>3</sub> cycle were needed to achieve a stoichiometry close to AlPO<sub>4</sub>. This work addresses also the film properties as attained when processing the 1:1 PO<sub>x</sub>:Al<sub>2</sub>O<sub>3</sub> cycle recipe (Al<sub>2</sub>PO<sub>6</sub>) as well as the 3:1 PO<sub>x</sub>:Al<sub>2</sub>O<sub>3</sub> cycle recipe (slightly phosphorus rich AlPO<sub>4</sub>). For both processes, highly uniform, conformal films could be obtained over large 200 mm substrates and over high aspect ratios. Mass spectrometry data suggests that the phosphorus precursor remains intact upon chemisorption, which limits the incorporation of phosphorus atoms. On the other hand, AlMe<sub>3</sub> has been shown to release the ligands in the form of CH<sub>4</sub> groups upon chemisorption. This is in line with literature studies of ALD Al<sub>2</sub>O<sub>3</sub> without PO<sub>x</sub>.<sup>19</sup>

## 7.2 Experimental

The AlP<sub>x</sub>O<sub>y</sub> thin films were prepared using a FlexAL™ ALD reactor of Oxford Instruments. The reactor is equipped with an inductively coupled plasma (ICP) source and has a rotary and turbo molecular pumping unit such that it can reach a base pressure of < 10<sup>-6</sup> Torr by overnight pumping. The pump unit as well as the ICP source are connected to the deposition chamber through gate valves.

Figure 7.1 presents a schematic overview of the developed process (the process development is discussed in section 7.3.1). AlP<sub>x</sub>O<sub>y</sub> films were deposited by combining

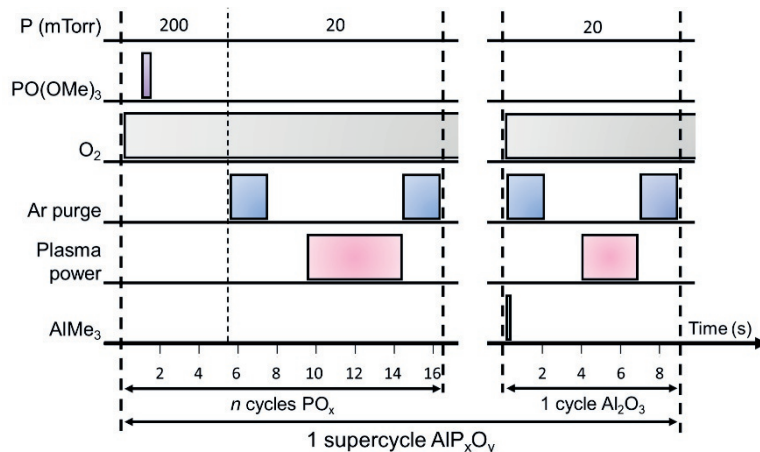


**Figure 7.1** Schematic of the pulsing sequence of the ALD supercycle for deposition of  $\text{AlP}_x\text{O}_y$ . The duration of the  $\text{AlMe}_3$  dose step is 50 ms. The reactor pressure is also indicated in the uppermost row.

cycles of  $\text{Al}_2\text{O}_3$  and  $\text{PO}_x$ . A constant oxygen flow through the ICP gate valve was adopted since it did not lead to any  $\text{Al}_2\text{O}_3$  or  $\text{PO}_x$  growth. For  $\text{PO}_x$ , cycles consisting of exposures to  $\text{PO}(\text{OMe})_3$  (97 %, Sigma-Aldrich) and to an  $\text{O}_2$  fed plasma are adopted, with Ar purge steps in between. The  $\text{PO}(\text{OMe})_3$  precursor was kept in a stainless steel container and introduced into the chamber by vapor draw. The  $\text{PO}(\text{OMe})_3$  precursor pod and supply line were heated to 70 and 90 °C respectively to prevent precursor condensation. The pressure was set to 200 mTorr during the  $\text{PO}(\text{OMe})_3$  dose step by slightly closing the gate valve connected to the turbo pump. Also a hold step was used. In this way the surface is exposed to more  $\text{PO}(\text{OMe})_3$  and for a longer period of time. Moreover, a stabilization step of 1 s was used to ensure the gas flow and pressure stabilized at 200 mTorr. For stabilization of the plasma, the reactor was filled with oxygen prior to switching on the power supply. The plasma power was set at 100 W for the  $\text{PO}_x$  cycle. The  $\text{Al}_2\text{O}_3$  cycle consists of alternating exposures to  $\text{AlMe}_3$  (> 99 %, Sigma-Aldrich) and  $\text{O}_2$ -fed plasma with purge steps in between. The  $\text{AlMe}_3$  precursor was also kept in a stainless steel container and introduced into the chamber by vapor draw. For the  $\text{AlMe}_3$  precursor pod and supply line temperatures of 30 and 60 °C were used, respectively. The plasma power for the  $\text{Al}_2\text{O}_3$  cycle was set to 200 W.

One ALD supercycle consists of  $n$   $\text{PO}_x$  cycles and 1  $\text{Al}_2\text{O}_3$  cycle. Depositions were carried out on Si substrates with native oxide for standard characterization and on substrates with wurtzite (WZ) InP nanowire arrays for conformality studies. These substrates are placed on a 200 mm carrier wafer. The deposition table temperature was set between 25 and 300 °C. The reactor wall is maintained at a temperature of 120 °C, except for the deposition at 25, 50 or 100 °C, where the reactor wall is kept at

25, 50 or 100 °C, respectively. The actual substrate temperature might be slightly lower for table set point temperatures > 120 °C since it is unlikely that the substrate could reach exactly the same temperature as the table due to a reduced thermal contact in vacuum.

The film thickness and dielectric function were monitored *in situ* by spectroscopic ellipsometry (SE) with a J.A. Woollam, Inc. M-2000F (245 - 1000 nm) system and *ex situ* using variable angle spectroscopic ellipsometry (VASE) with a J.A. Woollam, Inc. M-2000D (190 - 1000 nm) system. *Ex situ* measurements were performed from 60 - 80° with steps of 5°. PO<sub>x</sub> as well as AlP<sub>x</sub>O<sub>y</sub> films appeared to be transparent within the measured range. The dispersion relationship for the films was well-described by the Cauchy formula ( $n(\lambda) = A + B/\lambda^2 - C/\lambda^4$ ). Transmission electron microscopy (TEM) was used to probe the thickness of the films along individual InP nanowires. The wires had a length of ~1.5 μm and a hexagonal cross-section with an average diameter of ~180 nm and were arranged in a square array with a 500 nm pitch. Energy dispersive X-ray spectroscopy (EDX) was used to probe the chemical composition along the InP nanowires. The combination of TEM and EDX gives insight into the conformality of the AlP<sub>x</sub>O<sub>y</sub> films.

Elastic recoil detection (ERD) and Rutherford backscattering spectroscopy (RBS) were carried out to determine the composition and mass density of the films. The hydrogen profiles were determined by ERD using a 2 MeV He<sup>+</sup> beam impinging on the sample under 15° glancing incidence, and 30° recoil angle. RBS is performed in channeling mode, to reduce the background under the C and O features, using the same beam and with detectors at scattering angles of 170° and 105°. X-ray photoelectron spectroscopy (XPS) spectra were recorded by a Thermo Scientific K-Alpha<sup>+</sup> system using monochromatic Al Kα X-rays. The spot size of the beam was 400 μm and the base pressure of the system was 10<sup>-8</sup> mbar. The measurements were performed without the use of depth profiling, and it was found that these results are consistent with the RBS/ERD results. It is therefore expected that they are representative for the bulk part of the films. The crystallinity of the AlP<sub>x</sub>O<sub>y</sub> layers was investigated using a Philips X'Pert MPD diffractometer equipped with a Cu Kα source (1.54 Å radiation).

A Pfeiffer Vacuum mass spectrometer with a mass-to-charge (*m/z*) range of 100 atomic mass units (amu) was connected to the deposition chamber through a pipeline and a 150 μm diameter pinhole. The system is equipped with a Channeltron detector and the energy of the electrons in the ionizer was set to 70 eV. The pressure in the QMS was maintained below 10<sup>-6</sup> Torr using differential pumping with a turbomolecular pump. Prior to every measurement the reactor was conditioned with a AlP<sub>x</sub>O<sub>y</sub> film and the background signal of the reactor was measured as a reference. The measuring time per atomic mass unit (amu) was set to 200 ms. For the time-resolved measurements, the selected *m/z* values were tracked per channel using a dwell time of 50 ms. The QMS data of at least 10 ALD cycles were monitored to verify

that steady-state values were achieved. The measurement procedure has been reported more extensively in Chapter 5.<sup>20</sup>

## 7.3 Results and discussion

### 7.3.1 ALD process optimization

As mentioned before, the plasma-assisted ALD process of  $\text{AlP}_x\text{O}_y$  consists of  $\text{PO}_x$  and  $\text{Al}_2\text{O}_3$  cycles. The plasma-assisted ALD process of  $\text{Al}_2\text{O}_3$  is well known from literature and its saturation behavior has been extensively investigated.<sup>21,22</sup> On the contrary, ALD of  $\text{PO}_x$  has been less explored so far. In a recent study it was mentioned that for  $\text{PO}_x$  growth no ALD saturation could be achieved.<sup>23</sup> The same behavior was found in our studies (see Figure S7.1). In addition, it was found that the growth per cycle of the film increases with increasing cycle number, i.e. the thickness of the film, also shown in Figure S7.1 of the appendix. Furthermore, the  $\text{PO}_x$  films showed high reactivity upon air exposure and therefore the stoichiometry of the films could not be determined by *ex situ* analysis (e.g. XPS).

The results of the saturation behavior of the  $\text{AlP}_x\text{O}_y$  supercycle are presented in Figure 7.2. This figure shows the saturation of the growth per supercycle as well as the [P]:[Al] ratio for a substrate temperature of 150 °C. The [P]:[Al] ratio gives an indication on the phosphorus incorporation in the films. The overall stoichiometry will be discussed in section 7.3.3. In Figure 7.2a, the saturation behavior of the  $\text{PO}(\text{OMe})_3$  precursor is shown. First, the growth per supercycle and composition were determined for a lower reactor pressure of 20 mTorr and without the use of a hold step after the  $\text{PO}(\text{OMe})_3$  dose (diamond symbols). As observed from the graph, both do not saturate. By using a hold step, the GPC and phosphorus content increased because the sample surface was exposed to precursor molecules for a longer period of time (square symbols). When adopting a higher set pressure during  $\text{PO}(\text{OMe})_3$  exposure, the gate valve connected to the turbo pump was further closed, leading to a higher partial pressure of  $\text{PO}(\text{OMe})_3$  (triangle symbols). As shown by the circular symbols, the phosphorus content and growth per supercycle increased by using a pressure of 200 mTorr and a hold step of 4 s after  $\text{PO}(\text{OMe})_3$  dose. As a side effect the dosage of the phosphorus precursor is more efficient, since a shorter phosphorus precursor dosing time is needed to achieve the same phosphorus content in the films. It seems that the growth per supercycle saturates faster than the [P]:[Al] ratio. A possible explanation is that the growth per supercycle is mostly determined by the  $\text{Al}_2\text{O}_3$  cycle (the growth per cycle is much higher for the  $\text{Al}_2\text{O}_3$  cycle compared to the  $\text{PO}_x$  cycle), whereas the [P]:[Al] ratio is determined by both cycles. Since our main goal was to increase the film phosphorus content, we focus here on the saturation of the [P]:[Al] ratio. This is achieved for 500 ms  $\text{PO}(\text{OMe})_3$  dosing and therefore chosen as the standard  $\text{PO}(\text{OMe})_3$  dose time. The [P]:[Al] ratio for the saturated process is then 0.5 and the growth per supercycle is equal to 1.78 Å.

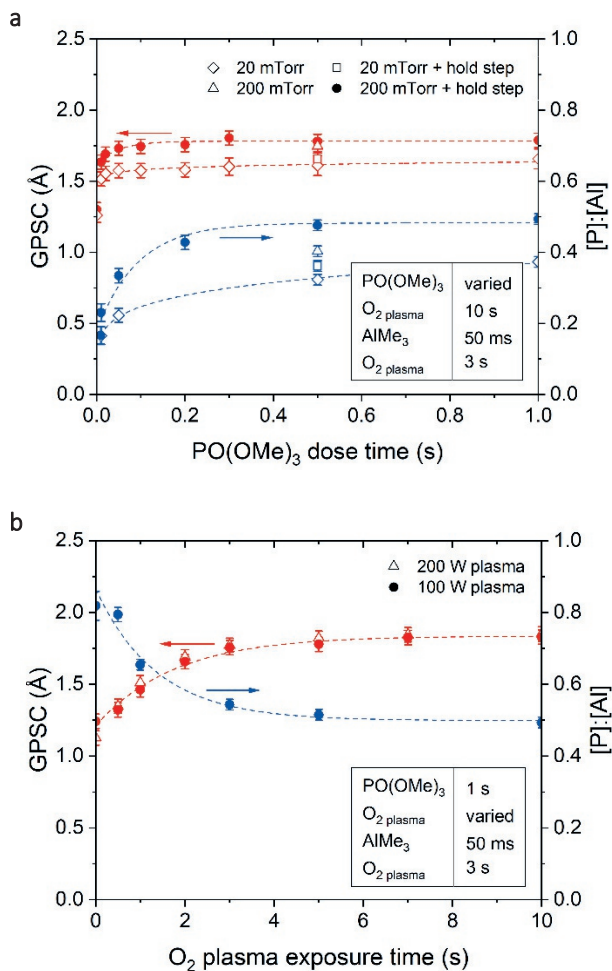


**Figure 7.2** The growth per supercycle (GPSC) obtained by SE (red circles) and the [P]:[Al] atomic ratio measured by XPS (blue circles) as a function of precursor dosing or coreactant exposure time. In a) and b) the results are presented for PO(OMe)<sub>3</sub> dose and O<sub>2</sub> plasma exposure after PO(OMe)<sub>3</sub>, respectively. Figure a) and b) also show data for different pressure and plasma power settings, respectively. In c) and d) the results of AlMe<sub>3</sub> dose and O<sub>2</sub> plasma exposure after AlMe<sub>3</sub> are presented. The lines serve as a guide to the eye. All samples were deposited using a deposition temperature of 150 °C.

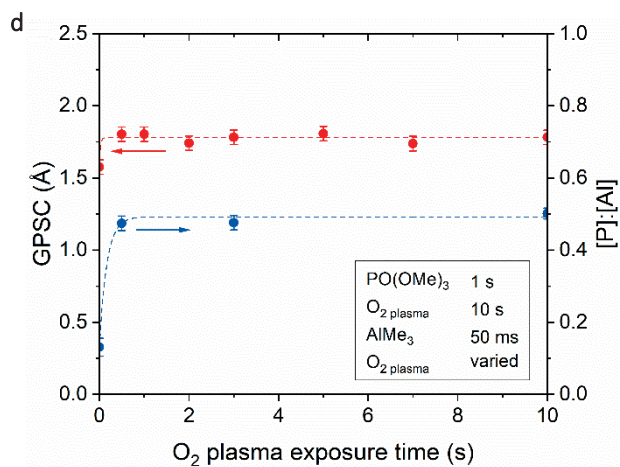
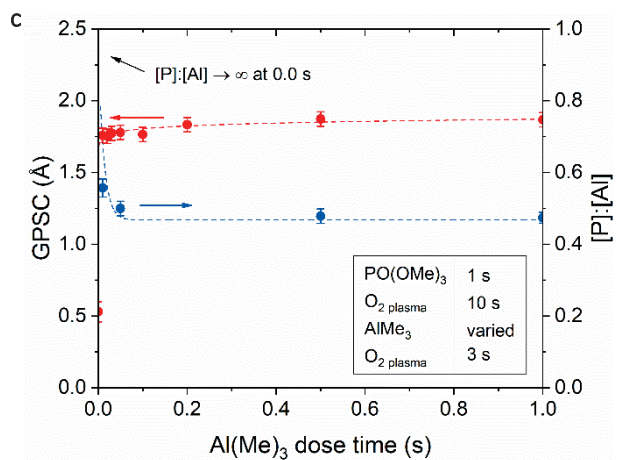




Figure 7.2b depicts the saturation behavior of the O<sub>2</sub> plasma after the PO(OMe)<sub>3</sub> dose step. The growth per supercycle and [P]:[Al] ratio both saturate at approximately 5 s plasma exposure. It can be observed that without the use of plasma after the PO(OMe)<sub>3</sub> exposure there was still film growth, however much lower (1.2 Å/supercycle) and also the [P]:[Al] ratio was relatively high (~ 0.8) compared to the saturated values obtained for the PO(OMe)<sub>3</sub> dose. The [P]:[Al] ratio decreased when the plasma exposure time was increased. This suggests that if longer plasma exposure times are used, the surface is more reactive to the AlMe<sub>3</sub> molecules in the following process step and therefore more aluminum will be incorporated. The oxygen plasma is expected to convert the methoxy-groups of the PO(OMe)<sub>3</sub> molecule into –OH and/or –O surface species. These surface species have been shown promote the chemisorption of AlMe<sub>3</sub>.<sup>19</sup> However, film growth was also proven for AlMe<sub>3</sub> in combination with PO(OEt)<sub>3</sub> without the use of coreactants,<sup>11</sup> and PO(OMe)<sub>3</sub> and PO(OEt)<sub>3</sub> are very similar. Most certainly the presence of –OH or –O surface species increase the reactivity a lot, however the removal of the methoxy-groups seems not to be necessary for chemisorption of AlMe<sub>3</sub>.

The saturation behavior of the AlMe<sub>3</sub> dose step is shown in In Figure 7.2c. As expected, the growth per supercycle as well as the [P]:[Al] ratio saturate quickly for this highly volatile and reactive precursor. The standard AlMe<sub>3</sub> dose time was chosen to be 50 ms.

As was the case for the PO<sub>x</sub> cycle, there was still film growth without the use of plasma after AlMe<sub>3</sub> (see Figure 7.2d). Therefore it is very likely that reactions between AlMe<sub>x</sub> and PO (OMe)<sub>3</sub> can occur. The reason is probably that alkoxy groups of the phosphorus precursor are Lewis bases, which can bind to the Lewis acid aluminum center.<sup>24,25</sup> However, the growth per supercycle decreased, and [P]:[Al] ratio was much lower (0.13) when the plasma step was eliminated from the recipe. In addition, compared to previously reported literature data for a 1:1 cycle ratio process where AlMe<sub>3</sub> in combination with different coreactants were used (see Table 7.1), the phosphorus content is much higher for our plasma-based process. The oxygen plasma presumably not only removes the organic ligands, but also enhances the reaction of the layer with a metal organic precursor to form a metal phosphate. Interestingly, the surface reactions already saturate when the O<sub>2</sub> plasma exposure time is greater than 0.5 s. The *in situ* SE measurement only measures the middle of the sample, and it was observed in previous work on plasma-assisted ALD of Al<sub>2</sub>O<sub>3</sub> that film uniformity is improved for longer plasma exposures compared to the saturation time.<sup>21</sup> This is related to the fact that growth rate is usually slightly higher in the center where the flux of plasma species is highest. Therefore, the standard value for the O<sub>2</sub> plasma exposure time after AlMe<sub>3</sub> was chosen to be 3 s such that a better uniformity of the films can be expected. Film uniformity (and conformality) of the films will be discussed in section 7.3.2.

From the results in Figure 7.2b and d, we can conclude that the implementation of an  $\text{O}_2$  plasma greatly improves the surface reactivity of both precursors in the following process step. The plasma exposure time after  $\text{AlMe}_3$  saturates much faster than the plasma exposure time after  $\text{PO}(\text{OMe})_3$ . This could be related to a more efficient combustion and/or differences in reaction upon  $\text{AlMe}_3$  and  $\text{PO}(\text{OMe})_3$  precursor adsorption. In the standard recipe an  $\text{O}_2$  plasma power of 100 W was used for the  $\text{PO}_x$  cycle compared to 200 W for the  $\text{Al}_2\text{O}_3$  cycle. To exclude that the saturation is affected by a higher plasma power, which slightly increases the ion flux and slightly reduces the ion energy,<sup>26</sup> also 200 W was tested for the  $\text{PO}_x$  cycle (red open symbols), whereby all other settings remained unchanged. However, this does not influence the saturation time.

Overall, it is observed that the growth per supercycle saturates at 1.78 Å. Interestingly, this is approximately the sum of the growth per cycle of the plasma-assisted  $\text{Al}_2\text{O}_3$  process which is 1.30 Å,<sup>22</sup> and the growth per cycle for  $\text{PO}_x$  on Si with native oxide which is determined to be  $0.5 \pm 0.1$  Å over the first 100 cycles (see Figure S7.1). The [P]:[Al] ratio for the saturated process is 0.5.

As discussed in previous paragraph, there is a limit to the incorporation of phosphorus ([P]:[Al] ratio of 0.5) when  $\text{AlP}_x\text{O}_y$  films are deposited at 150 °C using the 1:1  $\text{PO}_x$ : $\text{Al}_2\text{O}_3$  cycle ratio. The film composition can be tuned by varying the number of  $\text{PO}_x$  cycles while the number of  $\text{Al}_2\text{O}_3$  cycles is kept constant. Figure 7.3 shows the growth per supercycle and [P]:[Al] ratio as a function of the number of  $\text{PO}_x$  cycles used in the recipe. The [P]:[Al] ratio increased rapidly to almost 1 by only increasing the number of  $\text{PO}_x$  cycles to 2, corresponding to a stoichiometry close to  $\text{AlPO}_4$

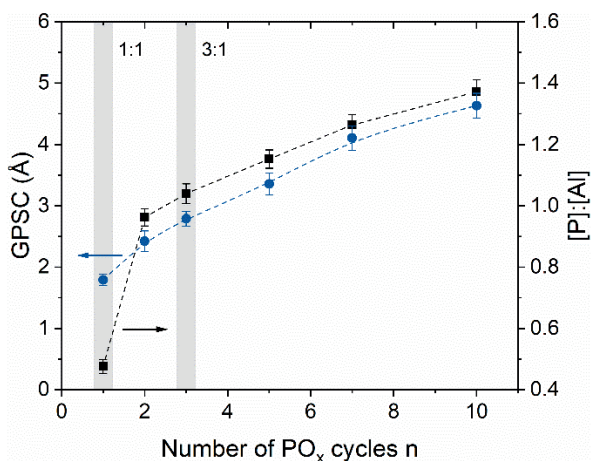


**Figure 7.3** The growth per supercycle (circles) and [P]:[Al] atomic ratio (squares) as a function of number of  $\text{PO}_x$  cycles for the  $\text{AlP}_x\text{O}_y$  process at a deposition temperature of 150 °C. The dashed lines serve as a guide to the eye.

(see section 7.3.3 for the film oxygen content). Upon further increasing the number of  $\text{PO}_x$  cycles, the  $[\text{P}]:[\text{Al}]$  ratio kept slightly increasing. The growth per supercycle also increases with number of  $\text{PO}_x$  cycles but does not follow the same trend. The phosphorus content in the films could be further increased for a number of  $\text{PO}_x$  cycles  $n > 10$ . As mentioned before,  $\text{PO}_x$  alone is unstable when exposed to air. For  $\text{AlP}_x\text{O}_y$  we found an upper limit in terms of P incorporation in the film, which is stable in air. This occurs when  $[\text{P}]:[\text{Al}] \leq 3.3$ . In the next sections we will focus on the 1:1 as well as the 3:1  $\text{PO}_x:\text{Al}_2\text{O}_3$  cycle ratio process as highlighted in Figure 7.3. The 3:1 cycle ratio is especially interesting, because it leads to a slightly phosphorus-rich aluminum orthophosphate ( $\text{AlPO}_4$ ) stoichiometry.

The film thickness and growth rate of the process were investigated for an extended range of deposition temperatures. Figure S7.2 shows the thickness evolution as a function of the number of ALD cycles for temperatures between 25 and 300 °C. The growth curve is linear for the whole temperature range. In Figure 7.4, the temperature dependence of the growth per supercycle is plotted for processes using a 1:1 as well as a 3:1  $\text{PO}_x:\text{Al}_2\text{O}_3$  cycle ratio. For both cases, the growth per supercycle decreases with an increase from room temperature up to 300 °C. This was expected since the growth rates for the processes of  $\text{PO}_x$  (Figure S7.1) and  $\text{Al}_2\text{O}_3$  separately also decrease with increasing temperature.<sup>21,22</sup> Furthermore, it can be observed that the slope for both cycle ratios decreases for temperatures  $\geq 150$  °C. This might be related to differences in the table temperature set point and the actual substrate temperature for table temperatures  $> 120$  °C (maximum wall temperature). As mentioned before, it is unlikely that the substrate could reach exactly the same

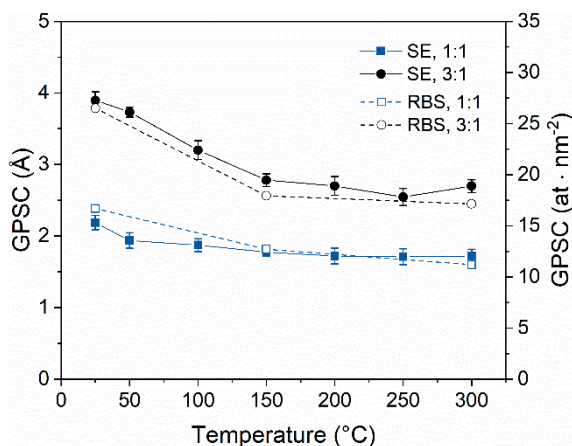


**Figure 7.4** Growth per supercycle as a function of substrate temperature for  $\text{AlP}_x\text{O}_y$  processes using a 1:1 (squares) and 3:1 (circles)  $\text{PO}_x:\text{Al}_2\text{O}_3$  cycle ratio. The dashed lines serve as a guide to the eye. The growth per supercycle is obtained from spectroscopic ellipsometry (in Å, closed symbols) and a combination of RBS and ERD (in  $\text{at} \cdot \text{nm}^{-2}$ , open symbols).

temperature as the table due to a reduced thermal contact in vacuum. Finally, it should be noted that the results obtained from SE are in line with those from RBS and ERD analysis: the number of deposited atoms (open symbols) scales with the growth per supercycle in terms of thickness (closed symbols).

### 7.3.2 Film uniformity and conformality

The uniformity and conformality were investigated to further demonstrate the ALD behavior of the  $\text{AlP}_x\text{O}_y$  process. Film thickness and refractive index non-uniformity were determined using SE-mapping of films deposited on a 200 mm wafer using a 1:1 and 3:1 cycle ratio (see Figure 7.5 and Figure S7.3). The non-uniformity (standard deviation, 1 sigma) of the thickness and refractive index for the 1:1 process were determined to be 1.4 % and 0.4 %, respectively. For the 3:1 process this was 1.9 % and 0.2 %, respectively. This points out to good uniformity for both processes. As observed from Figure 7.5a, a slight thickness gradient is visible, which could be related to the position of the injection of the precursors. The refractive index (Figure 7.5b) is lower at the spots where a higher thickness is observed. It is therefore more likely that the gradient is related to the flux of  $\text{PO}(\text{OMe})_3$  than  $\text{AlMe}_3$  molecules since the refractive index will be lower for a higher phosphorus content. For the 3:1 process, a similar gradient in the film thickness is observed (Figure S7.3a). However, this gradient was not observed in the contour plot of the refractive index (Figure S7.3b). This is probably related to the fact that 3  $\text{PO}_x$  cycles are deposited for every  $\text{Al}_2\text{O}_3$  cycle, and therefore variations in the phosphorus content and thus refractive index are below the sensitivity of the measurement.

The conformality of the 3:1 cycle process was studied by depositing on a InP nanowire array. The nanowires were separated and analyzed using TEM and EDX. Figure 7.6a shows a top-down and tilted SEM image of the nanowire array. Figure 7.6b-d clearly shows a conformal, ~ 23 nm thick aluminum phosphate film along the full length of a nanowire. The ratio between the thickness at the bottom and the top of the nanowire was determined to be > 0.9. The EDX mappings in Figure S7.4 show the presence of indium and phosphorus inside the wire and  $\text{AlP}_x\text{O}_y$  on top. The aluminum, phosphorus and oxygen contents were uniformly distributed over de wires. The combination of TEM and EDX results indicate conformal deposition of  $\text{AlP}_x\text{O}_y$  films on 3D structures.

### 7.3.3 Chemical, physical and optical properties

In section 7.3.1 we focused on the [P]:[Al] ratio in connection with the saturation behavior. In this part an in-depth study is carried out on the overall stoichiometry of the films, including the presence of impurities, and also verifying temperature dependence. The chemical composition of the deposited films was studied by *ex situ* XPS and a combination of RBS and ERD. 50 nm thick films were deposited using a 1:1 or 3:1  $\text{PO}_x:\text{Al}_2\text{O}_3$  cycle ratio. Carbon traces (~ 3 %) were detected at the surface;

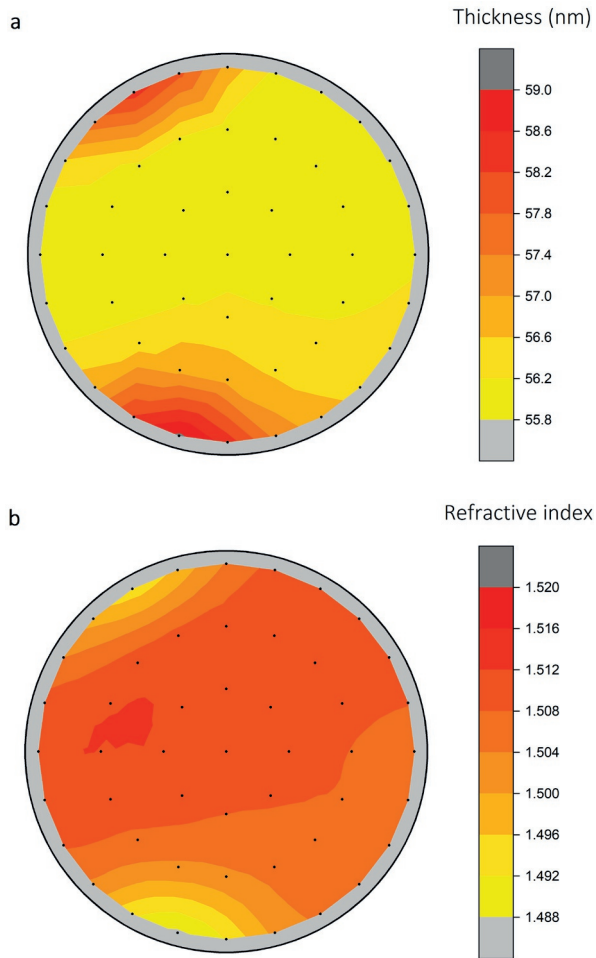


**Figure 7.5** Contour maps of a) thickness and the b) refractive index of  $\text{AlP}_x\text{O}_y$  films across 200 mm wafers as determined from SE mapping. The measurements were performed on  $\text{AlP}_x\text{O}_y$  films deposited at 150 °C using a 1:1  $\text{PO}_x:\text{Al}_2\text{O}_3$  cycle ratio. The grey circle indicates the dimensions of the wafer. An edge-exclusion of 6 mm was used.

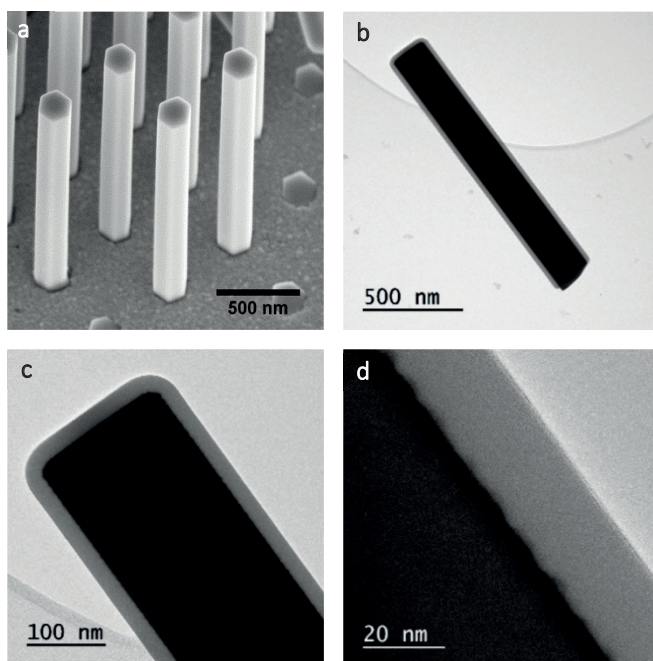


**Figure 7.6** a) 30° tilt SEM images of an as-grown WZ InP nanowire array. b) Bright-field TEM image of a single nanowire with an  $\text{AlP}_x\text{O}_y$  film prepared using a 3:1 cycle ratio. c-d) Bright-field TEM images taken around the c) top and d) center of the same nanowire.

sputtering of the surface led to less than  $\sim 1\%$  carbon in the bulk of the layer. This is shown in the survey spectra measured by XPS in Figure S7.5. Next to carbon, oxygen, phosphorus and aluminum were detected, as expected. In Figure 7.7, XPS measurements of  $\text{AlP}_x\text{O}_y$  films grown at  $150^\circ\text{C}$  are presented showing the a) Al 2p, b) P 2p, c) O 1s and d) C 1s core level spectra. The spectra were measured without sputtering, since it was found that these results are consistent with the RBS/ERD results shown hereafter. The binding energy scale was calibrated by using the C 1s adventitious carbon peak at 284.8 eV. The binding energy values are in agreement with those expected for aluminum phosphate reported in literature.<sup>27,28</sup> Specifically, the Al 2p, P 2p and O 1s peaks of the 3:1 process are located at the position expected for a  $\text{AlPO}_4$  film. The Al 2p and O 1s peak of the 1:1 process are slightly shifted towards a lower binding energy and are located between the expected position for  $\text{AlPO}_4$  and  $\text{Al}_2\text{O}_3$ . This outcome could suggest some presence of  $\text{Al}_2\text{O}_3$  in the films, however peak deconvolution could not be performed since the expected peak positions for  $\text{AlPO}_4$  and  $\text{Al}_2\text{O}_3$  are close to each other and the peaks are very symmetric. The obtained stoichiometry for the 1:1 cycle process is calculated to be  $\text{Al}_{0.5}\text{PO}_{3.4}$  and for the 3:1 process  $\text{Al}_{1.1}\text{PO}_{4.8}$ .

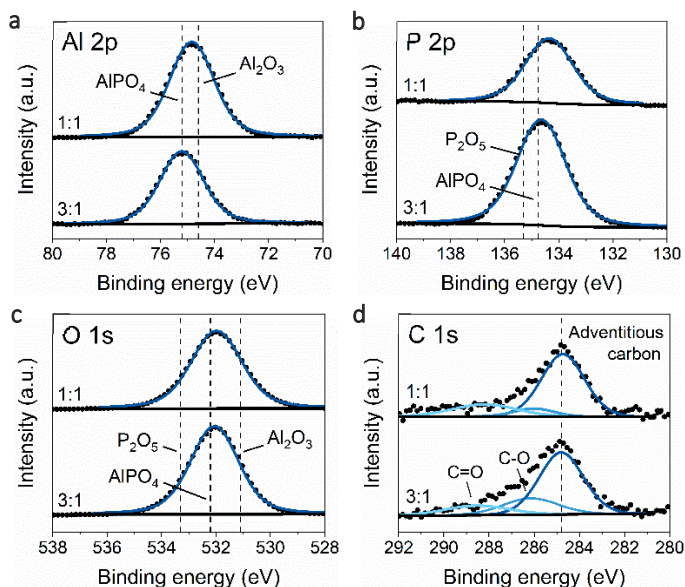


**Figure 7.7** a) Al 2p, b) P 2p, c) O 1s and d) C 1s spectra of a 50 nm aluminum phosphate film grown at 150 °C using a 1:1 (top) and 3:1 (bottom) cycle ratio. Measured data (black dotted lines) and fitted peaks (blue lines) are plotted. Carbon is only present at the surface of the films. The expected peak positions for  $\text{AlPO}_4$ ,  $\text{Al}_2\text{O}_3$  and  $\text{P}_2\text{O}_5$  films are indicated in the figure for reference.

The stoichiometry, atomic percentage of hydrogen and calculated mass density obtained by a combination of RBS and ERD are presented in Table 7.2. These measurements are generally accurate within  $\pm 1\%$  and can therefore be used to confirm the previously presented XPS data. The atomic percentages and stoichiometry from XPS for deposition temperatures between 25 - 300 °C are presented in Table S7.1. The [P]:[Al] ratio measured by RBS and ERD is in line with the ratio measured by XPS. Carbon was found only at the top surface of the films and always below 1.2 at. %, also in line with the XPS results. Without the application of sputtering, the amount of oxygen and carbon measured by XPS was slightly higher compared to the RBS and ERD measurements. This is attributed to the excess of carbon and oxygen present on the surface after air exposure as XPS only measures first few nanometers of the film. The use of higher substrate temperatures limits the incorporation of hydrogen impurities.

In Figure 7.8 the number of atoms deposited on a square nm per (super)cycle are reported, measured by a combination of RBS and ERD. The  $\text{AlP}_x\text{O}_y$  process using a 1:1 cycle ratio is compared to the  $\text{AlP}_x\text{O}_y$  process using 3:1 cycle ratio and an  $\text{Al}_2\text{O}_3$  plasma ALD reference process.<sup>22</sup> When the 3:1 cycle ratio was used instead of the 1:1 cycle ratio, the number of incorporated phosphorus and oxygen atoms increased, as

**Table 7.2** Properties of 50 nm AlP<sub>x</sub>O<sub>y</sub> films fabricated using a 1:1 and 3:1 cycle ratio at 25, 150, and 300 °C.

Cycle ratio	$T_{sub}$ (°C)	Stoichiometry <sup>a</sup>	[H] (at. %)	Mass density (g · cm <sup>-3</sup> )
1:1	25	AlP <sub>0.44</sub> O <sub>3.08</sub>	9.4 ± 1.2	2.3 ± 0.1
1:1	150	AlP <sub>0.47</sub> O <sub>2.93</sub>	4.7	2.3
1:1	300	AlP <sub>0.70</sub> O <sub>3.33</sub>	2.6	2.1
3:1	25	AlP <sub>1.38</sub> O <sub>5.37</sub>	6.6	2.1
3:1	150	AlP <sub>1.08</sub> O <sub>4.31</sub>	3.3	2.1
3:1	300	AlP <sub>1.15</sub> O <sub>4.50</sub>	2.5	2.1

<sup>a</sup>The stoichiometry was calculated from a combination of RBS and ERD measurements. The mass density was calculated by combining RBS, ERD, and SE results. In the first row the typical error is given for a certain parameter.

expected. The increase in number of phosphorus atoms does not scale linearly with the number of PO<sub>x</sub> cycles used. This is in line with the trend observed for the [P]:[Al] ratio as a function of PO<sub>x</sub> cycles shown in Figure 7.3. Based on the RBS/ERD data for the 3:1 recipe at 150 °C, 2.94 P atoms per nm<sup>2</sup> are incorporated every supercycle. The surface density in AlPO<sub>4</sub> units per nm<sup>2</sup> can be calculated via  $\left(\frac{\rho \cdot N}{\mu}\right)^{2/3}$ , where  $\rho$  is the mass density,  $N$  is Avogadro's number, and  $\mu$  is the molecular mass of AlPO<sub>4</sub>. Given the fact that one monolayer of aluminum orthophosphate contains roughly 5.4 AlPO<sub>4</sub> units, and therefore also 5.4 P atoms per nm<sup>2</sup> in each supercycle approximately half a monolayer of AlPO<sub>4</sub> is deposited. For reference, the same calculation was done for the Al<sub>2</sub>O<sub>3</sub> ALD process. For Al<sub>2</sub>O<sub>3</sub> ALD at 150 °C approximately 0.4 monolayer is deposited.

As was already shown in section 7.3.1, the total number of incorporated atoms and the amount of film thickness both depend on the substrate temperature (Figure 7.4). In Figure 7.8 it is shown that the number for each atom separately generally also follows this trend. The number of incorporated hydrogen atoms is equal for the AlP<sub>x</sub>O<sub>y</sub> 1:1 cycle process and the Al<sub>2</sub>O<sub>3</sub> process, and does not increase when the number of PO<sub>x</sub> cycles is increased to 3 (Figure 7.8d). This suggests that the incorporation of hydrogen is mostly dependent on the Al<sub>2</sub>O<sub>3</sub> cycle, which is similar for these processes.

For the AlP<sub>x</sub>O<sub>y</sub> 1:1 process, approximately the same number of phosphorus atoms are deposited per supercycle for different temperatures (Figure 7.8b). However, the number of deposited phosphorus atoms per supercycle for the AlP<sub>x</sub>O<sub>y</sub> 1:3 process and also the growth rate for the PO<sub>x</sub> ALD are temperature dependent (Figure S7.1). This suggests that the amount of PO(OMe)<sub>3</sub> adsorbed on a Al<sub>2</sub>O<sub>3</sub> substrate shows no clear temperature dependence, although PO(OMe)<sub>3</sub> adsorption on PO<sub>x</sub> does. The data in Figure 7.8b also suggest that the decrease in phosphorus content in the films for increased temperatures reported in Table 7.2 is mostly related to the decrease in



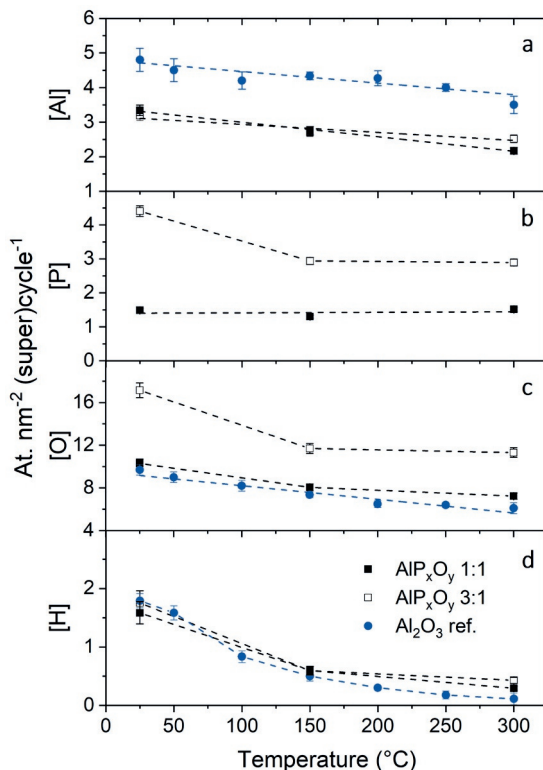


**Figure 7.8** The number of Al, P O and H atoms deposited per  $\text{nm}^2$  per (super)cycle as a function of deposition temperature measured by RBS and ERD. The  $\text{AlP}_x\text{O}_y$  1:1 process is compared to the  $\text{AlP}_x\text{O}_y$  3:1 process and an  $\text{Al}_2\text{O}_3$  plasma ALD reference.<sup>22</sup> For the  $\text{AlP}_x\text{O}_y$  processes we refer to the number of atoms per supercycle, whereas  $\text{Al}_2\text{O}_3$  consists of only one ALD cycle. The dashed lines serve as a guide to the eye.

number of incorporated aluminum atoms. This (in addition to the contribution of the lower reactor wall temperature) could also explain why the decrease in growth per supercycle is less for higher deposition temperatures compared to lower temperatures for the 1:1 cycle (Figure 7.3). As the deposition of Al atoms decreases with temperature, deposition of P atoms becomes more important; however, since phosphorus adsorption after an  $\text{Al}_2\text{O}_3$  cycle is not temperature dependent, the effect on the growth rate is much less.

The mass density for  $\text{AlP}_x\text{O}_y$  films deposited using a 1:1 cycle ratio varies between  $2.1$  and  $2.3 \text{ g} \cdot \text{cm}^{-3}$  for deposition temperatures from  $300$  down to  $25 \text{ }^\circ\text{C}$  (Table 7.2). The mass density of ALD  $\text{Al}_2\text{O}_3$  films is found to be  $\sim 2.8 \text{ g} \cdot \text{cm}^{-3}$ .<sup>21,22</sup> The incorporation of phosphorus in the film decreases the mass density. The mass density is slightly lower for higher substrate temperatures and this is expected to be related to an

increased phosphorus content in the films. Films deposited using a 3:1 cycle ratio have a mass density of  $\sim 2.1 \text{ g} \cdot \text{cm}^{-3}$  for deposition temperatures between 25 and 300 °C. This is in line with our hypothesis, since the phosphorus content does not vary that much for these samples either. In literature the mass density of P-doped  $\text{Al}_2\text{O}_3$  ALD films is reported to vary from  $2.2 \text{ g} \cdot \text{cm}^{-3}$  ( $[\text{P}]:[\text{Al}] = 1.3$ ) to  $2.9 \text{ g} \cdot \text{cm}^{-3}$  ( $[\text{P}]:[\text{Al}] = 0.1$ ).<sup>9,16</sup> Therefore, the obtained mass density for our ALD  $\text{AlP}_x\text{O}_y$  films lies within the lower limit of these literature values.

The as-deposited aluminum phosphate films were also characterized by XRD and were found to be amorphous for the whole temperature range of 25 to 300 °C (Figure S7.6). It has been shown that  $\text{AlP}_x\text{O}_y$  films can be crystallized using a heat treatment of the as deposited films.<sup>17</sup>

The optical constants of the  $\text{AlP}_x\text{O}_y$  films deposited at different temperatures were evaluated using *ex situ* VASE measurements as shown in Figure 7.9. The films are transparent over the whole measured range. The inset of Figure 7.9 shows the refractive indices of films deposited using a 1:1 and 3:1  $\text{PO}_x:\text{Al}_2\text{O}_3$  cycle ratio as a function of wavelength. The refractive indices follow a Cauchy dispersion relation yielding a value of 1.51 and 1.47 at 589 nm, respectively. From the difference in refractive index it can be concluded that when the P content is increased, the refractive index decreases. Our refractive indexes compares well to values reported in literature of ALD  $\text{AlP}_x\text{O}_y$  films, which vary from 1.47 to 1.53.<sup>17,18</sup> Moreover, the

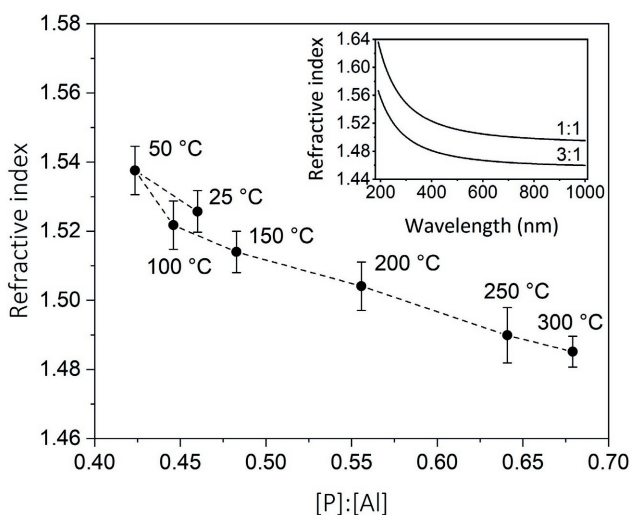


**Figure 7.9** The refractive index versus  $[\text{P}]:[\text{Al}]$  ratio for films deposited using substrate temperatures from 25 - 300 °C and an 1:1 cycle ratio. The refractive index and  $[\text{P}]:[\text{Al}]$  ratio were determined from SE and XPS analysis, respectively. The dashed line serves as a guide to the eye. The inset shows refractive index of films from 190 - 1000 nm determined by *ex situ* VASE for films deposited at 150 °C using a 1:1 and 3:1 cycle ratio.

refractive index for Al<sub>2</sub>O<sub>3</sub> ALD films is reported to be  $1.64 \pm 0.02$  (at 100 °C), also in line with this hypothesis.<sup>14</sup>

As observed from Figure 7.9, the refractive index decreases for higher deposition temperatures. This is expected since the phosphorus content of the films increases as well. Only the phosphorus content of the sample deposited at 25 °C is higher than expected.

### 7.3.4 Surface reactions

To gain more insight into the deposition process, the reaction products within the 1:1 AlP<sub>x</sub>O<sub>y</sub> supercycle recipe were analyzed by mass spectrometry. Insights into the surface reactions can help in understanding the limited incorporation of phosphorus in the film. Moreover, it can give insights into the benefits to use the O<sub>2</sub> plasma coreactant. To identify the species present in the reactor, first the spectra during precursor dosing were measured in the range of  $m/z = 0 - 100$ . As observed in Figure S7.7 in the appendix, the PO(OMe)<sub>3</sub> and AlMe<sub>3</sub> precursors can be tracked by following for example  $m/z = 15$  (CH<sub>3</sub><sup>+</sup>), 79 (PO<sub>3</sub><sup>+</sup>), and 57 (Al(CH<sub>3</sub>)<sub>2</sub><sup>+</sup>). Oxygen can be tracked by following  $m/z = 16$  (O<sup>+</sup>) which overlaps with CH<sub>4</sub>, or  $m/z = 32$  (O<sub>2</sub><sup>+</sup>) which overlaps with CH<sub>3</sub>OH. The typical combustion byproducts H<sub>2</sub>O and CO<sub>2</sub> can be tracked following  $m/z = 18$  (H<sub>2</sub>O<sup>+</sup>) and 44 (CO<sub>2</sub><sup>+</sup>) amu, respectively.

Figure 7.10 depicts the time resolved QMS data of one ALD cycle of AlP<sub>x</sub>O<sub>y</sub> using a 1:1 cycle ratio. In Figure 7.10a-f, the QMS measurements are reported for  $m/z = 15, 16, 18, 44, 57,$  and  $79$ . Additional mass to charge ratios 28 (CO<sup>+</sup> or C<sub>2</sub>H<sub>4</sub><sup>+</sup>), 29 (C<sub>2</sub>H<sub>5</sub><sup>+</sup>/CHO<sup>+</sup>), 30 (C<sub>2</sub>H<sub>6</sub><sup>+</sup>/CH<sub>2</sub>O<sup>+</sup>), 31 (CH<sub>3</sub>O<sup>+</sup>/P<sup>+</sup>), 32 (O<sub>2</sub><sup>+</sup>/CH<sub>3</sub>OH<sup>+</sup>) and 46 (CH<sub>2</sub>O<sub>2</sub><sup>+</sup> or C<sub>2</sub>H<sub>6</sub>O<sup>+</sup>) amu are measured and can be found in appendix Figure S7.8. Also the pressure in the system was monitored and is plotted in Figure 7.10g. The graph is divided into several intervals representing the different ALD process steps: i.e., PO(OMe)<sub>3</sub> dose, O<sub>2</sub> plasma exposure, AlMe<sub>3</sub> dose and O<sub>2</sub> plasma exposure, alternated by Ar purge steps. Compared to the ALD recipe for AlP<sub>x</sub>O<sub>y</sub> described in section 7.2, all purge steps are now extended to 5 s to clearly separate the process steps facilitating data interpretation. Extended purge times did not influence the process. In addition to the standard ALD recipe, also the curves are plotted for recipes when only one of the precursors combined with an O<sub>2</sub> gas flow are used. Since for these recipes no ALD growth occurred, it is possible to distinguish the ALD reaction products from other species present in the reactor, such as precursors, coreactants and background species. In addition, we can exclude species originating from fragmentation and ionization occurring in the mass spectrometer. In every plot three different curves are shown, corresponding to the following recipes: the standard 1:1 recipe, the recipe with only PO(OMe)<sub>3</sub> and O<sub>2</sub>, and the recipe with only AlMe<sub>3</sub> and O<sub>2</sub>.

The delivery of PO(OMe)<sub>3</sub> in the first subcycle led to an increase in signal for  $m/z = 15$  (CH<sub>3</sub><sup>+</sup>) and 79 (PO<sub>3</sub><sup>+</sup>). The increase is not just due to a pressure increase because the signal for the AlMe<sub>3</sub> + O<sub>2(g)</sub> recipe (blue dotted line) is much lower at

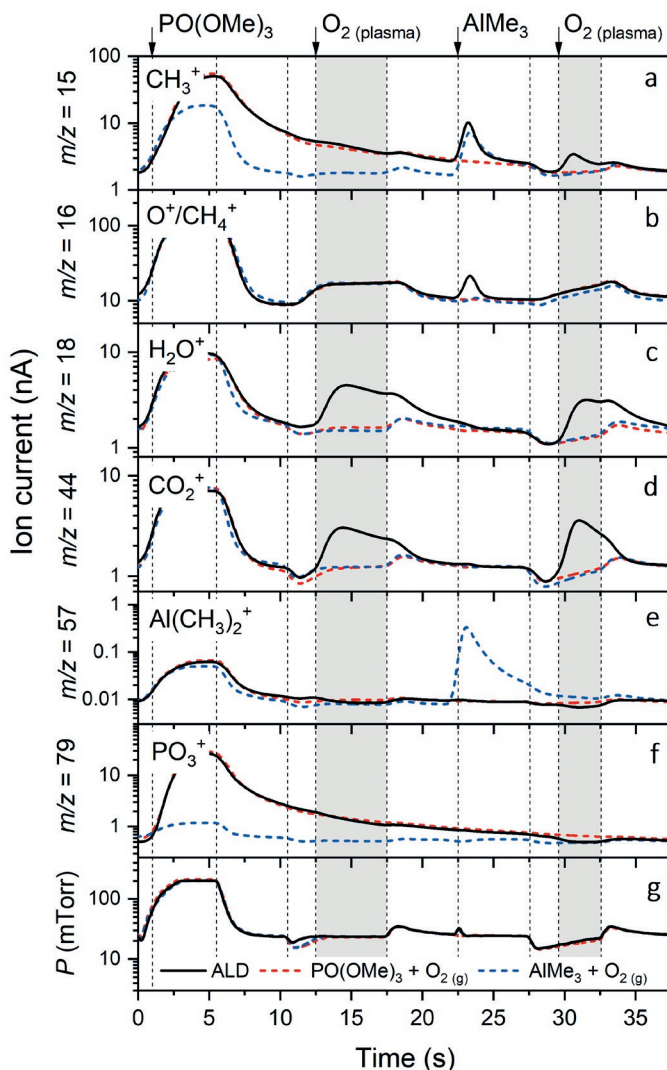


**Figure 7.10** Time-resolved QMS data of  $m/z = 15$  ( $\text{CH}_3^+$  from  $\text{CH}_4$ ,  $\text{PO}(\text{OMe})_3$  or  $\text{AlMe}_3$ ), 16 ( $\text{CH}_4^+$  from  $\text{CH}_4$  or  $\text{O}^+$  from  $\text{O}_2$ ), 18 ( $\text{H}_2\text{O}^+$  from  $\text{H}_2\text{O}$ ), 44 ( $\text{CO}_2^+$  from  $\text{CO}_2$ ), 57 ( $\text{Al}(\text{CH}_3)_2^+$  from  $\text{AlMe}_3$ ), and 79 ( $\text{PO}_3^+$  from  $\text{PO}(\text{OMe})_3$ ). The standard ALD recipe (black) is compared to the  $\text{PO}(\text{OMe})_3 + \text{O}_2$  recipe (red dotted) and  $\text{AlMe}_3 + \text{O}_2$  recipe (blue dotted). The precursor and coreactant dosing steps are alternated by argon purge steps of 5 s.

these  $m/z$  values, although the pressure is comparable. All masses related to the phosphorus precursor show an increase in ion current. This is most likely originating from dissociation of unreacted  $\text{PO}(\text{OMe})_3$  molecules in the mass spectrometer since the standard ALD recipe (black line) and  $\text{PO}(\text{OMe})_3 + \text{O}_2$  recipe (red dashed line)

overlap. The curves representing H<sub>2</sub>O and CO<sub>2</sub> species overlap for all recipes. This means that the CO<sub>2</sub> and H<sub>2</sub>O level were not altered within the measurement error when PO(OMe)<sub>3</sub> is introduced into the chamber. This suggests that no significant release of (precursor) reaction products into the gas phase was observed in the first cycle. Therefore, it can be presumed that the precursor chemisorbs by an association reaction of the complete precursor. In such an association reaction, the precursor remains intact without the release of reaction products into the gas phase.<sup>29</sup>

Next, the O<sub>2</sub> plasma is expected to convert the methoxy groups of the PO(OMe)<sub>3</sub> molecule into –OH or =O. As shown in Figure 7.10, a little amount of CH<sub>3</sub><sup>+</sup> was detected when the O<sub>2</sub> plasma is ignited. In addition, typical combustion byproducts were detected as well, i.e. H<sub>2</sub>O and CO<sub>2</sub>. Appendix Figure S7.8 shows additional formation of C<sub>x</sub>H<sub>y</sub> and C<sub>x</sub>H<sub>y</sub>O<sub>z</sub> byproducts. As observed in Figure 7.2b in section 7.3.1, the growth per supercycle and the relative aluminum content were enhanced in the presence of and for extended O<sub>2</sub> plasma exposure. This implies that when the hydrocarbon groups are removed by the O<sub>2</sub> plasma, surface groups are created that are prone to reactions with AlMe<sub>3</sub> in the next process step.

During the AlMe<sub>3</sub> dose step the formation of CH<sub>4</sub><sup>+</sup> and CH<sub>3</sub><sup>+</sup> products was observed. For CH<sub>3</sub><sup>+</sup>, the difference between the black and blue line is much smaller. CH<sub>3</sub> most certainly originates from dissociative ionization of CH<sub>4</sub> in the mass spectrometer. CH<sub>4</sub> is one of the classical reaction products observed by ALD of Al<sub>2</sub>O<sub>3</sub>. A reaction takes place in which methyl ligands (CH<sub>3</sub>) and hydroxyl groups on the surface combine and form CH<sub>4</sub>.<sup>15</sup> Moreover, it is found that we do not measure any AlMe<sub>3</sub>-related peak during AlP<sub>x</sub>O<sub>y</sub> standard ALD (see Figure 7.10e). AlMe<sub>3</sub> dissociates and/or is consumed by surface reactions with the substrate or reactor walls before it reaches the mass spectrometer. This makes sense since it is well-known that AlMe<sub>3</sub> has a high reactivity.<sup>29</sup> In the AlMe<sub>3</sub> + O<sub>2(g)</sub> recipe (blue dotted line), the molecules do not react or adsorb and stay intact because the substrate and reactor walls were already completely saturated with AlMe<sub>3</sub>. Therefore, we do see a high peak for the AlMe<sub>3</sub> + O<sub>2(g)</sub> recipe.

In the last process step, an O<sub>2</sub> plasma is used to remove the remaining methyl ligands by combustion. It was already shown in section 7.3.1 that without the use of the plasma coreactant the phosphorus content in the film was extremely low, indicating the low reactivity of PO(OMe)<sub>3</sub> with AlMe<sub>x</sub> and necessity for removal of these groups in this process step (see Figure 7.2d). As shown in Figure 7.10a and b, CH<sub>3</sub><sup>+</sup> ions are formed, but also the typical combustion products H<sub>2</sub>O and CO<sub>2</sub>. Figure S7.8 shows additional formation of C<sub>x</sub>H<sub>y</sub> and C<sub>x</sub>H<sub>y</sub>O<sub>z</sub> byproducts, similar to the combustion of the phosphorus precursor ligands. The formation of H<sub>2</sub>O in the plasma could lead to additional (thermal ALD like) reaction pathways, as was the case for Al<sub>2</sub>O<sub>3</sub>.<sup>19</sup>

It was shown in section 7.3.3 that the [P]:[Al] ratio is only 0.5 when a 1:1 cycle ratio is used. QMS data suggests that, unlike AlMe<sub>3</sub>, the relatively bulky phosphorus

precursor remains intact upon adsorption and limits the incorporation of phosphorus atoms by steric hindrance. Therefore, it can indeed be expected that the aluminum content of films deposited using the 1:1 cycle process is larger than the phosphorus content. In the  $\text{AlP}_x\text{O}_y$  paper by Dobbelaere et al,  $\text{AlP}_x\text{O}_y$  films are obtained with an [P]:[Al] atomic ratio of 1.8 using plasma polymerization.<sup>18</sup> In this case the  $\text{PO}(\text{OMe})_3$  molecules are partly dissociated in the plasma and therefore steric hindrance is not an issue. However, for our process the limited phosphorus incorporation can be overcome by using  $> 1 \text{ PO}_x$  cycles.

## 7.4 Conclusions

Amorphous aluminum phosphate thin films have been deposited by plasma-assisted ALD using a wide deposition temperature range of 25 to 300 °C. ALD behavior was achieved for every precursor and coreactant process step and the process resulted in ALD films with excellent uniformity and conformality as demonstrated on 200 mm wafers and nanowires, respectively. It has been shown that the use of an  $\text{O}_2$  plasma step is beneficial for increasing surface reactivity for the precursor molecules. When using a substrate temperature of 150 °C, the growth per supercycle saturates at  $\sim 1.8 \text{ \AA}$ . The [P]:[Al] atomic ratio for the saturated process is approximately 0.5 ( $\text{AlP}_{0.5}\text{O}_{2.9}$ ) and can be tailored by changing the ratio between the  $\text{Al}_2\text{O}_3$  and  $\text{PO}_x$  cycles and/or the substrate temperature. When using 2  $\text{PO}_x$  cycles, a composition close to  $\text{AlPO}_4$  is obtained. The use of higher substrate temperatures reduces the incorporation of hydrogen impurities and the adsorption of aluminum atoms, which, as a result, leads to an increase in the phosphorus content in the film. It is expected that the lower phosphorus limit of the  $\text{AlP}_x\text{O}_y$  1:1  $\text{PO}_x:\text{Al}_2\text{O}_3$  cycle process is determined by differences in chemisorption processes of both precursors and steric hindrance of the phosphorus precursor. Regarding this effect, it has been proposed that  $\text{PO}(\text{OMe})_3$  chemisorbs on the surface without the release of reaction products into the gas phase. Instead, the introduction of  $\text{AlMe}_3$  results in a release of  $\text{CH}_4$  groups in the gas phase, similar to the more commonly used ALD process of  $\text{Al}_2\text{O}_3$ . The two intermediate  $\text{O}_2$  plasma steps are needed to remove the (remaining) organic ligands of both precursor molecules and introduce surface groups that are prone to reactions with the precursors. Altogether, it has been shown that the use of an  $\text{O}_2$  plasma can offer advantages to more commonly used thermal ALD processes of  $\text{AlP}_x\text{O}_y$  and deliver high quality ALD films.

## Acknowledgements

This project is financially supported by ADEM, A green Deal in Energy Materials of the Ministry of Economic Affairs of The Netherlands. The authors gratefully acknowledge Dr. Marcel Verheijen for TEM analysis and Cristian van Helvoirt for technical assistance. Solliance and the Dutch province of Noord-Brabant are acknowledged for

funding the TEM facility. Furthermore, the authors would like to thank the Advanced Nanomaterials & Devices group of Prof. Erik Bakkers for providing the substrates with nanowire arrays.

## References

1. S. ChandraKishore and A. Pandurangan. Synthesis and characterization of Y-shaped carbon nanotubes using Fe/ $\text{AlPO}_4$  catalyst by CVD. *Chem. Eng. J.* **222**, 472–477 (2013).
2. F. Yaripour, M. Mollavali, S. M. Jam, et al. Catalytic dehydration of methanol to dimethyl ether catalyzed by aluminum phosphate catalysts. *Energy and Fuels* **23**, 1896–1900 (2009).
3. S. Deng, B. Xiao, B. Wang, et al. New insight into atomic-scale engineering of electrode surface for long-life and safe high voltage lithium ion cathodes. *Nano Energy* **38**, 19–27 (2017).
4. B. Xiao, B. Wang, J. Liu, et al. Highly stable  $\text{Li}_{1.2}\text{Mn}_{0.54}\text{Co}_{0.13}\text{Ni}_{0.13}\text{O}_2$  enabled by novel atomic layer deposited  $\text{AlPO}_4$  coating. *Nano Energy* **34**, 120–130 (2017).
5. Y. Lu, A. N. Mansour, N. Yabuuchi, et al. Probing the origin of enhanced stability of “ $\text{AlPO}_4$ ” nanoparticle coated  $\text{LiCoO}_2$  during cycling to high voltages: combined XRD and XPS studies. *Chem. Mater.* **21**, 4408–4424 (2009).
6. E. Jung and Y. J. Park. Characterization of thermally aged  $\text{AlPO}_4$ -coated  $\text{LiCoO}_2$  thin films. *Nanoscale Res. Lett.* **7**, 1–4 (2012).
7. S. Verdier, L. El Ouatani, R. Dedryvère, et al. XPS study on  $\text{Al}_2\text{O}_3$ - and  $\text{AlPO}_4$ -coated  $\text{LiCoO}_2$  cathode material for high-capacity Li ion batteries. *J. Electrochem. Soc.* **154**, A1088–A1099 (2007).
8. S. T. Meyers, J. T. Anderson, D. Hong, et al. Solution-processed aluminum oxide phosphate thin-film dielectrics. *Chem. Mater.* **19**, 4023–4029 (2007).
9. M. Tiitta, E. Nykänen, P. Soininen, et al. Preparation and characterization of phosphorus-doped aluminum oxide thin films. *Mater. Res. Bull.* **33**, 1315–1323 (1998).
10. W. Hong, X. Bin, L. Xiling, et al. The piezoelectric and elastic properties of berlinite and the effect of defects on the physical properties. *J. Cryst. Growth* **79**, 227–231 (1986).
11. S. Knohl, A. K. Roy, R. Lungwitz, et al. Nonaqueous atomic layer deposition of aluminum phosphate. *ACS Appl. Mater. Interfaces* **5**, 6161–6167 (2013).
12. J. Liu, Y. Tang, B. Xiao, et al. Atomic layer deposited aluminium phosphate thin films on N-doped CNTs. *RSC Adv.* **3**, 4492–4495 (2013).
13. K. M. Norelli, P. N. Plassmeyer, K. N. Woods, et al. Influence of composition and processing parameters on the properties of solution-processed aluminum phosphate oxide ( $\text{AlPO}$ ) thin films. *Solid State Sci.* **55**, 8–12 (2016).
14. S. M. George. Atomic layer deposition: An overview. *Chem. Rev.* **110**, 111–131 (2010).
15. A. J. M. Mackus, J. R. Schneider, C. Maclsaac, et al. Synthesis of doped, ternary, and quaternary materials by atomic layer deposition: A review. *Chem. Mater.* **31**, 1142–1183 (2019).



16. M. Nieminen, L. Niinistö and R. Lappalainen. Determination of P/Al ratio in phosphorus-doped aluminium oxide thin films by XRF, RBS and FTIR. *Mikrochim. Acta* **119**, 13–22 (1995).
17. J. Hämäläinen, J. Holopainen, F. Munnik, et al. Atomic layer deposition of aluminum and titanium phosphates. *J. Phys. Chem. C* **116**, 5920–5925 (2012).
18. T. Dobbelaere, A. K. Roy, P. Vereecken, et al. Atomic layer deposition of aluminum phosphate based on the plasma polymerization of trimethyl phosphate. *Chem. Mater.* **26**, 6863–6871 (2014).
19. S. B. S. Heil, J. L. Van Hemmen, M. C. M. Van De Sanden, et al. Reaction mechanisms during plasma-assisted atomic layer deposition of metal oxides: A case study for Al<sub>2</sub>O<sub>3</sub>. *J. Appl. Phys.* **103**, (2008).
20. N. Hornsveld, W. M. M. Kessels and M. Creatore. Mass spectrometry study of Li<sub>2</sub>CO<sub>3</sub> film growth by thermal and plasma-assisted atomic layer deposition. *J. Phys. Chem. C* **123**, 4109–4115 (2019).
21. J. L. van Hemmen, S. B. S. Heil, J. H. Klootwijk, et al. Plasma and thermal ALD of Al<sub>2</sub>O<sub>3</sub> in a commercial 200 mm ALD reactor. *J. Electrochem. Soc.* **154**, G165–G169 (2007).
22. S. E. Potts, G. Dingemans, C. Lachaud, et al. Plasma-enhanced and thermal atomic layer deposition of Al<sub>2</sub>O<sub>3</sub> using dimethylaluminum isopropoxide, [Al(CH<sub>3</sub>)<sub>2</sub>(μ-OiPr)]<sub>2</sub>, as an alternative aluminum precursor. *J. Vac. Sci. Technol. A Vacuum, Surfaces, Film.* **30**, 021505 (2012).
23. L. E. Black and W. M. M. E. Kessels. Investigation of crystalline silicon surface passivation by positively charged POx/Al<sub>2</sub>O<sub>3</sub> stacks. *Sol. Energy Mater. Sol. Cells* **185**, 385–391 (2018).
24. M. K. Templeton and W. H. Weinberg. Adsorption and decomposition of dimethyl methylphosphonate on an aluminum oxide surface. *J. Am. Chem. Soc.* **107**, 97–108 (1985).
25. M. B. Mitchell, V. N. Sheinker and E. A. Mintz. Adsorption and decomposition of dimethyl methylphosphonate on metal oxides. *J. Phys. Chem. B* **101**, 11192–11203 (1997).
26. H. B. Profijt, P. Kudlacek, M. C. M. van de Sanden, et al. Ion and photon surface interaction during remote plasma ALD of metal oxides. *J. Electrochem. Soc.* **158**, 88–91 (2011).
27. D. Hasha, L. S. de Saldarriaga, C. Saldarriaga, et al. Studies of silicoaluminophosphates with the sodalite structure. *J. Am. Chem. Soc.* **110**, 2127–2135 (1988).
28. H. He, K. Alberti, T. L. Barr, et al. ESCA studies of aluminophosphate molecular sieves. *J. Phys. Chem.* **97**, 13703–13707 (1993).
29. R. L. Puurunen. Surface chemistry of atomic layer deposition: A case study for the trimethylaluminum/water process. *J. Appl. Phys.* **97**, 121301 (2005).

## Appendix

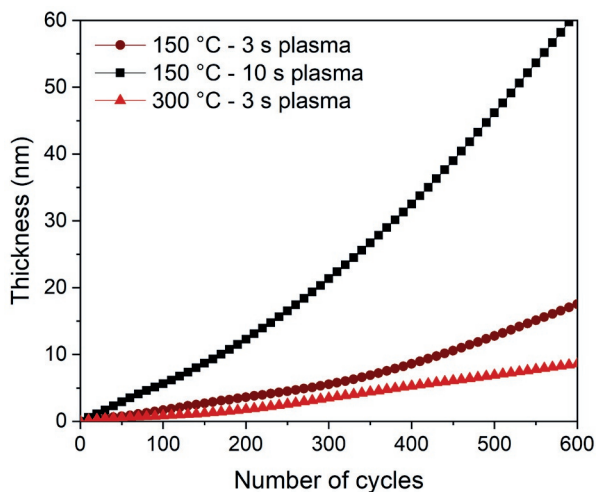


**Figure S7.1** *In situ* thickness measurement for ALD of  $\text{PO}_x$  at 150 °C using plasma exposure times of 3 s (circles) and 10 s (squares) and at 300 °C using a plasma exposure time of 3 s (triangles). The large difference between the 3 s and 10 s plasma exposure recipes shows that the growth per cycle does not saturate with respect to  $\text{O}_2$  plasma exposure time. The Ar purge time duration was 10 s.

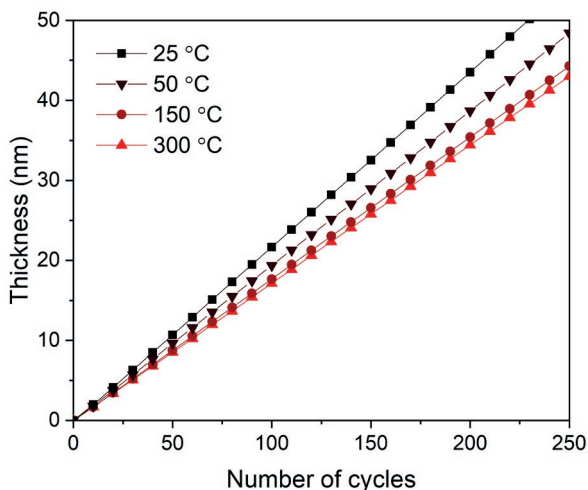


**Figure S7.2** *In situ* thickness measurements for ALD of  $\text{AlP}_x\text{O}_y$  at 25, 50, 150, and 300 °C.

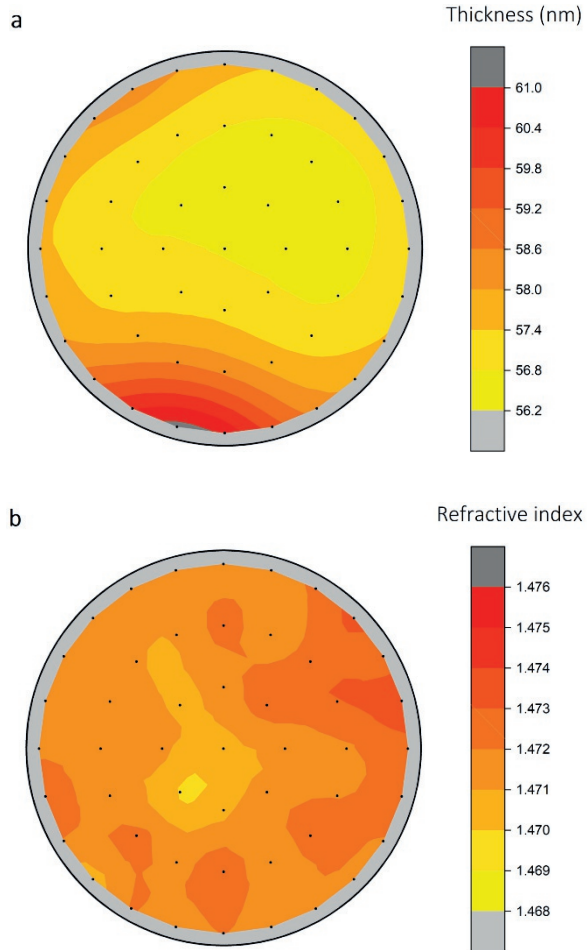


**Figure S7.3** Contour maps of a) thickness and the b) refractive index of  $\text{AlP}_x\text{O}_y$  films across 200 mm wafers as determined from SE mapping. The measurements were performed on  $\text{AlP}_x\text{O}_y$  films deposited at 150 °C using a 3:1  $\text{PO}_x:\text{Al}_2\text{O}_3$  cycle ratio. The black circle indicates the dimensions of the wafer. An edge-exclusion of 6 mm was used.

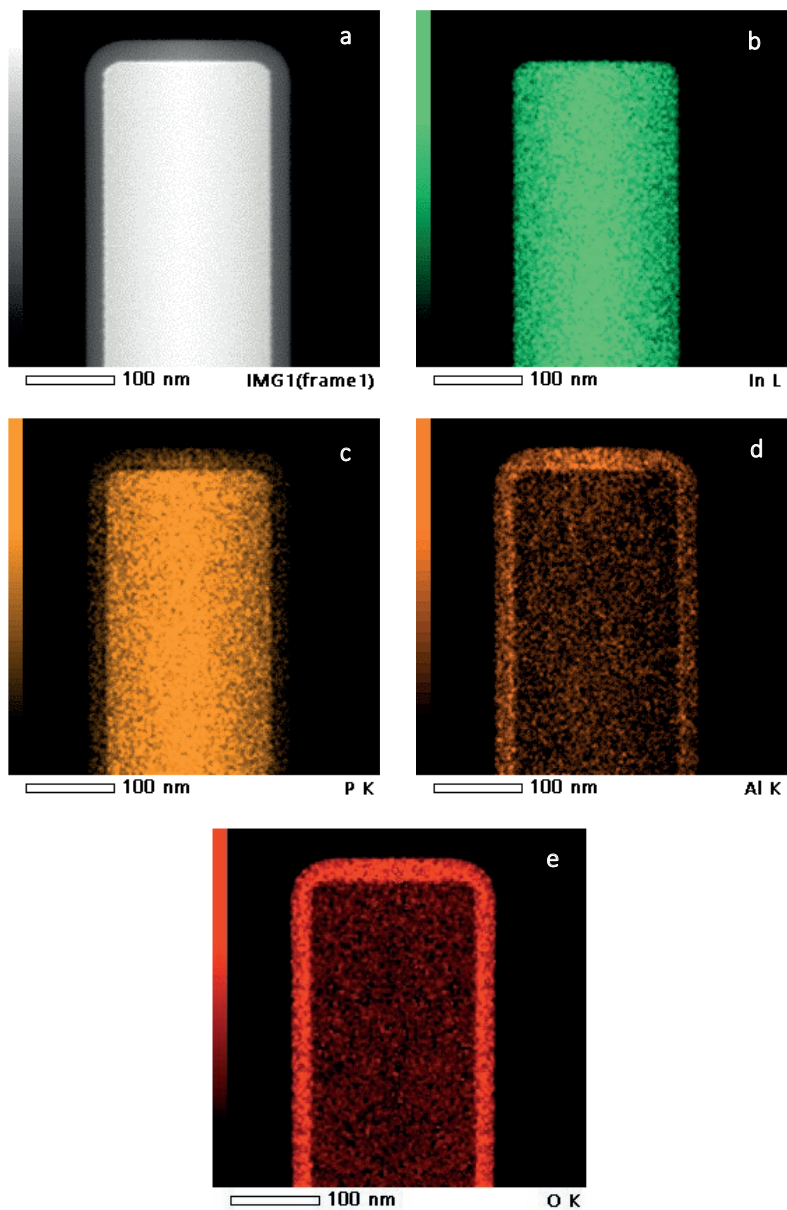


**Figure S7.4** Single WZ InP nanowire array with  $\text{AlP}_x\text{O}_y$  films prepared using a 3:1 cycle ratio. a) HAADF-STEM and b-e) EDX mappings showing b) indium, c) phosphorus, d) aluminum and e) oxygen. Indium and phosphorus are present inside the wire and a uniform film of  $\text{AlP}_x\text{O}_y$  is visible on top.

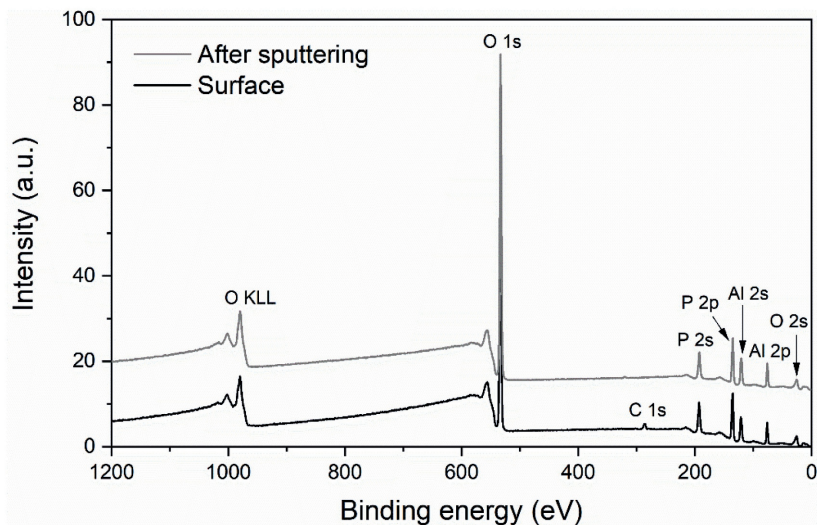


**Figure S7.5** XPS survey spectra of a 50 nm aluminum phosphate film grown at 150 °C using a 3:1 cycle ratio with (top) and without (bottom) the use of sputtering.

**Table S7.1** *Ex situ* XPS stoichiometry results for  $\text{AlP}_x\text{O}_y$  films deposited using 1:1 and 3:1  $\text{PO}_x:\text{Al}_2\text{O}_3$  cycle ratio and deposition temperatures from 25 - 300 °C. Note that with XPS no hydrogen could be probed.

Sample	[P]:[Al] ratio	[Al] (at. %)	[P] (at. %)	[O] (at. %)	[C] (at. %)
1:1 - 25 °C	0.46	19.6 ± 0.5	9.1 ± 0.5	67.9 ± 0.5	3.4 ± 0.5
1:1 - 50 °C	0.42	21.0	8.9	65.3	4.8
1:1 - 100 °C	0.44	20.5	9.1	66.8	3.2
1:1 - 150 °C	0.49	20.0	9.7	67.6	1.1
1:1 - 200 °C	0.56	18.9	10.5	66.3	4.2
1:1 - 250 °C	0.64	18.8	12.0	67.6	1.5
1:1 - 300 °C	0.68	18.4	12.5	67.2	2.0
<hr/>					
3:1 - 25 °C	1.44	11.8	17.0	68.6	2.6
3:1 - 50 °C	1.35	12.5	16.9	68.2	2.4
3:1 - 150 °C	1.11	14.1	15.7	67.0	3.2
3:1 - 250 °C	1.09	13.8	15.0	67.1	3.2
3:1 - 300 °C	1.18	14.3	16.9	65.8	3.0

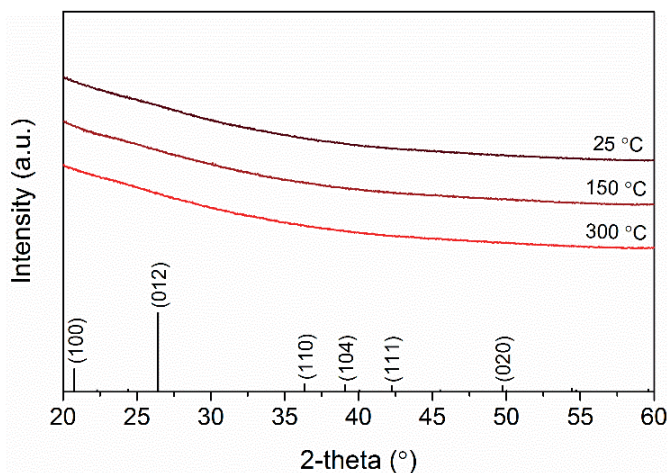


**Figure S7.6** XRD gonio scans of  $\sim 50$  nm thick  $\text{AlP}_x\text{O}_y$  films grown on Si with native oxide and using a 1:1 cycle ratio. The bars in the lower panel indicate the expected diffraction from an  $\text{AlP}_x\text{O}_y$  powder sample. The diffractograms do not show any peaks, indicating the films are predominantly amorphous in nature.

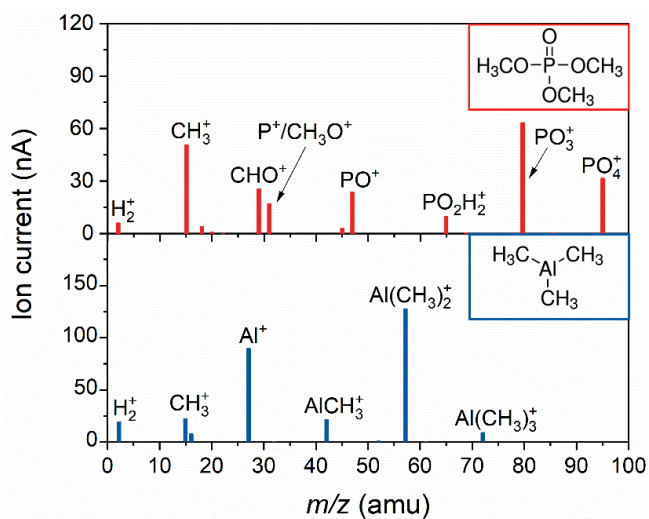


**Figure S7.7** The cracking patterns obtained by mass spectrometry during  $\text{PO}(\text{OMe})_3$  and  $\text{AlMe}_3$  precursor dose. The inserts show the chemical structure of the  $\text{PO}(\text{OMe})_3$  and  $\text{AlMe}_3$  precursor molecule, respectively.

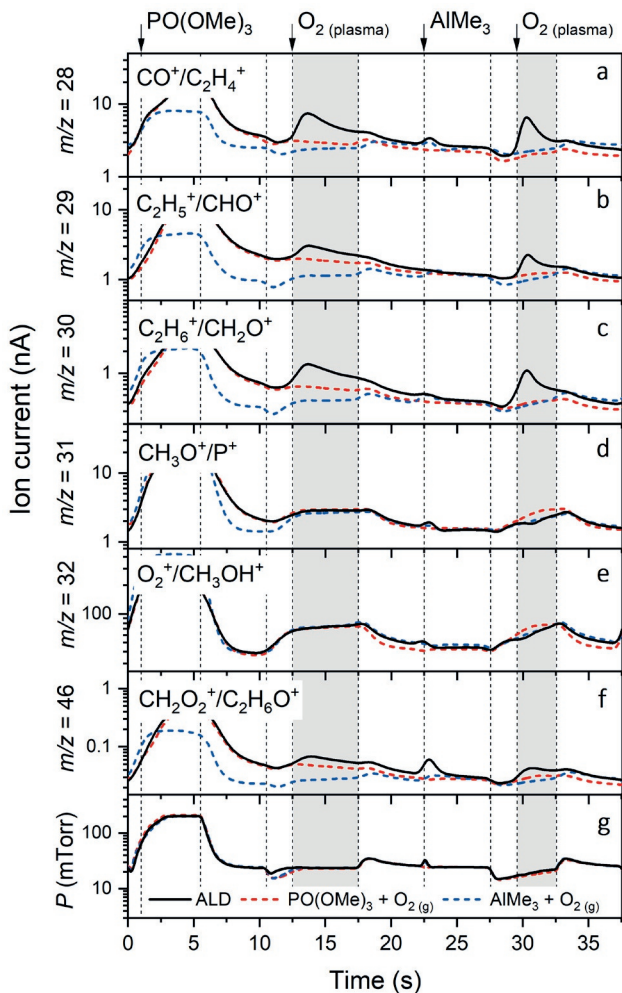


**Figure S7.8** Time-resolved QMS data of  $m/z = 28$  ( $\text{CO}^+$  or  $\text{C}_2\text{H}_4^+$  from  $\text{CO}$ ,  $\text{CO}_2$ ,  $\text{C}_2\text{H}_4$  or  $\text{C}_2\text{H}_6$ ), 29 ( $\text{C}_2\text{H}_5^+$  or  $\text{CHO}^+$  from  $\text{C}_2\text{H}_6$ ,  $\text{CH}_2\text{O}$  or  $\text{PO}(\text{OMe})_3$ ), 30 ( $\text{C}_2\text{H}_6^+$  or  $\text{CH}_2\text{O}^+$  from  $\text{C}_2\text{H}_6$  or  $\text{CH}_2\text{O}$ ), 31 ( $\text{CH}_3\text{O}^+$  or  $\text{P}^+$  from  $\text{CH}_3\text{OH}$  or  $\text{PO}(\text{OMe})_3$ ), 32 ( $\text{O}_2^+$  or  $\text{CH}_3\text{OH}^+$  from  $\text{O}_2$  or  $\text{CH}_3\text{OH}$ ), and 46 ( $\text{CH}_2\text{O}_2^+$  or  $\text{C}_2\text{H}_6\text{O}^+$  from  $\text{CH}_2\text{O}_2$ ). The standard ALD recipe (black) is compared to the recipe with only  $\text{PO}(\text{OMe})_3$  dose (red dotted) the recipe with only  $\text{AlMe}_3$  (blue dotted). The precursor and coreactant dosing steps are alternated by argon purge steps of 5 s.







# 8

## Conclusions and outlook

---

---

This chapter provides answers to the research questions posed in the introduction. Moreover, the conclusions clarify how the thesis makes a valuable contribution to the field of ALD for Li-ion batteries. Additionally, points of attention are being mentioned and discussed, and conclusions are drawn which lead to suggestions for future research.

## 8.1 Conclusions

The goal of this work was to develop and to understand existing and novel plasma-assisted and thermal ALD chemistries to deposited thin films which can serve as artificial EEI in Li-ion batteries. From the literature research in Chapter 2 it could be concluded that artificial EEIs are very promising for improvement of Li-ion batteries. However, there are still many opportunities in expanding the available ALD chemistries to deliver artificial EEIs as well as to improve understanding in the synthesis of ALD films. For instance, the existing literature studies do not yet explore the possibility to adopt plasma-assisted ALD for the synthesis of artificial EEIs, which could be especially interesting when processing time or temperature becomes crucial. The conclusions drawn from the remaining chapters in this thesis give answers to the research questions as outlined in the introduction and are summarized here.

### *The developed ALD chemistries and their typical growth behavior*

In the current work, various ALD chemistries have been developed and examined which are potentially useful for the synthesis of artificial EEIs. Specifically, in Chapter 4 it was shown that plasma-assisted and thermal ALD can be adopted to grow ultra-thin  $\text{Li}_2\text{CO}_3$  films between 50 and 300 °C using lithium tert-butoxide as a precursor and  $\text{O}_2$  plasma or  $\text{H}_2\text{O}/\text{CO}_2$  as coreactants. Both processes were shown to have a wide ALD temperature window in which self-limiting growth of  $\sim 0.8$  and  $0.60$  Å per cycle was obtained, respectively. In Chapter 6, a new ALD chemistry has been demonstrated to prepare LiF films using  $\text{LiN}(\text{SiMe}_3)_2$  and  $\text{SF}_6$  plasma. For this process, a growth per cycle of  $\sim 0.4$  Å was obtained. After an initial increase, the growth per cycle as a function of the plasma exposure time decreases again for extended plasma exposure times. Possible explanations are an etching effect of the  $\text{SF}_6$  plasma, inhibition of precursor adsorption after exposing the surface for a longer time to F radicals, or a change in film properties by the length of the plasma exposure time which subsequently effects the growth itself. Chapter 7 presents a novel plasma-assisted ALD chemistry to deposit aluminum phosphate ( $\text{AlP}_x\text{O}_y$ ) films using supercycles consisting of (i)  $\text{PO}(\text{OMe})_3$  dosing combined with  $\text{O}_2$  plasma exposure and (ii)  $\text{AlMe}_3$  dosing followed by  $\text{O}_2$  plasma exposure.  $\text{AlP}_x\text{O}_y$  thin films could be deposited between 25 and 300 °C. ALD behavior was achieved for every precursor and coreactant process step, and the process resulted in a growth per supercycle is found to be 1.8 Å using a 1:1  $\text{PO}_x:\text{Al}_2\text{O}_3$  cycle ratio.

### *Tunability of the film properties using the ALD process parameters*

For the developed ALD recipes, the properties of the as-deposited films were investigated. Moreover, the influence of the ALD process parameters on the film properties was studied. High purity films were obtained for all investigated processes. Also, the film properties of the deposited films did not show noticeable changes after prolonged exposure to atmosphere. These results suggest that the  $\text{Li}_2\text{CO}_3$ , LiF and

$\text{Al}_x\text{PO}_y$  films grown by ALD are stable under ambient conditions. For both  $\text{Li}_2\text{CO}_3$  processes, stoichiometric films could be deposited. The stoichiometry of the plasma-assisted ALD process of  $\text{Li}_2\text{CO}_3$  shows a temperature dependence. It is possible to deposit  $\text{Li}_2\text{O}$  at temperatures  $> 250\text{ }^\circ\text{C}$  through combustion of the organic ligands. The formation of  $\text{Li}_2\text{O}$  can be further promoted by prolonging the plasma exposure time. The thermal ALD deposition of  $\text{Li}_2\text{O}$  requires omitting the  $\text{CO}_2$  step from the process. The  $\text{Li}_2\text{CO}_3$  films are crystalline, however, the crystallinity is suppressed, and surface roughness increases when  $\text{Li}_2\text{O}$  is introduced in the films. For  $\text{Al}_x\text{PO}_y$ , the stoichiometry (i.e. [P]:[Al] atomic ratio) can be tailored by changing the  $\text{PO}_x:\text{Al}_2\text{O}_3$  cycle ratio or the substrate temperature. In literature reports where the same aluminum precursor was used, the [P]:[Al] atomic ratio was either limited to 0.2 or a very high number of phosphorus cycles was needed in order to increase the phosphorus content. Instead, in this thesis deposition of films with a composition close to  $\text{AlPO}_4$  by using a 2:1  $\text{PO}_x:\text{Al}_2\text{O}_3$  cycle ratio was demonstrated. The use of higher substrate temperatures reduces the incorporation of hydrogen and aluminum atoms, which, as a result, leads to an increase in the phosphorus content in the film. In contrast to the other ALD processes in this thesis, the  $\text{Al}_x\text{PO}_y$  ALD process led to deposition of amorphous films for the whole temperature range. The study of LiF ALD mainly focused on the effect of the  $\text{SF}_6$  plasma step. Within the measurement error, no deviation in film stoichiometry, crystallinity or density was found for the plasma conditions studied. However, prolongation of the plasma exposure time leads to an increase in optical absorption. Therefore, it is considered plausible to attribute the presence of the absorption features to the interaction of the  $\text{SF}_6$  plasma with the film. Also, lower growth per cycle values were obtained for longer plasma exposure times, and therefore short plasma exposure times are preferred.

#### *The reaction mechanisms of the selected ALD processes*

To gain more insight into the deposition process, the reaction mechanism of the developed ALD processes was investigated using mass spectrometry. For both  $\text{Li}_2\text{CO}_3$  processes it was concluded that in the first half-cycle the  $\text{LiO}^t\text{Bu}$  chemisorbs on the surface by an association reaction of the complete precursor whereas in the second half-cycle the organic ligand is abstracted as tert-butanol (see Chapter 5). The differences between the two processes mainly lie in the formation of  $\text{CO}_2$  and  $\text{H}_2\text{O}$  reaction byproducts in the second half-cycle when, instead of  $\text{H}_2\text{O}$ , an  $\text{O}_2$  plasma is used as coreactant. The formation of  $\text{CO}_2$  in the plasma is especially interesting as it allows for the fabrication of  $\text{Li}_2\text{CO}_3$  films directly: it is possible to deposit  $\text{Li}_2\text{CO}_3$  with less process steps since we do not need to add  $\text{CO}_2$  intentionally, as is the case for thermal ALD. The reaction with  $\text{CO}_2$  appears to be reversible at higher deposition temperatures ( $T \geq 250\text{ }^\circ\text{C}$ ) and by using extended plasma exposure times. Therefore, the composition of the plasma-assisted ALD films can be varied between  $\text{Li}_2\text{CO}_3$  and  $\text{Li}_2\text{O}$ . From the detected species during ALD of LiF it could be concluded the

$\text{LiN}(\text{SiMe}_3)_2$  ligand already partly dissociates during the precursor dosing step. In contrast to thermal ALD, additional formation of different fluoromethylsilane and fluorocarbon species was observed during the  $\text{SF}_6$  plasma exposure step. Most likely the  $\text{SF}_6$  plasma species promote the abstraction of the remaining ligands and their subsequent dissociation in the plasma. For the  $\text{Al}_x\text{PO}_y$  process, differences in chemisorption processes of both precursors and steric hindrance of the phosphorus precursor leads to a lower phosphorus content in the film. Regarding this effect, it has been proposed that  $\text{PO}(\text{OMe})_3$  chemisorbs on the surface without the release of reaction products into the gas phase. Instead, the introduction of  $\text{AlMe}_3$  results in a release of  $\text{CH}_4$  groups in the gas phase, similar to the more commonly used ALD process of  $\text{Al}_2\text{O}_3$ . The two intermediate  $\text{O}_2$  plasma steps are needed to remove the (remaining) organic ligands of both precursor molecules and to introduce surface groups that are prone to reactions with the precursors.

*The differences between the plasma-assisted processes and their thermal counterparts*

For the different model systems studied, the differences between plasma-assisted and thermal ALD are investigated. A comparison in terms of growth behavior, but also chemical, crystallographic, optical and electrochemical properties of the films are studied. The most remarkable conclusions are summarized here. A comparison between the two  $\text{Li}_2\text{CO}_3$  processes showed that plasma-assisted ALD allows for shorter deposition times and higher GPC values compared to its thermal ALD counterpart, leading to an increase in reactor throughput. Moreover, the use of plasma allows for the possibility to deposit at slightly lower process temperatures, which would be beneficial for temperature-sensitive substrates. In addition, the generation of  $\text{CO}_2$  in the plasma, makes it possible to deposit  $\text{Li}_2\text{CO}_3$  films directly by plasma-assisted ALD. When comparing the  $\text{AlP}_x\text{O}_y$  ALD studies in this thesis to earlier reported  $\text{AlP}_x\text{O}_y$  ALD studies using  $\text{H}_2\text{O}$  and  $\text{O}_3$  as coreactants or without using coreactants, the use of an  $\text{O}_2$  plasma generally leads to higher GPC values. Also, plasma-assisted ALD of  $\text{AlP}_x\text{O}_y$  was shown to have a wider temperature window compared to its thermal counterpart. For  $\text{LiF}$  thermal ALD reported in literature, no optical absorption features were observed. Besides, as  $\text{SF}_6$  plasmas etch Si-based materials, 10  $\text{AlO}_x$  ALD cycles ( $\sim 1.5$  nm) were needed as a protective layer prior to plasma-assisted  $\text{LiF}$  processing on Si.  $\text{LiF}$  can only be used on electrodes which are insensitive to etching of the  $\text{SF}_6$  plasma or in combination with a protective layer. Furthermore, all the developed processes in this thesis allow for conformal coating of high aspect ratio substrates (AR between 10 - 25) which can be important for future Li-ion batteries. The conformality on high aspect ratio pillars is slightly lower for the plasma-assisted ALD process of  $\text{Li}_2\text{CO}_3$ , compared to the thermal ALD process. In addition, the ionic conductivity for both  $\text{Li}_2\text{CO}_3$  processes is measured for the first time and is in the order of  $10^{-10} \text{ S} \cdot \text{cm}^{-1}$  for plasma-assisted as well as thermal ALD films.

---

*The merits of plasma-assisted ALD processes for deposition of materials which could serve as artificial EEI*

It is expected that the developed plasma-assisted ALD processes could be useful for deposition of artificial EEI films. This expectation is based on the good material quality of the deposited films and the ability to deposit uniform and conformal films on 3D structures. From the various results in this thesis selected merits are highlighted:

- The plasma-assisted processes of  $\text{Li}_2\text{CO}_3$  and  $\text{Al}_x\text{PO}_y$  generally have shorter cycle times and higher growth per cycle values and therefore allow for shorter deposition times over their thermal counterparts. This can be beneficial when process throughput becomes relevant.
- Plasma-assisted ALD of  $\text{Li}_2\text{CO}_3$  and  $\text{Al}_x\text{PO}_y$  have a wider ALD temperature window compared to their thermal counterparts.
- Unlike thermal ALD  $\text{Li}_2\text{CO}_3$ , the stoichiometry of plasma-assisted  $\text{Li}_2\text{CO}_3$  films, ranging from  $\text{Li}_2\text{CO}_3$  to  $\text{Li}_2\text{O}$ , can be controlled by substrate temperature and  $\text{O}_2$  plasma exposure time.
- It has been shown that the use of an  $\text{O}_2$  plasma step is beneficial for increasing surface reactivity for the precursor molecules for  $\text{Al}_x\text{PO}_y$  ALD.
- Fluorine plasmas are readily available in many plasma aided ALD reactors, making plasma-assisted LiF deposition accessible.

To summarize, several material systems were investigated and a considerable contribution to the fundamental understanding in ALD was generated. Specifically, understanding of plasma-assisted ALD processes, the different benefits of plasma-assisted ALD and the ability to coat 3D structures conformally could be very useful for further research on artificial EEIs and for potentially new application fields in which these properties will be required.

## 8.2 Perspectives of future work

A major part of this dissertation is aimed at the fundamental understanding of the ALD process and film properties. These aspects have been extensively investigated. With the obtained knowledge, excellent control over the film properties can be achieved. Based on the current results, it is expected that the developed ALD processes could be useful for deposition of artificial EEI films. Promising results were obtained, for instance, for the conformality of the  $\text{Li}_2\text{CO}_3$  ALD process on  $2 \times 50 \mu\text{m}$  pillars. However, for solid-state batteries AR of  $> 50$  (depending on the thickness of the electrode) might be needed to achieve high power capability.<sup>1</sup> The conformality should therefore be further investigated when certain applications are demanded. Moreover, experiments are needed to evaluate the electrochemical properties of the films. This especially holds for  $\text{Al}_x\text{PO}_y$  and LiF films; for  $\text{Li}_2\text{CO}_3$  the properties need to be investigated in more detail. For example, it should be tested if the films are

pin-hole free, allow for Li-ion transport and possibly electronically insulating (the latter depends on the battery configuration). In addition, the implementation of these films in a battery half-cell should be carried out and evaluated. Moreover, the mechanical properties of the films must be tested as the artificial EEs should be mechanically stable, especially for anodes that undergo large volume changes. The ALD process parameters and the evaluated film properties so far should be correlated to the electrochemical and mechanical properties. It would be interesting to investigate if the electrochemical and mechanical properties can be tuned by the ALD process parameters to achieve the best results for different electrodes. Eventually, it should be possible to rationally design films by ALD.

From the literature studies in Chapter 2, we can clearly see the effectiveness that ultrathin protective films by ALD generally have in improving the performance of both the anode and cathode in Li-ion batteries. Each of these materials have their own unique properties. However, a better understanding of why certain ALD chemistries work well on selected electrodes is needed. It is particularly important to address working mechanisms of the ALD films to be able to develop artificial EEs with more rational design. In this way, advanced characterization tools, especially *in situ* techniques to measure during battery operation, will play an essential part.

The excellent control over the quality of films and the straightforward deposition process promises a great potential for industry-level applications of ALD in the future. In this work, lab-scale substrates were used in various ALD processes. Moreover, the growth per cycle of a typical ALD process is on the order of 0.1 nm. For Li-ion batteries, but also for different energy-related applications, a technique which can fabricate materials in a relatively large amount and short time is required. Otherwise, cost effectiveness can not be achieved. ALD is still facing some challenges when it comes to industry-scale application. In the past years, spatial ALD (sALD) has been tested to decrease processing times. During sALD, the substrate moves through separated gas zones of constantly flowing reactants. Growth rates in sALD are determined primarily by substrate translation speeds rather than the purge times during temporal (conventional) ALD. Yet, sALD was employed, for instance, for ALD of  $\text{Al}_2\text{O}_3$  on porous  $\text{LiCoO}_2$  battery electrodes.<sup>2</sup> The results for improved battery performance were comparable for temporal and sALD-coated electrodes. Holst Centre and their spin-off LionVolt in the Netherlands are currently working on spatial ALD (sALD) to fabricate a prototype of a 3D solid-state battery.<sup>3</sup> Also, batch and inline deposition tools are being explored. Currently, there is a lot of interest in roll-to-roll ALD for application in Li-ion batteries.<sup>4,5</sup> This technique is an industrial, low-cost, high throughput method to deposited ALD films, which opens up possibilities for future battery design. It has already been shown that electrode or separator sheets up to 600 mm wide can be processed by roll-to-roll ALD. NMC cathodes were provided with ALD  $\text{TiO}_2$  films using the roll-to-roll technique with a speed of 2.4 meters per minute.<sup>4</sup> Delft Intensified Material Production (Delft IMP), a spin-off from TU Delft, is currently working on a

large scale project to deposit ultra-thin ALD films on powder material by a pneumatic transport reactor which allows for continuous deposition.<sup>6</sup> Moreover, Forge Nano has developed different kinds of rotary and fluidized batch reactors to deposit ALD films on particles. The company has plans to build a pilot facility to internally process up to 1,000 tons of anode material for the EV battery market this year.<sup>7</sup> Regarding the industrial application, benchmarking for ALD layers is needed. Up to now, very little is known on the current artificial EEs introduced at industrial level. Benchmarking would allow to properly compare the quality of typical ALD films for this application.

Moreover, molecular layer deposition (MLD) is attracting attention for battery applications. MLD is the organic counterpart of ALD and can fabricate organic and hybrid inorganic–organic thin films. The incorporation of organic segments in the MLD process offers additional combinations for the film structure, which could lead to unique mechanical, optical, and thermal properties.<sup>8</sup> Until recently, MLD has rarely been reported for deposition of artificial EEI films. The major concern is the instability at high voltage of the organic components in the MLD films. To be applicable on the cathode side, polymers with high voltage stability are needed. Moreover, polymers with good electronic or ionic conductivity should be developed. Nevertheless, it is still interesting to explore the application of MLD for artificial EEs due to the unique properties of MLD, such as high flexibility. Currently, artificial EEs with better mechanical properties are highly desired due to the large volume change of most promising anode materials (e.g. Si). Therefore, MLD films with high flexibility might be very promising for protecting the anode. The combination of hybrid ALD/MLD films could also be useful to meet the demands of specific applications.

The application of ALD/MLD for artificial EEs could also be interesting for battery technologies beyond  $\text{Li}^+$ , namely  $\text{Na}^+$ , Na-S, Na-Se, Na- $\text{O}_2$ ,  $\text{Zn}^+$  and  $\text{K}^+$  based batteries. In these types of batteries, similar problems arise at the electrode-electrolyte interface. Commercialization of certain next-generation batteries is inhibited by challenges such as structural changes and unfavorable side reactions at the interface. These issues need to be addressed in order to prevent rapid performance degradation and therefore limited battery lifetime.

Finally, the current work shows that the ALD toolbox could be further expanded, resulting in new ALD processes with unique properties. Also, excellent control over the film properties could be achieved. It is necessary to rationally engineer interphase of electrode materials to enhance battery performance. With this in mind, more opportunities and possibilities should arise for ALD and MLD chemistries in Li-ion battery applications. Hopefully, this thesis motivates researchers to explore the possibilities of ALD even further.



## References

1. S. Moitzheim, J. E. Balder, R. Ritasalo, et al. Toward 3D thin-film batteries: optimal current-collector design and scalable fabrication of TiO<sub>2</sub> thin-film electrodes. *ACS Appl. Energy Mater.* **2**, 1774–1783 (2019).
2. A. S. Yersak, K. Sharma, J. M. Wallas, et al. Spatial atomic layer deposition for coating flexible porous Li-ion battery electrodes. *J. Vac. Sci. Technol. A* **36**, 01A123 (2018).
3. TNO. Revolutionary battery. [www.tno.nl/en/focus-areas/techtransfer/spin-offs/lionvolt-revolutionary-battery](http://www.tno.nl/en/focus-areas/techtransfer/spin-offs/lionvolt-revolutionary-battery) (2021).
4. C.-T. Hsieh, C.-H. Chao, W.-J. Ke, et al. Roll-to-roll atomic layer deposition of titania nanocoating on thermally stabilizing lithium nickel cobalt manganese oxide cathodes for lithium ion batteries. *ACS Appl. Energy Mater.* **3**, 10619–10631 (2020).
5. A. Manzoor Soomro, J.-W. Lee, M. Waqas, et al. A robust surface-modified separator fabricated with roll-to-roll atomic layer deposition and electrohydrodynamic deposition techniques for high temperature lithium ion batteries. *J. Electrochem. Soc.* **167**, 160507 (2020).
6. Delft IMP. Dutch deep tech start-up Delft IMP secures €10 million series A funding to scale up technology that radically extends battery life. <https://delft-imp.nl/news/press-release-series-a> (2021).
7. Forge Nano. Forge Nano begins battery grade graphite enhancement program with Gratomic. <https://www.forgenano.com/forge-nano-begins-battery-grade-graphite-enhancement-program-with-gratomic> (2021).
8. Y. Zhao, L. Zhang, J. Liu, et al. Atomic/molecular layer deposition for energy storage and conversion. *Chem. Soc. Rev.* **50**, 3889–3956 (2021).





## Summary

Li-ion batteries power several portable electronic devices ranging from microsystems and portable electronics, up to electric vehicles. Moreover, batteries will play a crucial role in the future energy system and the strive to create a carbon-neutral society. However, further advancement of Li-ion battery technology is necessary to meet the future needs regarding power and energy density, but also battery safety and lifetime. One of the main obstacles in the improvement of Li-based battery performance is the electrode-electrolyte interface. Interfacial reactions often lead to unfavorable phenomena that can compromise the overall performance of Li-ion batteries. To achieve good interface compatibility between the electrolyte and electrode, artificial electrode-electrolyte interphases (EELs) are designed and engineered to stabilize and protect the electrodes. Fabrication of artificial EELs has drawn increasing attention due to its effectiveness in performance improvement, the ability for synthesis via scalable manufacturing technologies, and the tunability of properties in all aspects. Ideally, the artificial EEL should be ultrathin and continuous, block diffusion of electrons through the layer (depending on the nature of electrodes) and have a good mechanical strength. In this respect, the application of nanolayers prepared by atomic layer deposition (ALD) has attracted notable interest from the battery community because of the excellent conformality and precise growth control that can be achieved. These merits enable processing virtually on any substrate, from powders to porous substrates, or any other complex electrode surface structures for next generation batteries. In addition, ALD offers tunable film composition and relatively low deposition temperatures to design coatings specifically applicable to certain electrodes.

This PhD dissertation contains a review of the emerging applications of ALD for Li-ion batteries with a major focus on ALD processes for artificial EELs. A large part of existing literature studies focuses on the application of artificial EELs and the effect on the battery performance. The current work aims to develop and understand existing and new plasma-assisted and thermal ALD chemistries applicable for the synthesis of such layers. Specifically, lithium carbonate ( $\text{Li}_2\text{CO}_3$ ), lithium fluoride (LiF), and aluminum phosphate ( $\text{AlP}_x\text{O}_y$ ) are selected as these are promising candidates for artificial EELs. Insights into these ALD processes are achieved in terms of film growth behavior, surface reactions occurring during the ALD half-cycles, and film crystallographic, optical, electrical, and chemical properties, as well as film conformality on 3D structures. The common denominator among the chapters is the adoption of diagnostics during the ALD process, such as spectroscopic ellipsometry and mass spectrometry, to identify the surface reaction mechanisms and to learn how to tune the above-mentioned properties of the deposited films.

---

In the case-study of  $\text{Li}_2\text{CO}_3$ , the differences between the plasma-assisted process using  $\text{LiO}^t\text{Bu}$  and  $\text{O}_2$  plasma and the thermal process using  $\text{LiO}^t\text{Bu}$ ,  $\text{H}_2\text{O}$  and  $\text{CO}_2$  are identified in terms of film growth, reaction mechanism, stability upon ambient exposure and conductivity. The plasma-assisted process shows several advantages, such as a shorter cycle time, a higher growth per cycle, a larger temperature window, and the ability to form  $\text{Li}_2\text{CO}_3$  directly without using  $\text{CO}_2$ . By varying the deposition temperature and plasma exposure time, the reaction chemistry and hence the film stoichiometry and crystallinity of the films can be tuned. The  $\text{Li}_2\text{CO}_3$  films are shown to be purely Li-ion conductive, therefore potentially suitable as artificial EEI. ALD of LiF is investigated for a cycle including  $\text{LiN}(\text{SiMe}_3)_2$  and  $\text{SF}_6$  plasma. Interestingly, the LiF films show no changes in film stoichiometry, crystallinity or mass density for the various plasma conditions studied. Extending the plasma exposure time, however, leads to an increase in optical absorption and lower growth per cycle. Also, the gas phase reaction products are identified, and a reaction mechanism is proposed for the LiF process. Overall, the work demonstrates that  $\text{SF}_6$  plasma offers a promising alternative to other coreactants for ALD of high purity LiF. Furthermore, the process development and materials characterization of ALD  $\text{AlP}_x\text{O}_y$  using  $\text{AlMe}_3$ ,  $\text{PO}(\text{OMe})_3$  and  $\text{O}_2$  plasma is described. High purity, uniform films are achieved using a large deposition temperature window. Compared to earlier reported  $\text{AlP}_x\text{O}_y$  ALD studies using  $\text{H}_2\text{O}$  and  $\text{O}_3$  as coreactants or without coreactants, the adoption of  $\text{O}_2$  plasma generally leads to higher growth per cycle values and promotes phosphorus incorporation in the film. These findings are confirmed by investigation of the reaction products during the ALD half-cycles and result in the ability to grow better quality films.

In conclusion, this work provides key insights into the development of ALD processes as well as into the accurate control over film properties relevant for application in Li-ion batteries. The excellent control over the quality of the layers offered by ALD promises great potential for future Li-ion battery applications.





## Contributions of the author

The work presented in this thesis is the original work of the author. Some of the work was carried out in collaboration with individuals from academic and industrial institutions. Their contributions are stated below:

- RBS, EBS and ERD measurements in Chapter 4, Chapter 6 and Chapter 7 and were performed by W. Arnold Bik (Detect99).
- TEM images in Chapter 7 were obtained by dr. M.A. Verheijen.
- The electrochemical characterization in Chapter 4 was performed at Imec.
- *Ex situ* SE measurements in Chapter 6 were performed at J.A. Woollam Co.





## List of publications

Peer reviewed

### Atomic layer deposition of LiF using LiN(SiMe<sub>3</sub>)<sub>2</sub> and SF<sub>6</sub> plasma.

N. Hornsveld, W.M.M. Kessels, R.A. Synowicki and M. Creatore, *Physical Chemistry Chemical Physics* **23**, 9304-9314 (2021)

### Atomic layer deposition of Al<sub>x</sub>PO<sub>y</sub> using AlMe<sub>3</sub>, PO(OMe)<sub>3</sub> and O<sub>2</sub> plasma: film growth and surface reactions.

N. Hornsveld, W.M.M. Kessels and M. Creatore, *Journal of Physical Chemistry C* **124**, 5495–5505 (2020)

### Plasma-assisted ALD of LiPO(N) for solid state batteries.

B. Put, M.J. Mees, N. Hornsveld, S. Hollevoet, A. Sepúlveda, P.M. Vereecken, W.M.M. Kessels and M. Creatore, *Journal of the Electrochemical Society* **166**, A1239-A1242 (2019)

### Mass spectrometry study of Li<sub>2</sub>CO<sub>3</sub> film growth by thermal and plasma-assisted atomic layer deposition.

N. Hornsveld, W.M.M. Kessels and M. Creatore, *Journal of Physical Chemistry C* **123**, 4109-4115 (2019)

### Plasma-assisted and thermal atomic layer deposition of electrochemically active Li<sub>2</sub>CO<sub>3</sub>.

N. Hornsveld, B. Put, W.M.M. Kessels, P.M. Vereecken and M. Creatore, *RSC Advances* **7**, 41359-41368 (2017)

### Plasma-assisted ALD of LiPO(N) for solid state batteries.

B. Put, M.J. Mees, N. Hornsveld, A. Sepúlveda, P.M. Vereecken, W.M.M. Kessels and M. Creatore, *ECS Transactions* **75**, 61-69 (2017)

To be published

### Atomic layer deposition of Li<sub>x</sub>AlF<sub>y</sub> using LiN(SiMe<sub>3</sub>)<sub>2</sub>, AlMe<sub>3</sub> and SF<sub>6</sub> plasma for Li-ion batteries.

N. Hornsveld, M.M. Ameen, W.M.M. Kessels, S. Unnikrishnan and M. Creatore, *Manuscript in preparation*



## Acknowledgements

Finally, a long journey will come to an end. There have been many times when I thought I would never be able to arrive at the point where I could write this page. The past years sometimes felt like one obstacle after the other, but then again, I probably wouldn't have learned as much as I have now. Looking back on this adventure, there are many people I would like to thank. You all made it possible for me to reach to the final pages of my thesis and to close this chapter of my life.

To start with, I would like to thank **Adriana, Erwin** and **Maarten** for the opportunity to start the PhD project in the first place. I remember when I first came to Eindhoven for my interview. You all were spontaneous and friendly and the atmosphere at the university was really good. In the final interview with Erwin, he asked me about my hobbies and he told me that PMP had their own futsal team. At that time, I didn't know that in the future I would regularly play futsal for even four times a week. This is one of the things that made my time at PMP, and in Eindhoven in general, very pleasant. Adriana, it hasn't always been easy, but I am profoundly grateful for everything you've done for me. You always paid attention that I would investigate my data extensively and that I worked very accurately. This always led to better results. Also, your expertise on the chemical part of the project was very helpful. I learned a lot from your strength and perseverance. We are two very different personalities, and I am proud that we have delivered great work together. Erwin, you taught me the importance of building a good story and to deliver a strong message. Your critical view on my papers and thesis were very valuable. Thank you for improving the quality of my work a lot. Also, I would like to thank you for the good atmosphere within PMP, which of course is made possible by your effort as group leader. Maarten, your enthusiasm not only made me start the PhD, but also sparked my interest in lithium-ion batteries. Unfortunately for me, your new adventure at Imec soon caused our ways to separate. Thank you for being a friend and sharing beers, sports, coffees, and science with me during the first year of my PhD.

I am particularly grateful for the technical assistance given by **Cristian, Martijn, Jeroen, Joris, Caspar** and **Janneke**. You were always there to think along and offer support for the many technical problems that had to be solved during my PhD. There were days that we no longer held possible that something would go wrong again, but then it did. We have worked together tirelessly in the lab and I am very thankful for that. Besides, it was also just fun talking to you and to drink good quality coffee in the office in Spectrum. It was nice to share our frustrations when one disaster after another occurred in the lab. Your humor kept me going strong and helped me to put everything into perspective. Luckily, it was often very sunny in front of Spectrum and the little stairs near the ground floor entrance provided me a perfect spot for short

---

breaks. It would have been impossible to finish my PhD without your help. I am pretty sure the lithium powder left some indelible traces behind at TU/e..

I would like to thank **Jeanne** and **Lianne** for their assistance. You were always happy to help out with paperwork related issues. You both keep PMP very structured and organized. Jeanne, thank you for keeping track of all the deadlines and reminding me from time to time during the last phase of my PhD.

My sincere thanks go to **Brecht** with whom I collaborated a lot, mostly in the early stage of my PhD. When Maarten left the group, you were an excellent replacement. Despite the language barrier and misconceptions regarding Belgian and Dutch words we got along very well. I learned a lot from you about Li-ion batteries. It makes total sense that your colleagues from Imec called you mister impedance. It was great to work with you and I will never forget the conference in Hawaii and your wedding party. Only at the very end of the PhD I started collaborating with **Mahmoud**. It's a shame that we started collaborating only then, because I think we made a great team. Even though we did not reach to the results we were aiming for, I think some good progress was made. I really like your positive attitude and spirit to keep on going. In addition, I would like to thank **Harm** and **Marcel** for scientific discussions and giving me advice on several occasions.

Next to the conference in Hawaii, I also have great memories from the one in Boston. **Bas, Nick, Vincent** and **Bart**, thank you for the amazing road trip afterwards. Not only did I have a great time exploring many new places, we also got to know each other better. From champagne in a jacuzzi to cans of beer under a tarp in the rainy forest. Thank you for being so adventurous and for preventing (or setting?) a fire at my roof terrace. Bas, thanks for being as crazy as me and for offering support in the last phase of my PhD. Nick, thank you for sleeping through my coughing during our snowboard holidays and for being the most organized person during our trips. Vincent, I truly admire your sincere interest in almost everything, your general knowledge is fascinating. Also, thank you for always waking up at 6:00 a.m. to pre-explore the surroundings for us. Bart, thank you for being able to work on your VENI proposal in the smoke from the fireplace and introducing me to many new special beers and tricks to open bottles of beer. Unfortunately, it was impossible to keep up with my vegetarian diet with you guys. Nevertheless, thank you for all the barbecue parties. Hopefully, we will ever make it to an actual klup!

I would like to express my very great appreciation to **Dibya, Valerio, Martijn, Jimmy, Maria Antonietta, Gerben, Shashank, Karsten, Willem-Jan** and all the others that have been sharing Flux 3.096 with me. We usually spent very long days in the office and I always felt at home there. I hope you enjoyed the Nespresso coffee machine too, because I did. It was nice to have the Christmas tree in the office for almost a year. Ever since I left PMP I have been working at "flex" workplaces and I am missing the office so much. **Morteza, Sara,** and **Reyhaneh** thank you for the fun talks every now and then and for introducing me to some delicious exotic candies and other

food from your home countries. I would also like to thank all the other members of the **PMP group**. I had many amusing coffee breaks, drinks, and group outings because of you.

I want to thank my **friends** who were there during this journey. Thank you for the entertainment outside of work and for being understanding. Thank you for going on adventures with me, making me laugh and preventing me from throwing my laptop out of the window sometimes. After surviving my PhD together, I hope I can share a lifetime with you. **Aida, Sanne, Tom, Izy, Leandra, Seline, Ingeborg, Maeva, Sharon** and **Laura**, you especially supported me in some way I will never forget.

Many thanks to all my **family**. If I could choose my family members, there would be no doubt that it would be you as well. Although many of you never understood why I wanted to keep on “studying”, you have always supported me. Special thanks go to my parents, **Henk** and **Rie**, for being who you are and always inspiring me in your own way. **Leon**, I’m happy to have you as a brother and friend. **Keet**, what would I do without you? Thanks for being in my life. **Oma**, I also couldn't have finished this without you. Hopefully, time will allow us to catch up on some weeks I missed out on enjoying your lovely company.

Norah Hornsveld - December 16<sup>th</sup>, 2021



## Curriculum Vitae

November 25, 1989	Born in Soest, The Netherlands
2007 - 2011	Bachelor of Engineering degree Amsterdam University of Applied Sciences
2011 - 2012	Pre-master certificate Applied Physics University of Twente
2012 - 2014	Master of Science degree Applied Physics University of Twente
2015 - 2021	PhD candidate in the Plasma & Materials Processing group Department of Applied Physics Eindhoven University of Technology
2019 - Present	Lecturer Mechanical Engineering Institute for Design and Engineering Utrecht University of Applied Sciences







